III-V OMVPE GROWTH AND CHARACTERISATION OF GRADED $Al_xGa_{1-x}As$-GaAs LAYERS AND HETEROINTERFACES FOR THE DEVELOPMENT OF GRIN-SCH LASERS AND GUNN DIODES

Rajan Thavar

Submitted to the University of Cape Town
in fulfilment of the requirements for the
Degree of Master of Science in Engineering.

Department of Chemical Engineering
University of Cape Town
Rondebosch
Cape Town
South Africa

May 1994

To my wife , Jane

and my child , Nessan

ACKNOWLEDGEMENTS

The III-V material development program was largely funded by the CSIR with the aim of developing a local expertise in the growth and characterisation of microstructures. The author is grateful to the CSIR for providing the opportunity to carry out research in this field.

I would like to thank my supervisors Dr Jack C.Q. Fletcher and Ronny Muller for many helpful discussions and their support in the course of this work. The excellent guidance of Dr Jack C.Q. Fletcher is gratefully acknowledged. I am also indebted to many colleagues for their contributions :

Frik Snyman for technical assistance with the III-V reactor.

Martin J. van Staden and Wynand Louw for SIMS and Auger analyses.

Mario Marais and Greg Hayes for X-ray diffraction measurements.

Philip Jensen and Dr Klaus Möller for photoluminescence measurements.

Loughborough Consultants Ltd, UK for SIMS analyses.

Prof Danie Auret of the University of Pretoria for C-V analyses.

Dr Jeanne Basson and Craig Taylor for assistance with the project.

Finally, I wish to thank my wife, Jane Thavar, and my parents for their encouragement and support in this project. Special thanks to Jane for helping with the preparation of this manuscript.

SYNOPSIS

AlGaAs-GaAs graded index single confinement heterostructure single quantum well (GRIN-SCH SQW) lasers and both 35 GHz and 94 GHz Gunn diodes have been satisfactorily grown by organometallic vapour phase epitaxy (OMVPE). This work is based on the material development of such device structures and systematically shows the steps taken to achieve the final goal of repeatedly producing high quality devices geared towards small-scale production. The key elements of the process are the realisation of high quality AlGaAs compositionally graded layers, abrupt GaAs-AlGaAs as well as dopant heterointerfaces and silicon-dopant spikes.

A consistently high quality of epitaxial GaAs and AlGaAs is achievable with controllable silicon, tellurium and zinc doping on both material systems. The OMVPE system is sufficiently calibrated to grow sharp transitions in GaAs doping interfaces and quantum wells in the order of 2.5 nm. SIMS measurements showed almost square doping profiles in the 35 GHz Gunn diode structure and was able to resolve a 5 nm Si-spike doping layer in GaAs. The SIMS results of the 94 GHz Gunn diode material clearly indicates the presence of all layers with certain measured values evolving exactly as designed. These achievements are attributed to the fine pressure and flow control implemented on the reactor system by using automated steps to control the growth process.

A demonstration growth of doping grading of GaAs using silicon as a n-type dopant showed excellent results in terms of the linearity and quality of the grade. The choice of grading strategy for automated $Al_xGa_{1-x}As$ compositional grading, with a chosen attenuation resulting in AlAs steps of x = 0.02, was found to be suitable producing grades of high quality and any desired shape to suit the material application. A time-based compositional grading algorithm is useful in maintaining a consistent quality in the grown layers for producing satisfactory GRIN-SCH laser devices. GRIN-SCH SQW lasers, operated in pulsed mode, have produced power outputs as high as 5 W with differential quantum efficiencies of 55% whilst ridge waveguides have produced 80 mW continuous power. 94 GHz Gunn diodes have been produced with operation at 16 mW at 93 GHz at a phase noise of -85 dBC/Hz.

TABLE OF CONTENTS

LIST OF FIGURES

LIST OF TABLES

NOMENCLATURE

$Al_xGa_{1-x}As$	Aluminium gallium arsenide with mole fraction of AlAs = x.
AsH_3	Arsine.
Cs^+	Caesium used as primary ion source for SIMS.
Cu K-alpha 1	Radio-active Cu X-ray source.
C-V	Capacitance-voltage measurements.
cw	Continuous wave.
DETe	Diethyltellurium.
DEZn	Diethylzinc.
DH	Double heterostructure.
E_g	Bandgap energy of semiconductor.
Ga	Gallium.
GaAs	Gallium arsenide.
GRIN-SCH	Graded-index separate-confinement heterostructure.
GRIN-SCH SQW	Graded-index separate-confinement heterostructure single quantum-well.
GRIN-SCH MQW	Graded-index separate-confinement heterostructure multi-quantum-well
HB	Horizontal Bridgeman.
H_2	Free hydrogen.
H_2O	Water.
IC	Integrated circuit.
IR	Infrared spectroscopy.
LEC	Liquid encapsulated Czochralski.
LPE	Liquid phase epitaxy.
MBE	Molecular beam epitaxy.
mm-Wave	Millimetre-wave.
MOCVD	Metalorganic chemical vapour deposition.
MQW	Multi-quantum well
O_2^+	Oxygen used as primary ion source for SIMS.
OEIC	Opto-electronic integrated circuit.
OMVPE	Organometallic vapour phase epitaxy (also MOVPE).
P	Pressure (of growth, etc.).
PH_3	Phosphine.
pp_i	Partial pressure of component i.
ppm, ppb	Parts per million, parts per billion.
QW	Quantum well.
sccm, slm	Standard cubic centimeters per minute, standard liters per minute.
SEM	Scanning electron microscopy.
SH	Single heterostructure.
Si	Silicon used as n-type dopant for III-V materials.
SiH_4	Silane.
SIMS	Secondary ion mass spectrometry.
T	Temperature (of growth, etc.).
Te	Tellurium used as n-type dopant for III-V materials.
TEM	Transmission electron microscopy.
TMG	Trimethylgallium.
TMA	Trimethylaluminium.
VPE	Vapour Phase Epitaxy.
x	Mole fraction of AlAs in $Al_xGa_{1-x}As$.
XPS	X-ray photoelectron spectroscopy.
XRD	X-ray diffraction.
Zn	Zinc used a p-type dopant for III-V materials.
III-V	Group V and group III combination of elements to form semiconductors.

1. INTRODUCTION

The investigation of III-V compound semiconductor devices utilizing compositionally graded material and abrupt heterojunctions has shown promise for a variety of applications, including lasers, detectors, waveguides, transistors and a host of other novel devices. To understand and develop such specialised growth techniques, a knowledge of the growth mechanism and material characterisation methods is required. This work focusses on the organometallic vapour phase epitaxy of the GaAs-AlGaAs material system. In particular, compositional grading of AlGaAs, abrupt GaAs-AlGaAs heterojunctions, sharp doping interfaces and silicon doping spikes are key features pertinent to the development of two selected device structures viz. graded index separate confinement heterostructure lasers and millimeter-wave Gunn diodes.

1.1 History and Development of OMVPE

Bulk growth of compund semiconductors from a melt via liquid encapsulated Czochralski (LEC) and horizontal Bridgman (HB), can produce large quantities of single crystal material. However, for extremely fine control of thickness, composition and doping, epitaxial methods are necessary. Three major competing epitaxial technologies are currently used. These are liquid phase epitaxy (LPE), molecular beam epitaxy (MBE) and vapour phase epitaxy (VPE). In LPE, the crystalline growth results from a direct precipitation of a crystalline phase from a supersaturated solution. MBE growth utilizes an ultra-high vacuum system where growth results from molecular beams of the constituent elements impinging and condensing on a heated substrate. In VPE, the epitaxial growth results from a chemical reaction or decomposition of materials from a gaseous ambient. This study utilizes a VPE technique known as organometallic vapour phase epitaxy (OMVPE).

While LPE is the workhorse of epitaxial crystal growth, it lacks growth capabilities for more sophisticated structures. Conversely, MBE is particularly suited for high resolution growth of superfine structures. Nonetheless, OMVPE is the dominant growth method for new material structures and small-scale production, although, MBE is fast becoming a

more popular tool for those laboratories that can afford the high costs. Presently, OMVPE technology includes a wide variety of approaches each having its own characteristic advantages and disadvantages. For example, pre-pyrolysis of arsine has been employed to make better use of the available arsenic at the substrate [Shealy,1983]. New adduct compounds have also been investigated for use in OMVPE. An interesting approach still being developed by several laboratories [Heinecke et al.,1985; Heckingbotton and Prior,1985] involves a hybrid version of OMVPE and MBE where an MBE apparatus is modified to use organometallic sources. Alternative technologies, such as ion implantation and diffusion are limited in the kind of structures they can induce, although they are widely employed for GaAs integrated circuit (IC) fabrication.

The first satisfactory growth of GaAs single crystal by OMVPE was reported by Manasevit as early as 1968. He showed conclusively that GaAs could be deposited on GaAs, Ge and sapphire substrates by an essentially complete pyrolytic decomposition involving trimethylgallium (TMG) and arsine (AsH_3) in a hydrogen ambient according to the reaction :

$$Ga(CH_3)_3\ (g) + AsH_3\ (g) \rightarrow GaAs\ (s) + 3CH_4\ (g) \qquad (1.1)$$

He subsequently showed [Manasevit and Simpson,1969; Manasevit,1971] that it was possible to grow the entire range of III-V compounds using group III organometallics and group V hydrides containing Ga, Al, In and As, P, Sb, N respectively. Device quality AlGaAs grown by OMVPE was demonstrated in the early eighties [Saxena et al.,1981; Stringfellow,1981], although growth of this material had already been attempted as early as 1971 by Manasevit and coworkers. The dominant problem with AlGaAs growth was the incorporation of free oxygen, this being seriously enhanced by the reactivity of Al.

1.2 Technical background of OMVPE

In the most basic sense, OMVPE involves the transport of elemental constituents to the substrate surface where energy considerations result in their ordered incorporation via

epitaxial growth into the periodic crystalline array of the substrate. In this process, reactive precursors such as the organometallic group III compounds, eg. trimethylgallium (TMG), trimethylaluminium (TMA), triethylindium (TEI) and the toxic hydrides of the group V elements, eg. arsine (AsH_3) and phosphine (PH_3) are transported in the gas phase. The organometallic sources are liquids or solids supplied by a vendor in stainless steel bubblers through which a carrier gas (hydrogen) is passed. The carrier gas becomes saturated with the vapour and is transported by conventional gas flow to the crystal growth chamber. The hydrides are supplied in conventional gas cylinders. With known vapour pressures of the organometallics and known concentrations of the hydrides, control over the molar ratio of precursors can be effected. Although horizontal and vertical reactor configurations are possible, the reactor used in this study is horizontal and the discussion will be limited to this aspect.

Figure 1.2-1 The OMVPE reactor used in this study.

The fundamental processes occuring during crystal growth are commonly subdivided into thermodynamic and kinetic components, although the mechanism of growth is still largely speculative. It is believed to consist of a number of reactions involving both

homogeneous and heterogeneous pyrolysis of the group III and group V source molecules. These are subsequently reduced to elemental radicals followed by dynamic adsorption and desorption on the substrate surface. The exact mechanisms of pyrolysis are discussed extensively in Stringfellow [1989]. The hydrodynamics and mass transport, which are closely linked, control the rate of transport of material to the growing solid-vapour interface. Leys and Veenvliet [1981] showed that increasing the flow velocity, which results in a decreased boundary layer thickness, increases the growth rate. These observations point to mass transfer resistance being the rate limiting step at typical growth temperatures of 823 K to 1023 K. However, at lower temperatures, the growth rate decreases with decreasing temperature suggestive of a process limited by reaction kinetics [Stringfellow,1989]. Saxena et al. [1981] has reported the growth rate to be independent of substrate orientation. Additionally the growth rate was found to have a linear dependence on the group III flow rate when transport resistance is the rate limiting step for crystal growth. Furthermore, resulting crystal quality is influenced by the growth temperature such that there is no one set of growth parameters that can give optimum results for all applications in the OMVPE process. Consequently, the standard approach has been to treat the total process as a "black box" and the optimum conditions pertinent to the particular type of application and equipment are determined empirically.

The gas flow dynamics over the heated graphite susceptor has a large influence on crystal growth rates and uniformity and has been extensively investigated for the reactor of this study [Fletcher and Dickens,1991]. Reactants contained in the laminar flow are delivered to the growth surface at zero velocity by diffusion through a stagnant boundary layer. By careful manipulation of flowrates and tube geometry, the growth rates and uniformity can be controlled and, to some extent, predicted.

By far, the most research has been performed on GaAs and AlGaAs. The ternary, AlGaAs, is more sensitive to growth changes and hence requires more careful control of growth parameters. In addition, the reactivity of Al, which forms strong bonds with carbon and oxygen, presents difficulties in the growth of good quality material.

In the OMVPE growth of GaAs, S, Se, Te, Sn and Si are all used as n-type dopants. Si

is a desirable n-type dopant because of its low elemental vapour pressure and low diffusion coefficient in GaAs crystals. These properties are favourable for growing multi-structures with abrupt doping profiles [Liu et al.,1987; Mashito,1989; Shimazu et al., 1987]. Furthermore, silane does not exhibit a "memory effect"; this is a process whereby dopant species attach onto reactor sidewalls, etc. and outgas during later stages in growth to cause unintentional doping of subsequent layers. However, it should be noted that Si incorporation into GaAs is strongly dependant on growth temperature, hence any variation in growth temperature will cause non-uniform doping. Diethyltellurium as an n-dopant source is known to adsorb onto the reactor walls hence having "memory effect" problems that prevent the growth of structures with extremely abrupt doping profiles. The distribution coefficient of tellurium is also susceptible to temperature influences especially across the growth susceptor. Zinc is also by far the most widely used p-dopant in OMVPE and hence well documented in the literature [Bass and Oliver,1977; Masu et al.,1980; Yang et al.,1982]. It does however have a high diffusion coefficient. Magnesium, the only other major competitor, is extremely reactive with oxygen.

The two problems associated with the growth of $Al_xGa_{1-x}As$ and related to doping are oxygen and carbon incorporation into growth material [Stringfellow,1981; Shealy,1983; Terao and Sunakawa, 1984; Schaus, 1986]. With the high purity of organometallics and gases available and the leaktight integrity of the system, oxygen did not appear to have severely affected the layers.

1.3 GRIN-SCH Lasers and Gunn Diodes

Many possible applications for material bandgap engineering exist, e.g. modulation-doped field effect transistors (MODFET), heterojunction bipolar transistors (HBT), high electron mobility transistors (HEMT), etc.. In particular, two device structures have demanding bandgap and hence composition profile requirements, viz. the graded-index separate-confinement heterostructure (GRINSCH) quantum well laser and the millimeter-wave Gunn diode.

Figure 1.3-1 Schematic of GRIN-SCH SQW structure showing the variation of $Al_xGa_{1-x}As$ composition in the growth direction.

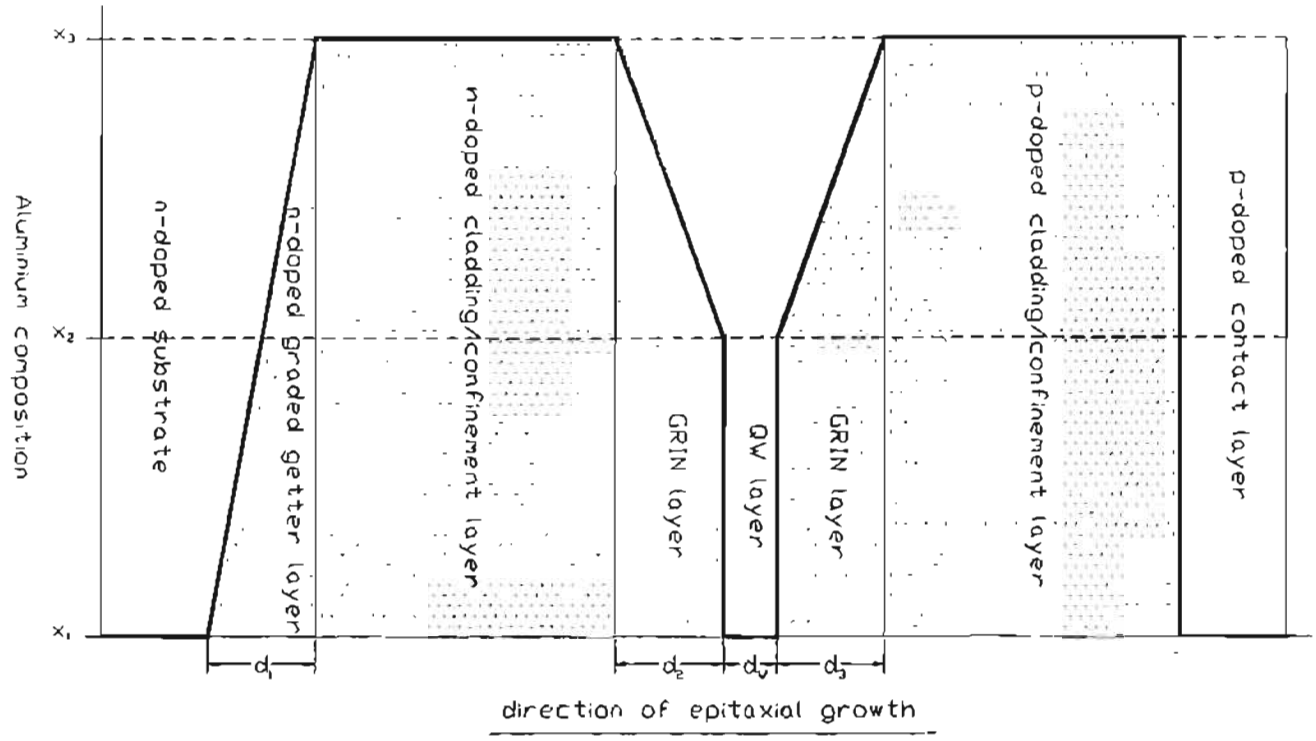

GRINSCH is one of the preferred laser structures for achieving high lasing-power at low threshold current densities and higher operating temperatures in comparision to double heterostructure (DH) lasers. Current applications that require low power consumption and high operating temperature include coherent optical communication, interferometric fiber optical sensors, magneto-optical disc drives and optoelectronic integrated circuits (OEIC) with low threshold characteristics. A theoretical model for graded-index, separate-confinement heterostructure, single quantum-well (GRIN-SCH SQW) lasers is presented by Chinn et.al. [1988]. It provides the necessary formulae for calculating the electron and hole energy states and the optical field distribution in GRIN-SCH SQW structures. These parameters are important in predicting the emission wavelength, modal gain and far-field patterns of lasers.

GaAs-$Al_xGa_{1-x}As$ GRIN-SCH SQW structures have been grown by OMVPE. A schematic illustration of the structure is shown in Figure 1.3-1 . The narrow GaAs quantum well is sandwiched between the considerably wider AlGaAs $Al_xGa_{1-x}As$ GRIN layers. The

GRIN layers have a linear compositional grading between x_2 and x_3. The cladding layers are doped p-type and n-type, respectively, in order to lower the series resistance of the laser diode. The structure provides separate carrier and optical confinement, hence the name separate-confinement heterostructure. The step in bandgap between the GaAs and the $Al_xGa_{1-x}As$ GRIN layers is large enough to confine most of the injected carriers within the GaAs quantum-well. If the $Al_xGa_{1-x}As$-GaAs junction is not abrupt, significant carrier leakage occurs which results in higher threshold currents required for lasing [Shealy,1987, Holonyak et al.,1980; Zhu et al.,1989]. This transition does not confine light for narrow GRIN layers. A well width of 5 to 10 nm is suggested to provide optimum performance for such devices [McIlroy et al.,1985]. The thickness of the quantum well can be estimated from the measured lasing wavelength. The graded composition of wider GRIN layers provides the varying refractive index necessary for light confinement and thereby forms the optical waveguide. The optical confinement factor for the waveguide is a function of the $Al_xGa_{1-x}As$ GRIN layer thicknesses and shape. Knowledge of the optical field distribution makes it possible to design laser structures with lower operating threshold currents and higher power outputs. If the GRIN layers were omitted from the conventional structure, shown in Figure 1.3-1, the result would be a conventional double heterostructure (DH) laser; this structure offers single confinement of both light and electrical carriers. Hence, the addition of GRIN layers, widely reported to result in higher efficiency devices, is paramount to improving performance of the laser.

A crucial requirement for realising the advantages of the GRIN-SCH SQW structure shown in Figure 1.3-1 relates to the ability to implement the controlled grading of AlGaAs. In addition, the shape of the GRIN layer, i.e. refractive index or AlGaAs composition versus layer thickness, influences device performance. This requirement represents a difficult task in the growth process. Nonetheless, such procedures are justified by the advantages of introducing GRIN layers, viz.

i. first and foremost, the graded region would act as a "funnel" to enhance the collection of electrons in the active layer [Hersee et al.,1983],
ii. they act as optical waveguides, as would be the case for an optical fibre of graded refractive index [Hersee et al.,1983; Schaus,1985],

iii. they prevent rectification at the interfaces [Escobosa et al.,1982],

iv. the most significant effect of the GRIN profile is on the thermalised carrier populations, which affects the non-radiative recombination rate in the GRIN layer. There is also evidence for more efficient carrier trapping in linearly graded layers [Chinn et al.,1988],

v. the graded layers offers the possibility of varying the wave propagation characteristics of the laser and controlling the far field beam distributions [Tsang,1981]. This could be used to match the particular type of optic fibre or imaging optics for maximum system benefit.

Thus, in general, the majority of work in the field of GRINSCH lasers assumes maximum advantage for linear grades [Chinn,1984; Hersee et al.,1983; Zhu et al.,1989]. However, for experimental simplicity, the regions of graded composition have typically been by a "staircase" variation of aluminium mole fraction rather than a continuous "smooth" variation. Whilst it is known that the stepped growth as opposed to a smooth grade is disadvantageous to device performance, the extent of this influence is unknown. In a more recent publication by Hirayama et al. [1992], a comparison is made between step, parabolic and linear GRIN layers. Using the same well size, it was found that the carrier injection efficiency is highest for the linear-GRINSCH laser because of low leakage of carriers into the optical-confinement layers. This means a lower optical loss and better device performance. Hersee et al. [1982] also reported a slight improvement in laser threshold for lasers having linearly graded GRIN layers as opposed to parabolic grades. This has not influenced other workers who use parabolic grades in their development of GRINSCH lasers [Tsang,1982; Kasemset et al.,1983; Ruyven et al.,1984].

Gunn diodes or transferred electron oscillators represent another class of devices that place stringent demands on crystal growers. In general, for simple Gunn diode structures, an n^+ (contact layer) ; n (active layer) ; n^+ (buffer layer) GaAs epitaxial structure is grown on low resistivity n^+ substrate material. Typical buffer layer thicknesses are 1000 nm to 5000 nm whilst contact layer thicknesses are 500 nm to 1000 nm. The active layer thickness is nominally 2000 nm to 4000 nm for devices operated in the fundamental mode at Ka-band frequencies of between 26 GHz and 40 GHz [Paolella et al.,1986]. In

the pursuit of higher power output for the traditional structure, a graded doping active region has been suggested, however, the device limits are soon realised and new approaches to material structure design are required.

For millimeter-wave Gunn diodes, one such solution is the incorporation of a hot electron injector element [Spooner and Couch,1987; Neylon et.al.,1989]. A schematic illustration of such a structure is presented in Figure 1.3-2. The hot electron injector incorporates both the graded gap and spike/collector layers. Its purpose is to provide the electrons with a large increase in energy (approximately 0.3 eV) over a few nanometers before they are launched into the active region during device operation. The injector functions by tailoring the electric field, current and charge distribution at the cathode end of the active region. The phenomena occuring during Gunn diode operation, especially in those devices which involve the concept of bulk negative differential resistivity, are detailed in Paolella et.al. [1986], Spooner and Couch [1989] and Neylon et.al. [1989].

Figure 1.3-2 Schematic of 94 GHz Gunn diode structure.

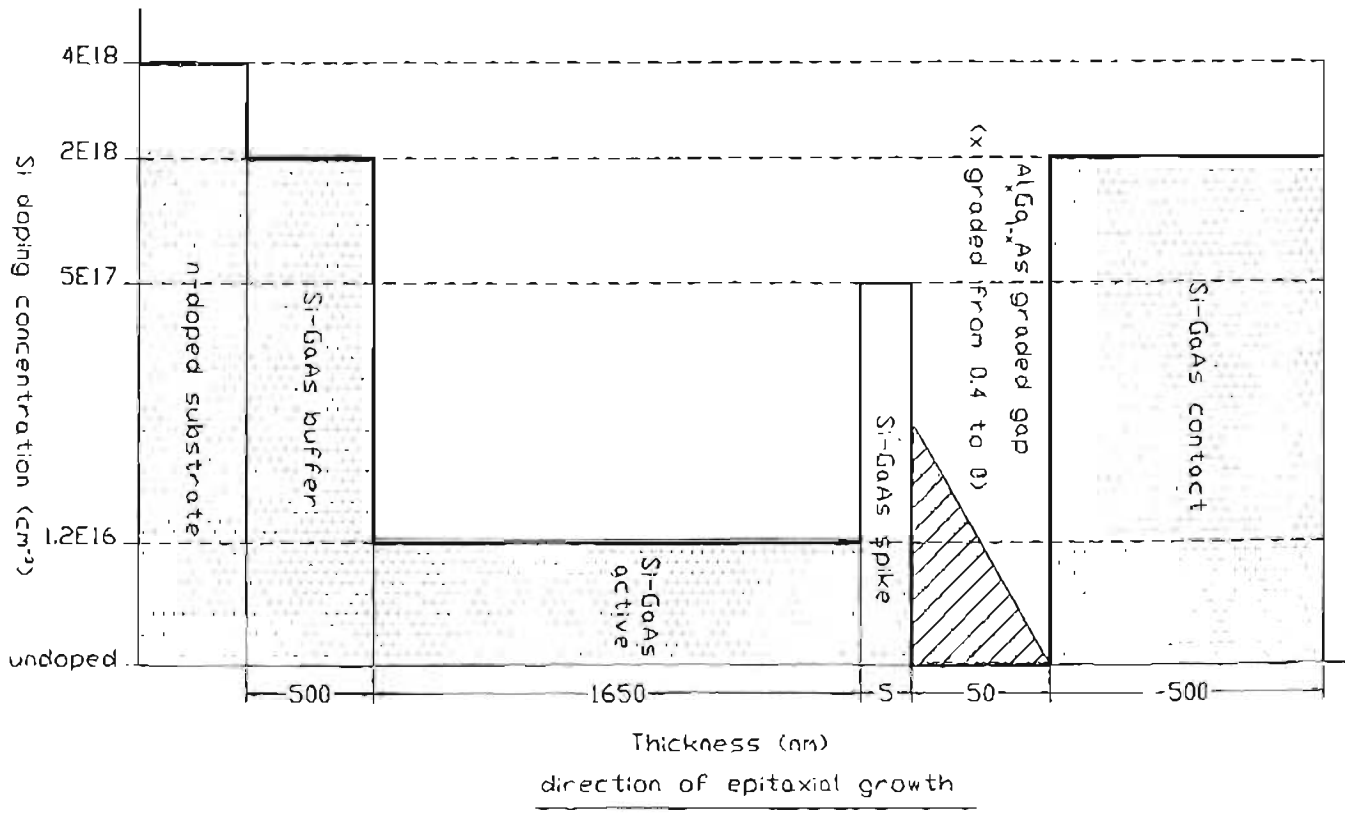

For the purposes of materials growth issues, the critical aspects of the Gunn diode structure are :

i. The thickness of the active layer. This dimension determines the transit length of the electrons and therefore the operational frequency.

ii. The doping level of the active region which influences device efficiency.

iii. The height of the potential barrier resulting from the linear AlGaAs grade. The barrier height determines the increase in energy of the electrons prior to entering the active layer, which in turn determines the efficiency of the hot electron injector.

iv. The doping level in the Si-spike. The carrier concentration needs to be large enough to limit the depletion layer associated with the AlGaAs-GaAs heterojunction .

v. The width of the Si-spike. In order to limit electron scattering, the width of the Si-spike must be less than the electron mean free path.

vi. A further requirement is that the junction between the active layer and the contact layer must be abrupt.

An optimally designed structure should produce up to 100 mW output power with greater than 3% efficiency at 94 GHz. Most Gunn diode structures have been grown using the MBE technique, which provides the precise control over the growth rate and doping level that is required [Paolella et al.,1986]. However, organometallic vapour phase epitaxy (OMVPE) has also achieved demanding specifications with respect to doping control, heterointerface abruptness and compositional grading [Tischler,1990].

1.4 Analytical Techniques

1.4.1 Photoluminescence

The composition of the ternary AlGaAs is controlled by the ratio of the two group III reagents trimethylgallium and trimethylaluminium (TMG and TMA) at the reaction site. The most widely used method for determining the solid composition is

photoluminescence. This technique gives a direct measurement of bandgap energy, which, from extensive literature results [Berolo and Woolley,1971; Onton et al.,1971; Dingle et al.,1977; Casey and Panish,1978; Stringfellow and Linnebach,1980; Schaus,1986; Prakask,1986; Menna et al.,1986; Kuech et al.,1987], can be related to the ternary composition. In AlAs the X indirect conduction band is lower than the L indirect conduction band and the Γ direct conduction band. Several determinations of the composition dependance of the energy gaps in $Al_xGa_{1-x}As$ show that the largest uncertainty is in the assignment of the energy gap (E_g) to x. In the aluminium mole fraction (x, $Al_xGa_{1-x}As$) composition region of x = 0.35 to x = 0.45 the ternary changes from direct bandgap to indirect bandgap material. The photoluminescence of indirect bandgap material is very poor and this technique is inadequate in this range. An alternative such as X-ray diffraction is more useful for determination in the full range of $Al_xGa_{1-x}As$ compositions. Both room temperature and 12 K measurements were used in assessments. Ideally low temperature measurements at 2 to 4 K are required for analysis however actual analysis at 12 K did not significantly influence the assessments. Low temperature measurements yield narrower peak widths in the spectra which are more easily resolved than broadened peak widths from room temperature measurements. Table 1.4-1 shows a summary of the equations used for compositional determination.

Table 1.4-1 $Al_xGa_{1-x}As$ composition equations ($E_g = a + bx$) for photoluminescence measurements based on a measurement temperature T.

Reference	a	b	T	Eqn. No.
Stringfellow and Linnebach, 1980	1.512	1.245	2 K	(1.4-1)
Casey and Panish, 1978	1.424	1.247	300 K	(1.4-2)
Kuech et al., 1987	1.512	1.455	2 K	(1.4-3)
XRD data regression	1.512	1.390	12 K	(1.4-4)

The more popularly used Stringfellow and Linnebach [1980] equation (2 K) is largely based on data from Dingle et al. [1977]. It is useful for the alloy composition range of $0 < x < 0.35$. There still remains uncertainties as far as the energy associated with the

bound exciton emission (usually 7 meV). Potential errors of 3 meV was however only representative of an error of 0.002 in the value of x. The more recent Kuech et al. [1987] equation (2 K) is claimed to be more accurate since it has been correlated with a nuclear reaction technique combined with Rutherford backscattering to yield the alloy composition. A 0.3% error limit is reported on values from the composition equation offered at compositions not exceeding 37% AlAs, at which point the material was found to be indirect bandgap. The regression equation obtained from XRD composition data shows a closer resemblance to the Kuech et al. [1987] equation. Room temperature measurements are analysed with the Casey and Panish [1978] equation applicable in the composition range up to $x = 0.45$. At higher compositions up to $x = 1$, an additional term, $+1.147(x-0.45)^2$, may be added for assessment of the X indirect energy gap.

1.4.2 X-ray Diffraction

X-ray diffraction represents a more direct approach to compositional assessment since it directly measures the lattice structural character which relates to composition. It is less influenced by impurities contained in the material and temperature effects. X-ray double crystal diffractometry is used to probe directly and non-destructively the atomic scale structural or lattice correlations. In the determination of AlGaAs there is an added advantage that the determination of the lattice parameter and hence the composition does not have to be done on an absolute scale. The epilayers are always grown on a substrate of a pure binary material, and so in a Bragg measurement we always see a Bragg peak from the substrate material. As we know the lattice parameter of the substrate very accurately, it can act as an internal standard.

From Braggs law ($n\lambda = 2d \sin\theta$) , it can be shown that :

$$\frac{\Delta d}{d} = \frac{\sin\theta_2}{\sin\theta_1} - 1 \qquad (1.4\text{-}5)$$

where, θ_2,θ_1 = Bragg angle of substrate and epilayer respectively.

d = lattice parameter.

n = wavelength of incident ray.

It can also be shown [Bartels and Nijman,1978] that :

$$\Delta\frac{d}{d} = (\Delta\frac{a}{a})_{\perp} \cos^2\psi \qquad (1.4\text{-}6)$$

where, ψ = angle between the crystal planes and crystal surface

$(\Delta a/a)_{\perp}$ = the measured difference in the lattice plane spacing perpendicular to the growth surface.

Also [Bartels and Nijman,1978] :

$$(\Delta\frac{a}{a})_{relax} = (Correctionfactor)\ (\Delta\frac{a}{a})_{\perp} \qquad (1.4\text{-}7)$$

where, $(\Delta a/a)_{relax}$ = the difference in lattice constant of the pure substrate and pure epilayer at room temperature (eg. for AlGaAs/GaAs it is $14x10^{-4}$).

The correction factors for various ternary semiconductor compounds, taking into account anisotropic elasticity, have been calculated by Honstra and Bartels [1978]. For AlGaAs/GaAs the correction factor = 0.525. Epilayers are grown on a (001) plane of the substrate, so $\psi = 0°$.

Thus from Equation (2.3-2) :

$$(\Delta\frac{d}{d}) = (\Delta\frac{a}{a})_{\perp} \qquad (1.4\text{-}8)$$

And from Equation (2.3-3) :-

$$(\Delta\frac{a}{a})_{relax} = 0.525\ (\Delta\frac{d}{d}) \qquad (1.4\text{-}9)$$

The aluminum content (x) is then determined by linear interpolation of $(\Delta a/a)_{relax}$ between the lattice constants of $Al_xGa_{1-x}As$ and GaAs i.e. 14×10^{-4}.

Therefore :

$$x = 375\ (\frac{\sin\theta_2}{\sin\theta_1} - 1) \qquad (1.4\text{-}10)$$

To compensate for the slight misorientation of substrate material, usually 2° off the (110) plane, rocking curves are done at R=0° and R=180°, and the Bragg angle is averaged from these, i.e.,

$$\theta_1 = \frac{\theta_1(0°) + \theta_1(180°)}{2} \qquad (1.4\text{-}11)$$

$$\theta_2 = \frac{\theta_2(0°) + \theta_2(180°)}{2} \qquad (1.4\text{-}12)$$

Hence, the final composition equation :

$$x = 375\ (\frac{\sin\theta_2}{\sin\theta_1} - 1) \qquad (1.4\text{-}13)$$

1.4.3 Hall Measurements and C-V Profiling

Hall measurements are performed using the Van der Pauw [1958] technique. Both room temperature and 77 K measurements are attainable from which carrier concentration and mobility of the material is derived.

In C-V analysis, a depletion layer is formed underneath the Schottky contact and the capacitance due to this layer is measured. The rate of change of the capacitance with the reverse bias voltage is a measure of the carrier concentration. With increasing reverse bias of the Schöttky contact the width of this depletion layer increases and this is the method used to do a depth profile of the carrier concentration. The fundamental

limitation on the resolution is the Debye length which varies with carrier concentration. The accuracy of the depth scale is limited by the uncertainties in the values of the dielectric constant and the area of the Schottky diode. The value obtained for carrier concentration was experimentally found to be within 3% of the correct value.

1.4.4 Secondary Ion Mass Spectrometry

SIMS analysis is performed on the basis of secondary ion counts and sputter times. Interpretation of depth profiles are complicated by a number of factors such as matrix effects (secondary ion yields and sputtering rate are dependant on layer composition) and the finite depth resolution attainable with sputtering methods. Matrix mixing as a result of ions released from side walls of the sputter hole and unstable ion beams with regard to energy are primarily responsible for a poor reflection of the true abruptness of an interface. Exponential tails, as they are referred to are commonplace and theoretical descriptions of such behaviour involve processes such as collisional mixing and selective sputtering. This is particularly noticeable when the sputtering proceeds from a layer of high aluminium or dopant concentration to a low one. It should also be noted that at beam energies in excess of 6 keV even a 50 nm thick layer of GaAs is incompletely resolved. Boudewijn et al. [1986] have performed extensive work in this regard and the reader is referred to their paper for more thorough explanations.

1.4.5 Quantum Well Thickness versus Lasing Wavelength

The Bastard and Brum [1986] model provides information about the discrete energies of an electron in a quantum well that is surrounded by AlGaAs cladding layers. Chinn et al. [1988] present a valuable model for GRIN-SCH SQW lasers which can be used to obtain valuable information about the operating characteristics of laser devices fabricated from a particular structure. The lasing wavelength of the laser diode can be predicted by calculating the quantised energies of the electron, light hole and heavy hole states in the GaAs quantum well. On the other hand, the thickness of the quantum well can be estimated from the measured lasing wavelength. The energy of the first electron is measured relative to the GaAs conduction band edge, whilst the hole energies are

measured relative to the GaAs valence band edge. The lasing wavelength corresponds to the electron-to-heavy hole transition whilst the electron-to-light hole transitions are a function of the quantum well thickness. The energy of transition is obtained by adding the quantised energies of the electron and hole states to the GaAs bandgap energy. Whilst the mathematical models for estimation of the quantum well parameters versus lasing or luminescence wavelength are too elaborate to reflect any kind of detail here, the reader is referred to the paper by Chinn et al. [1988] for the model and material constants from Casey and Panish [1978] for detailed analytical procedures. Using the design material parameters for quantum well structures, both 4 K and 300 K luminescence or lasing data can be analysed for quantum well thickness estimations.

1.5 Research objectives

The objective of this study is the material development of complex semiconductor device structures that require thin films, abrupt heterojunctions and homojunctions and compositionally graded material structures using the OMVPE process. In particular, compositional grading which forms the integral part of many devices and other stringent material constraints for two sophisticated devices are investigated. These devices are the GRINSCH quantum well laser and the millimeter wave Gunn diode. The material growth processes and characterisation techniques described in Section 2 are intended to provide a full understanding, albeit from empirical processes, of the development of these advanced semiconductor device structures. Suitable preliminary development stages where the individual characteristics of the more elaborate structures are investigated and shown in Section 3 together with the final development of device structures. A brief discussion ensues to relate the individual workpieces to the main purpose of the work.

The detailed investigative procedures are intended to fully qualify the process, so that reproducible and consistently high quality device structures could evolve and be accurately modelled for products with a technological edge. It is clear that compositionally graded material, finely controlled doping, abrupt heterointerfaces and quantum-well heterostructures represent areas requiring intensive development. The

validity of crystal-growers' claims are vitally important when predicted theoretical performance or modelling of the material is matched against actual performance. To this end, the growth techniques are carefully sized up against the empirically-obtained material characteristics and subsequently optimised for producing satisfactory devices.

Hence, the suitability of using OMVPE for the development of GaAs-AlGaAs GRIN-SCH SQW lasers and Gunn diodes and its applicability as a tool for commercial production is tested.

2. EXPERIMENTAL

2.1 Organo-metallic Vapour Phase Epitaxy

2.1.1 Growth System

High purity hydrogen passed through a palladium diffusion cell and containing less than 1 ppm of water or oxygen was used as the carrier gas. The pure organometallics, contained in bubblers at controlled temperatures, were transported by bubbling hydrogen through the liquids and saturating the carrier gas with the species. All gases were regulated and piped in through a gas manifold comprising of dual mass flow controllers, pneumatic valves for timeous operations and manual safety and purge valves to prevent cross contamination and undesirable leakages. The dual flow controllers were installed to extend the effective flow ranges while maintaining accurate flow control rated at 0.1% accuracy.

The OMVPE growth chamber consists of a horizontal double quartz tube assembly as shown in Figure 2.1-1. The outer tube is cylindrical, approximately 80 mm in diameter, and semi-permanently attached to the incoming gas and exhaust lines. The rear of the tube is flanged and sealed to a stainless steel flange and door assembly via viton o-rings under compression. The inner tube joins to the outer via a conical ground quartz joint at the front of both tubes afterwhich it is flared out to a rectangle quartz tube, 63 mm wide and 31 mm high. Outlet slots towards the rear of this inner tube are located on both the roof and floor of the tube duct. A graphite susceptor or sample holder, 150 mm long and 13 mm thick, is positioned (using an attachable quartz "push-rod") with its rear approximately 40 mm in front of the outlet slots of the inner tube. A control thermocouple, sheathed in a sealed thin-walled quartz tube, is introduced via an o-ring seal in the reactor door through the inside of the "push-rod" into the suspector to a distance of 43 mm from the rear of the susceptor. This point corresponds to the centre of the 50 mm wafer position. The susceptor leading edge is beveled at 45° and the susceptor growth surface is angled at 4° to the incoming gas flow by means of a graphite plate at rear of the susceptor. Slots for positioning samples are recessed 0.4 mm into the

susceptor surface. The reactor geometry was found to be hydrodynamically suitable for the OMVPE process in producing excellent uniformity in the characteristics of the material [Fletcher and Dickens,1991]. Susceptor heating is achieved via RF induction using a 12 kW RF generator. Quartz tubes and graphite susceptors were cleaned in aqua regia and gaseous hydrochloric acid/hydrogen mixture respectively after each growth.

Figure 2.1-1 Schematic of reactor tube assembly.

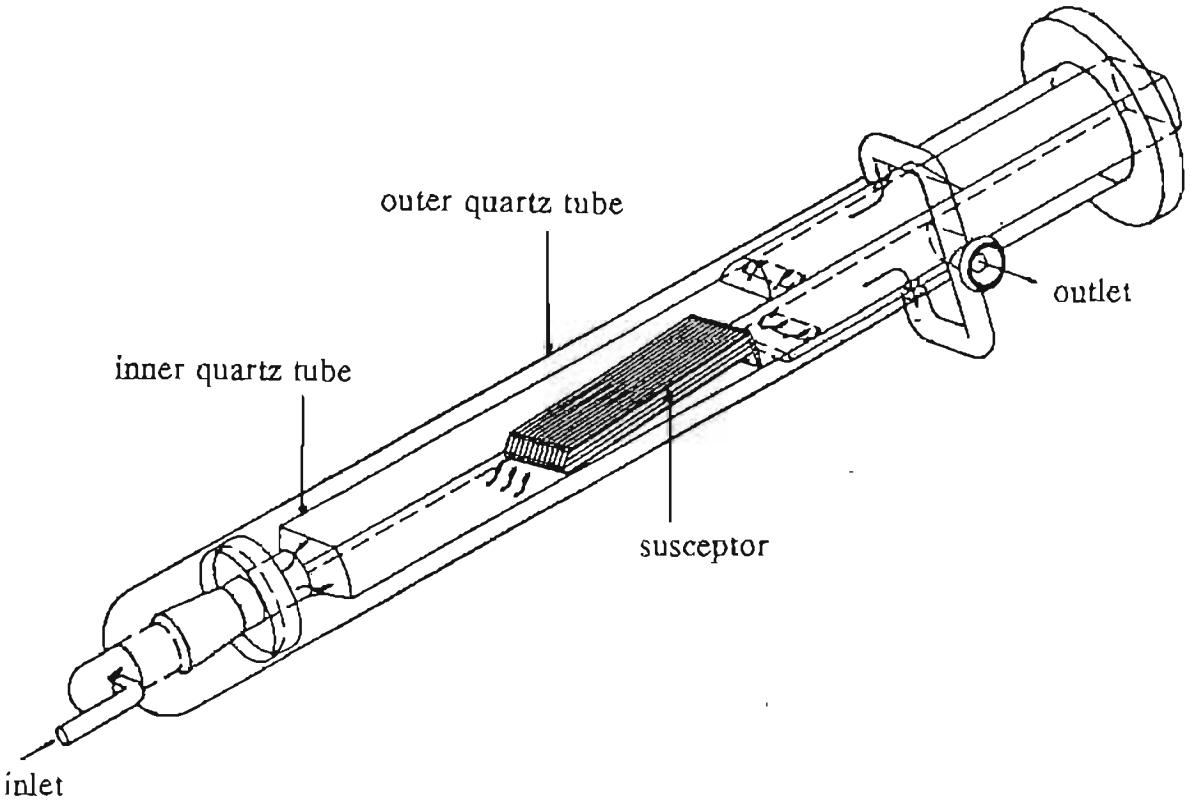

An eight-port radial switching manifold, just prior to the entrance to the reactor tube, switches all gas steams either to the reactor or to a vent line. A control valve, between the radial switching manifold and the tube entrance, controls upstream pressure at 1 bar absolute whilst a second control valve in the vent line maintains pressure balance between vent and reactor lines. Another control valve in the reactor exhaust line controls reactor growth pressure at any set point below atmospheric pressure. Prior to growth, the reactor tube assembly is evacuated to below $6x10^{-3}$ mbar for 20 minutes to check for sealing integrity and then brought back to atmospheric pressure under flowing hydrogen.

The single most important disadvantage of the OMVPE process is the use of extremely toxic hydrides and pyrophoric organometallics. Arsine has a threshold limit value of 50 ppb in the atmosphere. However, safety interlock systems and gas detection alarms have been specifically designed to create a safe working environment. Medical diagnostics and emergency procedures as well as breathing apparatus, breathing oxygen unit, appropriate fire extinguishes are readily available. Workers were tested twice annually for blood arsenic levels. These measures complied with guidelines adopted for a safe working environment.

2.1.2 Growth Conditions

Heated substrates have a tendency to lose arsenic oxides preferentially to gallium oxides, particularly at temperatures in excess of 623 K. A steady 1 mbar partial pressure of arsine was always maintained at excessive temperatures to reduce loss of the more volatile species which leads to surface defects on the substrate.

From previous experiments, it was found that the optimum AlGaAs quality was achieved at a growth temperature of 973 K and a growth pressure of 100 mbar with a total flow of 10 slm of hydrogen and precursors. The arsine partial pressure was maintained at 1 mbar and the group V to group III reagent molar ratio was held at 100.

GaAs material was grown under similar conditions with the exception of the group V to group III molar ratio (which was changed to 150 for better morphology) and the growth temperature. For homogeneous GaAs structures, a growth temperature of 923 K was used for lower background doping except in cases where the growth of multi-layered homogeneous structures were intended as test structures for the development of final heterogeneous device structures; these were grown at 973 K.

Low pressure OMVPE has the advantage of reduced autodoping and abrupt growth interfaces. Automated simultaneous switching of valves on the reactor, particularly on the radial switching manifold which is situated in close proximity to the reactor, for reagent flow lines during growth further ensure abrupt transitions at material interfaces.

2.1.3 Growth Technique

A typical growth procedure starts with designing an operations table that is suited to the desired material layered structure. All valve and mass flow controller operations are automatically controlled by a Hewlett Packard multiprogrammer that receives instructions from an algorithm executed from a Hewlett Packard HP9836 computer system. The algorithm interprets and executes the operations table systematically. A simple procedure for the growth of a GaAs single epilayer consists of the following steps:

i. Manually load sample onto susceptor in reactor; seal and purge reactor by direct pumping through the exhaust vacuum pump;

ii. Use flowing hydrogen carrier gas at approximately 6 slm to manually achieve a stable growth pressure of 100 mbar.

iii. Activate automated control of the reactor by loading and running the computer algorithms that execute the operations table. All operations from this point are automated.

iv. Introduce the first reagent line containing arsine to the reactor; the arsine partial pressure in the reactor should be 1 mbar; the balance of hydrogen to make up 8 slm total flow into the reactor.

v. Start RF heating of the susceptor to 1023 K and maintain at this temperature for 10 minutes to strip off native oxides of the substrate surface.

vi. Reduce substrate temperature to 923 K and allow 3 minutes to stabilise.

vii. Introduce the second reagent line containing TMG at the desired flow based on the V/III molar ratio of 150; the balance of hydrogen to make up 10 slm total flow into the reactor; growth commences at this point.

viii. Switch the second reagent line to vent at the desired end of growth; the time of growth is based on the growth rate of GaAs and desired epilayer thickness.

ix. Wait for 3 minutes before cooling sample down to 623 K; when the temperature is reached, switch the first reagent line containing arsine to vent.

x. Switch off RF heating; all reagent flows are closed off; lines are purged via a secondary vacuum system; hydrogen flows reduced to a total of 2 slm into the reactor; the reactor may also be brought up to atmospheric pressure; allow sample to cool to room temperature before unloading.

Two lines are used to pipe the group III/V reagents through to the radial manifold at the entrance to the reactor. Dopant streams are individually fed to the radial manifold at the reactor entrance. A main feed line carries 6 slm of hydrogen carrier gas into the reactor. The two III/V reagent lines each carry 2 slm (reagents with the balance being hydrogen) to make up a total flow of 10 slm. Should a dopant line also be fed to the reactor, then the flowrate in one reagent line being used is reduced by the flowrate of the dopant line eg., when running both III/V reagent feed lines and 200 sccm of silane dopant in hydrogen, the line carrying the group III reagents is reduced from 2000 sccm to 1800 sccm. A line permanently connected to vent carries 2 slm of hydrogen to flush the vent line and maintain a reasonable flow for reactor/vent differential pressure control.

It is standard practice to use one line to carry group III reagents and the other to carry group V reagents, both in hydrogen mixtures and each having a total flow of 2 slm. Both lines can be rapidly switched into the reactor or to vent by commands from the HP computer via a multiprogrammer control unit that switches the addressable pnuematic valves. This procedure is suitable when an homogeneous material structure such as the 35 GHz Gunn diode structure is chosen for growth. In the case of heterogeneous structures like the AlGaAs-GaAs system, a switch from GaAs growth to AlGaAs growth involves a sequence of steps that may have undesirable consequences in the final structure. The steps involved are :

i. Switch the line containing TMG to vent after the GaAs layer is grown. Note that a growth pause is necessary here and that the arsine stream in the other line is maintained to the reactor to preserve the heated substrate from decomposition and hence surface damage.

ii. Include the TMA flow in the line containing TMG and flowing to vent. Leave to stabilize after approximately 30 seconds.

iii. Switch the line containing the TMG and TMA into the reactor to initiate growth of AlGaAs.

The consequences of this process are :

i. switching of a line to vent and then to reactor causes a substantial reactor pressure fluctuation that could adversely affect the heterointerface abruptness and AlGaAs composition profile in the grown structure.

ii. Pressure imbalances propagate through the feed manifold and cause uneven pickup and contamination of reagents in the bubblers.

A solution to this problem is to place all the reagents for the growth of GaAs into one line and a second set of reagents for the growth of AlGaAs into the other line. Both lines are controlled at exactly 2 slm, the balance of gas in each line is made up of hydrogen carrier gas. The main hydrogen carrier line contains 8 slm of carrier gas. Simultaneously switching of the reagent lines, viz. the one into the reactor and the other to vent as desired, causes little pertubation to reactor pressure and hence minimizes any influence of the switching procedure.

2.1.4 Compositional Grading Techniques

Compositional grading is focussed on AlGaAs material although such grading for other ternary materials are also possible. The automated sequence of operations to enable compositional grading of AlGaAs involves optimizing a series of steps that alter the flowrates of the group III reagents controllably and in accordance with growth conditions for calibrated AlGaAs standards. The grading strategy employed (group V calculation basis) is to fix the group V hydride flow and hence the group V mole fraction whilst varying both the group III flows so that the group III total mole fraction remains constant. This implies that the group V-III molar ratio remains constant but the ratio of group III organometallics varies to suit the desired compositional change. Whilst it is known that the group III reagant concentration dominantly controls growth rates, the choice of using group V as the calculation basis rather than group III means that growth rates change with changing compositions. Historically, data collected for the single-layered growths were performed on the group V basis and hence it would have to entail

a vast amount of repeat experimentation and costs to change to the better group III calculation basis. The change in total flowrate, group V calculation basis, of reagants to the growth chamber is insignificant and hence does not affect pressure balancing or undesirable growth pertubations.

Grading, of the same material only, is implemented by selecting the start and end layers of different composition and specifying grading of a selected profile. Grading is determined according to equation (Equation 2.1.1) shown below :

$$x = f(t) \tag{2.1-1}$$

where,

x = mole fraction AlAs in AlGaAs,

t = growth time in seconds.

Whilst the precise shape of the curve is unlimited, it should be monotonic, giving the user total flexibility as to determining the exact profile required. A user-specified attenuator specifies the number of sub-levels within the grade; the smaller the step size in the staircase structure, the closer it resembles a smooth grade. A pre-determined function relating the group III mole fractions to the resultant solid composition is also required to enable the right choice of flowrates to implement the growth and remains a manual input to the growth process.

$$R_{III} = f(x) \tag{2.1-2}$$

where,

R_{III} = (TMA)/(TMG+TMA) reagant molar ratio.

This equation is obatined from calibration data collected from the compostion measurements of single AlGaAs epilayers grown under known conditions. It is possible to grow up to 10 graded layers in any single structure with the current algorithms. A total of 800 operations represents the upper limit in a single growth.

2.1.5 Dopant Grading Techniques

Dopant grading is implemented by continuously driving the dopant MFC between the extreme values set for it by appropriate start and end sublayers of the graded region. Thus in order to grade the carrier concentration in a given layer, the user specifies the carrier concentration from which grading is to begin (as the start layer) , the final carrier concentration at which grading must finish (as the end layer), the profile of the grading (carrier concentration as a function of time) and the profile "smoothness" (grading attenuator). Since the dopant flow rate is small in comparison to the total flow rate, the total flow rate is not compensated for the change in dopant flow rate during grading. Dopant grading equations are analogous to compositional grading equations and take the general form:

$$n = f(t) \tag{2.1-3}$$

where,

n = carrier concentration (cm^{-3}) in crystal,

t = growth time in seconds.

and

$$N_i = f(n) \tag{2.1-4}$$

where,

N_i = gas phase dopant mole fraction.

Dopant grading is possible for all dopants over the full range of mass flow controllers available. The grading techniques reflected here were employed for all of the subsequent work in this study and will be referred to henceforth.

2.1.6 Reagents

Commercial ultra-high purity grades of trimethylgallium, trimethylaluminium, pure arsine, diethyltellurium in hydrogen, diethylzinc and silane in hydrogen were used as precursor material. The organometallics were sourced from Epichem (UK) and the hydrides and

hydrogen mixtures from BOC (UK), Phoenix (USA) or Air Products (SA). These materials were chosen as a consequence of being the first commercially available high-purity sources. Arsine supplied by BOC yielded material of the best quality. Although new alternatives with different characteristics , for example, triethylgallium that produces lower carbon doping levels and organometallic arsine for lower pyrolysis temperatures, are entering the field, these were not investigated as part of this study. Whilst, in principle, gas sources from different vendors should not affect growth results provided they are specified in much the same way, recalibration to obtain composition and doping behaviour was always undertaken after every cylinder changeover. This was mostly because the gas and impurity concentrations within a specific cylinder was not accurately specified by vendors because it not undertaken on each cylinder.

The vapour pressure (V_p) equations used for the organometallic bubblers are presented below. The equation for trimethylgallium was obtained from Air Products (UK) and those equations for trimethylaluminium and diethylzinc were obtained from data from Strem Chemicals (USA). The temperature (T_b) range applicable to each bubbler is given in brackets together with the chosen control temperatures used in this study.

Trimethylgallium (applicable range : 253 K < T_b < 273 K ; control T_b = 264 K):

$$Log\, V_p = 8.07 - \frac{1703}{T_b} \qquad (2.1\text{-}5)$$

Trimethylaluminium (applicable range : 290 K < T_b < 303 K ; control T_b = 293 K):

$$Log\, V_p = 5.8851 - \frac{962}{T_b - 98.5} \qquad (2.1\text{-}6)$$

Diethylzinc (applicable range : 268 K < T_b < 303 K ; control T_b = 273 K):

$$Log\, V_p = 8.286 - \frac{2110}{T_b} \qquad (2.1\text{-}7)$$

Epilayers were grown on either undoped GaAs substrates oriented (100) 2° off towards <110> or Si-doped GaAs substrates oriented (100) and with a doping level of 1-4x10^{18} cm^{-3}. Substrates were purchased from either Sumitomo Corporation (Japan) or Nippon Mining (UK). These substrates were pre-packed in clean environments (designated Class 100) and required no prior chemical cleaning.

2.2 Assessment of Material Surfaces and Growth Rates

Visual inspection of the material surfaces on a microscopic scale gave an indication of the topographical features such as pyramids, mounds, dislocation lines, dendrites and waviness of the material using Normarski differential interference microscopy. Such physical defects were easily viewed even without chemical staining. More accurate tests employing X-ray topography for surface quality measurements were not necessary for these experiments.

For cross-sectional thickness measurements, samples were first stained with the A-B etchant [Olsen and Ettenberg,1974] prepared with $AgNO_3$ and HF in the aqueous A solution and CrO_3 in the aqueous B solution and adding equal volumes of A and B solution when the etchant is desired. Occasionally, a less harsh etchant was employed for AlGaAs and GaAs layers to obtain a proper contrast for thickness measurements. This consisted of mixing H_2O_2 and NH_3 buffered to pH = 7.9 . Because etch rates of bulk GaAs, epitaxial GaAs and AlGaAs are different, subtle differences in etched depth of these layers allows for easy distinction of the layers using interference microscopy. The stained samples were subsequently viewed with an optical microscope or scanning electron microscope to obtain the epilayer thicknesses. It should be noted that the etchants do cause rounding of edges which lead to erroneous measures of thicknesses. The duration of etching in these cases were minimised to seconds so that only stain-etching and not severe etching is obtained.

2.3 Determination of AlGaAs Composition

Both X-ray diffraction and photoluminescence were used for the determination of AlGaAs composition. Photoluminescence was used as a complementary and confirmatory technique to the more accurate X-ray diffraction technique.

2.3.1 Photoluminescence

The photoluminescence system comprised of the following equipment : a Spectra Physics Ar^+ laser Model 2020 using the 514.5 nm line for sample excitation at between 0.14 to 0.5 Watts; a Jobin-Yvon monochromator Model HR640 with enhanced PC prism software yielding a controlled resolution of 0.05 nm; an Air Products Helium sample cryostat capable of operation down to 12 K only and two thermoelectrically-cooled S1 and S10 photomultiplier tubes with detection capability of up to 850 and 1150nm. No sample preparation was necessary except for good smooth surface quality.

Analysis of data from photoluminescence spectra were performed by identifying the peak positions and using them in the equations by Stringfellow and Linnebach [1980] for 2 K measurements, Casey and Panish [1978] for 300 K measurements and Kuech et al. [1987] for 2 K measurements. These equations are shown in Table 1.4-1. The equation by Kuech et al. was used for later studies of AlGaAs as it was found to be more accurate when compared to X-ray diffraction results.

2.3.2 X-ray diffraction

Measurements on GaAs and AlGaAs material were performed using a Philips HRXRD diffractometer with a four-crystal monochromator consisting of high quality germanium crystals. Samples were impinged with a high flux of monochromatic, collimated Cu K-alpha1 X-rays incident at a wavelength of 0.1541 nm , and the (004) reflections were observed. Equation 1.4-13 in Section 1.4.2 was used to determine composition from the resultant Bragg peaks in the diffractograms.

2.4 Electrical Characterisation

2.4.1 Hall Measurements

The carrier concentration and mobility of single epilayers were assessed by Hall measurements. The Van der Pauw technique employed for this purpose required the deposition of four metallic contacts on the corner of a square sample whose dimensions were 5 mm x 5 mm. Annealed tin contacts were used for n-type GaAs whilst a tin-zinc alloy was used for p-type GaAs. Indium proved sufficient for both n-type and p-type AlGaAs. These contacts were found to be ohmic when using measurement currents of approximately 1 mA. Both room temperature and 77K measurements are achievable on the system, the latter requiring the use of a liquid nitrogen dewar for submersing the sample. The Hall measurement technique was found to be satisfactory for characterising material in the range of doping levels considered in this study using a magnetic field of 1500 Gauss. Measurements done on doped GaAs calibration samples showed variations that seldom exceeded 5% of the true values for carrier concentration and mobility as tested on known samples.

2.4.2 C-V Profiling

Wet electrochemical C-V profiling with a Polaron 4200 C-V profiler. Standard C-V measurements were performed at the Physics Department of the University of Pretoria. In the C-V measurement technique two electrical contacts were deposited on each sample, a Schöttky contact on the epilayer and an ohmic contact on the back surface of the n^+ substrate. In order to improve the resolution of the technique, the samples were cooled down to 11 K.

2.5 Qualitative Assessment of Heterostructures

2.5.1 Secondary Ion Mass Spectrometry

Local SIMS analysis was done on a VG ESCALAB MKII fitted with both gallium and an argon/oxygen duoplasmotron primary ion sources as well as a 0-800 amu quadropole mass spectrometer. Analysis of the AlGaAs grades were mostly performed using primary gallium ions at a beam current of 5 nA and energy of 10 kV with the beam rastered over an area of 0.175 mm x 0.165 mm at 10% gating for analysis. Whilst compositional and depth analysis was possible by using suitable calibration data, the extensive amount of work involved in calibration for the exercise was performed once only and subsequently abandoned. SIMS profiles were analysed on the basis of secondary ion counts and sputter times. SIMS on the Si spike doping test structure was done on a CAMECA IMS4F at Loughborough Consultants, UK. Both Cs^+ and O_2^+ primary ion bombardment was used. The Cs beam enables the measurement of the Si doping level at the 10^{16} cm^{-3} level, while the O_2^+ beam enables better resolution of the Si-doped layers. The Si doping level was quantified to an accuracy of approximately 10%, the depth scale to approximately 4%. The beam was rastered over 0.25 mm x 0.25 mm, while ions were collected from a circle of 0.06 mm diameter in the middle of the sputtered area.

2.5.2 Aüger Electron Spectroscopy

A Scanning Aüger Microprobe PHI595 was used for the Auger analysis of the AlGaAs samples. The background pressure was $2x10^{-9}$ Torr whilst the Argon sputter pressure was $2x10^{-8}$ Torr. A beam voltage of 5 kV was used and the beam current was 0.2 μA.

2.6 Device Measurements

The testing of GRIN-SCH SQW lasers were performed on crudely made devices processed from growth material. This comprised of full surface metallization of both n- and p-type faces using a Au-Ge-Ni alloy for n-type contacts and Au-Zn alloy for p-type

contacts. The block lasers measured 0.6 mm x 0.3 mm or 0.9 mm x 0.3 mm and were usually between 0.05 mm to 0.1 mm thick. Pulsed mode lasing was produced from the entire 0.3 mm edge facet; a more efficiently-performing device would have been a ridge waveguide or striped metallization structure in continuous-wave (cw) mode of operation, however, the crudely processed block lasers represented the quickest method for obtaining important device characteristics. Lasing characteristics were evaluated on a spectrum analyser and silicon-PIN detector system; the light capturing efficiency of the detection system was not evaluated. Lasing wavelength (λ), threshold current density (J_{th}), power output and differential quantum efficiency (DQE) were measured in pulsed mode operation using a 1 μs pulse width at 1 kHz pulse repetition frequency .

Chinn et al. [1988] presents a valuable model predicting the operating characteristics of GRIN-SCH SQW lasers based on a particular material structure. Reference to this model and a brief discussion appear in Section 1.4.5 .

Measurements on processed Gunn diodes were undertaken at another laboratory and information regarding the processing and measurement techniques is protected by secrecy agreements between the two organisations.

3. RESULTS

3.1 Development of Homogeneous Materials

3.1.1 Gallium Arsenide

3.1.1.1 Undoped GaAs

During early experimentation epitaxial GaAs was grown by OMVPE for a range of reactor pressures, susceptor temperatures, arsine partial pressures, group V to group III reagent molar ratios and gas flowrates. Increasing the temperature from 923 K to 973 K causes an increase in residual donor and acceptor doping when trimethylgallium and arsine are the precursor sources. At lower V-III ratios the material is p-type with high carbon impurity doping as indicated by photoluminescence measurements. At V-III ratios exceeding 80 the material is found to be n-type. Growth at low pressure is found to cause a slight improvement in electrical characteristics. Growth at lower reactor pressures increases the diffusion coefficient of growth species and hence the mass transport rate. A total flowrates of 10 slm was sufficient to create laminar conditions without the appearance of flow pertubations. These results are in agreement with the findings obtained by Stringfellow [1989].

The standard conditions for the growth of GaAs are :

temperature = 923 K,
pressure = 0.1 bar,
group V-III molar ratio = 150,
total flow rate = 10 slm,
arsine partial pressure = 0.001 bar.

The best results for a single epilayer grown under these conditions were a 300 K carrier concentration of 2×10^{14} cm^{-3} and a 77 K mobility of 141000 $cm^2V^{-1}s^{-1}$. Although this record was never matched in subsequent trials, subsequent growths in preparation for device development yielded consistently high purity material with background carrier concentrations lower than 1×10^{15} cm^{-3}.

Typical growth rate at the optimum conditions, as determined by edge staining of the samples and observing under a Normarski microscope, was found to be 0.556 nms^{-1}. Thicknesses of epilayers up to 20000 nm layers have been grown. Non-uniformity in background doping across a 50 mm diameter wafer was small. Ignoring edge-effects on a two-inch wafer, approximately 10% of the rim area of a wafer, the growth rate uniformity showed a 6% variation in both the flow direction and laterally [Fletcher and Dickens,1991].

3.1.1.2 Silicon-doped GaAs

Several growths were conducted to obtain GaAs carrier concentrations for various silane mole fractions in the reagant gas. Both 47 ppm and 290 ppm silane in hydrogen sources were available for doping GaAs. The growths were conducted at temperatures of 923 K and 973 K. Figure 3.1-1 shows the relationship between the dopant mole fraction in the reagant gas and the carrier concentration in the epilayers.

Figure 3.1-1 Silicon doping of GaAs.

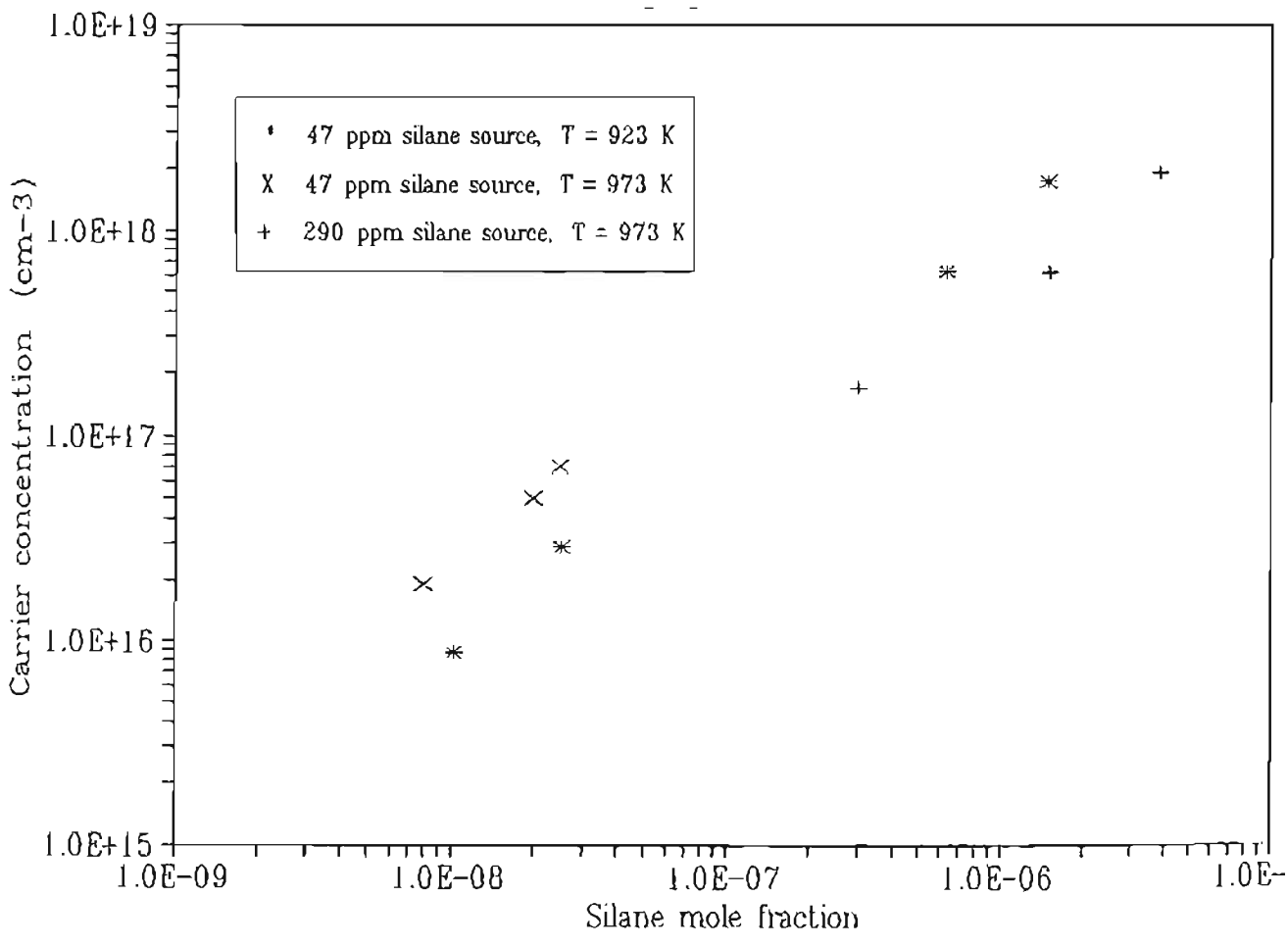

Epilayer thicknesses of samples grown over one hour were observed at 1800 nm for those grown at a temperature of 923 K and 2000 nm with a variation of 50 nm for those grown at a temperature of 973 K. The growth rate for Si-doped GaAs is not influenced by the doping levels considered in this study. When the silane mole fraction is fixed at $2.5x10^{-8}$, a change in the growth temperature from 923 K to 973 K causes a corresponding change in doping from $3x10^{16}$ cm^{-3} to $7x10^{16}$ cm^{-3}.

From the XRD data in Table 3.1-1, it is clear that doping causes a small shift in the Bragg peak position for undoped GaAs. This suggests little distortion to the lattice from the dopant species. Furthermore, the consistently small values for full width at half maximum (FWHM) imply good crystal quality has been achieved.

Table 3.1-1 Results of X-ray diffraction measurements on silicon-doped GaAs.

Growth Number	Doping in cm^{-3}	Bragg peak in °	FWHM in arc sec
GA110	undoped	31.0295	14.9
GA114	$8.7x10^{15}$	31.1885	14.4
GA111	$2.9x10^{16}$	31.2120	18.0
GA113	$6.3x10^{17}$	31.4675	16.0

Photoluminescence spectra of a Si-doped GaAs epilayer at 12 K indicate a lower energy peak (830 nm to 832 nm) when compared to the GaAs exciton peak (815 nm to 819 nm). The FWHM of the peak due to silicon doping is of the order of 18.4 meV. The broad peak is probably due to the measurement temperature of 12 K which is currently the lowest possible temperature achievable on the measurement system; other impurity responses are not distinguishable, hence analyses of impurity levels at the high measurement temperature are difficult.

3.1.1.3 Tellurium-doped GaAs

Figure 3.1-2 shows the dependance of carrier concentration on the diethyltellurium mole fraction in the reagant at a growth temperatures of 973 K.

Figure 3.1-2 Tellurium doping of GaAs.

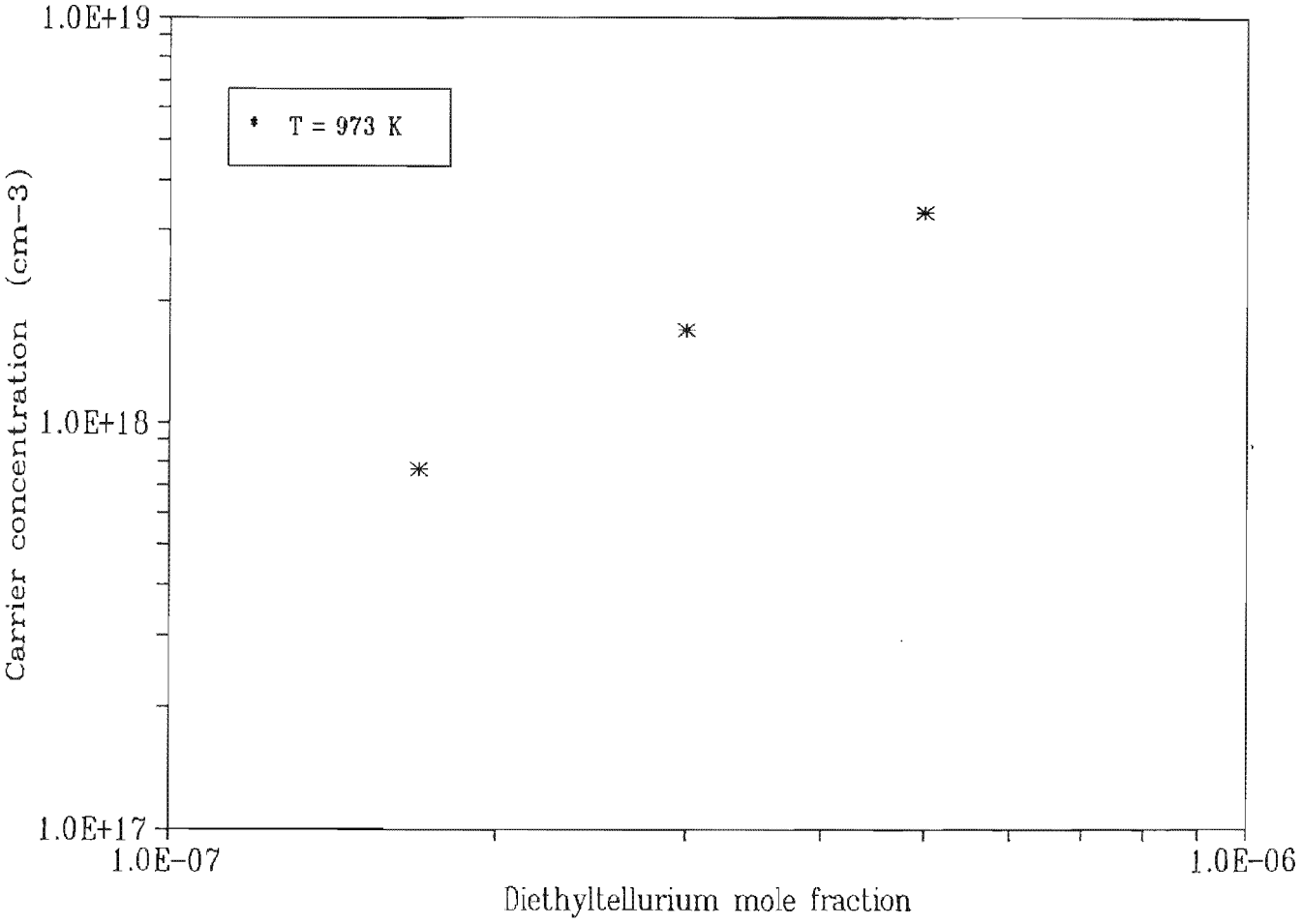

Two growth experiments were undertaken to determine the doping uniformity from front to back across a two-inch wafer. Results from Hall measurements show that the carrier concentrations decreased from 9.4 x 10^{17} cm^{-3} to 8.4 x 10^{17} cm^{-3} and from 2.1 x 10^{17} cm^{-3} to 1.8 x 10^{17} cm^{-3} in the two wafers analysed. This variation can be attributed to depletion of dopant species downstream in the gas flow and a slight temperature variation on the susceptor.

3.1.1.4 Zinc-doped GaAs

Diethylzinc was chosen as the p-type dopant because of its controllable incorporation and the wide range of doping levels achievable in GaAs. Several growths were conducted to obtain GaAs doping concentrations for various diethylzinc mole fractions in the reagant gas. Figure 3.1-3 shows the relationship between carrier concentration, as measured by the Hall technique, and the diethylzinc mole fraction.

Figure 3.1-3 Zinc doping of GaAs.

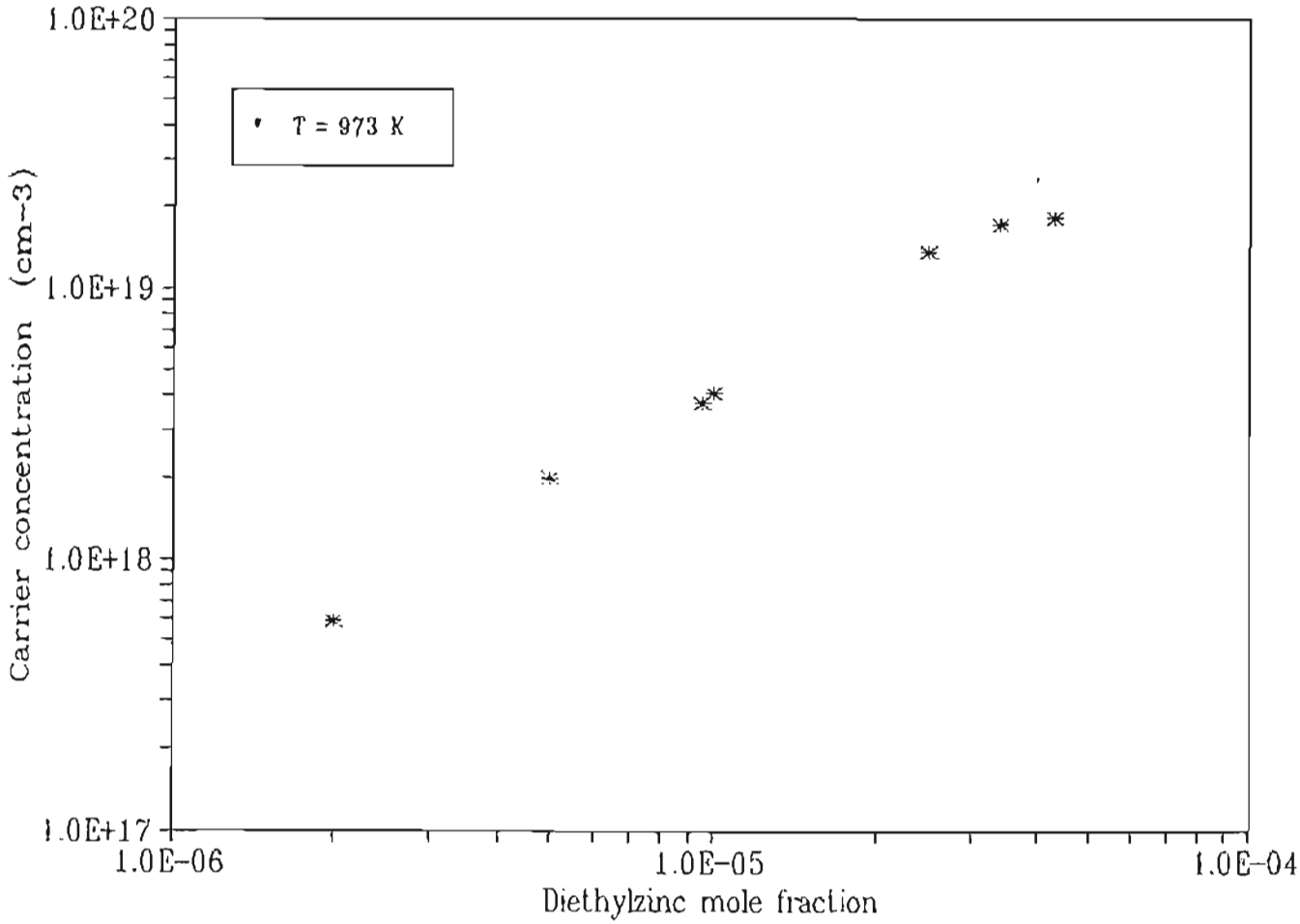

Doping uniformity across a 50 mm diameter wafer for a Zn-GaAs capping layer, used for obtaining good ohmic contacts in devices, ranged in doping from 4.1 x 10^{18} cm^{-3} to 3.4 x 10^{18} cm^{-3} when grown at 923 K.

3.1.2 Aluminium Gallium Arsenide

3.1.2.1 Undoped AlGaAs

Earlier work

The standard AlGaAs growth conditions were :

temperature = 973 K,
pressure = 0.1 Bar,
group V-III molar ratio = 100 ,
total flow rate = 10 slm.

The AlGaAs grown was specular to the unaided eye and although numerous defects described as "coin" features in the literature [Johnson and Legg,1988] were present, the surfaces between these defects were featureless when inspected by Normarski optical microscopy. Photoluminescence on $Al_xGa_{1-x}As$ in the range x = 0 to x = 0.45 showed sharp well-defined exciton peaks indicating material of good optical quality. These PL spectra are shown in Appendix II. Electrical properties of $Al_xGa_{1-x}As$ at a composition of x = 0.5 show the carrier concentration at room temperature at $8.7x10^{15}$ cm^{-3} and the mobility at room temperature at 167 $cm^2V^{-1}s^{-1}$. These characteristics are typical of an $Al_xGa_{1-x}As$ composition of x = 0.5 [Kaneko et al.,1977].

In arriving at the above conditions, the growth conditions were varied to ascertain which parameters have a dominant influence on the surface morphology. The effect of growth temperature, pressure and group V-III ratio on surface morphology were investigated. Growths carried out at 923 K in addition to the standard temperature of 973 K showed negligible effect on morphology. Similarly a higher growth pressure of 0.860 Bar had no apparent effect. In general, the morphology of the grown material is substantially influenced by V-III ratio. The morphology improved as V-III ratio was increased with a great reduction in surface defects at a V-III ratio of 100.

AlGaAs growth uniformity, in the direction of gas flow, was determined from experiments with 4 samples measuring 10 mm x 15 mm placed along the centreline of the susceptor. The results of this test are presented in Table 3.1-2.

Table 3.1-2 AlGaAs composition uniformity (x in $Al_xGa_{1-x}As$) over the susceptor. Positions 1,2,3 and 4 are in line with gas flow.

Growth Number	Sample Position 1	Sample Position 2	Sample Position 3	Sample Position 4
AGA12	0.253	0.253	0.253	0.290
AGA9	0.371	0.371	0.392	0.410
AGA10	-	0.437	0.437	0.478
AGA17	0.575	0.575	0.600	0.652

Position 2 and 3 cover approximately 90% of the length occupied by the 50 mm diameter wafer typically used for crystal growth with position 1 and 4 lying upstream and downstream of the wafer position.

In order to implement AlGaAs compositional grading and to ensure accurate compositional control in multilayered device structures, two growth calibrations are required : the first between AlGaAs solid composition and the (TMA)/(TMA+TMG) gas phase molar ratio (group III molar ratio), and the second between AlGaAs solid composition and the growth rate. Since the material and device structures of this study were grown over a period of approximately 3 years, the calibrations were determined several times during the course of this study. The reasons for recalibration of the growth data were :

i. Different commercial sources of organometallics were used with different bubbler dimensions and purity levels of reagents,

ii. Improved analytical techniques were employed on grown layers with each new development.

iii. The reactor system configuration was modified twice during this period of study.

For the purpose of these calibrations, samples of $Al_xGa_{1-x}As$ in the composition range x = 0 to x = 0.6 were performed at various (TMA)/(TMG+TMA) ratios, each over a period of 1 hour. Measurement of the resultant epilayers involved photoluminescence (PL) and X-ray diffraction spectroscopy (XRD) for composition and scanning electron microscopy (SEM), optical microscopy and infrared (IR) measurements for layer thicknesses . Calibration standards for AlGaAs were grown on four separate occasions, each yielding slightly different outcomes. The results are presented under the individual calibrations of composition and growth rate for AlGaAs. X-ray diffractograms and photoluminescence spectra are presented in Appendix II.

First Calibration of Composition and Growth Rate

Initially, a fixed growth rate of 1.111 nms^{-1} was assumed for all $Al_xGa_{1-x}As$ compositions in the range x = 0 to x = 0.5 . The AlGaAs solid composition resulting from various group III gas phase molar ratios are presented in Table 3.1-3 and Figure 3.1-4. These were derived using XRD data in conjunction with equation (1.4-13) of Section 1.4.2.

Table 3.1-3 Measured AlGaAs data from the first calibration of composition and growthrate.

Growth Number	Reagant molar ratio (TMA)/(TMA+TMG)	x in $Al_xGa_{1-x}As$ using XRD data
OMA011	0.0244	0.065
OMA007	0.0476	0.105
AGA47	0.0870	0.200
AGA50	0.2632	0.500

Figure 3.1-4 $Al_xGa_{1-x}As$ composition curve from the first calibration.

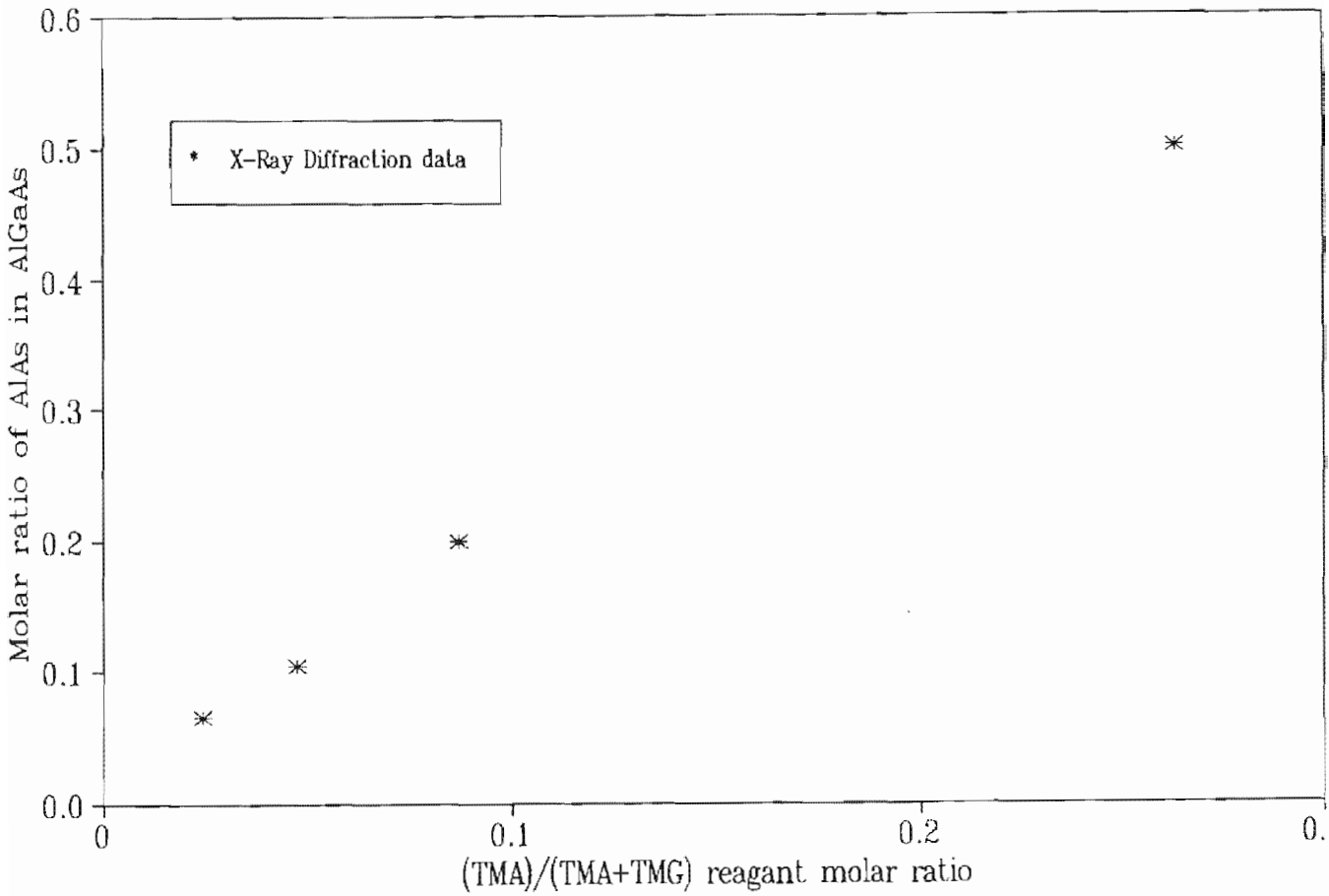

Second Calibration of Composition and Growth Rate

X-Ray diffraction and photoluminescence measurements were performed on these growth samples. The AlGaAs solid composition versus group III gas phase molar ratio data together with SEM results are presented in the Table 3.1-4. Equations (1.4-13) and (1.4-1) were used for the interpretation of X-ray diffraction and photoluminescence data respectively.

Table 3.1-4 Measured AlGaAs data from the second calibration of composition and growth rate.

Growth Number	Reagant Molar Ratio	x in $Al_xGa_{1-x}As$		Growth rate (nms^{-1})		
	$\frac{TMA}{TMG+TMA}$	XRD	PL	SEM	MICRO SCOPE	IR
AGA58	0.034	0.078	0.075	0.952		1.050
AGA56	0.091	0.216	0.209	1.014	0.850	1.042
AGA57	0.125	0.294	0.287	1.050	0.944	1.072
AGA60	0.170	0.377	0.373	1.236		
AGA59	0.220	0.478		1.217	1.167	1.183

Thickness values obtained from stained samples under an optical microscope are consistently lower than other results. This can be attributed to etching and rounding of edges during the stain-etching process prior to microscopy. The infrared results obtained from interference fringes in an IR measurement of the layer is not thought to be accurate because it is subject to composition variation and absolute thickness influences. It does however correspond well with the SEM results. SEM measurements without prior staining of the samples were possible using the backscattering technique which is sensitive to material matrix changes. The SEM results have the highest resolution.

Graphical representation of the data is shown in Figures 3.1-5 and 3.1-6. A bowed curve is seen when the percent of AlAs in the solid ternary is plotted against the reagant molar ratio (TMA)/(TMA+TMG). Both SEM and optical microscope data show the growth rate to increases with aluminium composition in the solid.

Figure 3.1-5 $Al_xGa_{1-x}As$ composition curve from the second calibration.

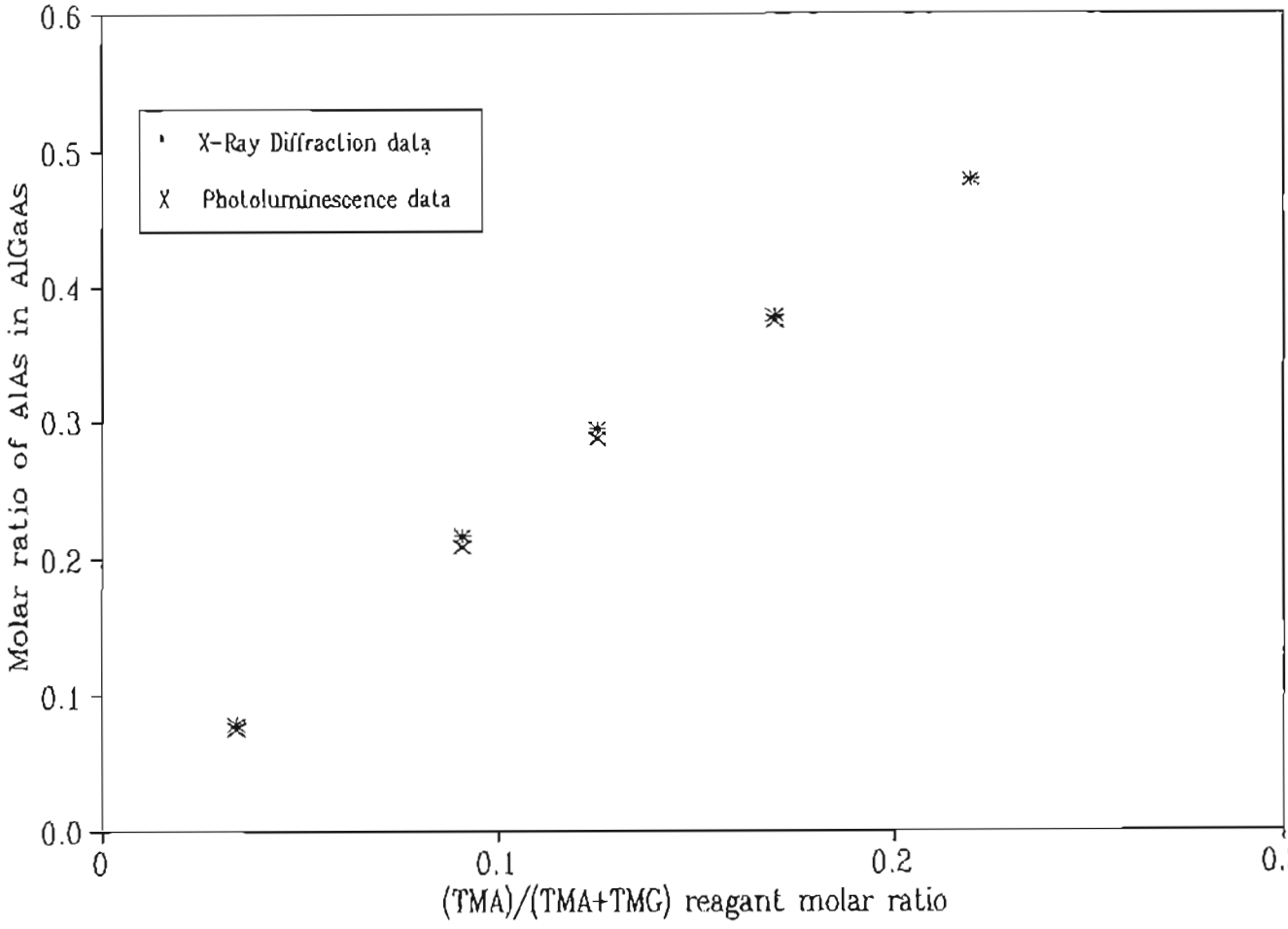

Using the least squares curve-fit technique, the following empirical relation was obtained between the group III gas phase molar reagent ratio and AlGaAs solid composition.

$$R_{III} = 0.0011 + 0.3828x + 0.1587x^2 \qquad (3.1\text{-}1)$$

where,

R_{III} : (TMA)/(TMG+TMA) reagent molar ratio.

x : Mole fraction AlAs in AlGaAs.

Using SEM data of Table 3.1-4, a linear relationship was obtained between the growth rate as given by equation (3.1-2).

$$t_g = 0.8798 + 0.6880x \qquad (3.1\text{-}2)$$

where,

t_g : AlGaAs growth rate in nms^{-1}.

These equations were subsequently used in some of the GRINSCH laser development trials by OMVPE and are discussed later.

Figure 3.1-6 $Al_xGa_{1-x}As$ growth rate curve from the second calibration.

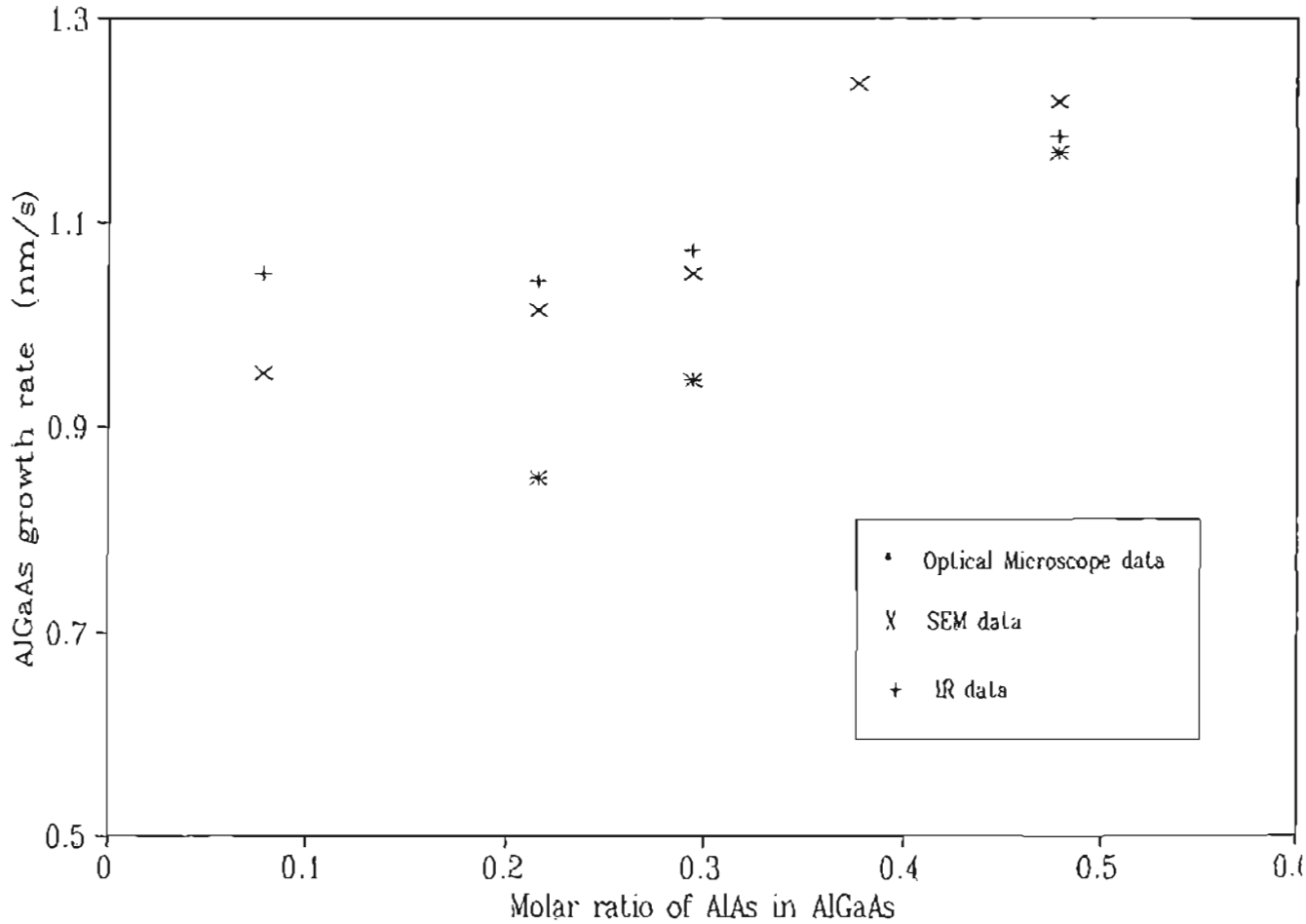

Third Calibration of Composition and Growth Rate

In addition to XRD and photoluminescence determinations, AlGaAs composition was also measured by X-ray photoelectron spectroscopy (XPS). These data were acquired as a result of testing the accuracy of XPS for AlGaAs composition determination, since the XPS technique provided results more quickly than its counterparts. AlGaAs composition determinations from XRD and photoluminescence measurements were derived from equations (1.4-13) and (1.4-1) respectively.

Table 3.1-5 Measured AlGaAs data from the third calibration of composition and growth rate.

Growth Number	Reagant Molar Ratio	x in $Al_xGa_{1-x}As$			Growth rate nms^{-1}	
	$\frac{TMA}{TMG+TMA}$	XRD	XPS	PL	SEM	Micro-scope
AGA76	0.069	0.196	0.180	0.195	0.583	0.667
AGA87	0.069	0.211				0.778
AGA75	0.103	0.289	0.280	0.295	0.667	0.639
AGA77	0.141	0.408	0.380	0.407	0.944	0.792
AGA78	0.167	0.440	0.370		1.611	0.797
AGA86	0.200	0.495				0.944
AGA74	0.224	0.554	0.490	0.485	0.972	0.931

The XPS results differ significantly from those obtained by XRD and photoluminescence. Graphical representation of the data is shown in Figures 3.1-7 and 3.1-8.

Figure 3.1-7 $Al_xGa_{1-x}As$ composition curve from the third calibration.

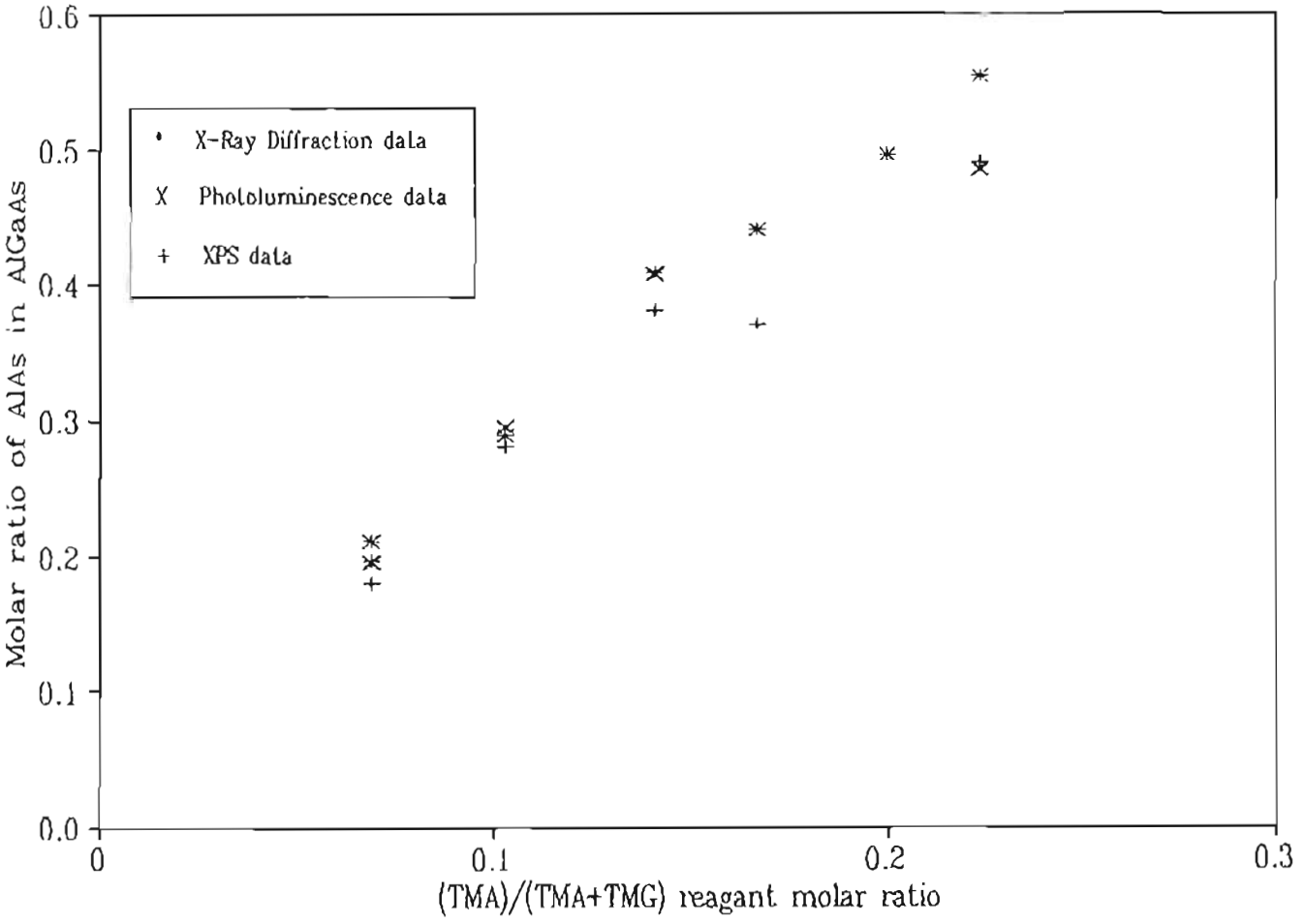

The following empirical relations were derived from selected data using XRD and optical microscope results. The relationship between group III gas phase molar ratio and AlGaAs solid composition is :

$$R_{III} = 0.0015 + 0.2758x + 0.2270x^2 \qquad (3.1\text{-}3)$$

The changing growth rate with aluminium composition in the solid yielded a linear empirical relation :

$$t_g = 0.5437 + 0.6545x \qquad (3.1\text{-}4)$$

Figure 3.1-8 $Al_xGa_{1-x}As$ growth rate curve from the third calibration.

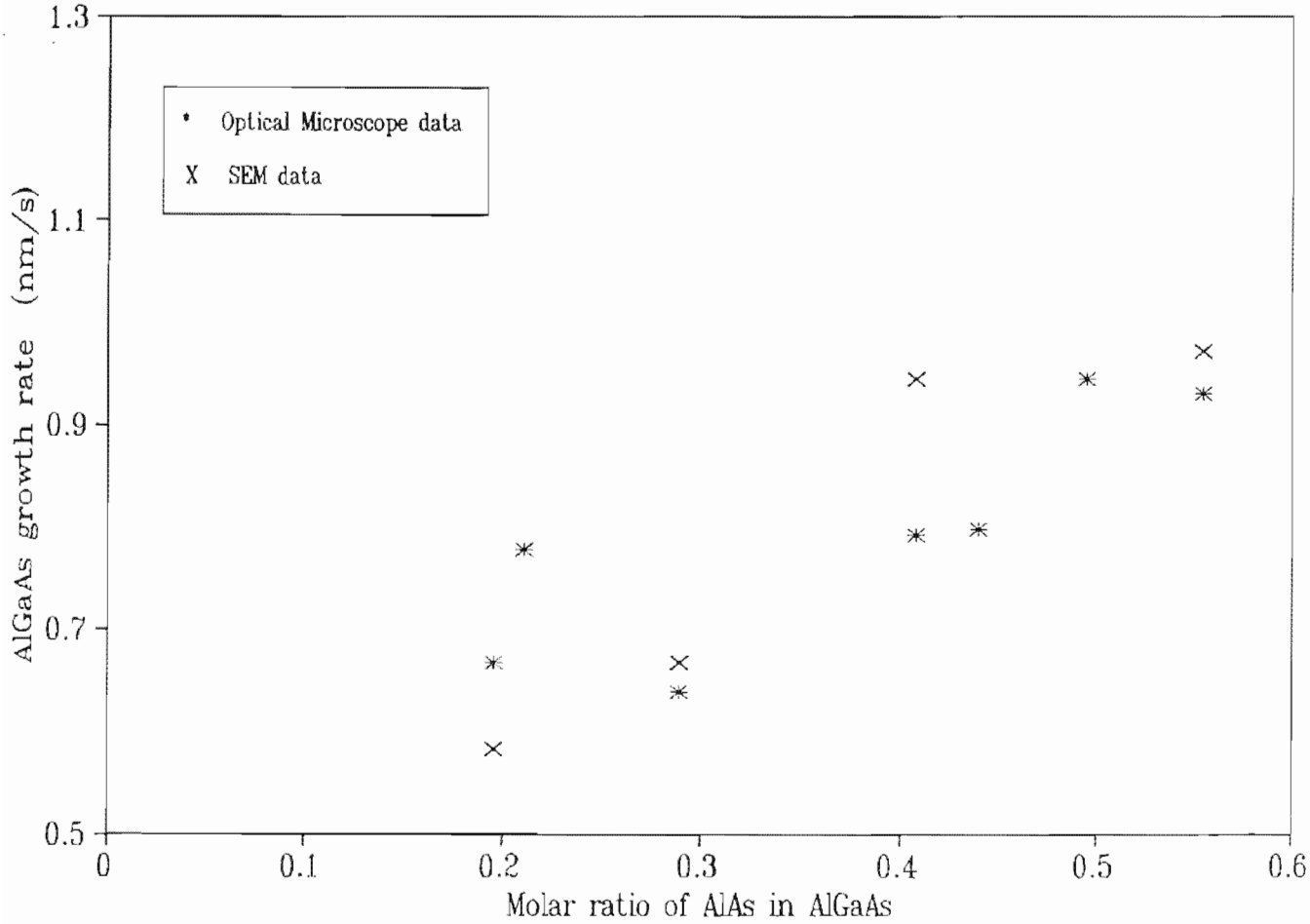

The large scatter in data is attributed to errors incurred in rounding of edges during the staining of these samples and hence poor estimates in the actual layer edges.

Fourth Calibration of Composition and Growth Rate

For this calibration only the already established XRD technique for composition measurements in conjunction with equation (1.4-13) and optical microscopy without stain-etching samples for epilayer thickness assessments were used. The data is presented in Table 3.1-6.

Table 3.1-6 Measured AlGaAs data from the fourth calibration of composition and growth rate.

Growth Number	Reagant Molar Ratio $\frac{TMA}{TMG+TMA}$	x in $Al_xGa_{1-x}As$ XRD	Growth rate nms^{-1} Optical Microscope
OMD69	0.043	0.087	0.839
OMD71	0.057	0.112	
AGA122	0.097	0.197	0.889
AGA92	0.105	0.227	
AGA93	0.148	0.303	0.978
AGA123	0.200	0.389	1.000
AGA120	0.250	0.470	1.064
AGA96	0.244	0.433	

Graphical representation of the data is shown in Figures 3.1-9 and 3.1-10.

The following empirical relations were derived from selected data. The relationship between group III gas phase molar ratio and AlGaAs solid composition is :

$$R_{III} = 0.0002 + 0.4550x + 0.1599x^2 \qquad (3.1\text{-}5)$$

The changing growth rate with aluminium composition in the solid yielded a linear empirical relation :

$$t_g = 0.7643 + 0.6204x \qquad (3.1\text{-}6)$$

Figure 3.1-9 $Al_xGa_{1-x}As$ composition curve from the fourth calibration.

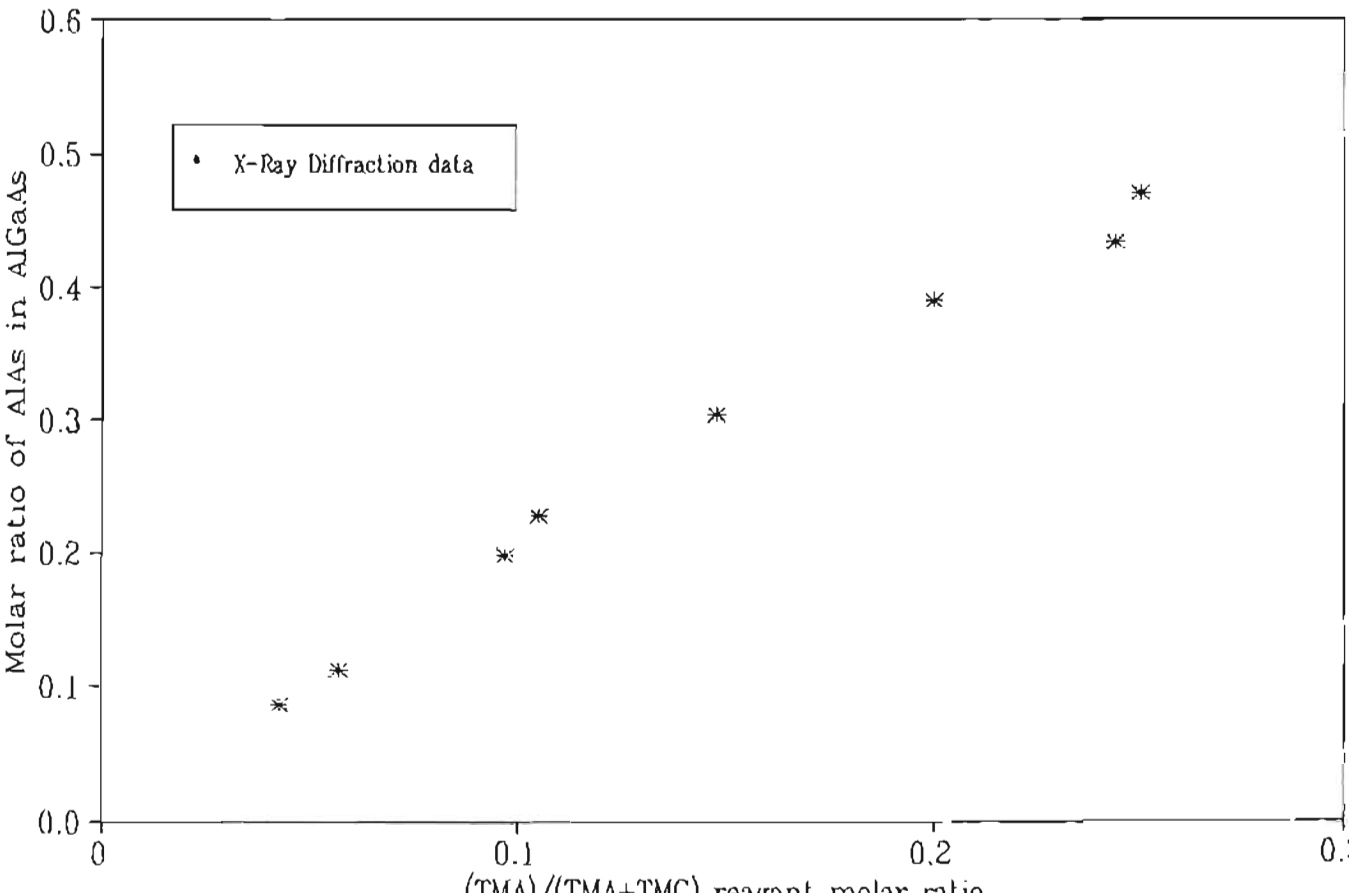

Figure 3.1-10 $Al_xGa_{1-x}As$ growth rate curve from the fourth calibration.

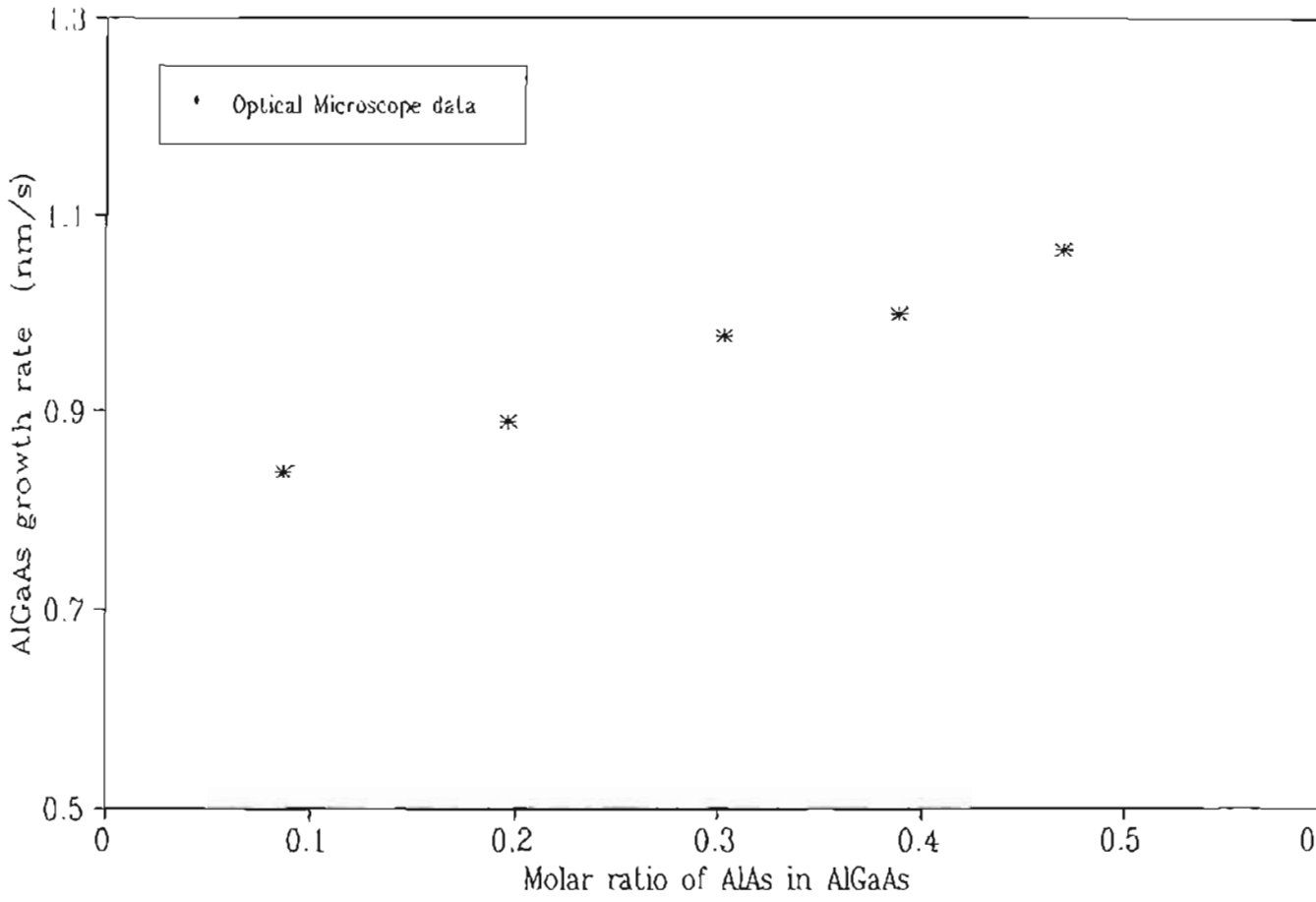

3.1.2.2 Doping of $Al_xGa_{1-x}As$

Carbon from the organometallic sources is primarily responsible for the high background n-type doping levels AlGaAs. This unintentional doping did not represent a problem to device development since the $Al_xGa_{1-x}As$ material showed excellent photoluminescence results as discussed in Section 3.1.2.1. Historically diethyltellurium, silane and diethylzinc were used to grow both n- and p-type $Al_xGa_{1-x}As$.

Figure 3.1-11 N-doping of AlGaAs.

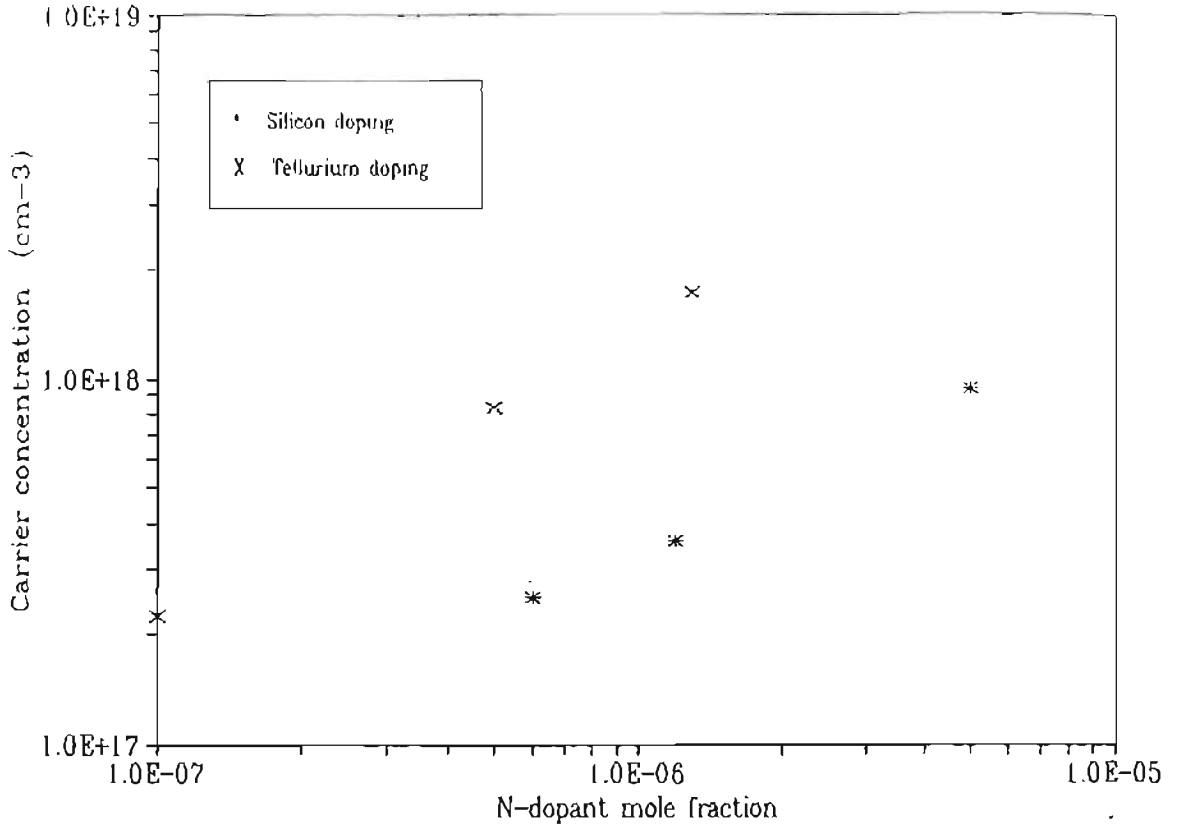

Figure 3.1-12 Zinc doping of AlGaAs.

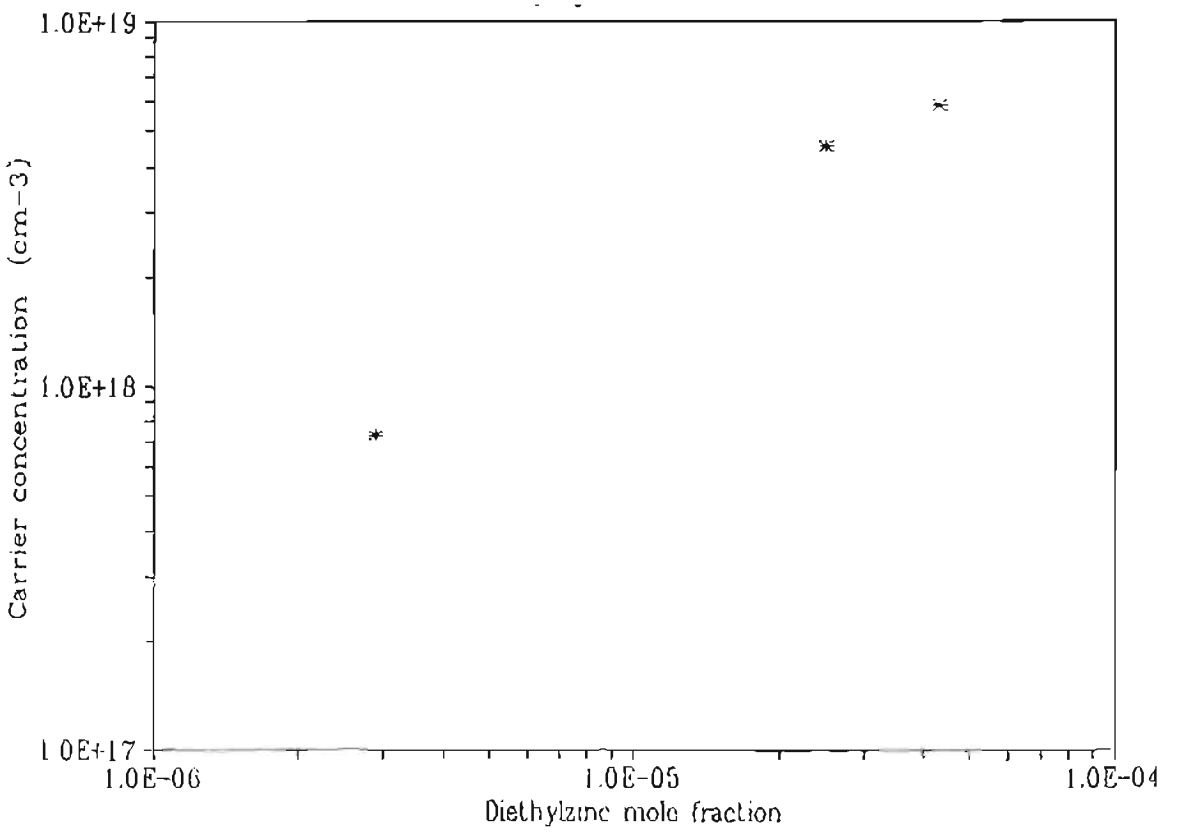

Doping studies were done at x = 0.265 in AlGaAs for Te and Zn and at x = 0.3 in $Al_xGa_{1-x}As$ for Si. It is important to note that dopant incorporation varies slightly with varying AlGaAs composition. Higher AlGaAs compositions require slightly higher gas phase dopant concentrations to ahieve the same carrier concentration. For all dopants, the relationship between carrier concentration and gas phase dopant mole fraction are linear. Graphical representation of the data are shown in Figures 3.1-11 and 3.1-12.

3.2 Spike Doping and Abrupt Interfaces

3.2.1 Silicon Spike Doping of GaAs

In order to evaluate the capability of the OMVPE system to grow doping spikes in GaAs, several spikes were grown in a single sample. This is shown schematically in Figure 3.2-1.

Figure 3.2-1 Schematic of Si-spike doping test structure.

layer 13	Si-GaAs ($n = 1.2 \times 10^{16}$ cm^{-3})	50 nm
layer 12	Si-GaAs ($n = 5.0 \times 10^{17}$ cm^{-3})	5 nm
layer 11	Si-GaAs ($n = 1.2 \times 10^{16}$ cm^{-3})	50 nm
layer 10	Si-GaAs ($n = 5.0 \times 10^{17}$ cm^{-3})	5 nm
layer 9	Si-GaAs ($n = 1.2 \times 10^{16}$ cm^{-3})	50 nm
layer 8	Si-GaAs ($n = 5.0 \times 10^{17}$ cm^{-3})	5 nm
layer 7	Si-GaAs ($n = 1.2 \times 10^{16}$ cm^{-3})	50 nm
layer 6	Si-GaAs ($n = 5.0 \times 10^{17}$ cm^{-3})	10 nm
layer 5	Si-GaAs ($n = 1.2 \times 10^{16}$ cm^{-3})	50 nm
layer 4	Si-GaAs ($n = 5.0 \times 10^{17}$ cm^{-3})	15 nm
layer 3	Si-GaAs ($n = 1.2 \times 10^{16}$ cm^{-3})	50 nm
layer 2	Si-GaAs ($n = 5.0 \times 10^{17}$ cm^{-3})	20 nm
layer 1	Si-GaAs ($n = 1.2 \times 10^{16}$ cm^{-3})	500 nm
substrate	n^+ GaAs ($n = 1\text{-}4 \times 10^{18}$ cm^{-3})	

Layers 2, 4 and 6 were designed to provide an indication of the depth resolution of the SIMS and C-V techniques while layers 8, 10 and 12 were included to provide an indication of reproducibility and the effect of SIMS ion mixing on spike resolution.

Figure 3.2-2 Overlay of SIMS depth profiles of the silicon spike doping structure.

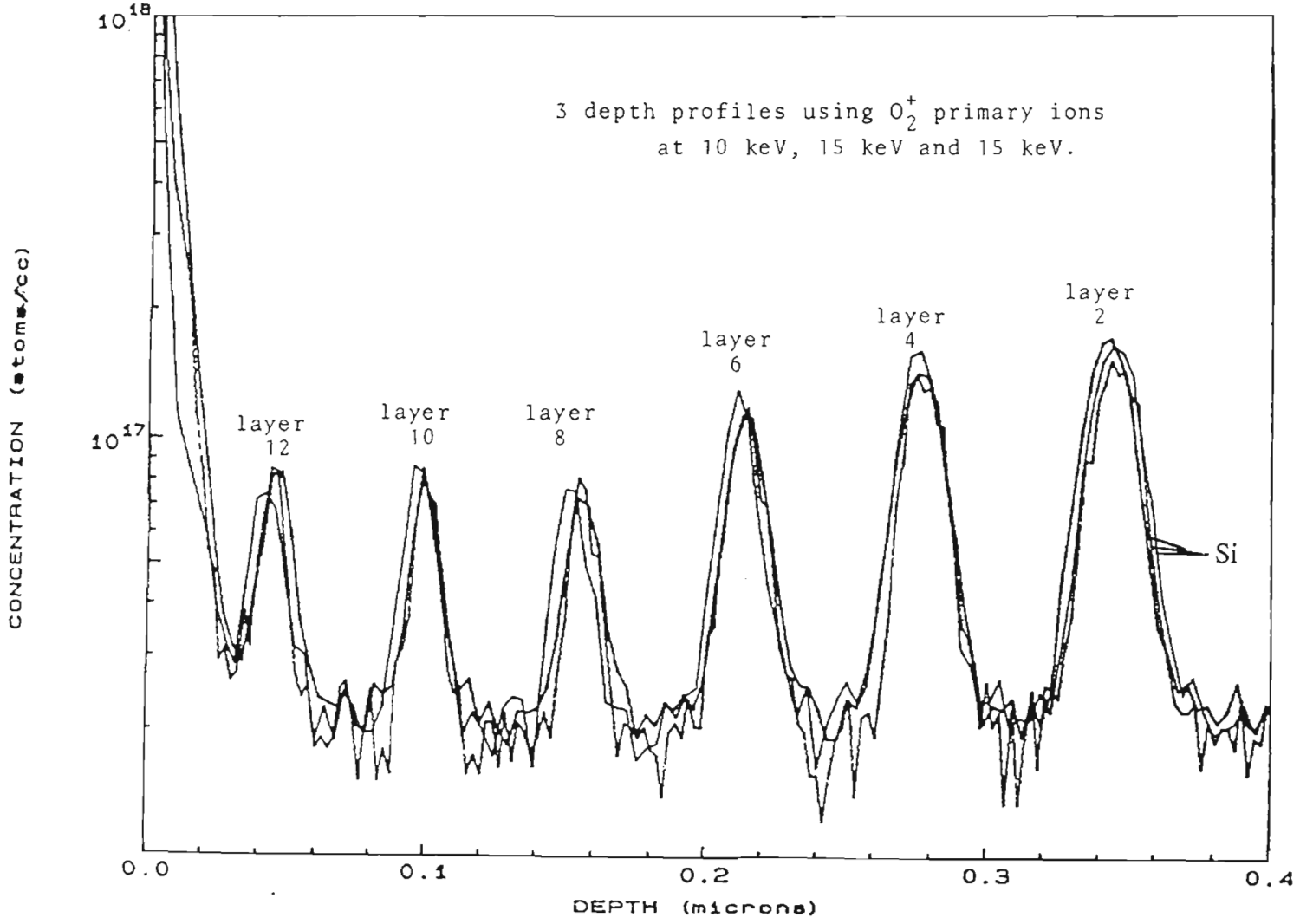

The structure was grown by using separate lines for group III and group V reagents as described in Section 2.1.3. Two separate dopant lines, containing 47 ppm and 290 ppm silane in hydrogen sources, were used for the lower and higher doping levels respectively. The lines were switched simultaneously when the desired doping changed, i.e. one line was switched into the reactor and the other vented as dictated by the required doping level. The total flow of each of the dopant lines did not exceed 200 sccm. Although the lines had different flowrates, they were small enough not to cause serious reactor pressure pertubations that could have adversely affected the quality of layer interfaces. Dopant mole fractions based on the desired level of doping at a growth temperature of 973 K was selected from Figure 3.1-1.

Three SIMS depth profiles using an O_2^+ primary ion beam were undertaken on the grown layers, one at a beam energy of 10 keV and two at 15 keV. The lower beam energy conditions were chosen because they provide better resolution of the narrow doped-layers. In Figure 3.2-2 the three depth profiles are overlaid. The similarity of the profiles indicate that the widths of the Si spikes are most likely to be sample related and not purely an artefact of the SIMS process. It is difficult to quantify this since ion-induced mixing is present and will increase the width of the measured peak profile.

Table 3.2-1 Measured SIMS inter-layer separations of the silicon spike test structure.

Technique	Inter layer separations (peak-to-peak) in nm					
	12 to 10	10 to 8	8 to 6	6 to 4	4 to 2	2 to subs
As designed	55	55	57.5	62.5	67.5	510
SIMS	51		55	60	64	462
CV	49	52	52	55	61	-

The inter-layer separations (peak-to-peak) are listed in Table 3.2-1 since it was not possible to obtain individual layer thicknesses. The separations are 4-10% less than the desired values. The total thickness of the epilayer is measured as 785 ± 30 nm, some 9% less than the intended value of 860 nm.

Figure 3.2-3 Doping profile determined using C-V of silicon spike doping structure.

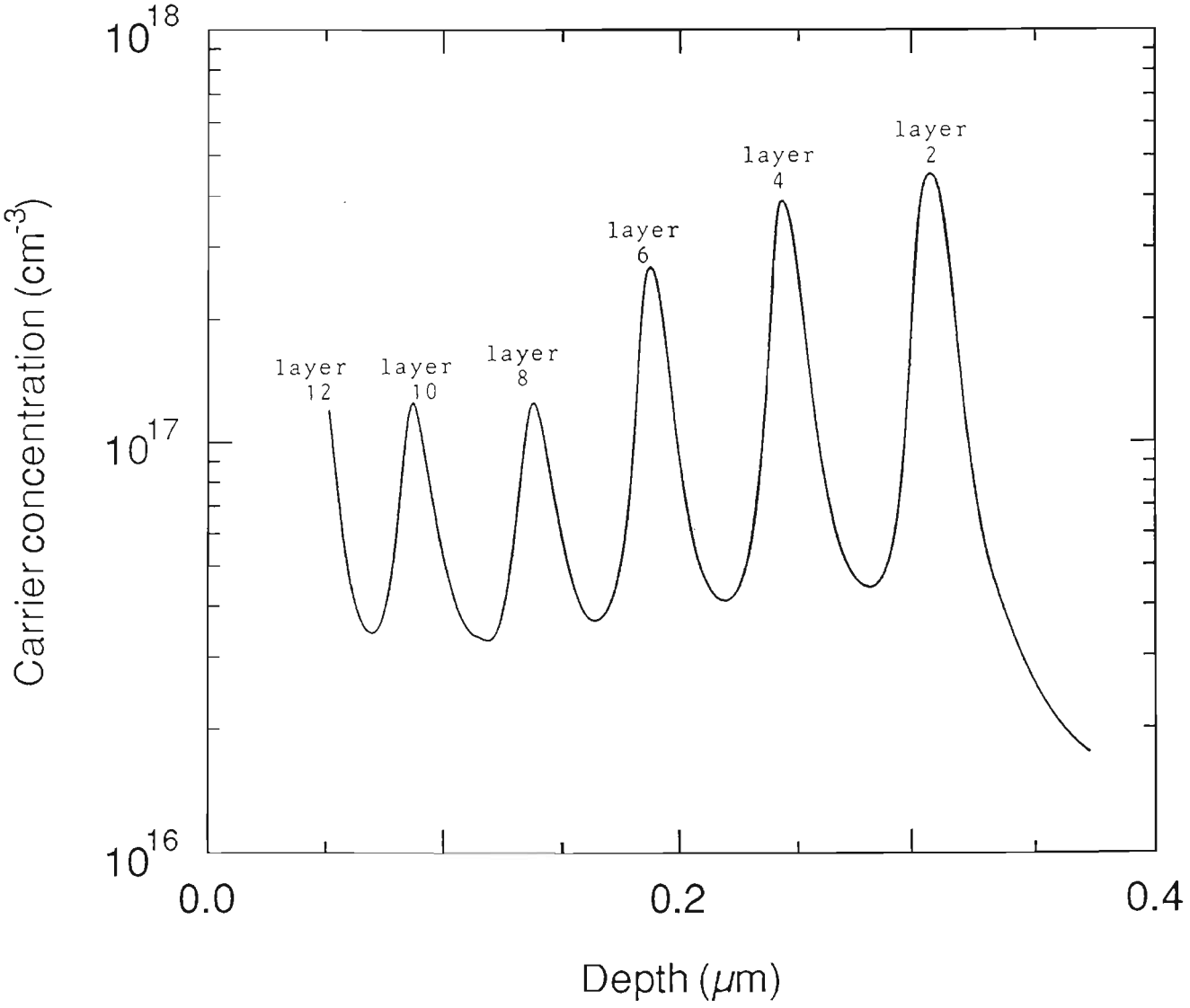

Cs^+ primary ion bombardment and negative secondary ion detection was also used to obtain optimum sensitivity to Si. The impact energy of the Cs^+ primary ions is high compared to the O_2^+ primary ion beam that was also used. Ion-induced mixing is increased and this limits the resolution that can be achieved. The peak doping level of layer 2 was measured as 1.5×10^{17} cm^{-3}. Layer 1, which was intended to have a doping level of 1.2×10^{16} cm^{-3}, measured $1.5 \pm 0.3 \times 10^{16}$ cm^{-3}. The n^+ substrate, specified as 1 to 4×10^{18} cm^{-3}, is measured to be 1.4×10^{18} cm^{-3}. The areas of the Si-doped layers in the O_2^+ spectra were determined in order to obtain the total amount of dopant present in a layer (see Table 3.2-2). The ratio's of the peak areas correspond well with the designed ratio's of 1:1:1:2:3:4. The fact that the peak concentration of the spikes level increases as the thickness of the spike increases, even though the doping levels are constant, indicates that ion-induced mixing in the SIMS technique has limited the depth resolution severely. The average peak areas of the nine measurements of the three 5 nm layers is $7.3 \pm 0.7 \times 10^{10}$ cm^{-2}, this is 30% of the expected value of 25×10^{10} cm^{-2}. Assuming that the growth rate is lower by 9%, the peak areas would have decreased accordingly to 90% of the expected values. Although there is a fairly large uncertainty in the measurement of the peak areas, it is clear that the dopant level is significantly lower than expected. Since, for device purposes, it is important to ensure the amount of dopant in the spike, these results indicate that the carrier concentration should be increased to 1.5×10^{18} cm^{-3} if the thickness is kept at 5 nm.

In Figure 3.2-3, the C-V plot of the test structure shows five of the six Si-doped layers. The very first 5 nm layer, layer 12, is obscured since the carrier depletion layer due to the Schottky contact on the surface extends into the sample deeper than layer 12. The sheet doping densities are determined by integration of the peaks in the C-V profile measurements shown in Table 3.2-2. The areas are much larger than the SIMS values. The mean of both measurements of the 5 nm layers is 1.9×10^{11} cm^{-2}, which is 76% of the expected value of 2.5×10^{11} cm^{-2}. The areas of the thicker layers are even closer to the expected values, with a high of 81% for layer 6. The ratios of the peak areas do conform to the expected 1:2:3:4 ratio.

Table 3.2-2 Integrated peak areas of silicon doping levels in the spike structure.

Technique	Total amount of dopant or sheet doping density (cm^{-2})					
	Layer 12	Layer 10	Layer 8	Layer 6	Layer 4	Layer 2
As designed	$25x10^{10}$	$25x10^{10}$	$25x10^{10}$	$50x10^{10}$	$75x10^{10}$	$100x10^{10}$
SIMS	$7.3x10^{10}$			$14x10^{10}$	$22x10^{10}$	$30x10^{10}$
C-V	$1.9x10^{11}$			$4x10^{11}$	$5.8x10^{11}$	$7.7x10^{11}$
	Area ratios					
As designed	1			2	3	4
SIMS	1			2.0	3.0	4.1
C-V	1			2.1	3.1	4.1

Another major difference between the C-V and the SIMS results is the level of the signal measured between the thin layers. In the SIMS profiles the Si concentration drops to $2x10^{16}$ cm^{-3} between the layers. In the C-V plots the carrier concentration drops to 3 to 4×10^{16} cm^{-3}. The maximum concentration values of the layers are much larger in the C-V measurement. The peak value for layer 2 is 4.5×10^{17} cm^{-3} which is close to the expected value of 5×10^{17} cm^{-3}. The maximum value measured by SIMS is 1.5×10^{17} cm^{-3} for layer 2. The carrier concentration of layer 1 is measured as 1.8×10^{16} cm^{-3} which corresponds well with the SIMS measurement of $1.5 \pm 0.3 \times 10^{16}$ cm^{-3}. The increase in the peak concentration level with thickness of the layers indicates that the depth resolution is limited for C-V profiling, as is the case for SIMS as well. Both SIMS and C-V do not clearly resolve the true dopant profile.

3.2.2 AlGaAs-GaAs Heterojunction

A systematic study was undertaken for the purpose of realizing high quality heterointerfaces. In particular, the growth of GaAs quantum wells were used as test structures, each well sandwiched between AlGaAs layers. The abruptness of AlGaAs-GaAs heterointerfaces is dependant on gas switching technique, pressure balances in the gas system and reactor geometry. The experimental procedure used for growing this structure was to use the separate lines for group III reagents and group V reagents as described in Section 2.1.3. A 10 second pause between the growth of consecutive layers was also implemented.

The multi-quantum well test structure used for this study is schematically shown in Figure 3.2-4. The GaAs growth rate used was 0.625 nms^{-1} and data from the first AlGaAs composition and growth rate calibration (Section 3.1.2.1) were used in the growth procedure.

Figure 3.2-4 Schematic of quantum well test structure.

Layer 11	$Al_{0.4}GaAs$ spacer	60 nm
Layer 10	GaAs quantum well	2.5 nm
Layer 9	$Al_{0.4}GaAs$ spacer	60nm
Layer 8	GaAs quantum well	3.75 nm
Layer 7	$Al_{0.4}GaAs$ spacer	60nm
Layer 6	GaAs quantum well	5 nm
Layer 5	$Al_{0.4}GaAs$ spacer	60nm
Layer 4	GaAs quantum well	7.5 nm
Layer 3	$Al_{0.4}GaAs$ spacer	60nm
Layer 2	GaAs quantum well	10 nm
Layer 1	$Al_{0.4}GaAs$ buffer	500 nm
Substrate	Semi-insulating GaAs	

Figure 3.2-5 SIMS profile of quantum well test structure OMQ006.

(layer numbers refer to Figure 3.2-4)

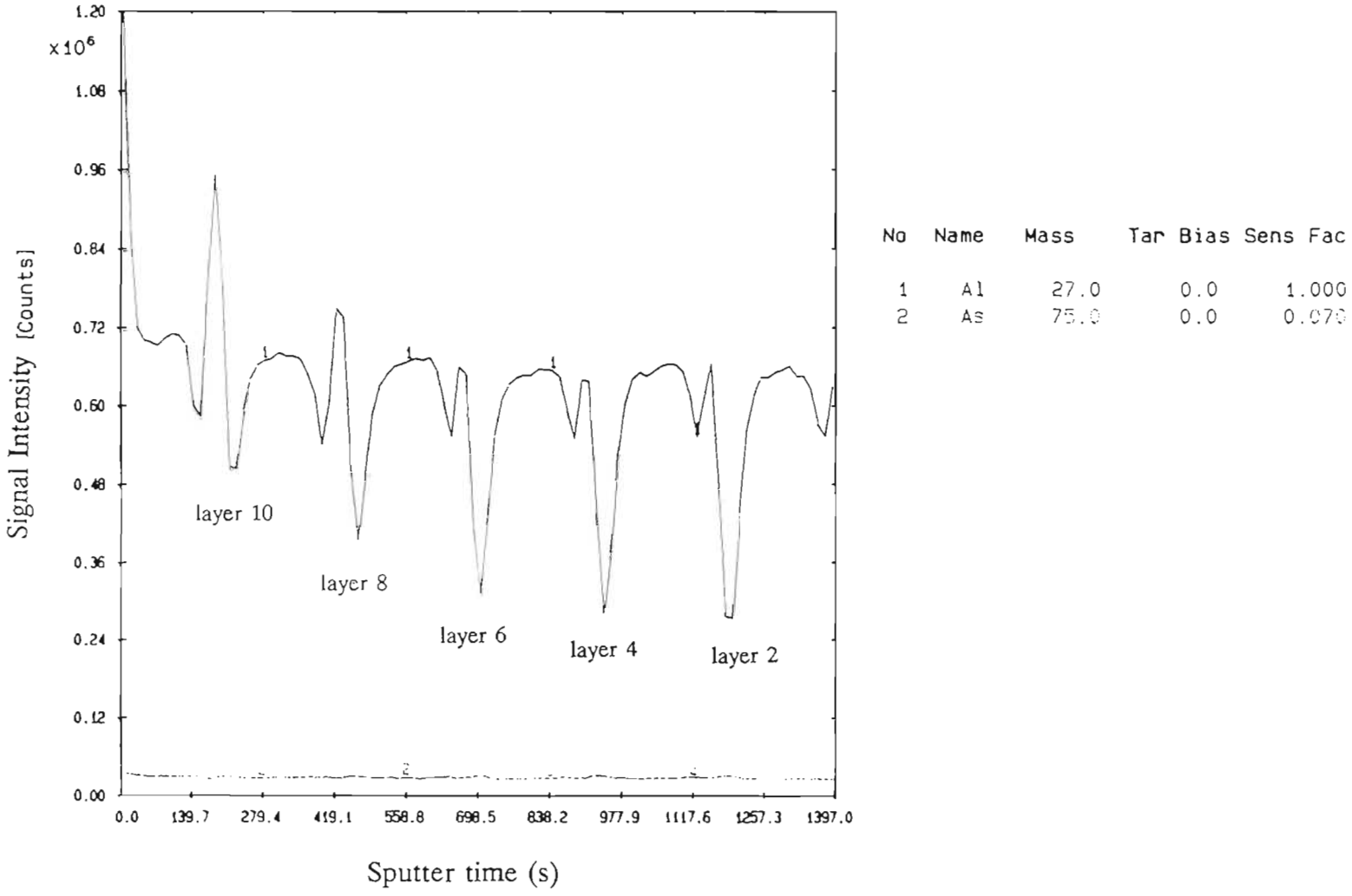

An initial test structure, designated OMQ006, was grown with the aim of investigating heterostructural interface quality. SIMS measurements showing the secondary ion counts as a function of sputter time is shown in Figure 3.2-5. The five wells are indicated in the profile. The depth profiles also reveal a relatively wide aluminium 'spike' at each of the GaAs-AlGaAs interfaces indicating that the aluminum composition is enhanced when an AlGaAs layer is grown on top of a GaAs quantum well layer. This 'spike' is attributed to :

i. Pressure imbalances in the OMVPE growth chamber when switching the gas carrier lines for the growth of the consecutive GaAs and AlGaAs layers.

ii. Inconsistencies in the concentration of reagants as a result of pressure imbalances propagating to the organometallic bubblers and causing uneven pick-up of reagant sources.

With such inconsistencies in the layers, attempts to quantify the well sizes would be futile since the layer boundaries are not clearly indicated in the profile.

Certain corrective measures were adopted, namely :

i. Reagents for GaAs and reagents for AlGaAs layers were piped through in separate lines to effect no imbalance in flowrates when lines were switched i.e. one line is switched to vent simultaneously with the other line being switched into the reactor. This is described in Section 2.1.3.

ii. There was no growth pause between the growth of consecutive layers.

iii. Optimisation of the reactor pressure control resulted in maximum growth pressure fluctuations during growth of 1 mbar on 100 mbar for reactor pressure and 7 mbar on 760 mbar gauge for the input line pressures.

The SIMS and photoluminescence profiles of the subsequent growth of the same structure, designated OMQ007, and using the same growth parameters with the above-mentioned corrective measures are shown in Figures 3.2-6 and 3.2-7 respectively.

Figure 3.2-6 SIMS profile of quantum well test structure OMQ007.

(layer numbers refer to Figure 3.2-4)

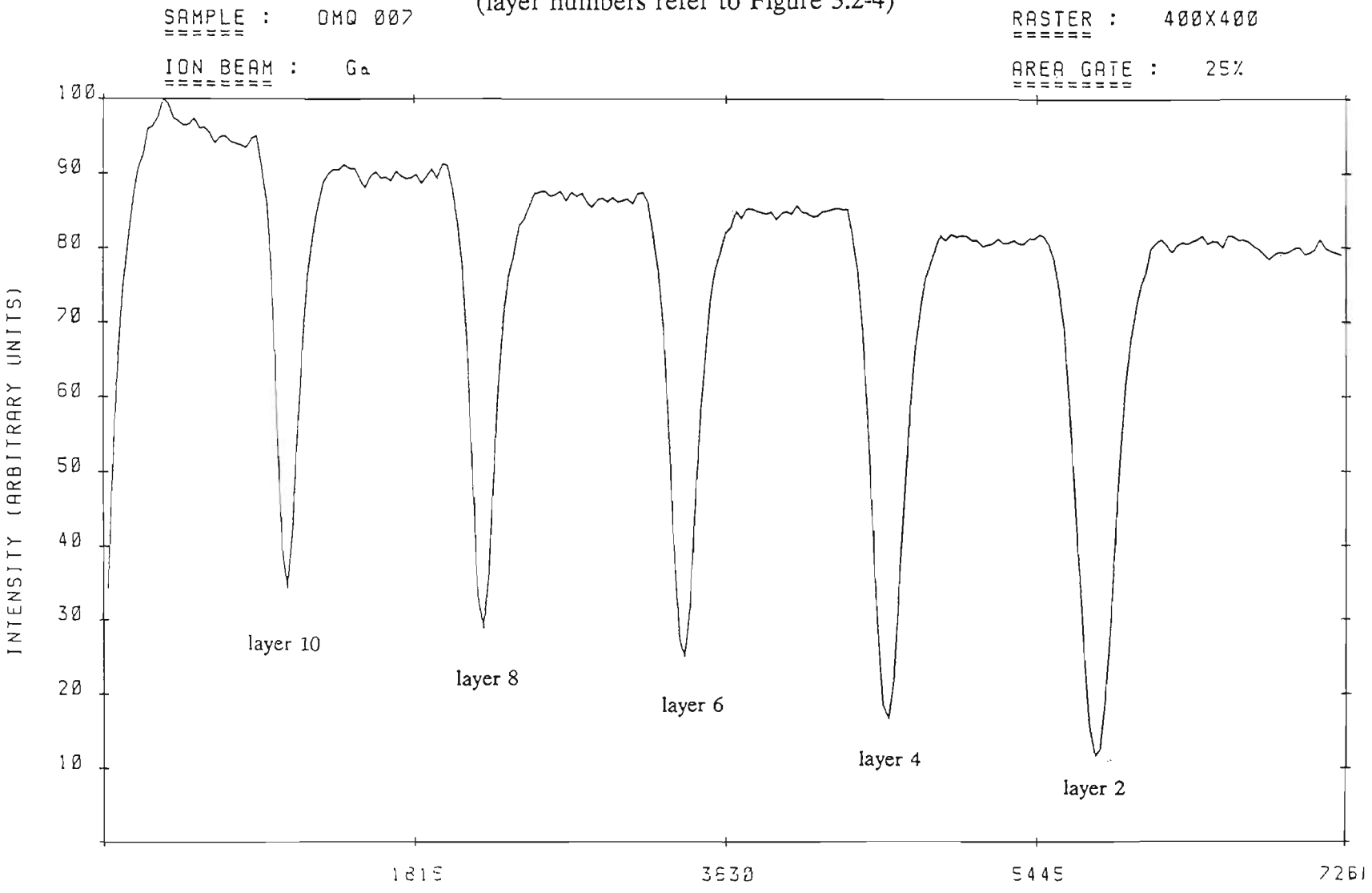

Figure 3.2-7 Photoluminescence of quantum well test structure OMQ007.

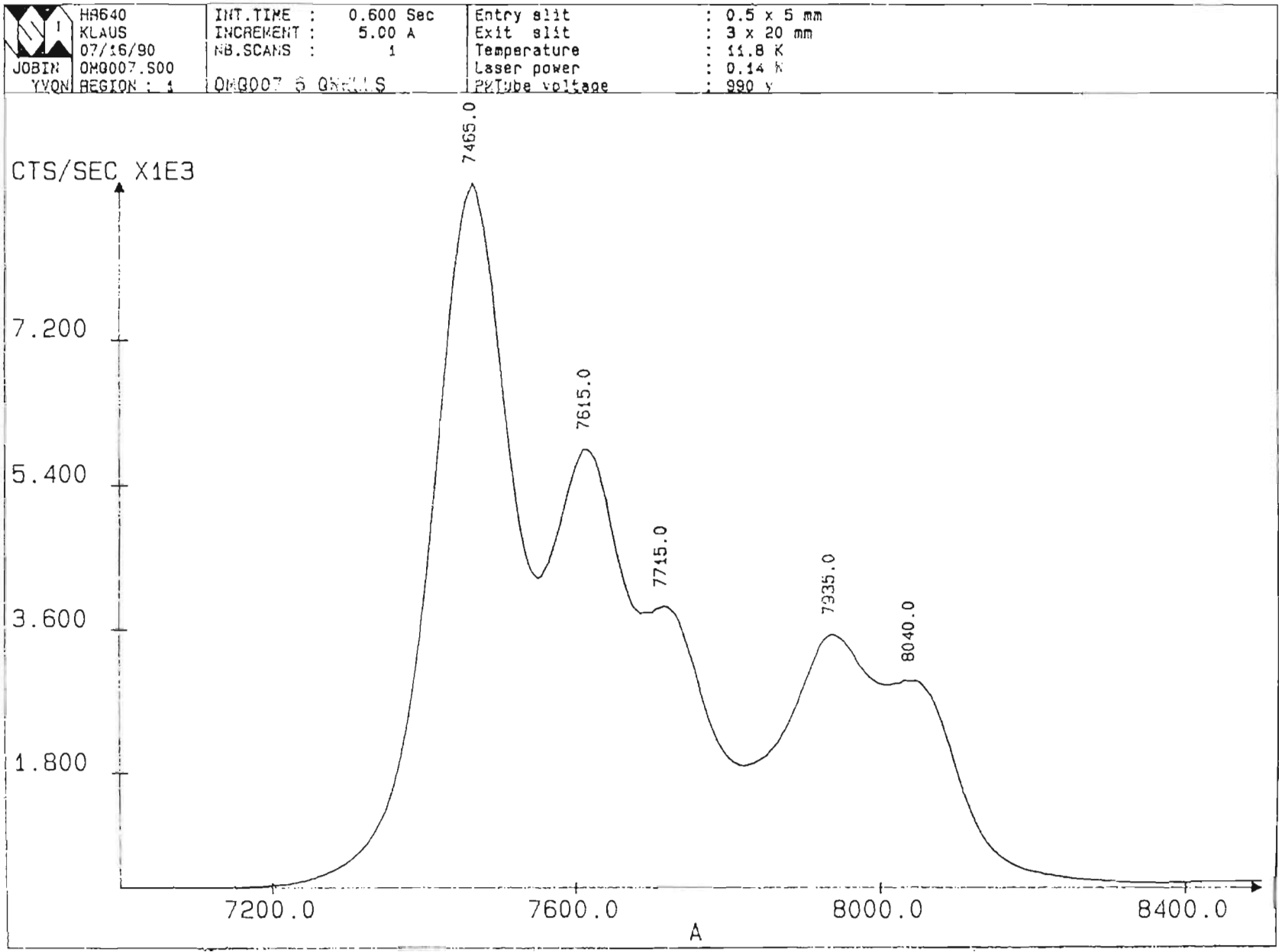

The SIMS profile qualitatively depicts the five quantum wells with no aluminium 'spiking'. The tailing of the aluminium signal from approximately 96 counts to 80 counts is probably an instrumental feature attributed to the gallium gun not being heated to equilibrium and loss of aluminium signal with depth of sampling. The ratio of the widths of peaks do not sufficiently qualify the thickness of wells since their triangular shape is a direct result of ion beam mixing effects in SIMS and cannot be accurately resolved into square well profiles. The larger well sizes do however reflect deeper profiles. Narrow peaks in the PL spectrum do indicate well defined GaAs layers in the measured structure. Table 3.2-3 compares the measured well thickness using PL with the intended well dimensions of the structure in Figure 3.2-4. The measured widths are derived from model predictions [Chinn et al.,1988] and discussed in Section 1.4.5.

Table 3.2-3 Summary of photoluminescence data and quantum well thicknesses for growth OMQ007.

Layer	Targeted width	PL data	Measured width
layer 2	10 nm	8040 Å	9.8 nm
layer 4	7.5 nm	7930 Å	7.0 nm
layer 6	5 nm	7715 Å	4.1 nm
layer 8	3.75 nm	7610 Å	3.3 nm
layer 10	2.5 nm	7460 Å	2.3 nm

From Table 3.2-3, it is clear that good agreement exists between the measured and intended well widths based on experimetally determined growth rates and the predictions of the theoretical model of Chinn et al. [1988] described in Section 1.4.5, particularly considering any experimental error associated with growth rate data.

3.3 Dopant Grading of GaAs

Although dopant grading in the active layer of the 35 GHz Gunn diode (Section 3.6.1) is beneficial to the performance of the device [Paolella-1986], it was not employed. However, a demonstration layer of silicon doping grading was undertaken.

3.3.1 Development of the Doping Grading technique

Two silane sources were available for this study : 47 ppm in hydrogen and 290 ppm in hydrogen cylinders. Growth calibrations were undertaken using both sources at two growth temperatures and the results are shown in Figure 3.1-1 in Section 3.1.1.2 . It is clear that that the relations are linear.

Table 3.3-1 Silicon doping data at growth temperatures of 923 K and 973 K and silane sources of 47 ppm and 290 ppm in hydrogen.

Growth Number	Silane mole fraction	Doping in cm^{-3}		
		47ppm, 923 K	47ppm, 973 K	290ppm, 973 K
GA114	$1.03x10^{-8}$	$8.70x10^{15}$		
GA111	$2.51x10^{-8}$	$2.92x10^{16}$		
GA113	$6.34x10^{-7}$	$6.30x10^{17}$		
GA119	$1.49x10^{-6}$	$1.74x10^{18}$		
GA136	$8.00x10^{-9}$		$1.90x10^{16}$	
GA137	$2.00x10^{-8}$		$5.00x10^{16}$	
GA116	$2.50x10^{-8}$		$7.10x10^{16}$	
GA133	$3.00x10^{-7}$			$1.70x10^{17}$
GA134	$1.50x10^{-6}$			$6.20x10^{17}$
GA135	$3.80x10^{-6}$			$1.90x10^{18}$

The requirement for the grading growth technique was to first achieve an empirical relation between the solid carrier concentration and the dopant mole fraction in the gas phase. Hence, using the empirical data in Table 3.3-1, simple linear equations may be derived for use in the grading process as described in Section 2.1.5.

Using linear regression the following equations were derived :

At T = 923 K and using the 47 ppm cylinder of SiH_4,

$$N_i = 2.40905\times10^{-8} + 8.56779\times10^{-25}\, n \qquad (3.3\text{-}1)$$

where,

N_i = gas phase dopant mole fraction,

n = carrier concentration in cm^{-3}.

At T = 973 K and using the 47 ppm cylinder of SiH_4,

$$N_i = 2.19824\times10^{-9} + 3.31466\times10^{-25}\, n \qquad (3.3\text{-}2)$$

At T = 973 K and using the 290 ppm cylinder of SiH_4,

$$N_i = 9.71886\times10^{-8} + 1.97339\times10^{-24}\, n \qquad (3.3\text{-}3)$$

3.3.2 Silicon dopant grading

To investigate the grading capability of the OMVPE system, one dopant grading growth was undertaken under the following growth conditions :

growth temperature : 973 K

V/III ratio : 150

silane source : 290 ppm in hydrogen

growth pressure : 100 mbar

The test structure for the graded layer consisted of a carrier profile ranging from $2x10^{17}$ to $2x10^{18}$ cm^{-3} over a 1000 nm epilayer. A fixed growth rate of 0.555 nms^{-1} was assumed. Therefore equation (3.3-3) was used in conjunction with equation 3.3-4 shown below.

$$n = 2.0\times10^{17} + 1.0\times10^{15}\ t \qquad (3.3\text{-}4)$$

where, t = time in seconds,
n = carrier concentration in cm^{-3}.

Electrochemical C-V analysis of the resultant layer is shown in Figure 3.3-1. Three undesirable features of the measured profile are a direct result of the measurement instrument and technique. These are :

i. the absence of the peak doping at $2x10^{18}$ cm^{-3}; this is attributed to loss of material during the initial setup of the measurement experiment from debubbling and setting electrical parameters and consequently having material etched without logging data;

ii. the irregularities in the C-V trace are a result of continually adjusting the measurement voltages and currents with changing doping hence affecting the output;

iii. the non-linearity in the curve is a result of measuring from a higher to lower doping level which generate exaggerated doping levels in subsequent sub-layers.

The C-V trace does however reflect a definite doping profile in the layer as well as the lower doping level of $2x10^{17}$ cm^{-3} at a depth of 1000 nm.

Figure 3.3-1 C-V analysis of the dopant graded GaAs layer using a silane source.

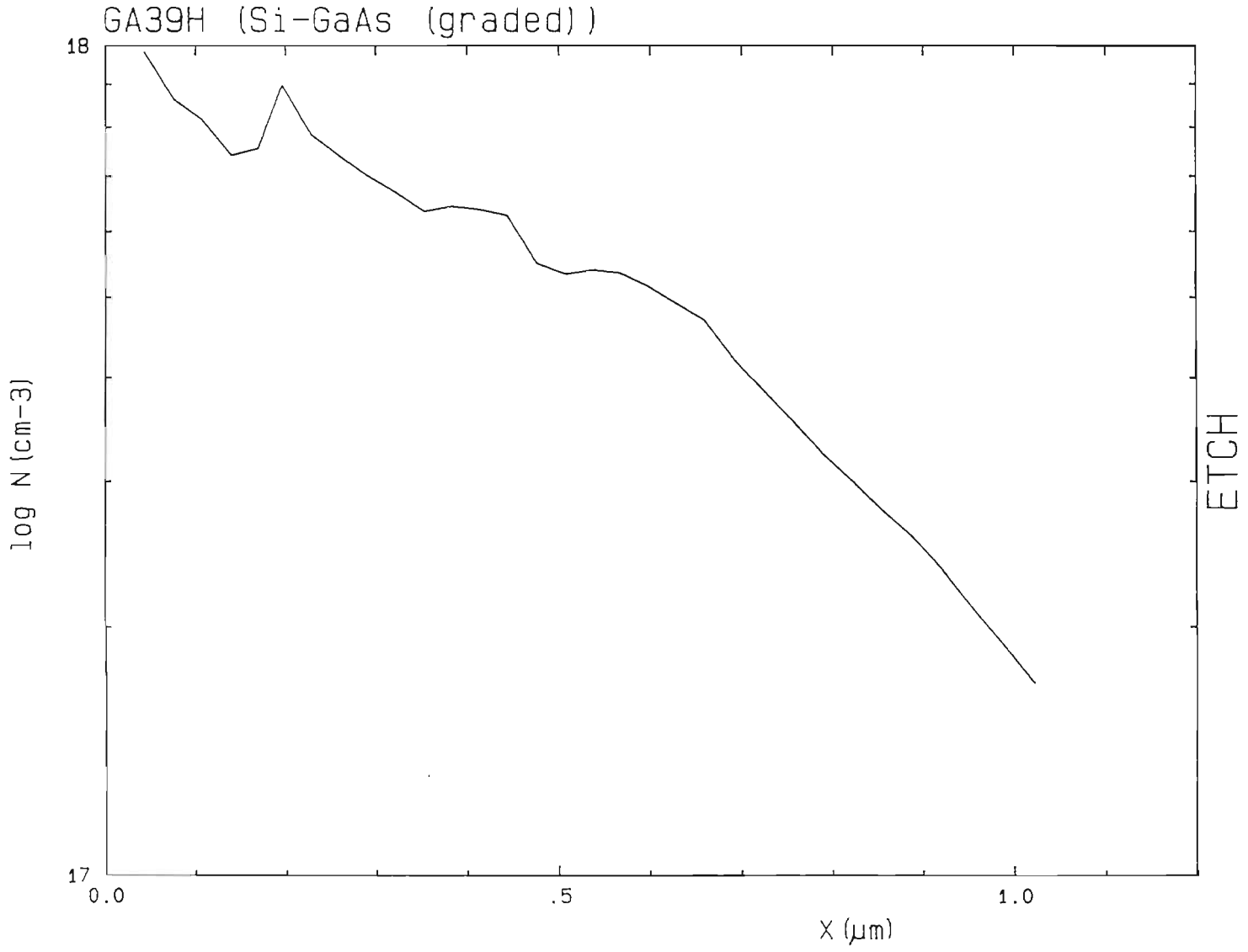

3.4 Compositional Grading of AlGaAs

3.4.1 Compositional analysis of single graded layers

Figure 3.4-1 shows a schematic of a tiered AlGaAs structure grown using the OMVPE technique based on data from the first calibration of AlGaAs composition shown in Section 3.1.2.1. Figures 3.4-2 and 3.4-3 show the corresponding X-ray diffractogram and photoluminescence spectrum respectively.

Figure 3.4-1 Schematic of tiered $Al_xGa_{1-x}As$ structure.

Layer 5	$Al_{0.5}GaAs$	1000 nm
Layer 4	$Al_{0.4}GaAs$	1000 nm
Layer 3	$Al_{0.3}GaAs$	1000 nm
Layer 2	$Al_{0.2}GaAs$	1000 nm
Layer 1	$Al_{0.1}GaAs$	1000 nm
Substrate	Semi-insulating GaAs	

Although the total thickness measures 5000 nm, strong X-ray diffraction reflections were observed for all the layers, indicating good depth penetration of the X-ray beams. The composition of the individual layers, as assessed by equation 1.4-13 of Section 1.4.2, are $x = 0.095$, 0.190, 0.285, 0.386 and 0.476 . This very closely approximates intended compositions given in Figure 3.4-1. The narrow full widths at half maximum of the diffraction traces for individual layers indicate that the layers are of uniform crystal quality. The photoluminescence technique does not provide information on all the layers. Figure 3.4-3 show a weak emission at 599.4 nm indicating a layer with an $Al_xGa_{1-x}As$ composition of $x = 0.447$ from using equation (1.4-1) in Section 1.4.1 . This is to be expected since this composition occurs in the region of indirect bandgap material. A pronounced emission at 632.4 nm is seen corresponding to a composition of $x = 0.361$. A further emission at 672.2 nm indicates $Al_xGa_{1-x}As$ material with a composition of $x = 0.267$. Clearly, photoluminescence is inadequate for this type of assessment given the relatively small penetration depth of the technique and the sample dimensions.

Figure 3.4-2 X-ray diffraction curve of tiered AlGaAs structure (sample AGA63).

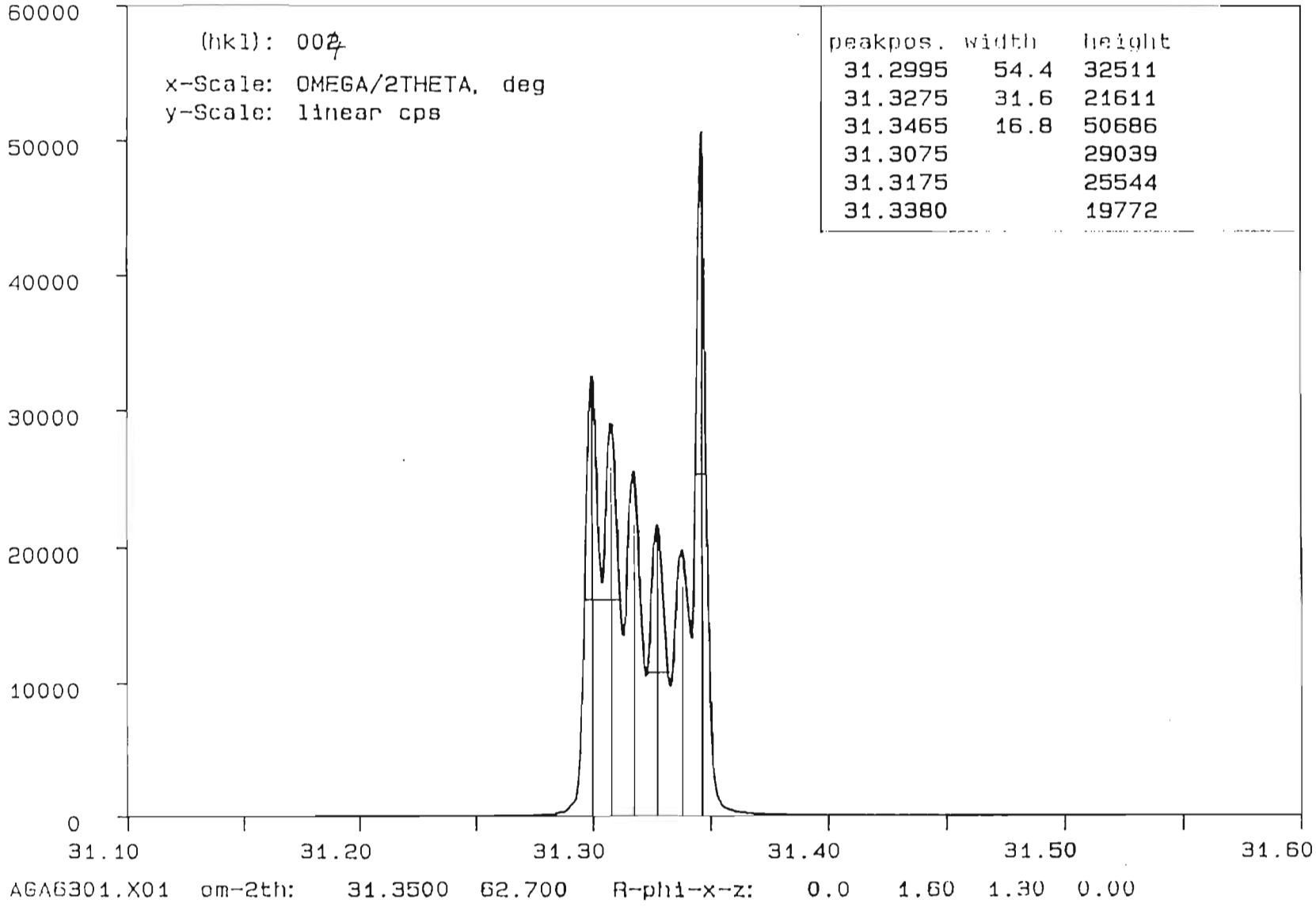

Figure 3.4-3 Photoluminescence curve of tiered AlGaAs structure (sample AGA63).

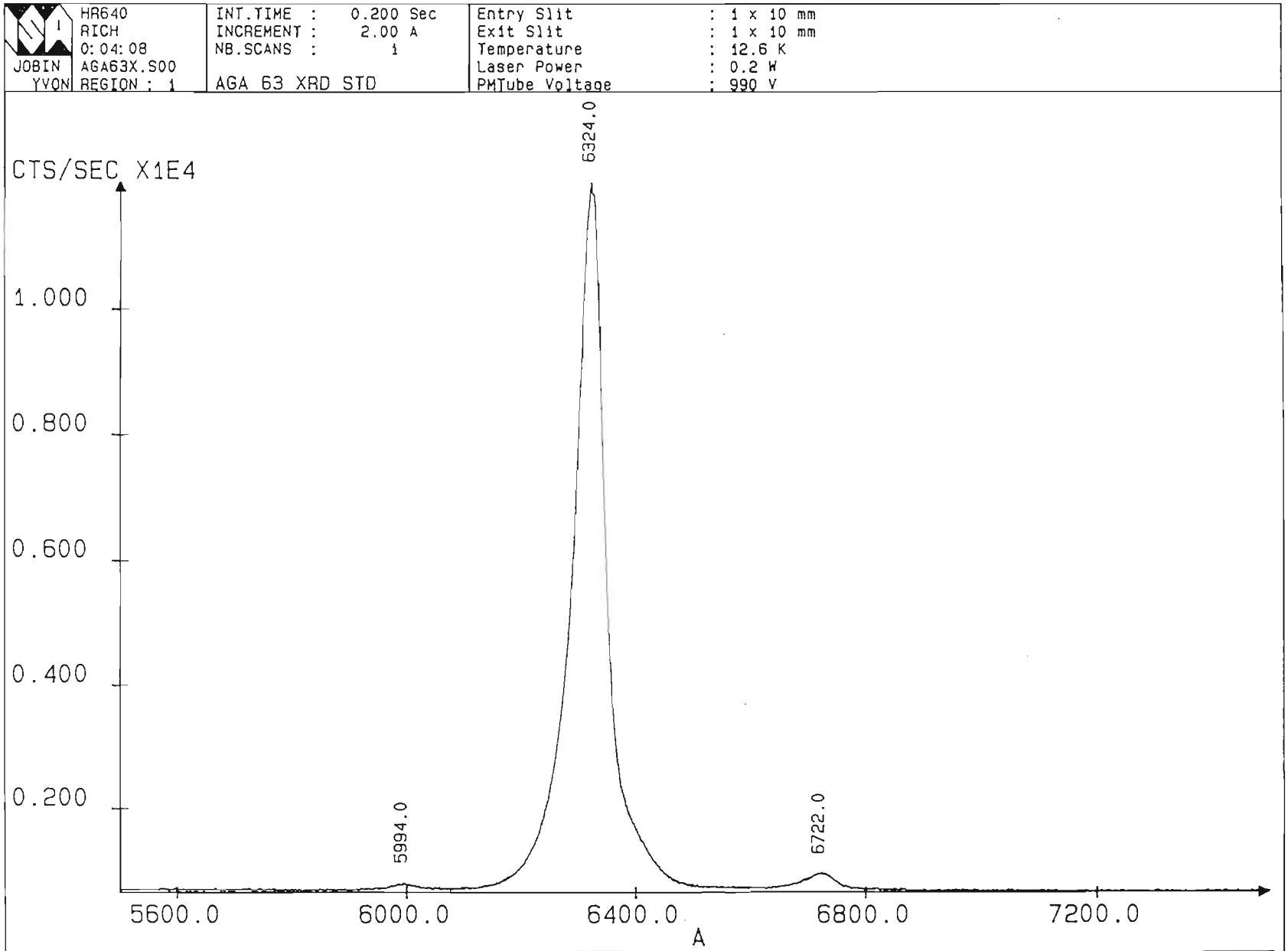

A more finely stepped structure (sample AGA52) with ten steps of x = 0.05 from x = 0 to x = 0.5 was manually grown in the growth chamber. A fixed growth rate of 1.111 nms^{-1} for all AlGaAs compositions, each grown for 900 s, was assumed for simplicity. The AlGaAs composition data was derived from the first calibration of AlGaAs composition presented in Section 3.1.2.1. Figure 3.4-4 shows the X-ray diffractogram and Figure 3.4-5 shows the photoluminescence spectrum of the graded layer. The XRD trace does not discern the sub-layers clearly whilst the photoluminescence spectrum shows several distinct emissions. The estimated compositions are shown in Table 3.4-1 using the XRD and photoluminescence measurement equations (1.4-13) in Sections 1.4.2 and (1.4-1) in Section 1.4.1 respectively.

Table 3.4-1 Calculated composition data from X-ray diffraction and photoluminescence measurements of sample AGA52.

X-ray diffraction		Photoluminescence	
Ave reflection	x in $Al_xGa_{1-x}As$	Peak position	x in $Al_xGa_{1-x}As$
33.1767°	0.113	759.5 nm	0.113
33.1692°	0.188	721.5 nm	0.182
-	-	690.5 nm	0.244
-	-	661.0 nm	0.309
33.1520°	0.361	641.0 nm	0.356
-	-	621.5 nm	0.405

Although there appears to be some correlation in the two sets of data, several peaks in both the photoluminescence and XRD traces are not resolvable. The missing emissions in photoluminescence are probably the result of using a high measurement temperature of 13 K and not 4 K and hence not fully resolving lower compositions as well as the

Figure 3.4-4 X-ray diffraction curve of stepped AlGaAs structure (sample AGA52).

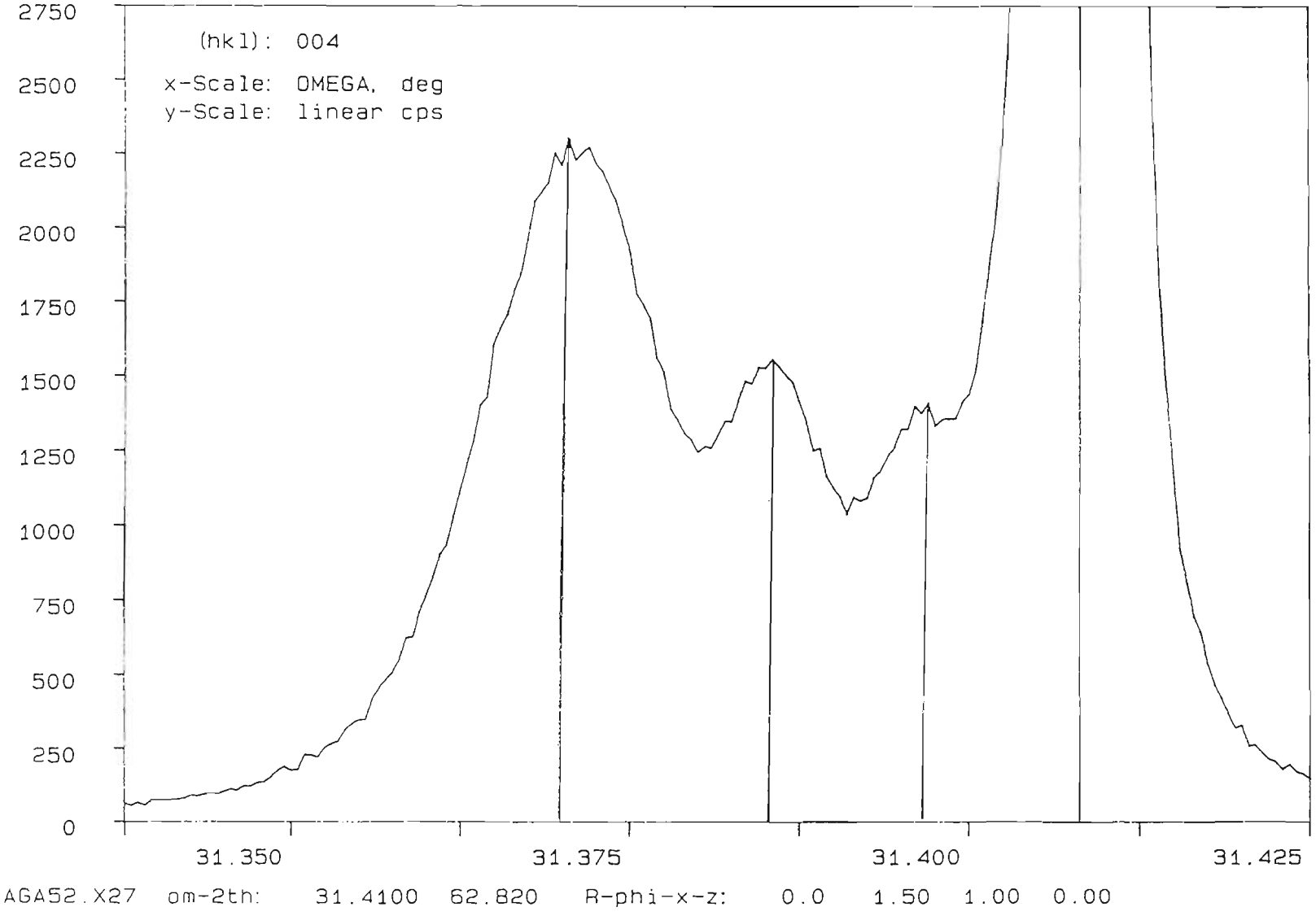

Figure 3.4-5 Photoluminescence curve of stepped AlGaAs structure (sample AGA52).

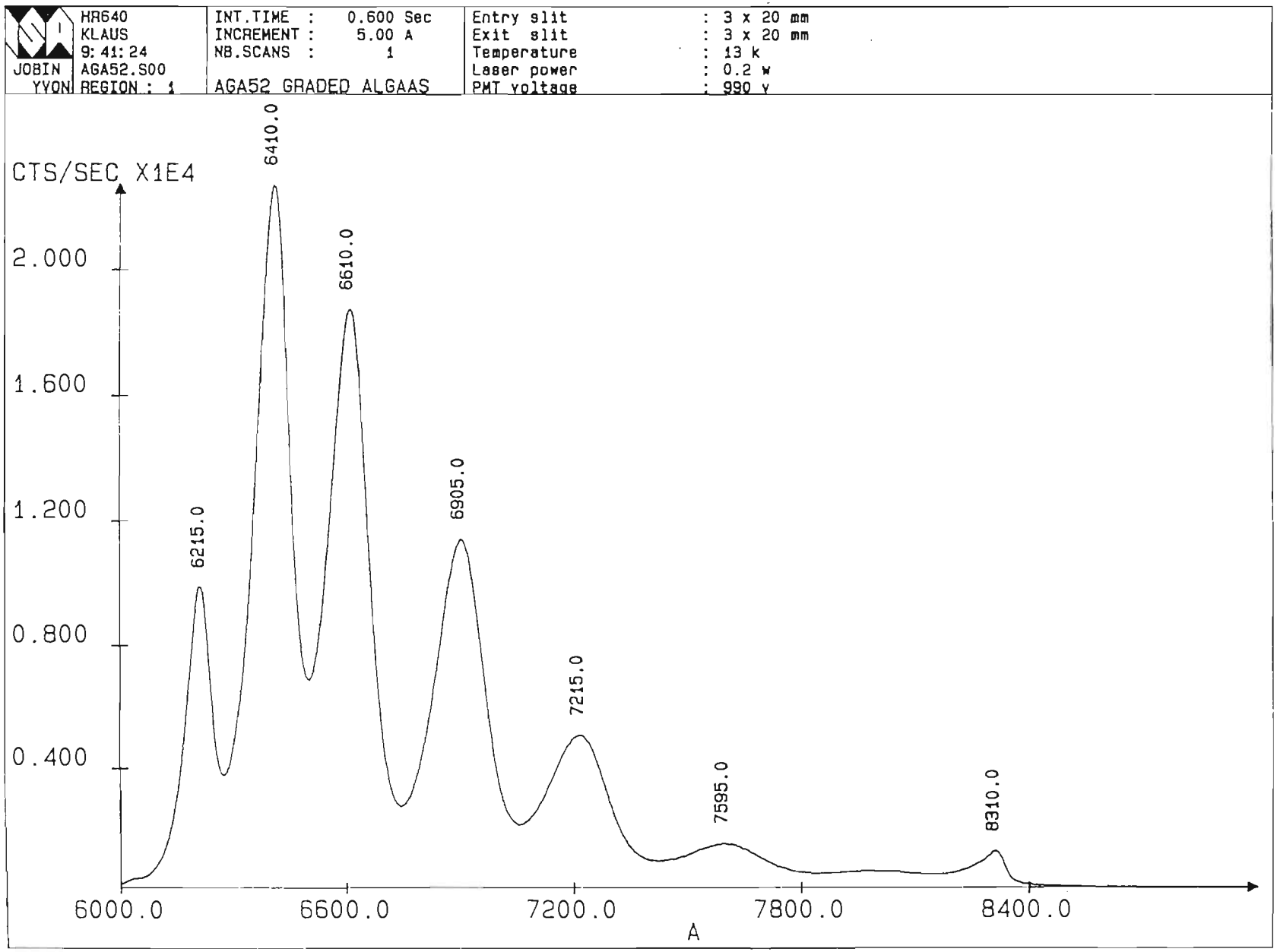

Figure 3.4-6 SIMS curve of stepped AlGaAs structure (sample AGA52).

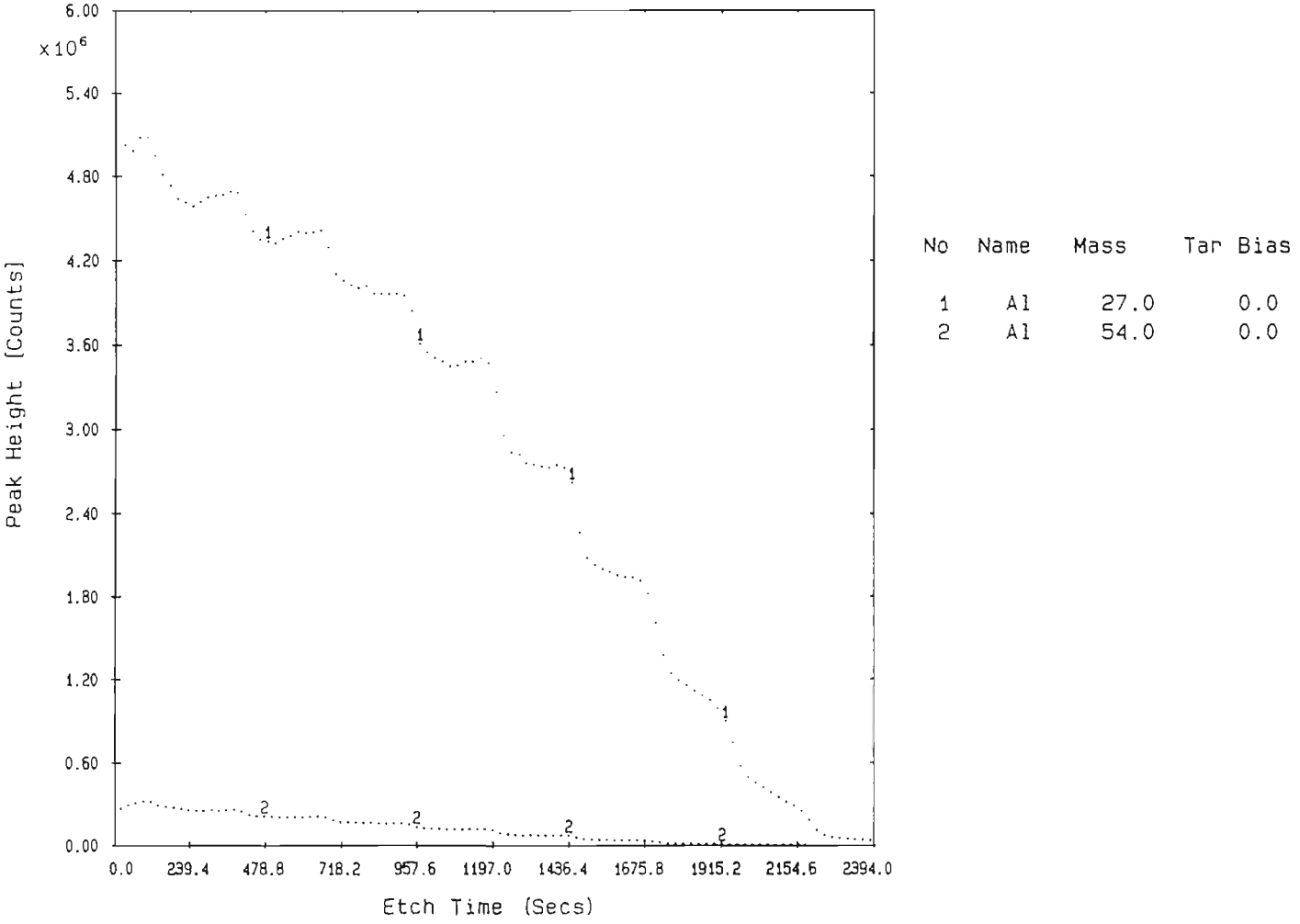

indirect bandgap material for AlGaAs compositions of $x > 0.4$. The X-ray diffractogram does not distinguish most sub-layers probably because the sub-layers are too narrow to resolve clearly and reflections for sub-layers are overlapped in the trace. Figure 3.4-6 shows the SIMS trace of the stepped layer. This curve, whilst not quantitative, indicates ten steps in the layer.

An automatically graded layer with 25 steps from $x = 0$ to $x = 0.5$ over 1000 nm (sample AGA62) using data from the second calibration of AlGaAs composition and growthrate presented in Section 3.1.2.1 was grown. The grading equation employed was (3.5-1) shown later in Section 3.5.1. No quantitative data could be derived from the analysis of the X-ray diffractogram shown in figure 3.4-7. Figures 3.4-8 and 3.4-9 show the photoluminescence and SIMS measurements of a 500 nm graded layer (sample AGA55) identical to sample AGA62. The sub-layers are barely distinguishable in the SIMS trace revealing an excellent quality grade in terms of the smoothness and linearity. Whilst a distinct emission at 812.6 nm in the photoluminescence spectrum is shown for the GaAs substrate, no emissions are visible for the sub-layers in the grade.

Figure 3.4-7 X-ray diffraction curve of graded AlGaAs structure (sample AGA62).

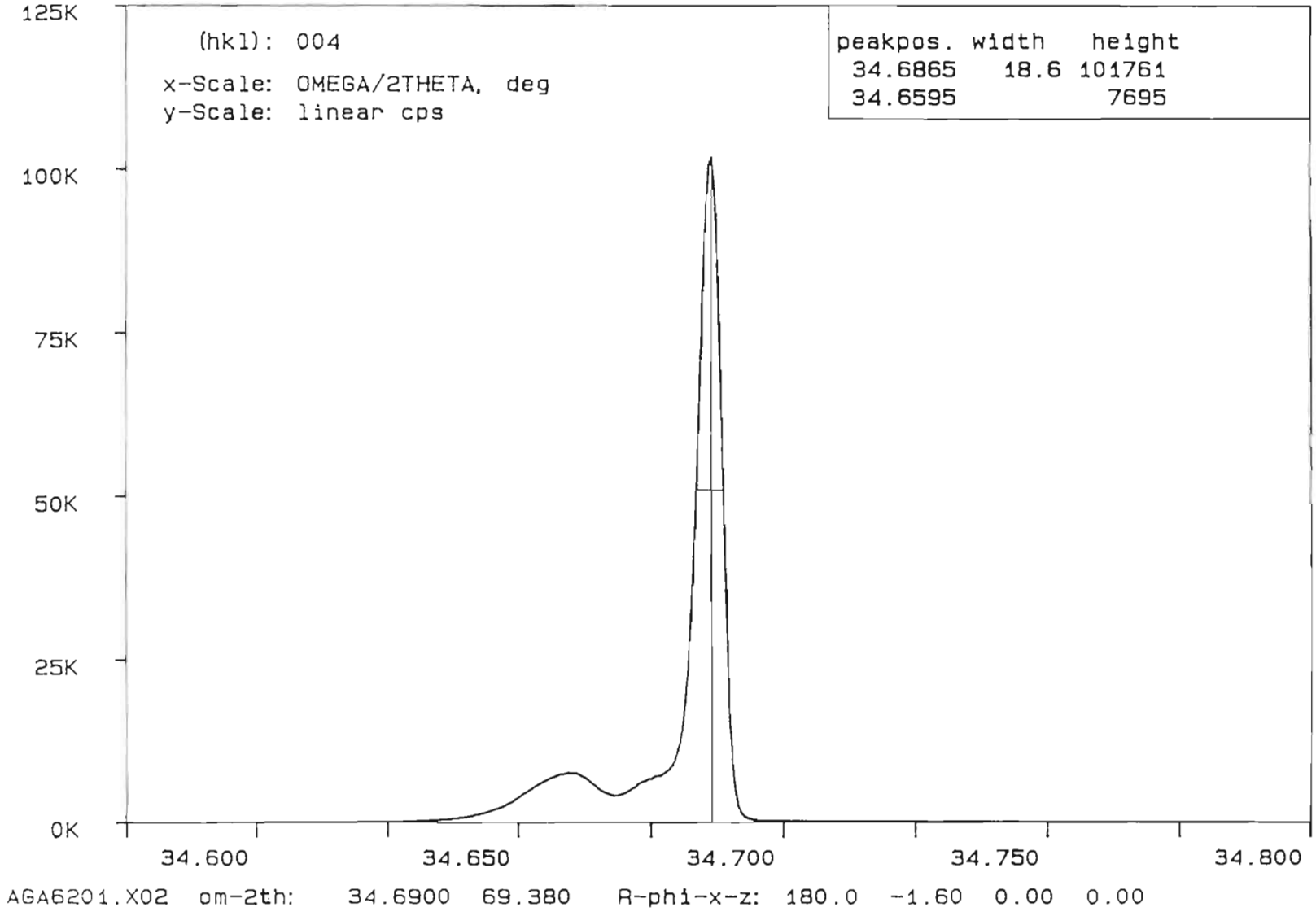

Figure 3.4-8 Photoluminescence curve of graded AlGaAs structure (sample AGA55).

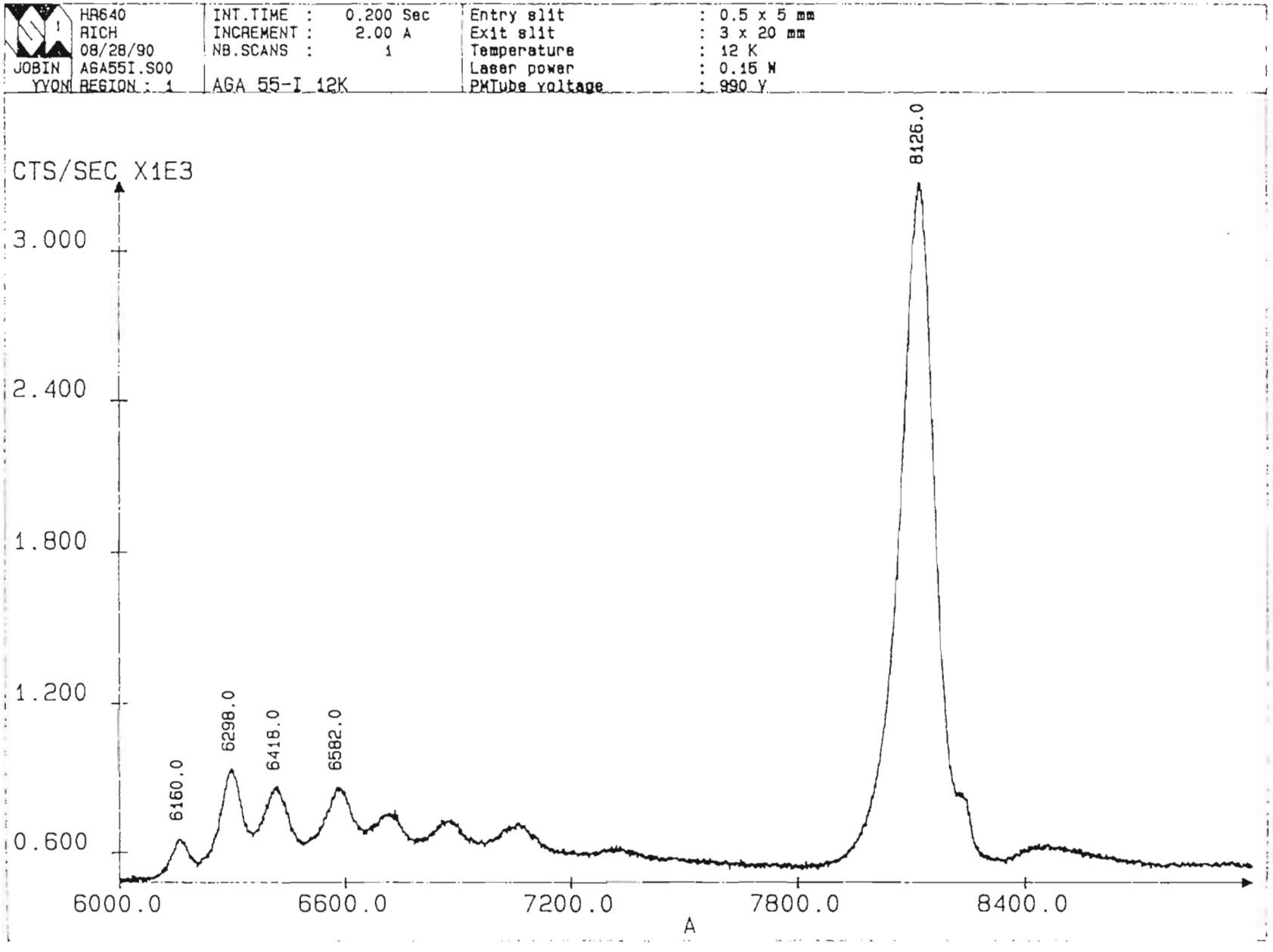

Figure 3.4-9 SIMS curve of graded AlGaAs structure (sample AGA55).

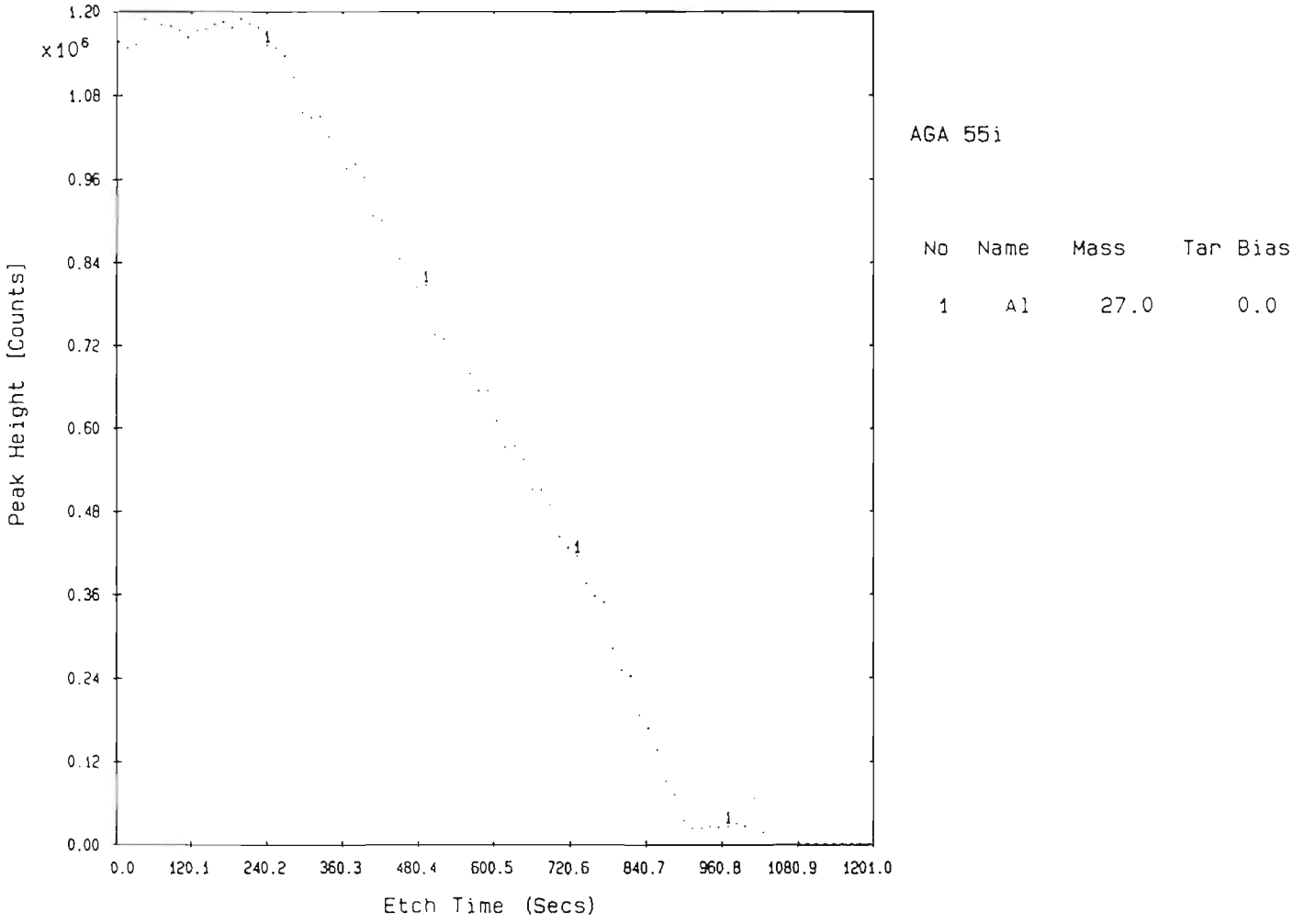

3.4.2 Assessment of step size

The structure in Figure 3.4-10 was designed to test the grading capability based on differing step sizes i.e. the extent to which the staircase variation in aluminium composition in AlGaAs is resolvable.

Figure 3.4-10 Schematic of AlGaAs graded-gap test structure.

layer 8	undoped GaAs	50 nm
layer 7	$Al_xGa_{1-x}As$ (graded x from 0.4 to 0, 8 steps)	50 nm
layer 6	undoped GaAs	50 nm
layer 5	$Al_xGa_{1-x}As$ (graded x from 0.4 to 0, 6 steps)	50 nm
layer 4	undoped GaAs	50 nm
layer 3	$Al_xGa_{1-x}As$ (graded x from 0.4 to 0, 11 steps)	50 nm
layer 2	undoped GaAs	50 nm
layer 1	$Al_xGa_{1-x}As$ (x=0.4)	100 nm
substrate	undoped GaAs	

With the required $Al_xGa_{1-x}As$ grade from x = 0.4 to x = 0 over 50 nm for all three graded layers, the time-based grading equation used is (3.4-1). Data from the fourth AlGaAs calibration of composition and growth rate (refer to Section 3.1.2.1) was used.

$$x = 1.6319e^{-0.004963t} - 1.2319 \qquad (3.4\text{-}1)$$

The number of steps in each of the graded layers 3, 5 and 7, as specified by different attenuation in the grading algorithm, is 11, 6 and 8 respectively.

In Figure 3.4-11 the SIMS spectrum is shown. Whilst the graded layers and plateau of the single layer are evident in the profile, the severity of ion beam mixing on the $Al_{0.4}Ga_{0.6}As$-GaAs interface does not allow an accurate measure of the thickness of these

layers nor the composition of the AlGaAs layers. To resolve the compositions of the spectra, a standard sample of x = 0.389 as measured by XRD was used to calibrate the Auger instrument. The test structure was then sputtered in the SIMS instrument to reveal the AlGaAs layers after which Auger surface scans were implemented. The peak composition of the grades correspond to a slightly higher value of x than the calibrated standard but certainly predicted to be within 10% of the required x = 0.4.

Depth analysis of the graded layer was derived by first sputtering a crater by SIMS to the last AlGaAs-GaAs interface and then using a TENCOR Alpha Step 200 depth measuring instrument to assess the total thickness of the epilayers. This was found to be 450 nm as designed. Furthermore, it is evident after elimininating ion beam mixing effects that the overall widths of the graded layers are within 5 nm of the designed width of 50 nm.

The AlGaAs structure was designed for SIMS analysis and is not ideally suited to XRD analysis since the reflections for the the AlGaAs graded layers will overlap in the XRD measurement. Nonetheless, a simulation of the X-ray rocking curve was undertaken and the overlay of the experimental spectrum and the simulation is shown in Figure 3.4-12.

As can be seen the agreement is excellent, especially on the low angle side of the GaAs reflection. Normally two diffractions would be visible, a GaAs reflection and an AlGaAs reflection on the low angle side of the GaAs reflection due to the larger lattice parameter of AlGaAs. In this case the thickest AlGaAs layer at 100 nm is not thick enough to cause a distinct reflection. The intensity on the high angle side of the GaAs reflection is caused by interference between all the 50 nm thick GaAs spacer layers and AlGaAs grades as well as the 100 nm AlGaAs layer. Computer simulations of the XRD measurement profiles have shown that a change of 10% in the thickness of the GaAs spacer layers introduces a measurable change in the spacing of the interference fringes. The complicating factor is that the thickness and composition of the AlGaAs grades also affects the spacing of the interference fringes. It is not possible to derive unique values for the above-mentioned parameters. Nevertheless, the XRD results do indicate that the thickness and AlGaAs compositions of the structure do not deviate drastically from the designed values.

Figure 3.4-11 SIMS analysis of graded-gap test structure.
(layer numbers refer to Figure 3.4-10)

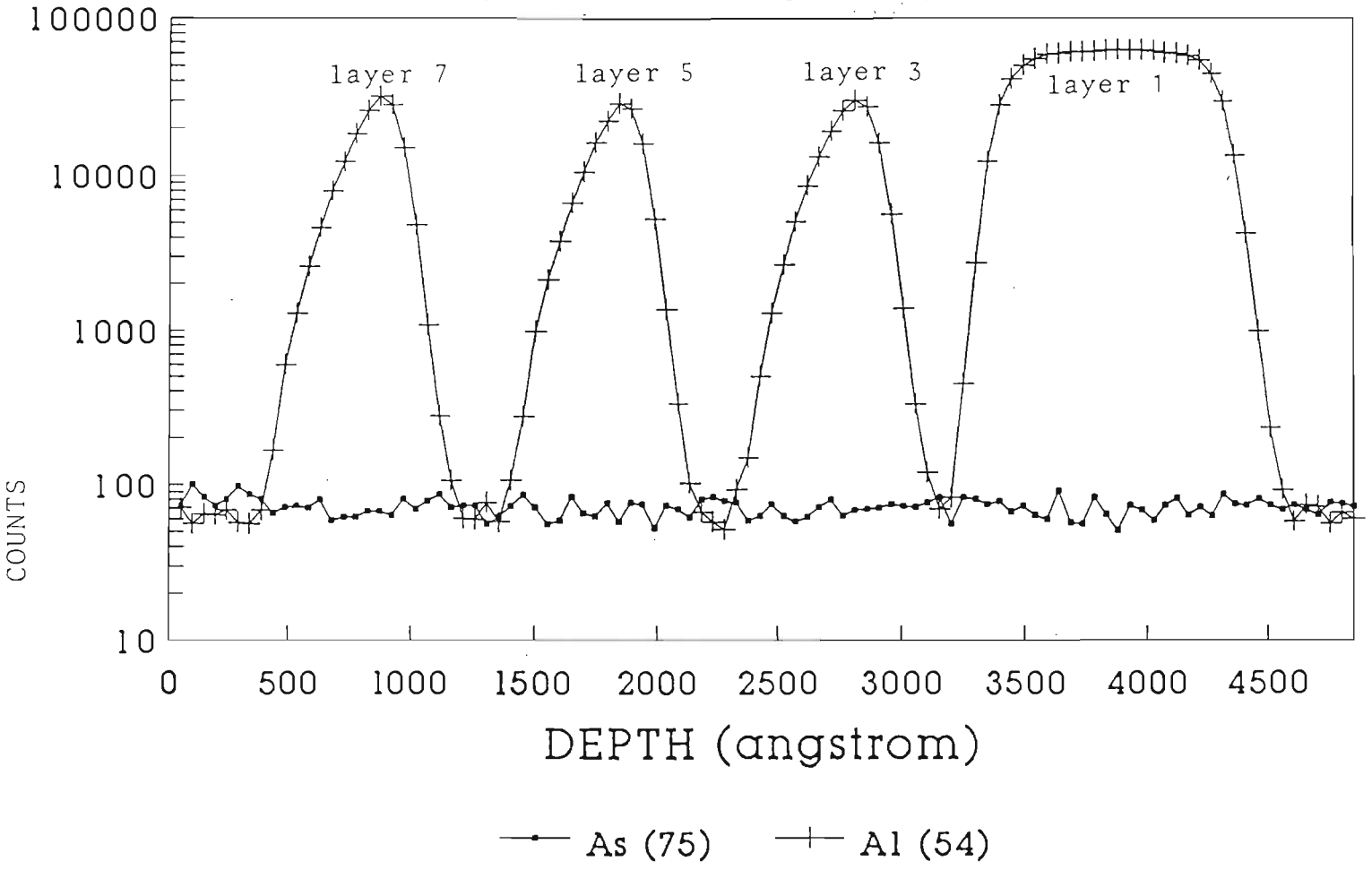

Figure 3.4-12 XRD analysis (measured and simulated) of AlGaAs graded-gap structure.

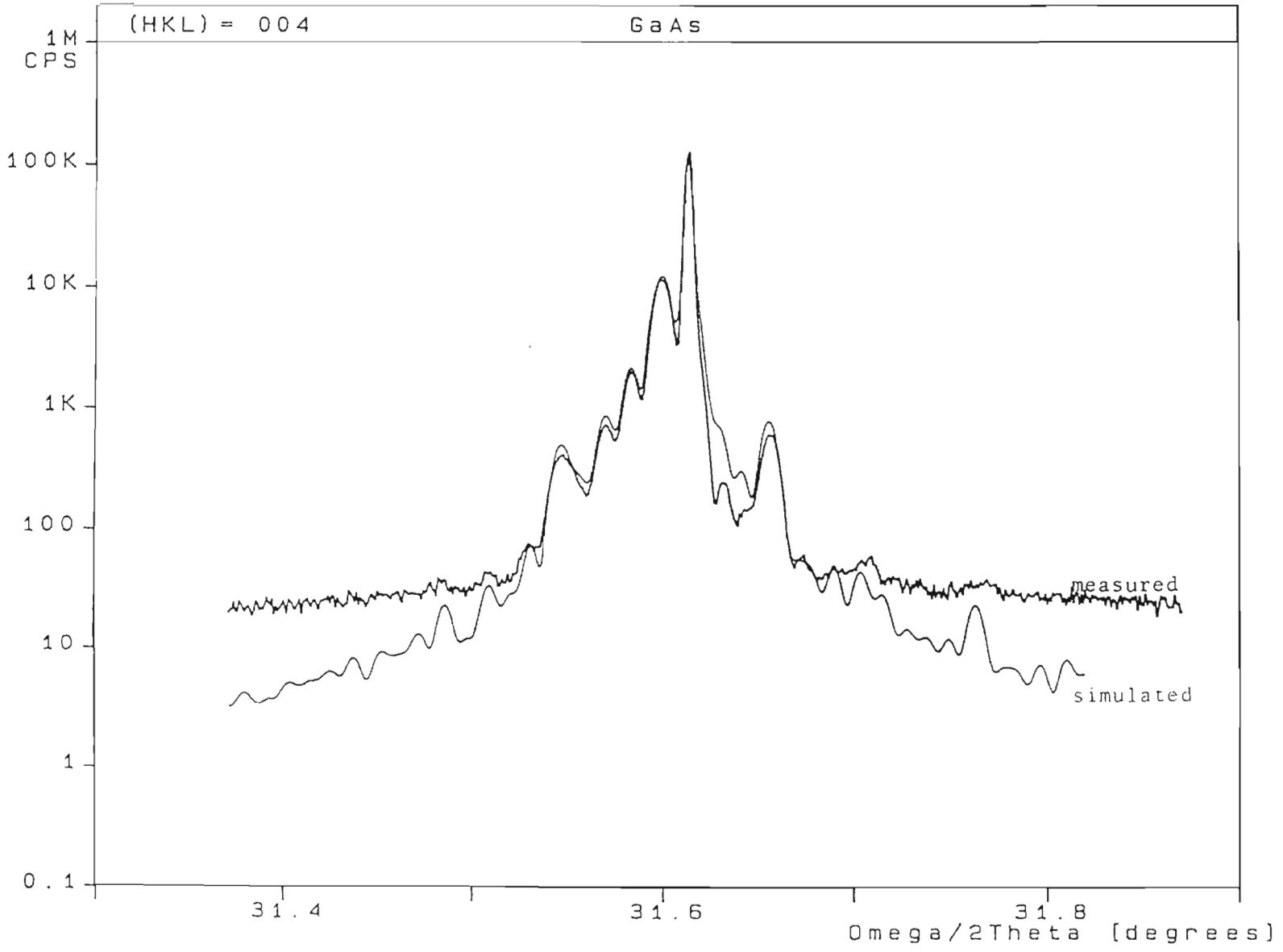

3.5 Development of GRIN-SCH SQW Laser Structures

With reference to GRIN-SCH SQW structure in Figure 3.5-1 (a graphical representation is shown in Figure 1.3-1), the width of the three graded layers and quantum well are denoted by d_1, d_2, d_3, d_w and x_1, x_2 and x_3 denote the $Al_xGa_{1-x}As$ composition at the ends of the grades. This notation will be used in the rest of this section. Thicknesses and doping of cladding and contact layers as well as the doping levels of graded layers are indicated in Figure 3.5-1 and are not critical aspects of the growth process.

Figure 3.5-1 Schematic of GRIN-SCH SQW structure.

contact layer	GaAs ($p > 2 \times 10^{18}$ cm^{-3})	1000 nm
cladding layer	$Al_xGa_{1-x}As$ with $x = x_3$ ($p = 5\text{-}10 \times 10^{17}$ cm^{-3})	500 nm
GRIN layer d_3	$Al_xGa_{1-x}As$ grade from x_2 to x_3 ($p = 1\text{-}5 \times 10^{16}$ cm^{-3})	d_3
layer d_w	GaAs quantum well (undoped)	d_w
GRIN layer d_2	$Al_xGa_{1-x}As$ grade from x_3 to x_2 ($n = 1\text{-}5 \times 10^{16}$ cm^{-3})	d_2
cladding layer	$Al_xGa_{1-x}As$ with $x = x_3$ ($n = 2\text{-}5 \times 10^{17}$ cm^{-3})	500 nm
layer d_1	$Al_xGa_{1-x}As$ grade from x_1 to x_3 ($n = 1 \times 10^{18}$ cm^{-3})	d_1
substrate	GaAs ($n > 1 \times 10^{18}$ cm^{-3})	

The GRIN-SCH development is shown sequentially in the next sections. SIMS profiling was the primary measurement technique used for analyses of these complex structures. Table 3.5-1 is a look up table which provides a reference to the AlGaAs calibration equations of Section 3.1.2.1 utilized for growth of the GRIN-SCH structures. A brief outline of the grading procedure is presented in Section 2.1.4.

Table 3.5-1 Easy reference of GRIN-SCH development and grading equations used.

Series	Growth	Growth Equations Referenced in Sect. 3.1.2.1
GRIN-SCH I	OMD44	First AlGaAs calibration : manual grading
GRIN-SCH II	OMD53	Second AlGaAs calibration : (3.1-1) and (3.1-2)
GRIN-SCH III	OMD58	Second AlGaAs calibration : (3.1-1) and (3.1-2)
GRIN-SCH IV	OMD65	Third AlGaAs calibration : (3.1-3) and (3.1-4)
GRIN-SCH V	OMD72	Fourth AlGaAs calibration : (3.1-5) and (3.1-6)
GRIN-SCH VI	OMD81	Fourth AlGaAs calibration : (3.1-5) and (3.1-6)

3.5.1 Development of the grading technique

Initial attempts at growing the GRIN-SCH SQW structure was undertaken by using discrete steps of x = 0.05 and manually effecting the growth of the grade at each step, i.e., each 0.05 AlAs step was assumed to be a single epilayer (herein referred to as sub-layers) in the complete process. To further simplify grading, a fixed growth rate of 1.111 nms^{-1} was assumed for $Al_xGa_{1-x}As$ and that for GaAs remained fixed at 0.556 nms^{-1}. The first generation of GRIN-SCH laser material produced is evidenced in sample OMD44 and designated GRIN-SCH I.

Table 3.5-2 shows the sub-layer calculations based on calibration data obtained from Section 3.1.2.1. The design dimensions were d_1 = 1000 nm, $d_2 = d_3$ = 200 nm, d_w = 5 nm and x_1 = 0, x_2 = 0.2 and x_3 = 0.5 (see Figure 3.5-1). All ten sub-layers shown in the Table 3.5-2 were used for the grade from x = 0 to x = 0.5 whereas sub-layers 4 to 10 were used for both GRIN layers requiring grades from x = 0.5 to x = 0.2 and x = 0.2 to x = 0.5 resulting in a 'staircase' variation of composition in the graded layers.

Table 3.5-2 Calculations for each sub-layer in the stepped grading procedure.

Sub-layer number	x in $Al_xGa_{1-x}As$	$\frac{TMA}{TMA+TMG}$	$\frac{TMG}{TMA}$
1	0.05	0.017	56.8
2	0.10	0.043	22.4
3	0.15	0.067	13.9
4	0.20	0.093	9.7
5	0.25	0.120	7.3
6	0.30	0.152	5.6
7	0.35	0.175	4.7
8	0.40	0.204	3.9
9	0.45	0.233	3.3
10	0.50	0.263	2.8

GRIN-SCH II has the same design dimensions as per the GRIN-SCH I structure. Unlike the manual grading procedure employed for GRIN-SCH I, the growth was automated using grading equations 3.5-1 to 3.5-3. The derivations of these equations are based on calculations shown in Example 1 of Appendix I. These calculations are also based on a fixed AlGaAs growth rate to simplify the algorithms used. The fixed rate is based on the growth rate of the median composition of each graded layer i.e., grade d_1 is based on the $x = 0.25$ growth rate of 0.889 nms^{-1} and grades d_2 and d_2 are based on $x = 0.35$ growth rate of 1.163 nms^{-1}. The data derived for growth rates as well as the composition versus the reagant concentrations are based on those obtained from the second calibration of AlGaAs composition and growth rate in Section 3.1.2.1.

Where the required grade d_1 ranges from x = 0 to x = 0.5 over 1000 nm ,

$$x = 0.00044t + 0 \qquad (3.5\text{-}1)$$

Where the required grade d_2 ranges from x = 0.5 to x = 0.2 over 200 nm ,

$$x = 0.5 - 0.00174t \qquad (3.5\text{-}2)$$

Where the required grade d_3 ranges from x = 0.2 to x = 0.5 over 200 nm ,

$$x = 0.00174t + 0.2 \qquad (3.5\text{-}3)$$

where, x : molar ratio of AlAs in $Al_xGa_{1-x}As$

t : time in seconds.

For GRIN-SCH III development, the design dimensions are the same as in the previous cases except that device structures with both 5 and 10 nm quantum wells were attempted. The grading equations were developed with linearly varying growth rates as per those shown in the second calibration of AlGaAs composition and growth rate. Example 2 of Appendix I provides the calculation basis.

Where the required grade d_1 ranges from x = 0 to x = 0.5 over 1000 nm ,

$$x = \frac{1.2788t}{2906.0t} \qquad (3.5\text{-}4)$$

Where the required grade d_2 ranges from x = 0.5 to x = 0.2 over 200 nm ,

$$x = \frac{3333.3 - 1.2788t}{t + 968.67} \qquad (3.5\text{-}5)$$

Where the required grade d_3 ranges from x = 0.2 to x = 0.5 over 200 nm ,

$$x = \frac{193.73 + 1.2788t}{968.67 - t} \tag{3.5-6}$$

Similarly, for GRIN-SCH IV, but using data from the third calibration of AlGaAs composition and growth rate in Section 3.1.2.1 and d_w = 10 nm,

Where the required grade d_1 ranges from x = 0 to x = 0.5 over 1000 nm ,

$$x = \frac{5.4372t}{20000.0 - 6.5453t} \tag{3.5-7}$$

Where the required grade d_2 ranges from x = 0.5 to x = 0.2 over 200 nm ,

$$x = \frac{3333.3 - 5.4372t}{6666.7 + 6.5453t} \tag{3.5-8}$$

Where the required grade d_3 ranges from x = 0.2 to x = 0.5 over 200 nm ,

$$x = \frac{5.4372t + 1333.3}{6666.7 - 6.5453t} \tag{3.5-9}$$

Using the data shown in Section 3.1.2.1 in the fourth calibration of AlGaAs composition and growth rate, GRIN-SCH V development uses equations also based on Example 2 of Appendix I. The high AlGaAs composition has been reduced to x = 0.45 and d_w = 10 nm.

Where the required grade d_1 ranges from x = 0 to x = 0.45 over 1000 nm ,

$$x = \frac{1.2319t}{3581.7 - t} \tag{3.5-10}$$

Where the required grade d_2 ranges from x = 0.45 to x = 0.2 over 200 nm ,

$$x = \frac{580.23 - 1289.4t}{1289.4 + t} \tag{3.5-11}$$

Where the required grade d_3 ranges from x = 0.2 to x = 0.45 over 200 nm ,

$$x = \frac{257.88t + 1.2319t}{1289.4 - t} \tag{3.5-12}$$

GRINSCH VI development uses data from the fourth calibration of AlGaAs composition and growth rate and equations for grading are derived from solving linear differential equations as shown in Example 3 of Appendix I. The first graded layer d_1 has been reduced to a thickness of 500 nm to reduce layer resistance; all other dimensions are the same as in the previous case.

Where the required grade d_1 ranges from x = 0 to x = 0.45 over 500 nm ,

$$x = 1.2319\, e^{0.000558t} - 1.2319 \tag{3.5-13}$$

Where the required grade d_2 ranges from x = 0.45 to x = 0.2 over 200 nm ,

$$x = 1.6819\, e^{-0.000776t} - 1.2319 \tag{3.5-14}$$

Where the required grade d_3 ranges from x = 0.2 to x = 0.45 over 200 nm ,

$$x = 1.4319\, e^{0.000776t} - 1.2319 \tag{3.5-15}$$

The equations for GRINSCH VI development represent the most accurate algoritms for the grading process since they fully account for the linearly varying growth rates of AlGaAs with composition.

3.5.2 Influence of the grading method on device structures

Figures 3.5-2 and 3.5-3 show the SIMS depth profile of GRIN-SCH I. Profiling through the entire 5400 nm of device structure means larger depth profiling steps are required hence lowering the sampling frequency. As a result, only five sampling points were recorded in the profiling procedure for both GRIN layers and the quantum well. This was not sufficient to draw any conclusion about the resolution of the graded layers, each of which contains 6 compositional steps. The SIMS profile of the complete structure does, however, show that the basic design is present. More detailed profiling of the GRIN layers was not undertaken owing to the high costs associated with several measurements required for an optimisation of measurement resolution. Figure 3.5-4 shows the X-ray diffractogram of the full structure, from which, no clear information can be extracted.

SIMS analysis performed at Loughborough (UK) is shown in Figure 3.5-5 for GRIN-SCH II. Large composition fluctuations are observed at the start of the GRIN region d_3. The variation in the Al and Ga signal at the start of the p^+-AlGaAs layer is possibly a SIMS artefact [Loughborough - private communication]. Steps in the Al profile is seen in the grade to the substrate (layer d_1) although this is not obvious in the GRIN layers. The shape of the graded profile appears linear for the GRIN layers (d_2 and d_3) but is curved for layer d_1. This is possibly in part due to matrix mixing effects in the analysis (refer to Section 1.4.4), the extent of which cannot be predicted accurately. The depth scale was obtained by measuring the sputtered crater depths by interference microscopy.

Figure 3.5-2 SIMS profile of GRIN-SCH I.

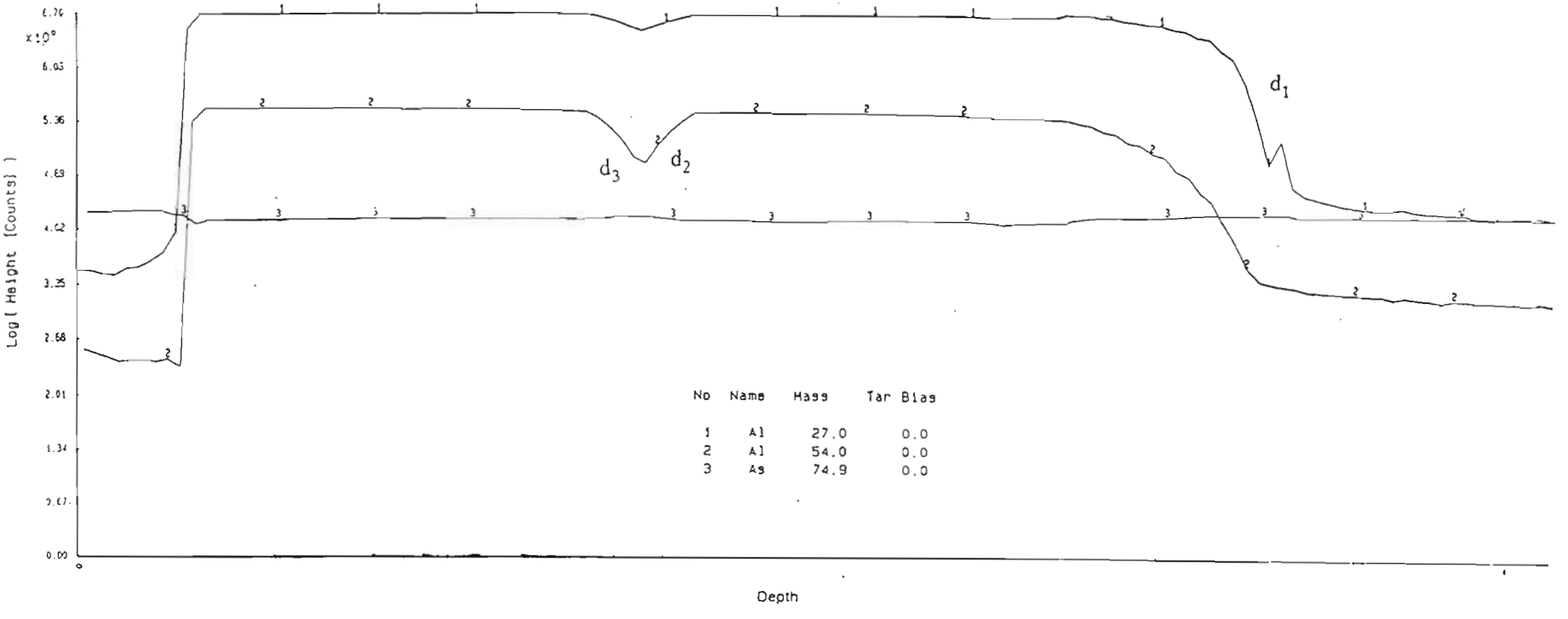

Figure 3.5-3 SIMS profile of GRIN layers of GRIN-SCH I.

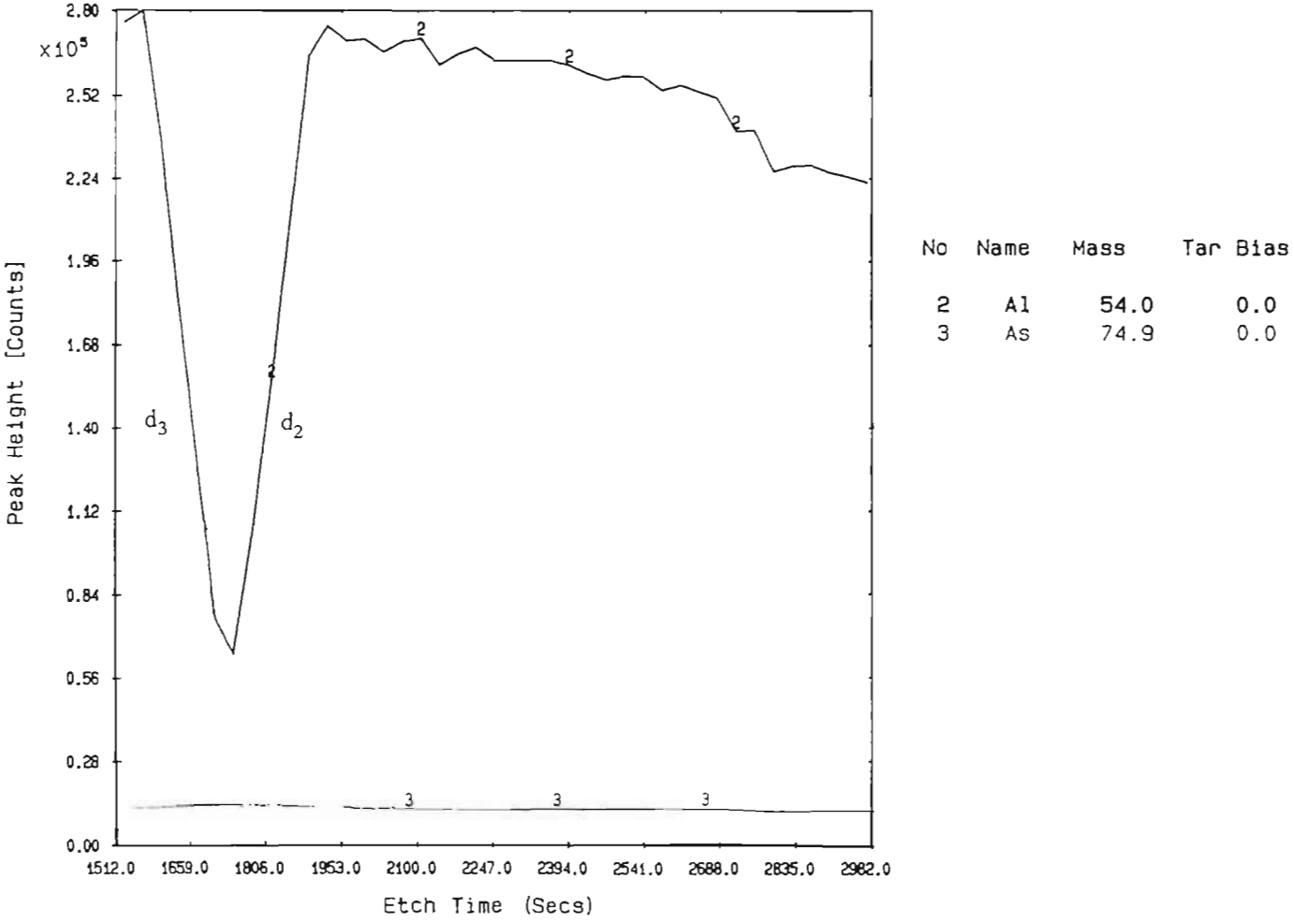

Figure 3.5-4 XRD results of GRIN-SCH I.

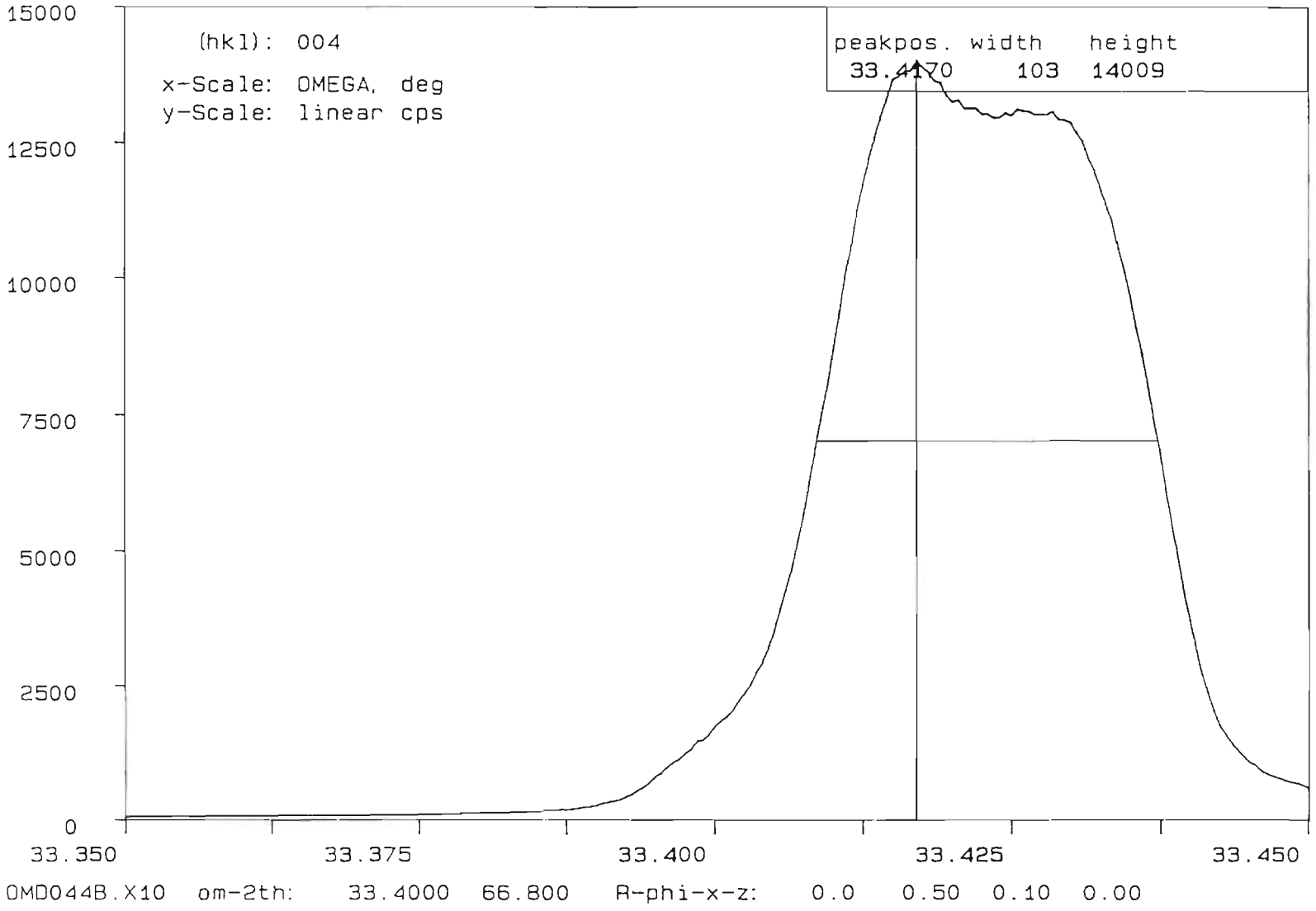

Figure 3.5-5 SIMS profile of GRIN-SCH II (source Loughborough, UK).

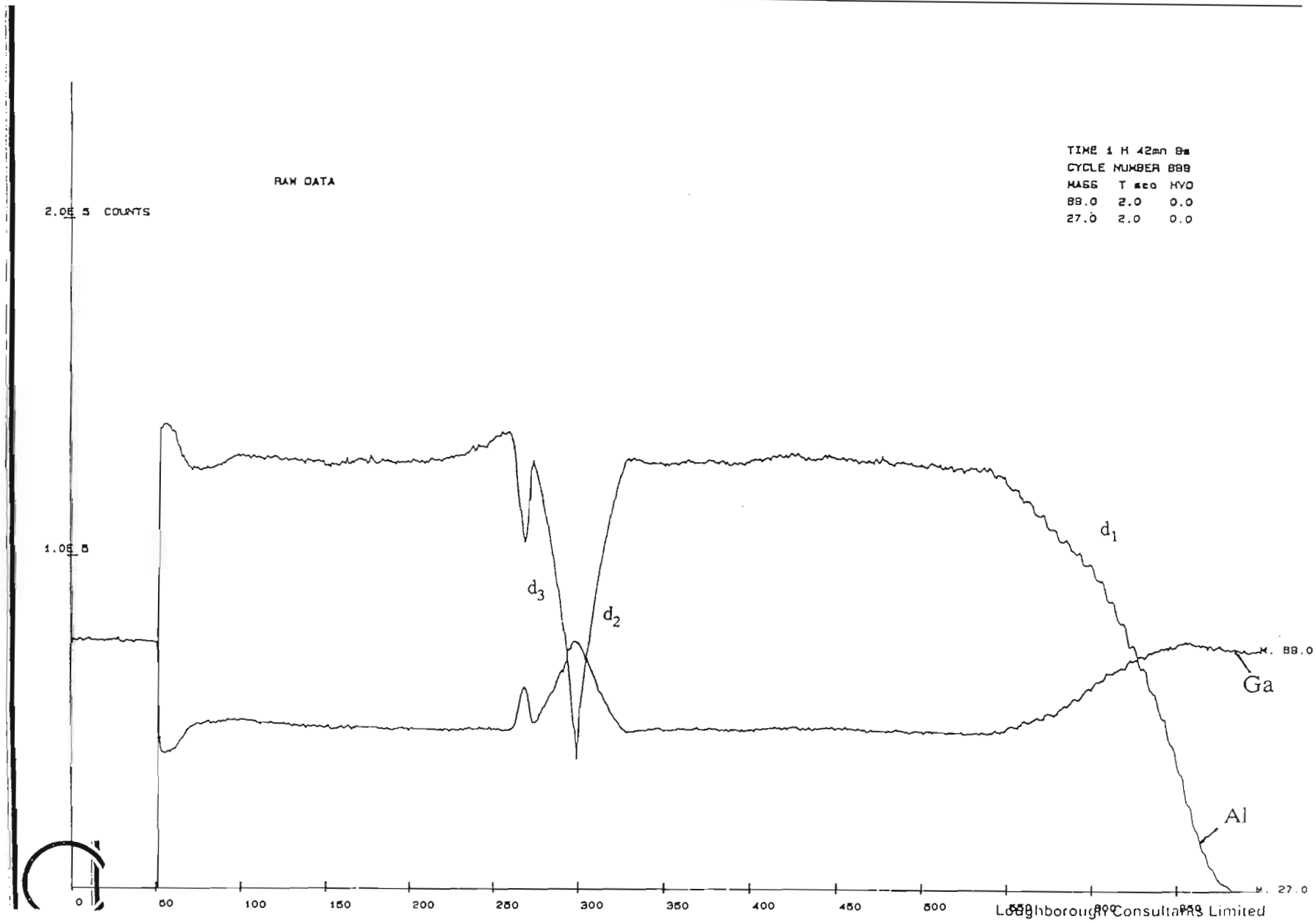

SIMS analysis performed on GRIN-SCH III is shown in Figure 3.5-6 and is very similiar to that for GRIN-SCH II. However, the composition fluctuations at the start of the d_3 GRIN layers is less pronounced than in the previous case. Steps are again visible in the graded layer d_1, although this is not obvious in the GRIN layers.

SIMS analysis of GRIN-SCH IV is shown in Figure 3.5-7 . Large Al spikes are seen at the onset of the graded layers d_1 and d_3. It is evident that the spikes are as a consequence of poor pressure control from gas switching during growth. The character of the device structure especially that of the graded layers cannot be assessed without first resolving the pressure problem of growth.

GRIN-SCH V was grown with the pressure problem resolved. Figure 3.5-8 shows the SIMS profile of the complete structure and Figure 3.5-9 shows a profile through the GRIN layers. The GRIN layers appear linear in the desired triangular format with little indication of stepping or aluminium spiking. The XRD trace in Figure 3.5-10 clearly distinguishes the GaAs substrate from the AlGaAs cladding layers. The measured composition of $x = 0.442$ closely resembles the designed value of $x = 0.45$.

The results of GRIN-SCH VI are shown in Figures 3.5-11 and 3.5-12 . These are similar to the previous measurements.

Figure 3.5-6 SIMS profile of GRIN-SCH III (source Loughborough, UK).

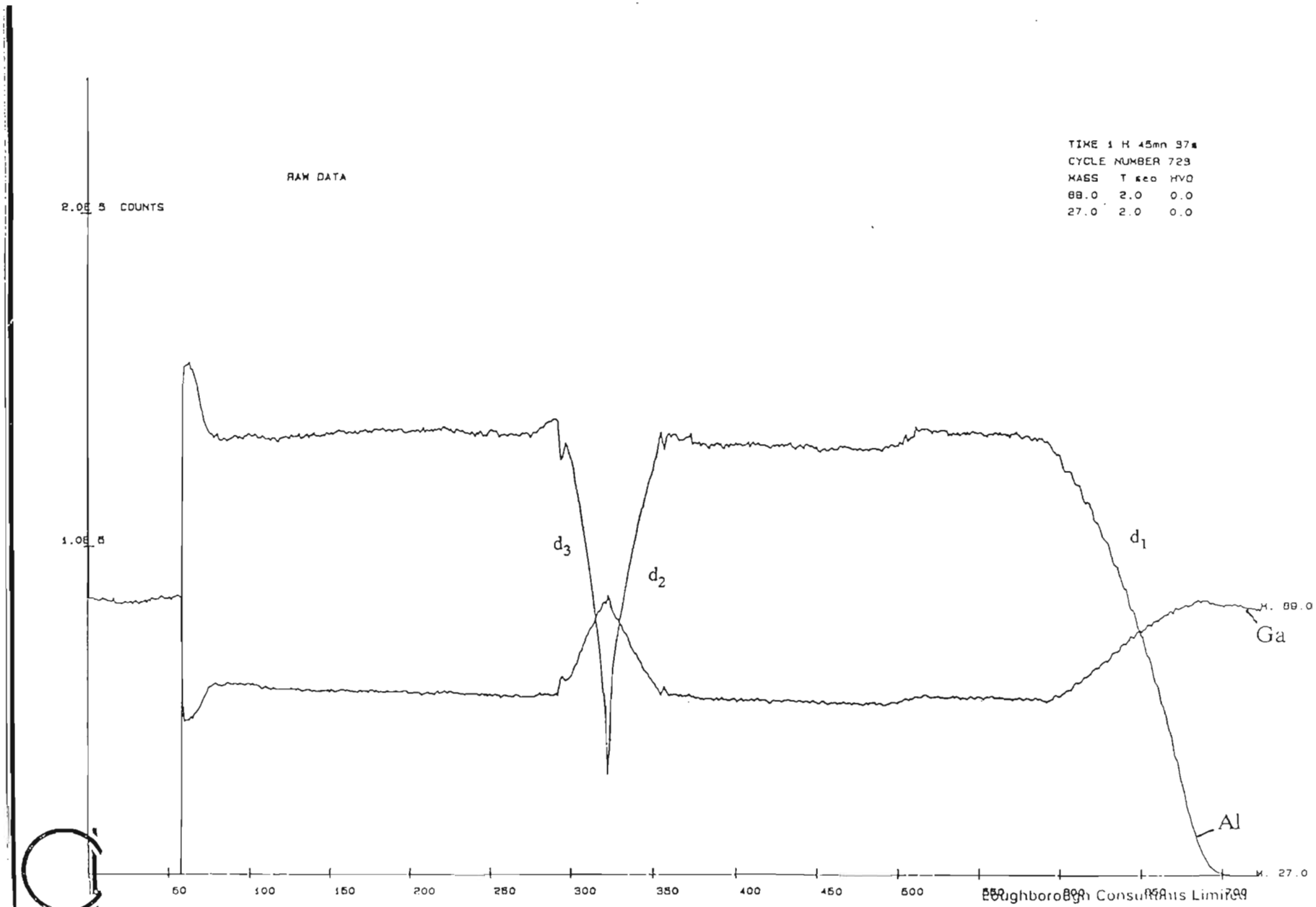

Figure 3.5-7 SIMS profile of GRIN-SCH IV.

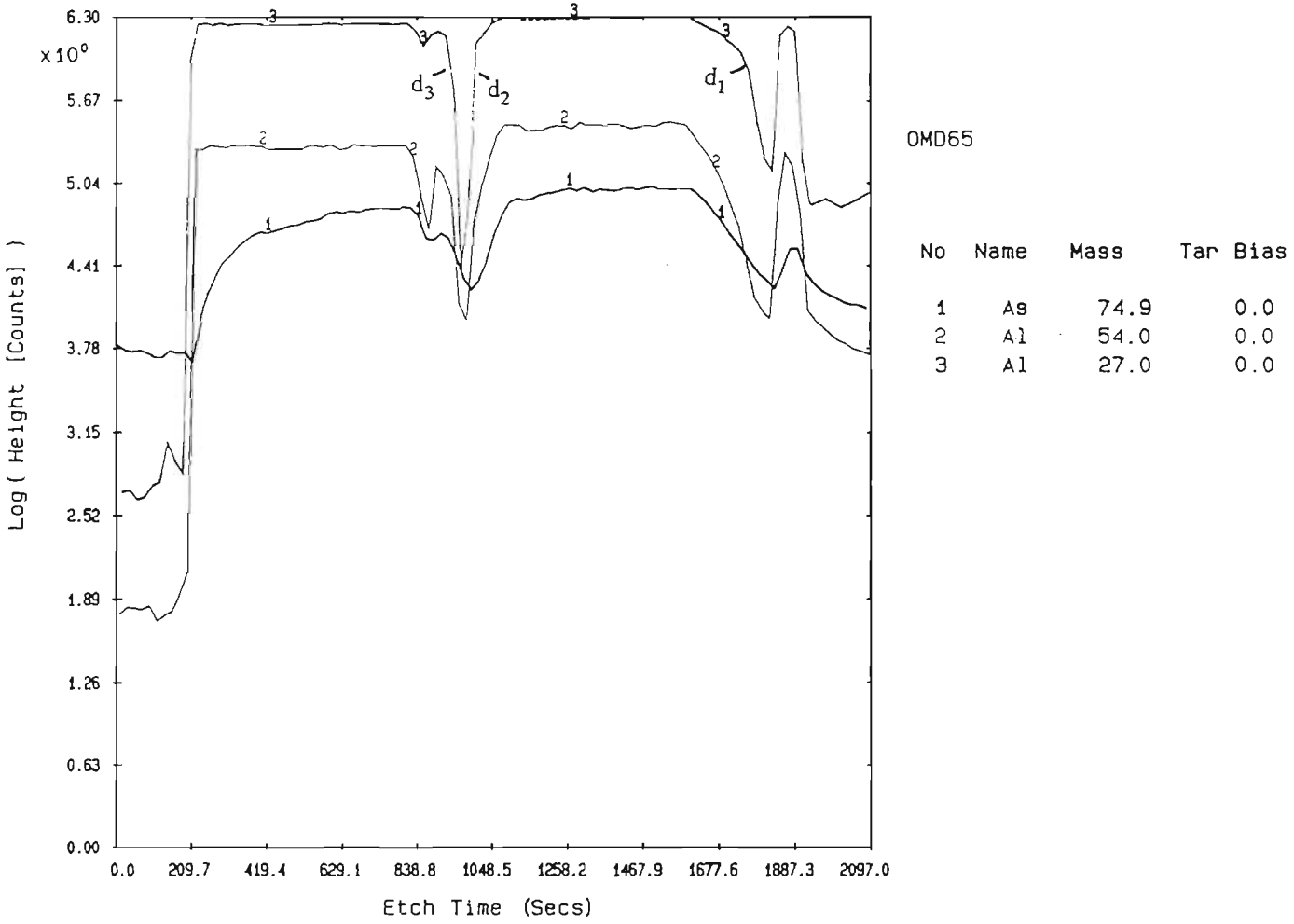

Figure 3.5-8 SIMS profile of GRIN-SCH V.

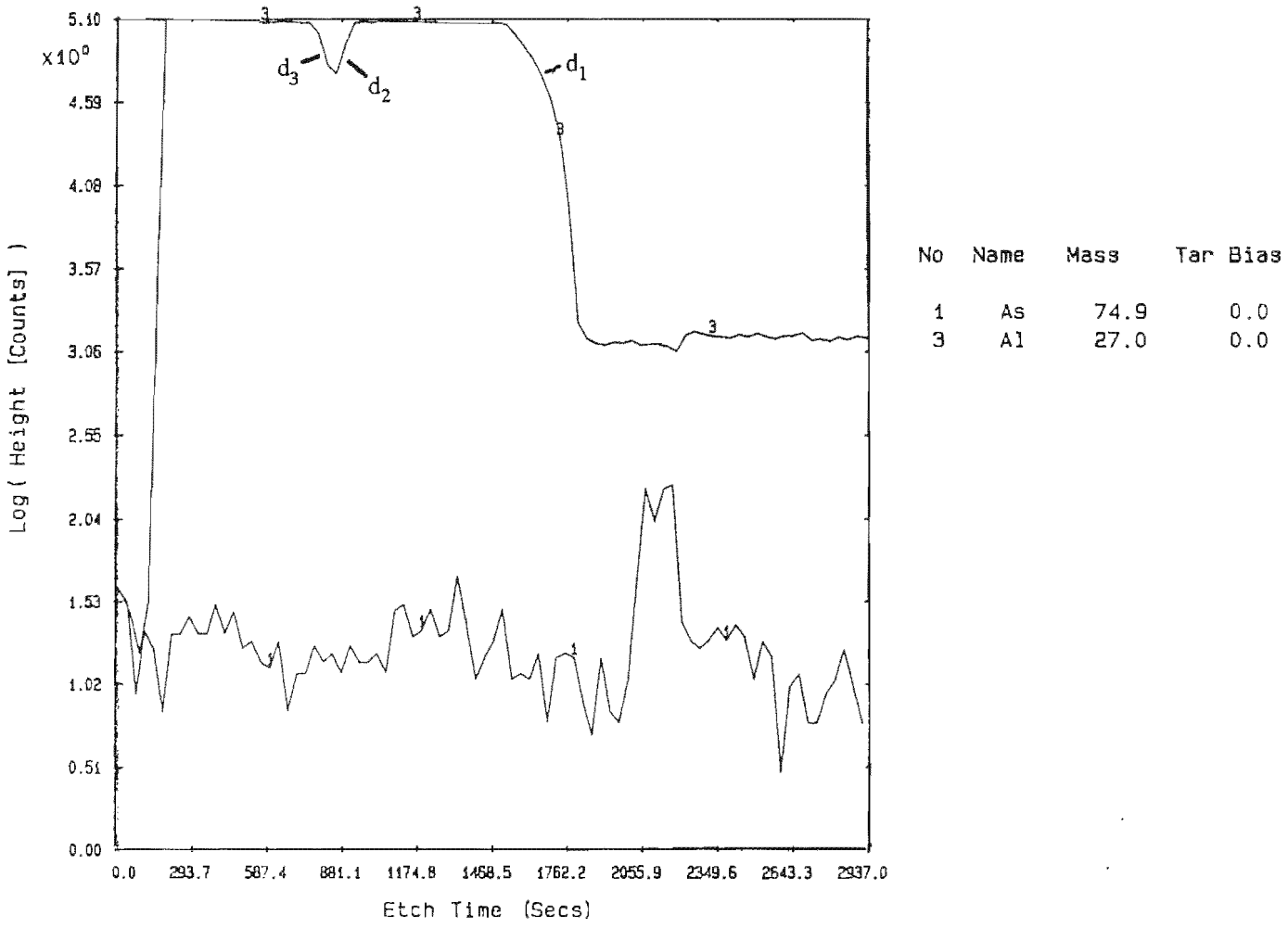

Figure 3.5-9 SIMS profile of GRIN layers of GRIN-SCH V.

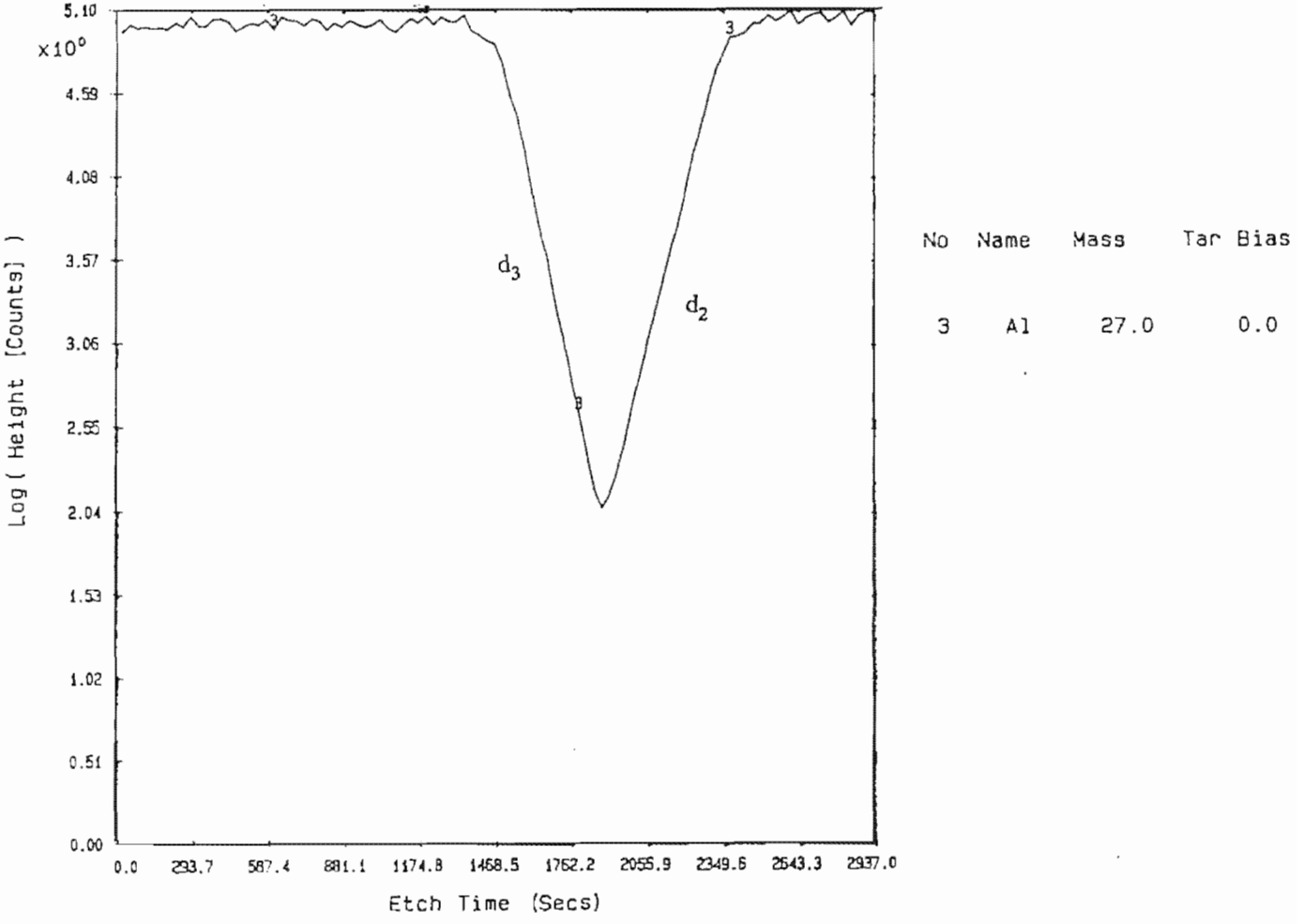

Figure 3.5-10 XRD results of GRIN-SCH V.

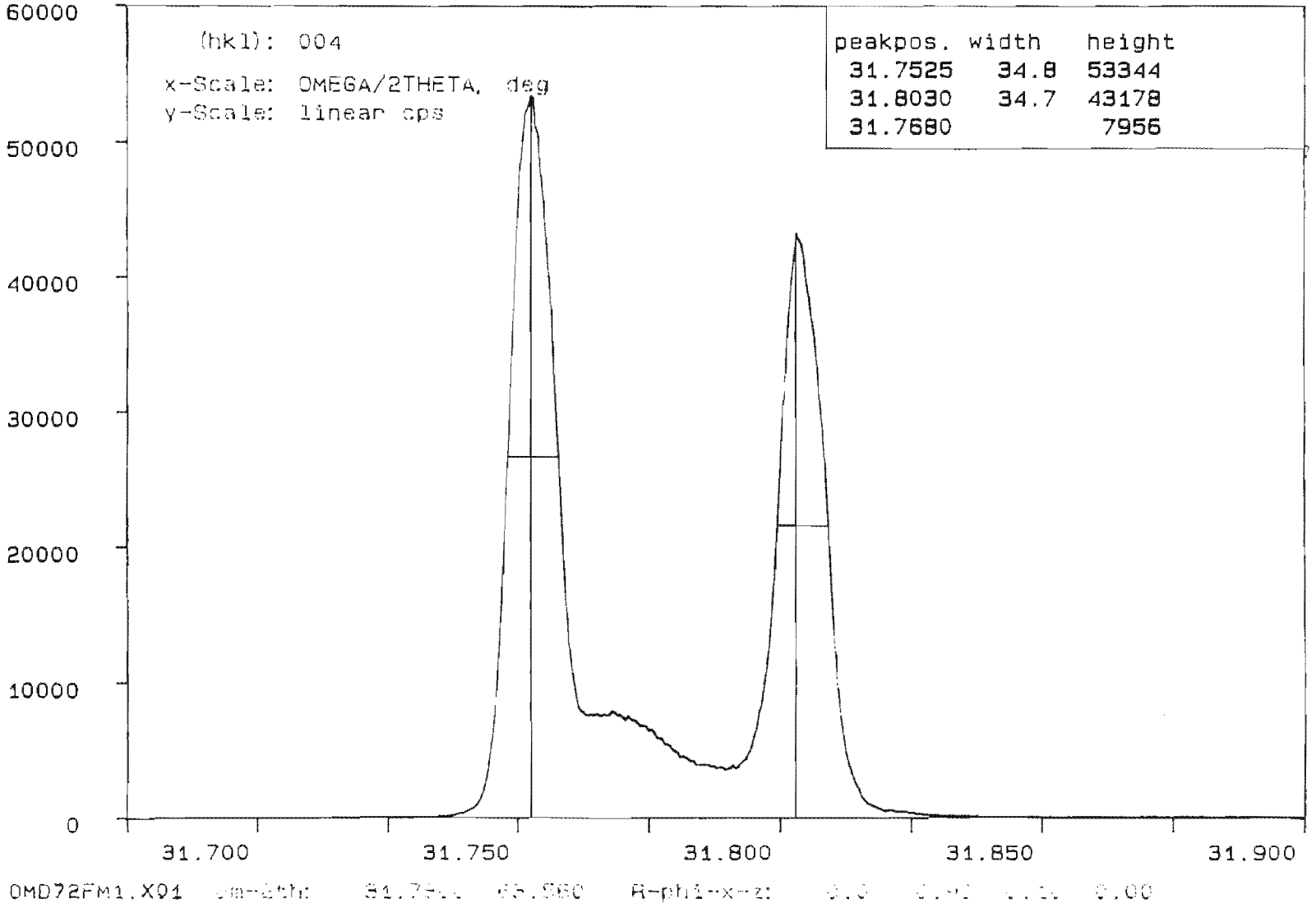

Figure 3.5-11 SIMS profile of GRIN-SCH VI.

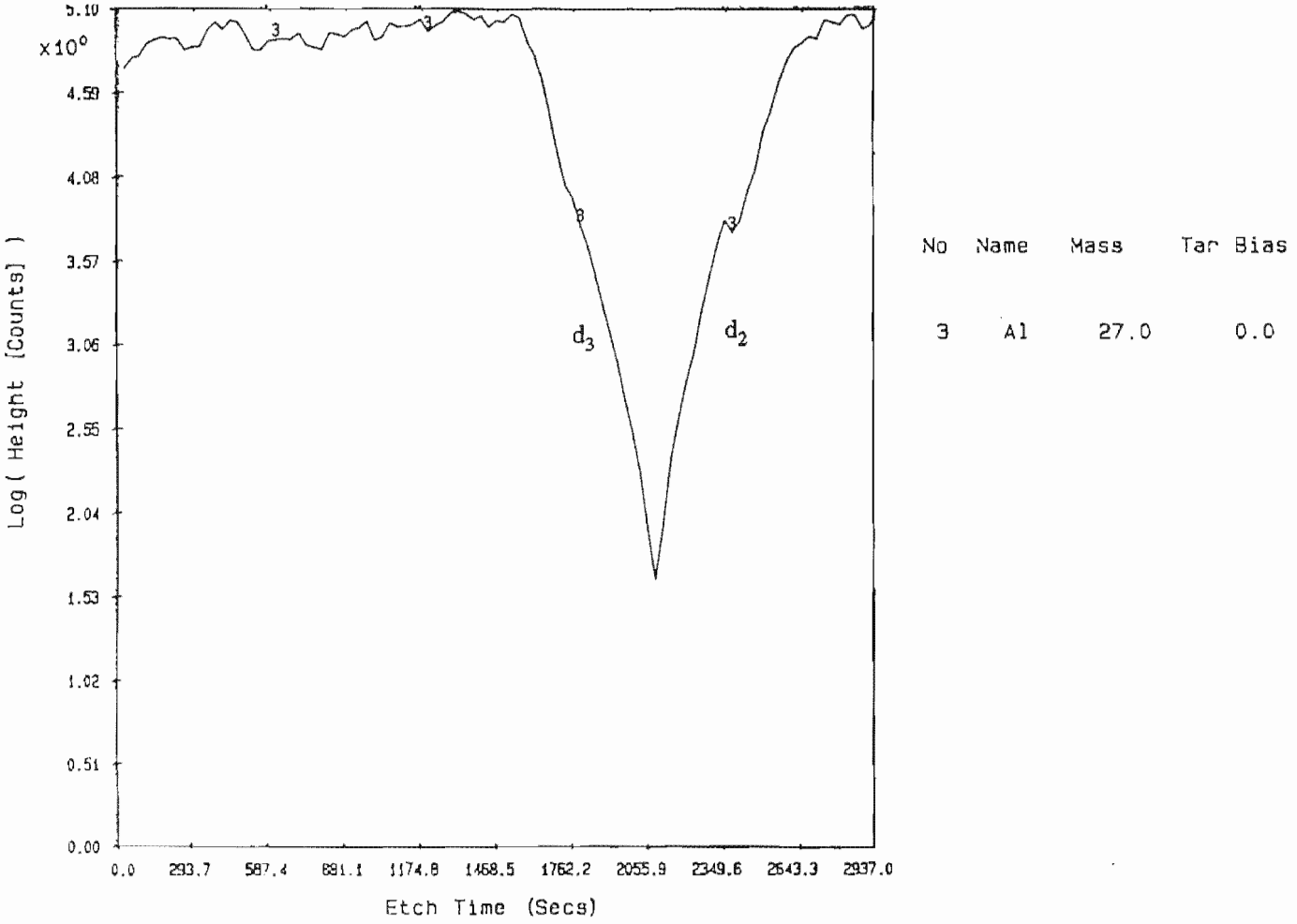

Figure 3.5-12 XRD results of GRIN-SCH VI.

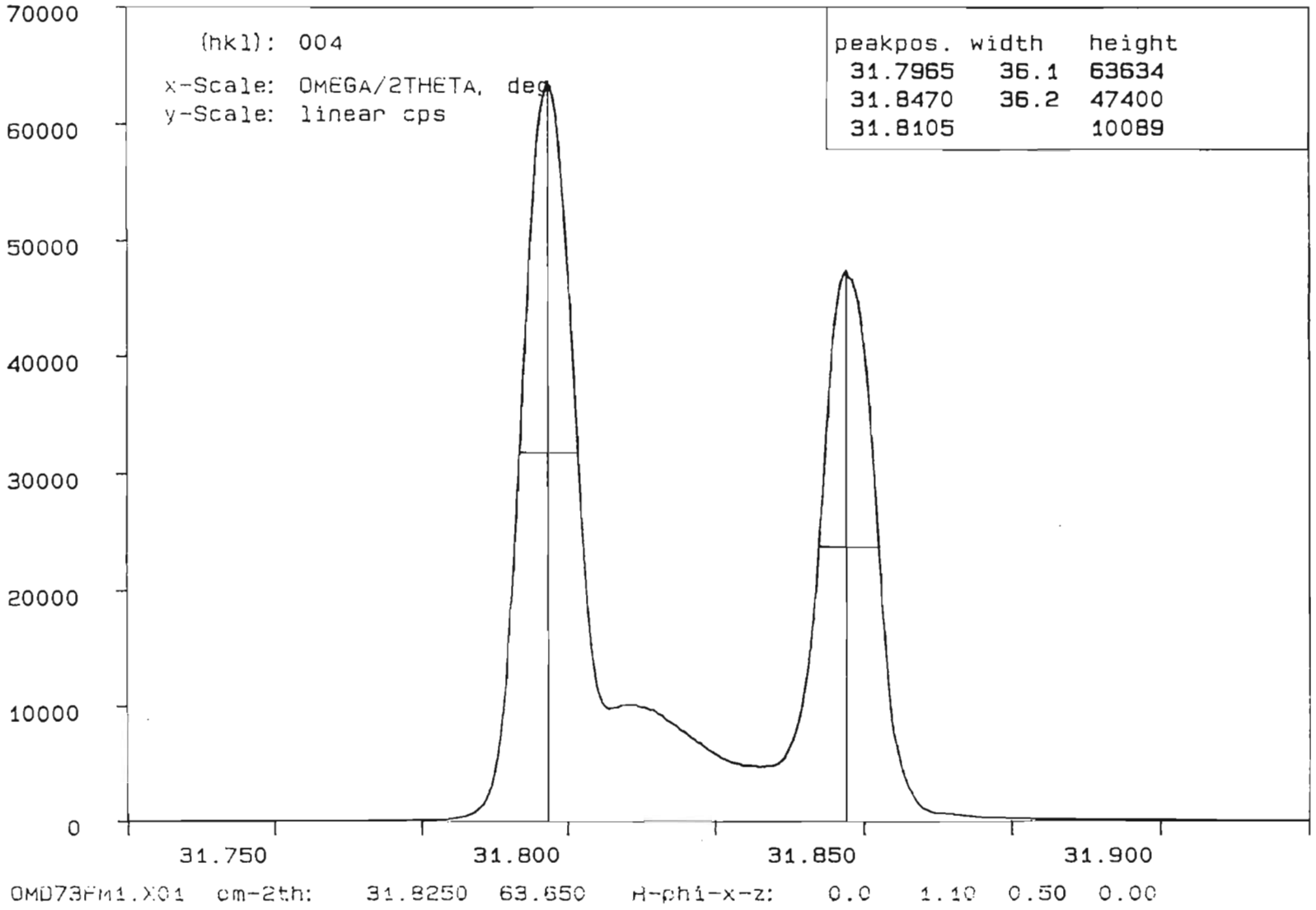

3.5.3 Comparision of Device Performance

The testing of lasers was performed on crudely made devices processed from growth structures as described in Section 2.6 . Table 3.5-3 shows a summary of typical values achieved for the various devices.

Table 3.5-3 Summary of nominal performance characteristics of devices made from OMVPE-produced material.

GROWTH SERIES	SIZE (mm x mm)	λ (nm)	J_{th} (Acm^{-2})	Power (mW @ A)	DQE (%)
DH LASER I	1 x 0.02	884	4167	2 @ 5.7	0.07
DH LASER II	0.6 x 0.3	878	1528	800 @ 7	26
GRIN-SCH I	0.6 x 0.3	830	394	600 @ 3	54
GRIN-SCH II	0.6 x 0.3	835	311	456 @ 2.1	42.7
GRIN-SCH III	0.6 x 0.3	860	296	158 @ 1.5	27.6
GRIN-SCH IV	0.6 x 0.3	823	347	358 @ 1.9	41.1
GRIN-SCH V	0.9 x 0.3	858	361	384 @ 3.6	20.21

The columns show wavelength (λ), threshold current density (J_{th}), power output in pulsed mode operation using a 1 μs pulse width at 1 kHz pulse repetition frequency and differential quantum efficiency (DQE). The results of tests for two double-heterostructure (DH) lasers also grown by OMVPE are presented for comparision. Samples from the GRIN-SCH VI study were not processed, hence no data is reported. The Chinn et al. [1988] model as discussed in Section 1.4.5 predicts lasing wavelengths of 869 nm and 840 nm for quantum well sizes of 10 nm and 5 nm in GRIN-SCH lasers respectively. The results in the table show nominal values and not necessarily the

optimum performance for lasers made from the indicated batch of material produced. The best results using GRIN-SCH IV material were 5000 mW at 17 A with a DQE of 55% for pulsed mode operation. On the same material, results on a cw ridge waveguide laser with 0.005 nm striped metallization yielded an output power of 80 mW.

3.6 Development of Gunn Diode Structures

3.6.1 35 GHz Gunn Diode Structure

The growth of a standard Gunn diode structure intended for 35 GHz operation consists of several layers of GaAs at different n-doping levels and thicknesses. The structure of a GaAs bulk effect device grown for this study is shown in Figure 3.6-1.

Figure 3.6-1 Gunn diode epitaxial structure with doping levels for 35 GHz operation.

GaAs contact layer	1000 nm	$n = 2x10^{18}$ cm^{-3}
GaAs active layer	2200 nm	$n = 1x10^{16}$ cm^{-3}
GaAs buffer layer	1000 nm	$n = 2x10^{18}$ cm^{-3}
GaAs substrate		$n = 1\text{-}4x10^{18}$ cm^{-3}

Cross-sectional microscopy on stained growth material is illustrated below in Figure 3.2.2

Figure 3.6-2. Cross section of edge-stained 35 GHz Gunn diode structure by Normarski microscopy.

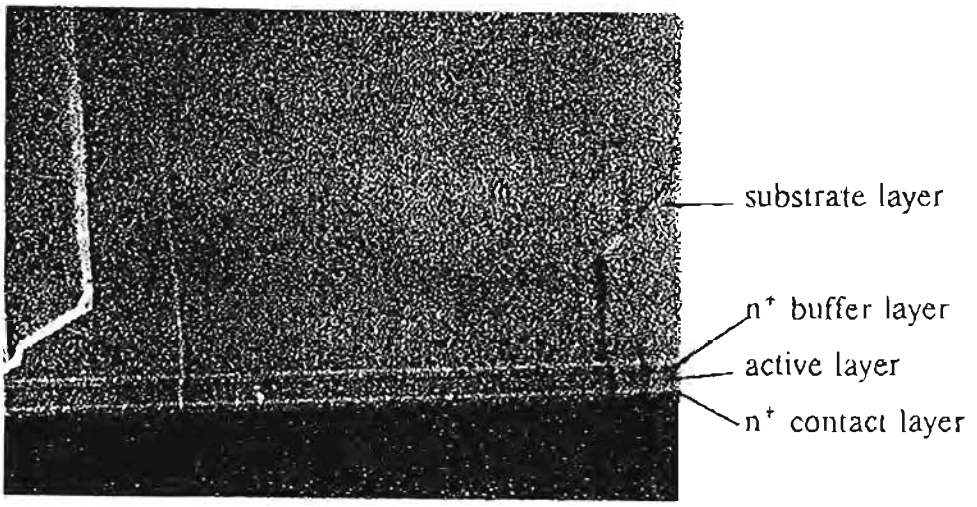

From the micrograph (Figure 3.6-2) the thicknesses, as measured by comparison with a graticule, of the buffer, active and contact layers are 1000 nm, 2200 nm and 1000 nm respectively.

Figure 3.6-3 shows the doping profile through the layers as assessed by electrochemical C-V profiling. Doping levels in the buffer and contact layers are constant with depth and greater than $1x10^{18}$ cm^{-3}. These layers appear to be 1000 nm thick, as desired. Accurate measurements are expected for the n^+ layers as they exhibit more consistent Schottky behaviour at the sample-electrochemical interface during measurement. The active layer, however, shows a discontinuity which is a result of the measuring apparatus : the C-V profiler cannot accurately profile from a highly-doped to a low-doped region as the measurement voltage and etch current fall outside the operable range when the active layer is reached. At this point the profiling was stopped and new conditions set before further measurements were taken. Hence the active layer thickness indicated on the plot is erroneous. Nonetheless, the sharp drop-off in doping on either side of the active layer indicates abrupt electrical interfaces and the active region is well defined at a doping level of $1.5x10^{16}$ cm^{-3}.

A SIMS profile (Charles Evans and Associates, USA) of the growth structure is shown in Figure 3.6-4. The thickness and doping levels, which are indirectly evaluated from SIMS data, closely resemble those indicated by microscopy and electrochemical C-V profiling. Furthermore, growth interfaces are definitely shown to be narrower than 60 nm which is 2.7% of the absolute active layer thickness. The sharpness of the interfaces also reflects the absence of the characteristic sloped curve on SIMS profiles for dopant species that have a high diffusion coefficient in the solid during growth such as tellurium.

Figure 3.6-3 Electrochemical C-V profile of 35 GHz Gunn Diode Structure.

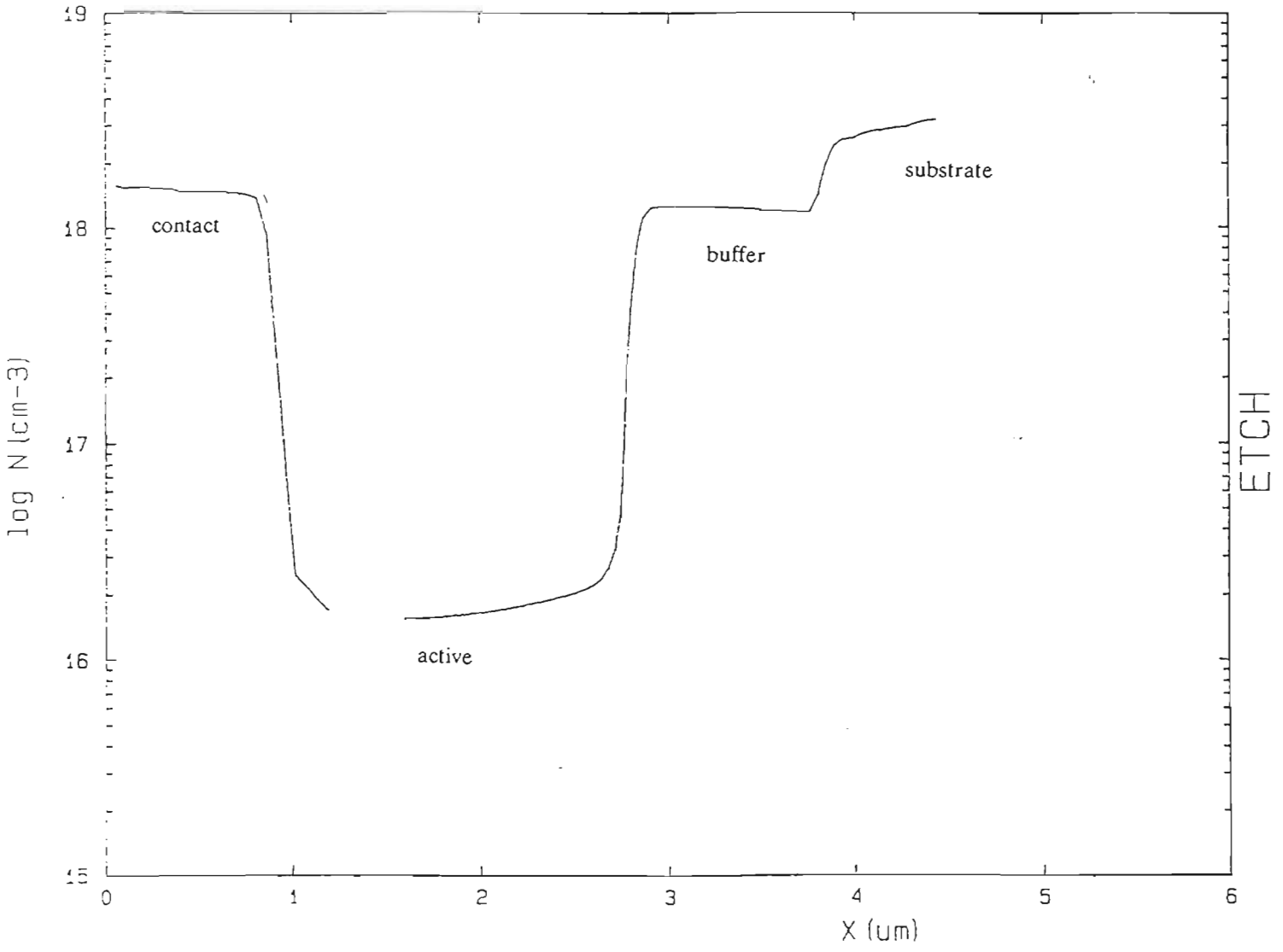

Figure 3.6-4 SIMS profile of 35 GHz Gunn Diode Structure.

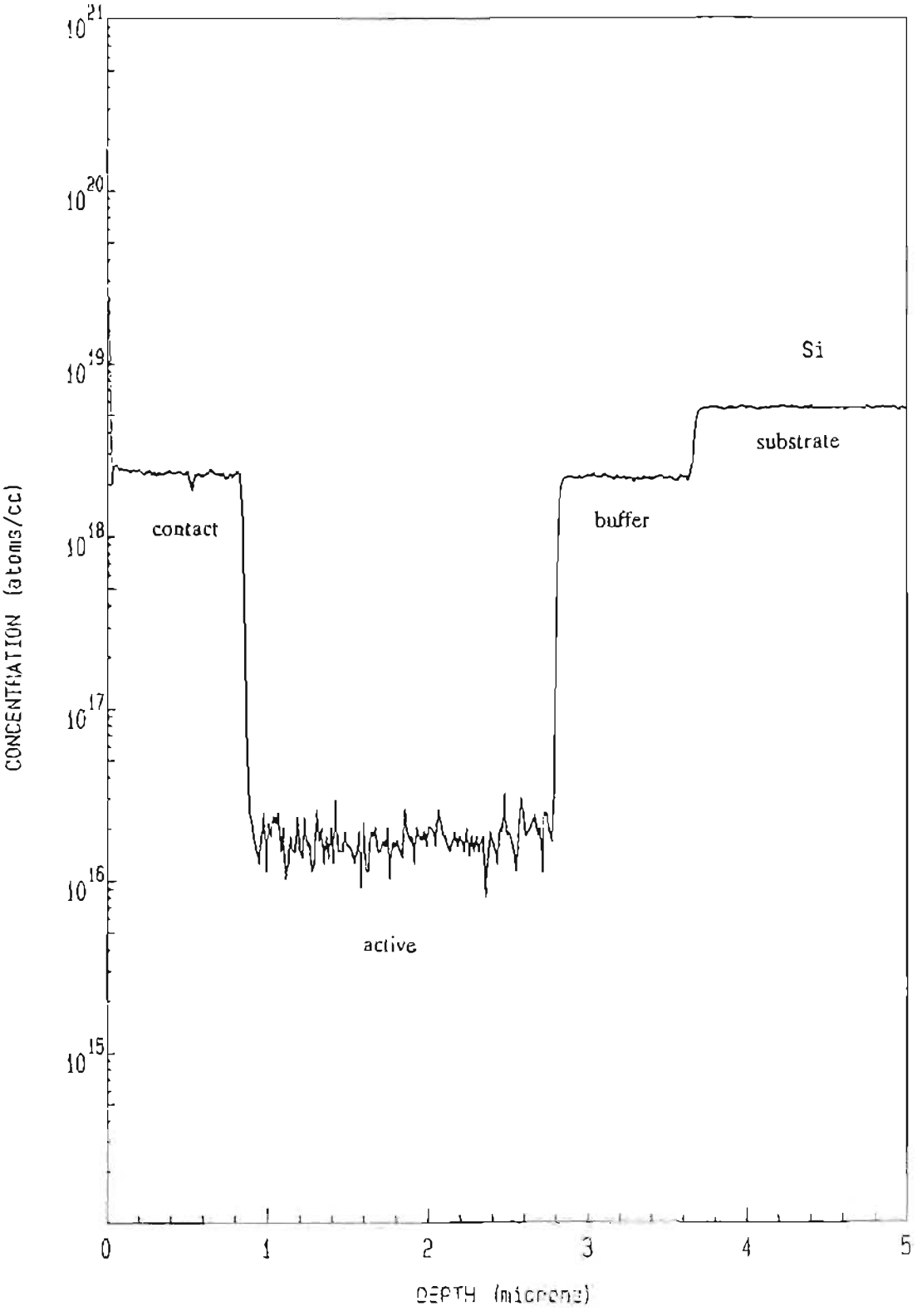

3.6.2 Millimeter-Wave Gunn Diode Structure

The design for a 94 GHz Gunn diode structure has already been discussed and graphically presented in Section 1.4; the growth structure is shown in Figure 3.6-5. The critical features are the AlGaAs graded gap and the spike doping or collector layers.

Figure 3.6-5 Schematic of 94 GHz Gunn diode structure.

layer 5	Si-GaAs contact layer (n = 2.0 x 10^{18} cm^{-3})	500 nm
layer 4	AlGaAs graded gap (x graded from 0.4 to 0)	50 nm
layer 3	Si-GaAs spike/collector (n = 5.0 x 10^{17} cm^{-3})	5 nm
layer 2	Si-GaAs active layer (n = 1.2 x 10^{16} cm^{-3})	1650 nm
layer 1	Si-GaAs buffer layer (n = 2.0 x 10^{18} cm^{-3})	500 nm
substrate	n^+ GaAs (n = 1-4 x 10^{18} cm^{-3})	

Figure 3.6-6 presents the SIMS profile (Loughborough, UK) of the final Gunn diode structure. Analysis of the sample was carried out using low energy O_2^+ primary ion bombardment and positive secondary ion detection to obtain a well-resolved profile of the aluminium grade. The depth scale was corrected for the different erosion rates of AlGaAs and GaAs and the graded layer was measured to be within 5 nm of the targeted value of 50 nm. The composition of the peak of the AlGaAs grade was not resolved by SIMS. Cs^+ primary ion bombardment and negative secondary ion detection was used to optimise the sensitivity to the dopant, silicon, and is shown in Figure 3.6-7. It was not possible to fully resolve the dopant spike next to the AlGaAs graded layer, as it is extremely thin at 5 nm. However, conditions were selected which allowed positive identification of its presence and the carrier density under the spike was calculated to be 1.7 x 10^{12} cm^{-2}; the targeted sheet doping density was 1 x 10^{12} cm^{-2}. The active layer doping was measured at 1 x 10^{16} cm^{-3} with a width of 1670 nm versus the design values of 1.2 x 10^{16} cm^{-3} over 1650 nm. The measured widths and doping levels of the contact and buffer layers closely resembled designed values.

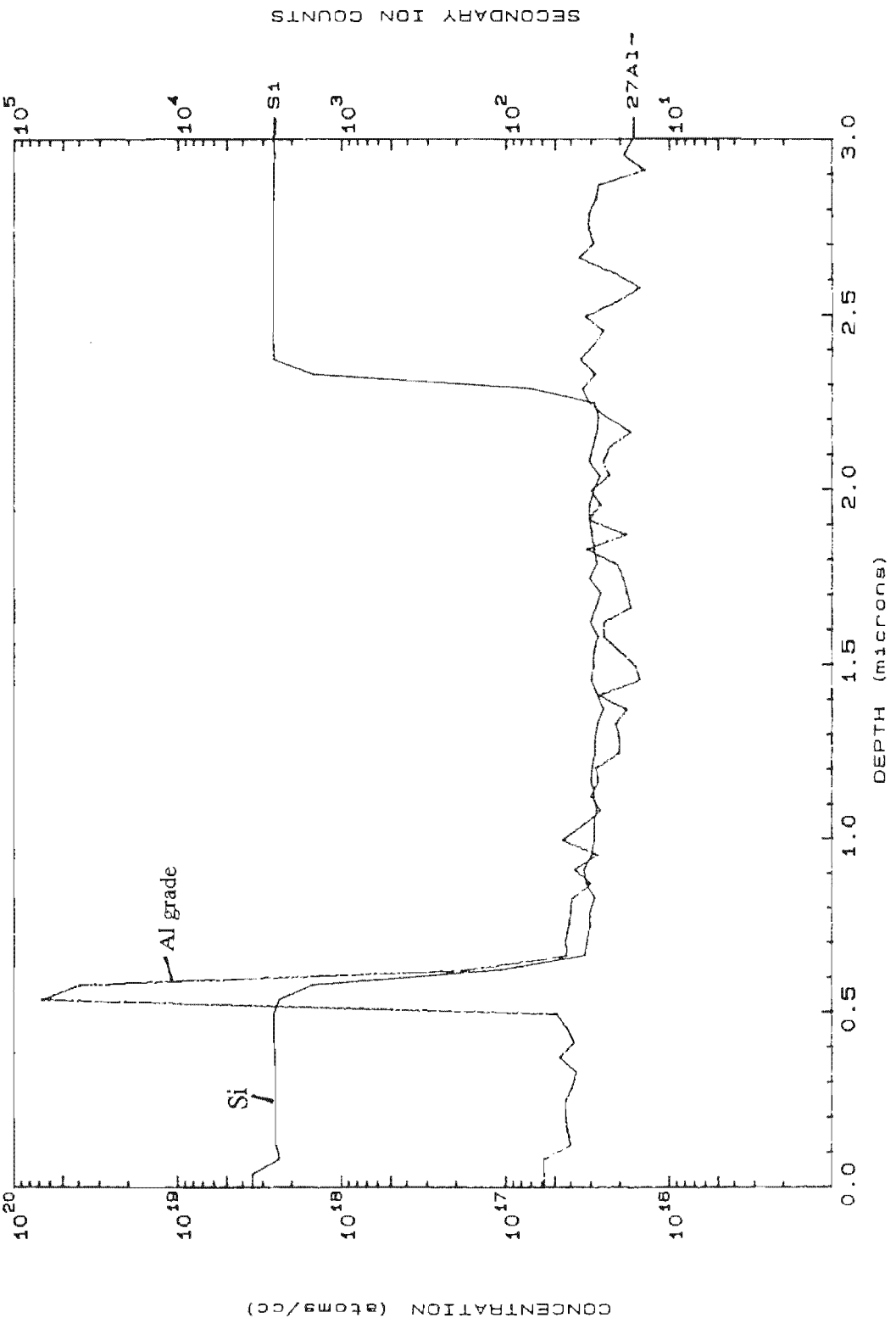

Figure 3.6-6 SIMS profile using O_{2+} primary ion bombardment of final Gunn diode material OMD79 (source Loughborough)

Figure 3.6-7 SIMS profile using Cs^+ primary ion bombardment of final Gunn diode material OMD79 (source Loughborough)

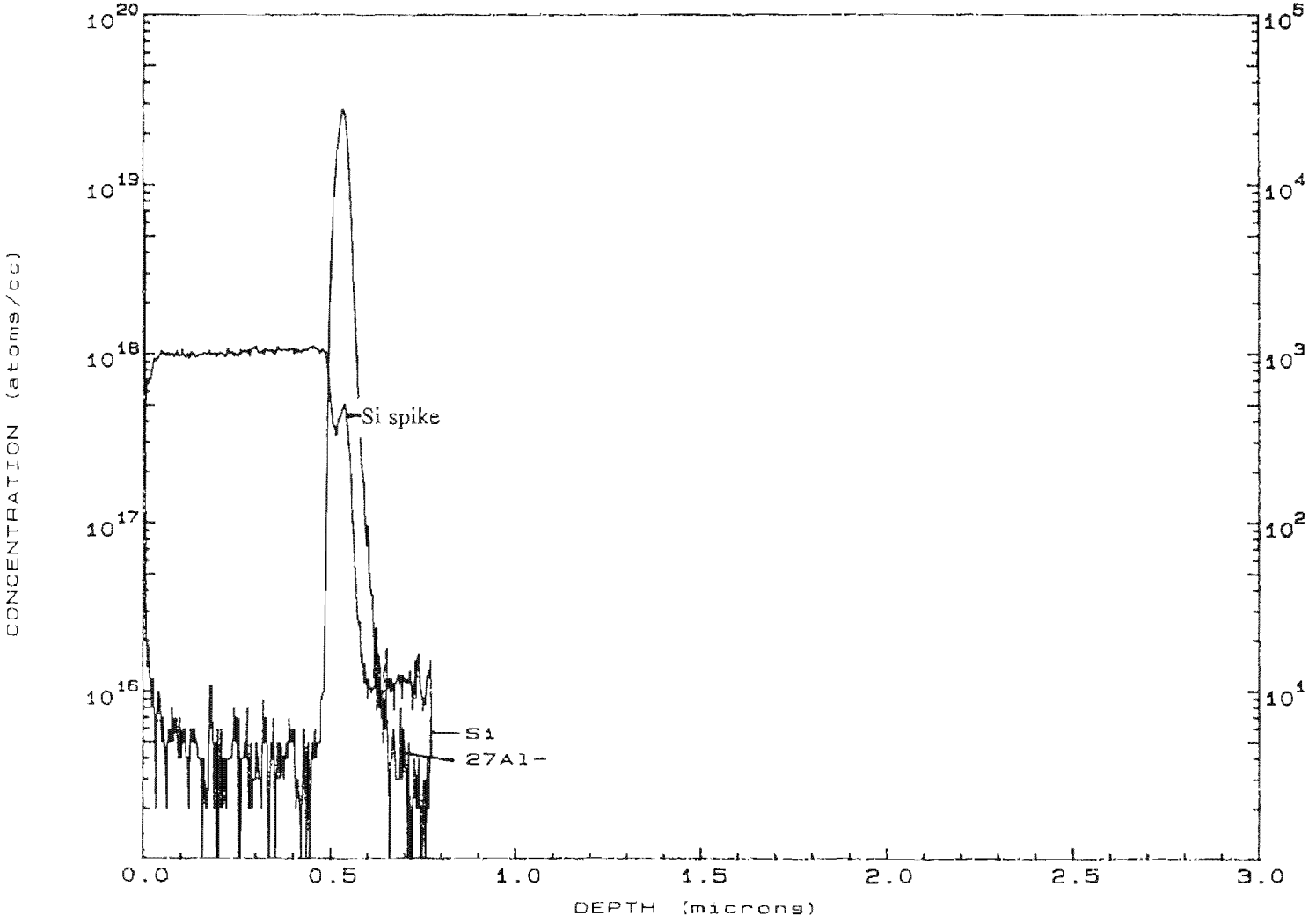

Measurements obtained from diodes processed from both OMVPE-produced (grown locally) and MBE-produced material (purchased from Varian Associates, Netherlands) are presented in Table 3.6-1. The OMVPE-grown Gunn diodes performed significantly better when compared to the MBE-grown diodes. The operation of the hot electron injector structure was clearly visible in the trace of output power versus applied bias. The hot electron injector operation manifests itself as a rapid, near-linear increase in power with increased bias. No indication of the hot electron injector operation was seen for MBE-grown Gunn diodes. The performance of the OMVPE-grown device of this study also compares well with other results obtained from diodes processed at Varian Associates, Netherlands using their own MBE material, viz., a phase noise of -75.3 to -84.7 dBc/Hz at 100 kHz; power outputs of 68 mW at 90 GHz using threshold currents of 1 to 1.2 A and 5 V bias voltage.

Table 3.6-1 Summary of performance characteristics for Gunn diodes processed from both OMVPE- and MBE-produced material.

Performance Characteristic	OMVPE material (Sample OMD79)	MBE material (Varian Associates)
Power Output	16 mW	2.5 mW
Frequency	93 GHz	94.3 GHz
Bias Voltage	4.5 to 5 V	3.8 V
Threshold Current	0.88 A	1 A
Phase Noise	-85 dBc/Hz at 20 kHz	-

4. SUMMARY AND DISCUSSION

4.1 Preliminary Findings

From previous experiments, it was found that the optimum GaAs quality was achieved at a growth temperature of 923 K and a growth pressure of 0.1 bar with a total gas flow of 10 slm. Under these conditions laminar flow without flow recirculation aided the growth of abrupt transitions in the material structure. Lower pressure also aids in growing more abrupt material interfaces. A low background doping concentration in unintentionally-doped material was also noted; the best achieved result for GaAs being a carrier concentration of 2×10^{14} cm^{-3} and a 77 K mobility of 141000 $cm^2V^{-1}s^{-1}$. The arsine partial pressure was maintained at 0.001 bar, sufficient to prevent the substrate surface being depleted of the arsenic species. The group V to group III reagent molar ratio was held at 150. For the growth of AlGaAs, the optimum growth temperature was found to be 973 K at a group V-III molar ratio of 100. Growth of AlGaAs-GaAs heterostructures were undertaken at 973 K, the optimum temperature for the ternary material.

The GaAs epilayer surfaces were consistently specular, suggestive of good morphology. AlGaAs surfaces, on the other hand, always had 'coin' features present, especially at the higher AlAs compositions. However, in view of the fact that photoluminescence spectra of both materials show sharp, well-defined exciton peaks, this material is of excellent optical quality with insignificant impurity or defect content. This is also confirmed by X-ray diffraction which indicated little lattice distortion in the narrow diffraction peaks obtained. A few AlGaAs samples were profiled by secondary ion mass spectrometry and revealed a flat composition profile indicative of good depth uniformity.

Doping of both GaAs and AlGaAs is vitally important in reducing the overall series resistance of devices whilst maintaining the semiconductor properties necessary for device operation. This means that careful control of the level of doping is essential to the final working model. The more commonly used dopants, namely silicon and tellurium for n-type material and zinc for p-type material were employed in this study.

The linear relationship between dopant mole fractions in reagant streams and solid doping allowed for ease of implementation of accurate doping. For GaAs, controllable silicon doping in the range 8.7 x 10^{15} cm^{-3} to 2.0 x 10^{18} cm^{-3} ; tellurium doping in the range 1.0 x 10^{17} cm^{-3} to 2.0 x 10^{18} cm^{-3} and zinc doping in the range 5.0 x 10^{17} cm^{-3} to 2.0 x 10^{19} cm^{-3} were satisfactory for all device development purposes. Similarly for AlGaAs at compositions as high as x = 0.5, satisfactory doping was achieved for the GRIN-SCH laser structures.

4.2 Calibration of AlGaAs Composition and Growth Rate

The $Al_xGa_{1-x}As$ grading algorithm for automated compositional grading requires two equations : the first relates the group III constituent ratio to solid composition and the second the growth rate to solid composition. In setting up such a procedure, certain prior requirements have to met. A set of single $Al_xGa_{1-x}As$ layers spanning the composition range x = 0 to x = 0.6 were grown so that data relating the solid composition to both group III reagant ratios and growth rates could be extracted. Several iterations of AlGaAs single layer developments were conducted during the period of this work as shown in Section 3.1.2.1; many iterations were necessary for the following reasons :

i. The dimensions of TMG and TMA bubblers as well as the liquid height both contribute to the degree of saturation of group III species in the carrier gas. Errors may result because the control algorithms assume a fully saturated carrier gas. The change in compositional characteristics of grown material is noticeable when bubblers are changed and hence ongoing calibration is required.

ii. Modifications to the reactor system that have an influence on the resultant growth layers such as replacement of non-stirred bubbler temperature baths being replaced with stirred baths or replacement and recalibration of critical mass flow controllers.

iii. More accurate data evolved from the use of the improved analytical techniques.

For each of the AlGaAs calibrations for composition and growth rate, XRD and photoluminescence were the dominant techniques for the determination of composition whilst optical microscopy and SEM were used for thickness determination. The relationship of growthrate versus composition was always linear with satisfactory regression fits ($r^2 > 0.98$). The increasing growth rate with AlAs composition is to be expected since the rate of incorporation of aluminium in the solid is higher than that for gallium. The relationship between the trimethylaluminium to total group III molar ratio and the solid composition is non-linear. This relates to the different rates of incorporation of the two group III species into the solid, since if they were the same, the relationship would be perfectly linear.

4.3 Characterisation

Visual inspection of material surfaces is the first indication of good crystal quality. Narrow peak traces in photoluminescence spectra and X-ray diffractograms also indicate good crystal quality. In $Al_xGa_{1-x}As$, for compositions of $x > 0.40$, photoluminescence was inadequate for resolving the material composition and X-ray diffraction is more appropriately used here. This is evident in the results shown in Section 3.1.2. There is excellent agreement between the two independent sets of composition measurements although photoluminescence is based on optical parameters and X-ray diffraction on crystal configuration parameters. In the $Al_xGa_{1-x}As$ composition region between 0.35 and 0.45, the ternary changes from a direct bandgap to indirect bandgap material. Photoluminescence of indirect bandgap material is poor and inadequate for composition assessments. This is the primary reason for using X-ray diffraction results to develop the final calibration expressions for solid $Al_xGa_{1-x}As$ composition versus group III reagent molar ratio. Photoluminescence, however, shows that the material is of high quality in terms of low defects or impurities in the AlGaAs and uniform compositional growth, in the uppermost 1000 nm at least, as revealed by the thin well-defined peaks in the traces. In one study, where Auger electron spectroscopy was used for $Al_xGa_{1-x}As$ compositional assessments, the results differed considerably from X-ray diffraction and photoluminescence measurements. Clearly, reliable calibration of the Auger method is required in order to obtain satisfactory results.

It is difficult to assess the influence of step-size on the performance of the resulting device, but the material profile can be clearly observed by SIMS profiling. To some extent, XRD and photoluminescence may also be employed for characterisation of graded layers. From the results shown in Section 3.4.2, it is evident that if the compositionally graded layer contains steps of $Al_xGa_{1-x}As$ compositional change greater than $x = 0.05$, resolution of the sub-layers of an $Al_xGa_{1-x}As$ graded layer is practical using photoluminescence provided two conditions are met :

i. as a guide, the depth penetration of the photoluminescence technique is approximately 1000 nm,

ii. the sub-layer with the highest aluminium content occurs on the surface of the graded layer so that reabsorption of the emitted light does not occur.

Should the total graded layer thickness exceed 1000 nm and $Al_xGa_{1-x}As$ compositional steps of greater than $x > 0.05$ is present in the grade, then XRD may be employed in preference to photoluminescence for resolution of the graded layer. XRD or SIMS measurements are also more appropriately applied to graded layers where the aluminium content of the sub-layer closest to the surface is lower than other sub-layers. However, at a finer compositional resolution typically for those used in autograding procedures ($Al_xGa_{1-x}As$ composition steps of $x < 0.02$), XRD and photoluminescence are inadequate and SIMS may be employed for the purpose of establishing the quality of the grade. Quantitative measurements on graded layers of this type are not accurate by any of the techniques.

SIMS is also the most appropriate technique for multi-layer structures. However, the true abruptness of a material interface is poorly reflected by the SIMS result because of complicating factors such as matrix mixing and non-consistent sputtering rates based on a changing medium. These and other factors are described in Section 1.4.4. The SIMS results, however, do appear promising when viewed as a qualitative measure of compositional or doping profiles.

4.4 Grading Methodology

All regions of graded composition were grown by a "staircase" variation of aluminium mole fraction rather than a continuous "smooth" variation for practical reasons. In selecting the step-like structure of the grade, the number of small composition steps required to achieve a pseudo-continuous grade may be varied such that the behaviour of the layer is equivalent to having a continuous grade. The $Al_xGa_{1-x}As$ grading process, automatically controlled by software algorithms, typically yielded a fine compositional step resolution (steps of $x < 0.02$) which was equivalent to having a pseudo-continuous grade for the physical material character as measured by SIMS.

The compositional grading strategy employed is to fix the group V constituents whilst varying the total amount and ratio of the group III constituents, i.e., the trimethylgallium and the trimethylaluminium precursors. This has historically been the strategy for all material developments since the commissioning of the reactor. Its singular biggest disadvantage is a varying growth rate with each different composition. Equations from the AlGaAs calibration for composition and growth rate were used in the automated grading process via a software algorithm to implement grading. This process was found to be very satisfactory in obtaining repeatability and consistency in the growth of graded layers. Although, any desired shape of grade could be controllably grown, only linear grades were investigated in this study. Those grading equations, where the composition relates to the growth time and that were derived by solving linear differential equations, and were far more accurate for precise control of the shape of the grade than those obtained by numerical solutions (i.e. example 3 versus example 2 in Appendix I).

Growth algorithms of doping as a function of time and input dopant concentration proved satisfactory in achieving linear silicon dopant grading as shown in Section 3.3 . In the grade from 2×10^{17} cm^{-3} to 2×10^{18} cm^{-3} over a 1000 nm thick layer, C-V analysis shows a near linear variation in doping. Non-linearity in the measured profile is directly attributed to instrument features as discussed in Section 3.3.2. Only the bottom doping of 2×10^{17} cm^{-3} is resolvable at a depth of 1000 nm; the upper limit represents a singular thin sub-layer far smaller than the depth resolution of the instrument.

4.5 Homojunctions and Heterojunctions

For a homogeneous growth structure, such as the case of the 35 GHz Gunn diode (see Section 3.6.1), group III and group V reagents channelled in separate reactor feed streams are satisfactory for achieving design dimensions in the final growth structure. This also minimizes wastage of reagents. Silicon was an ideal candidate for abrupt doping interfaces in GaAs because of its low elemental vapor pressure and low diffusion coefficient in GaAs crystals. Silicon dopant interfaces are shown in Section 3.6.1 representing the development of a 35 GHz Gunn device consisting of three layers of GaAs at different doping levels. Both electrochemical C-V analysis and SIMS profiles show abrupt doping transitions in the material with doping changes from 1 x 10^{16} cm^{-3} to 2 x 10^{18} cm^{-3}. Where the total material thickness measures 4200 nm, a 60 nm resolution was obtained. The resolution obtained is 2.7% of the active layer thickness and certainly satisfactory for acquiring the predicted operating frequency of the 35 GHz Gunn device.

For heterogeneous material structures, each of the two reactor feed lines carries precursors necessary for each material type during OMVPE growth. This allows for simultaneous switching of lines with controllable and minimal pressure perturbations. The 'separate lines' strategy, used for growth of homogeneous material discussed previously, is an inadequate approach because of pressure imbalances created during switching of lines and the requirement for growth pauses which lead to a poor quality of material interfaces. A GaAs-AlGaAs quantum well test structure was used to test the quality of heterointerfaces (see Section 3.2.2). The GRIN-SCH lasers reported in this study contained single wells. It is clear that abruptness of interfaces on either side of the well defines the well thickness and hence the lasing output characteristics of the devices. Ideally, a square-well shape is desired, since the well thickness could be easily determined to predict the lasing characteristics of final devices. In the test structure wells from 2.5 nm to 10 nm were designed to be sandwiched between $Al_{0.4}GaAs$ spacer layers. In the first attempt, aluminium spikes at the onset of each AlGaAs growth were detected by SIMS analysis. It became evident that the system pressure imbalances during the simultaneous switching of reagant flows drastically affected the solid growth profile.

Whilst this and other physical system parameters could be addressed to alleviate the problem, other issues such as high temperature diffusion of species in the solid causing intermixing at interfaces could hardly be controlled. A growth pause at the growth interface was found to cause large aluminium 'spikes'. Fortunately, a sensitive PID pressure control system could be tuned to provide very accurate and rapid pressure control during simultaneous switching of reagant lines and subsequent attempts at growing the test structure eliminated the 'spiking' entirely. Additionally, the 2.5 nm quantum well was observed in the SIMS spectrum, suggesting well sharpnesses better than the resolution capacity of the SIMS instrument. The resolution of the instrument is dependant on features such as ion beam mixing and inaccuracies in profiling and fixed target area. The targeted well size of 2.5 nm was estimated to measure 2.3 nm, within instrument error of the SIMS technique.

4.6 Spike Doping

A test structure to determine the suitability of OMVPE to produce the required doping spike was grown and characterized and is reported in Section 3.2.1. The simultaneous switching of two silane dopant reagant streams, one into the reactor and the other to vent, can accomplish the growth of narrow dopant spikes with little influence on the overall reactor pressure balance. The reason for this is that the dopant flowrate of less than 100 sccm is far less than the total flowrate of 10000 sccm to cause undesirable pressure pertubations. The SIMS and C-V measurements of the GaAs thicknesses in the Si-spike doping structure grown as per Figure 3.2-1 agree well and indicate a GaAs growth rate 5 to 10% less than that predicted from growth rate studies. The doping concentration of the 500 nm GaAs layer as measured by SIMS (1.5×10^{16} cm^{-3}) and C-V (1.8×10^{16} cm^{-3}), are in good agreement. The discrepancy between the SIMS and C-V results for the peak concentrations is therefore due to the higher resolution of the C-V technique. The C-V results for the peak concentration of the 20 nm layer show that the dopant concentration is correct. The peak areas as measured by C-V, which are approximately 75% of the expected values, indicate the extent to which the peak shapes deviate from the square-wave doping shape required. This is reinforced by the fact that the SIMS profiles with different ion beam energies have the same shape. The C-V

measurements enable the adjustment of either the dopant concentration or the thickness to achieve the required amount of dopant in the Si spike. The Si-doping spike cannot easily be resolved by the available techniques but when it is quantitatively assessed by integration of the doping shape, it does correspond to an absolute charge of approximately 75% of that required in the model.

4.7 Device Structures

The GRIN-SCH laser structure development presented sequentially in Section 3.5 comprises of six versions of device material produced. In the first and simplest case (designated GRIN-SCH I), grading was undertaken by manually implementing the input contributions for compositional changes. Both the first and second iterations assumed fixed growth rates for varying AlGaAs compositions, the consequences of which are non-linear grades and inaccurate thicknesses in the final graded layers. GRIN-SCH II, III and IV development were also based on simplified grading equations, the effect of which is only portrayed in the device performance. The later versions of laser material (designated GRIN-SCH V and GRIN-SCH VI) utilizing grading equations derived by solving linear differential equations show sharp linear transitions when view by SIMS profiling. GRIN-SCH IV certainly represented some of the best performing devices measured.

Section 3.5.2 shows the results of material assessment of the GRIN-SCH laser structures grown. The SIMS profile of the complete structure for GRIN-SCH I shows that the basic structure is present. SIMS spectra of GRIN-SCH II, GRIN-SCH III and GRIN-SCH IV material revealed large composition fluctuations at the end of the p-type GRIN region. It is evident that the spikes are as a consequence of poor pressure control from gas switching during growth. Steps in the Al profile are seen in the grades to the substrate (layer d_1 in Figure 1.3-1) although this is not obvious in the GRIN layers. The shape of the graded profile appears linear for the GRIN layers but is bowed for layer d_1. The quantum wells, designed at 5 and 10 nm, are seen in the SIMS profiles. GRIN-SCH V and GRIN-SCH VI were grown with the pressure problem resolved. The 10 nm quantum well is not detectable within the large depth of material profiled. Each GRIN layer

appears linear and together they appear in the desired triangular format with little indication of stepping or aluminium 'spiking'. The XRD trace of both structures clearly distinguishes the GaAs substrate from the AlGaAs cladding layers. The measured composition of x = 0.442 closely resembles the targeted x = 0.45 .

Typical, and not the best, lasing characteristics were ascertained from spectral analysis and optical power detection of crudely processed block lasers. Comparision is made between DH and GRIN-SCH SQW lasers and the different versions of GRIN-SCH lasers produced and shown in Table 3.5-3 in Section 3.5.3 . Lasers were operated in the pulsed mode using a 1000 ns pulse width at 1 kHz pulse repetition frequency. A large improvement in lasing characteristics is observed for GRIN-SCH SQW versus DH lasers, especially in the threshold current density which is reduced from 1528 Acm^{-2} to a low of 296 Acm^{-2}. The threshold current density also improves slightly in the later versions of the GRIN-SCH lasers. GRIN-SCH V characteristics are poor in comparision to earlier versions due to poor ohmicity in contact formation; this was realised when sampled block lasers were reported not to have been annealed after contact metallization. Using the Chinn et al. [1988] model as discussed in Section 2.6, predicted lasing wavelengths for 5 and 10 nm quantum well thicknesses correspond to 869 nm and 840 nm respectively. The results obtained closely resemble these wavelengths, 17 nm difference being the largest variation, suggesting insignificant variation from the targeted well sizes. No comparision can be made from the power output of devices since these results were subject to various non-material influences such as input current, ohmicity of contacts, sample mounting and heat dissapation. However there have been cases of power output as high as 5 W at 17 A with differential quantum efficiencies of 55% before 'burn-out' with lasers operated in the pulsed mode. 80 mW cw operation has also been recorded for ridge waveguide lasers. The differential quantum efficiencies are far superior for GRIN-SCH type lasers but show no improvement in later versions, due again to various non-material influences. GRIN-SCH I showed a high differential quantum efficiency of 54%. The overall performance characteristics of devices does however show slight improvements from the earlier to later versions of lasers produced. This can be largely attributed to more accurate growth for these devices based on using more accurate AlGaAs calibration standards as well as the more precise grading equations derived from

solutions of linear differential equations.

The results of the growth of a standard Gunn diode structure intended for 35 GHz operation is discussed in Section 3.6.1. The three layers are clearly distinguishable and microscopy measurements of the thicknesses indicate that they are the 1000 nm buffer layer, the 2200 nm active layer and the 1000 nm contact layer as designed. C-V electrochemical profiling confirm the microscope measurements. Abrupt doping interfaces on either side of the active layer indicate good electrical interfaces. The active region is well defined at a doping level of $1.5x10^{16}$ cm^{-3} whilst the contact layers are doped higher than $1.0x10^{18}$ cm^{-3}. SIMS measurements show interfaces to be better than 60 nm which is 2.7% of the total active layer thickness of 2200 nm. The sharpness of the interfaces also reflects the absence of the characteristic sloped curve on SIMS profiles for dopant species that have a high diffusion coefficient in the solid such as tellurium; Si is most suited for abrupt interfaces for this reason.

The OMVPE growth of a Gunn diode structure incorporating a hot electron injector was investigated and shown in Section 3.6.2 . The compositional and structural requirements of the Gunn diode material shown in Figure 1.3-2, in particular, the $Al_xGa_{1-x}As$ graded layer from x = 0 to x = 0.4 and a 50 nm Si-doped GaAs layer (Si doping spike) were achievable with III-V OMVPE growth. The measurements done on the test structures show that OMVPE may be sufficiently calibrated to grow the hot electron injector Gunn structures to an accuracy of better than 10%. The dimensions of the critical features of the hot electron injector structure, i.e. the 5 nm spike and 50 nm AlGaAs grade, are at the limit of the resolution of the SIMS, C-V and XRD analysis techniques. The results in section 3.4.2 show that the $Al_xGa_{1-x}As$ grade appears linear over the intended thickness and is certainly predicted at a peak composition within 10% of 0.4 . SIMS and XRD analyses of the AlGaAs grade structure show quantitatively that all the parameters are within 10% of the designed values.

After the neccessary adjustments for growth parameters, Gunn diode structures were grown by OMVPE and successfully processed into diodes. The SIMS results confirm the existance of the 50 nm graded gap layer and 1670 nm active layer. Spike doping results

in a slightly higher sheet doping density from the targeted value of 1 x 10^{12} cm^{-2} to a measured value of 1.7 x 10^{12} cm^{-2}. It should be borne in mind that the resolution of the SIMS instrument does not allow for precise measurements of thickness. The other features of the structure measure up to the designed values as indicated in Figure 1.3-2. The performance of these devices (16 mW at 93 GHz with a phase noise of -85 dBc/Hz using a bias voltage 4 V and a threshold current of 0.88 A) compares favourably to diodes fabricated from MBE material. Preliminary indications are that Gunn diodes intended for 94 GHz operation can be grown at significantly less cost by OMVPE than diodes grown by expensive MBE methods.

5. CONCLUSION

By use of the OMVPE growth technique, single crystal GaAs and AlGaAs multilayers in which the semiconductor properties are tailored for device requirements have been produced. After careful consideration to the III-V reactor system capabilities and material requirements, successful GRIN-SCH lasers and millimeter-wave Gunn diodes have been fabricated.

A consistently high quality of single GaAs and AlGaAs material is achievable with satisfactory semiconductor properties. Controllable silicon, tellurium and zinc doping on both material systems have also been demonstrated. Both photoluminescence and X-ray diffraction measurements are valuable for the assessment of the composition and quality of epitaxial layers. An investigation into sharpness of both homojunctions and heterojunctions in multi-layered material shows that OMVPE maybe sufficiently calibrated to grow sharp transitions in doping interfaces and quantum wells in the order of 2.5 nm. The quantum wells were easily detectable by photoluminescence and SIMS measurements. SIMS also showed almost square doping profiles in the 35 GHz Gunn diode structure and was able to resolve a 5 nm spike doping layer. Both of these achievements are largely attributed to the fine pressure and flow control implemented on the reactor system by using an automated growth method to control the process.

A demonstration growth of doping grading of GaAs using silicon as a n-type dopant showed excellent results in terms of the linearity and quality of the grade. The choice of grading strategy for the compositional grading, where a time-based algorithm is used to effect compositional changes during grading, was also found to be suitable producing grades of high quality. The algorithm utilizing linear differential equations allows for tailoring of grades in any desired shape to suit the material application. Although grading is conducted in a 'step-like' process, resulting in a 'staircase' variation of composition, such steps in the $Al_xGa_{1-x}As$ compositional graded layers are barely detectable by SIMS, XRD and photoluminescence measurements when the attenuation chosen results in AlAs steps of $x = 0.02$.

GRIN-SCH SQW lasers have been tailored to design specifications as confirmed by SIMS analyses and device performance. The lasing wavelengths have been correlated with designed quatum well sizes and device efficiencies show that the quality of AlGaAs grades and heterointerfaces are acceptable for high performance. The latest versions of GRIN-SCH SQW lasers produced have shown excellent lasing characteristics even for crudely processed block lasers. In pulsed mode operation, power outputs have been as high as 5 W with differential quantum efficiencies of 55% whilst ridge waveguides have produced 80 mW continuous power. 94 GHz Gunn diodes have been produced with operation at 16 mW at 93 GHz at a phase noise of -85 dBc/Hz. The SIMS results of the diode material clearly indicates the presence of all layers with certain measured values identical to designed values.

Indications are that the OMVPE growth method maybe sufficiently calibrated to produce satisfactory material structures for high quality Gunn diodes operating at 94 GHz and GRIN-SCH SQW lasers operating satisfactorily at infrared wavelengths.

6. REFERENCES

Adachi S., *J.Appl.Phys.*, **58**, (1985), pp R1-R9.

Balk P. and Veuhoff E., "Deposition of III-V Compounds by MOCVD and in Halogen Transport Systems - A Critical Comparison", *J. Crystal Growth*, **55**, (1981), pp 35-41.

Bartels W.J. and Nijman W., *J. Crystal Growth*, **44**, (1978), pp 518.

Bass S.J. and Oliver P.E., "Controlled doping of GaAs Produced by Vapor Epitaxy, Using Trimethylgallium and Arsine", *Inst.Phys.Conf.Ser.*, No. 33b, Chap.1, (1977), pp 1-10.

Bastard G. and Brum J.A., "Electronic States in Semiconductor Heterostructures", *IEEE J. of Quantum Electronics*, **QE-22** (9), (1986), pp 1625-1644.

Befhar-Rad A., Shealy J.R., Chinn S.R. and Wong S.S., "Effect of cladding layer thickness on the performance of GaAs/AlGaAs GRIN-SCH-SQW lasers", *IEEE Journal of quantum electronics*, **26** (9), (1990), pp 1476-1480.

Berolo O. and Woolley J.C., *Can.J.Phys.*, **49**, (1971), pp 1335.

Blakemore J.S., "Semiconducting and other major properties of gallium arsenide", *J.Appl.Phys.*, **53**, (1982), pp R123-R181.

Blom P.W.M., Haverkort J.E.M. and Wolter J.H., "Optimization of barrier thickness for efficient carrier capture in graded-index and separate-confinement multiple quantum well lasers", *Appl.Phys.Lett.*, **58** (24), (1991), pp 2767-2769.

Boudewijn P.R., Leys M.R. and Roozeboom F., "SIMS Analysis of $Al_xGa_{1-x}As$/GaAs Layered Structures Grown by Metal-Organic Vapour Phase Epitaxy", *Surface and Interface Analysis*, **9**, (1986), pp 303-308,

Casey Jr H.C. and M.B. Panish, "Heterostructure Lasers - Part A", *Academic Press*, New York, 1978.

Casey Jr H.C. and Panish M.B., *J.Appl.Phys.*, 40, (1969), pp 4910.

Chen H.Z., Ghaffari A., Morkoc H. and Yariv A., "Very Low Threshold Current Densities (under 100 A/cm^2) in AlGaAs/GaAs Single-Quantum-Well GRINSCH Lasers grown by OMVPE", *Electronic Letters*, **23** (25), (1987), pp 1334-1335.

Chinn S.R., "Model Analysis of GRIN-SCH and triangular-well waveguides", *Applied Optics*, **23** (20), (1984), pp 3508-3509.

Chinn S.R., Zory P.S. and Reisenger A.R., "A Model for GRIN-SCH-SQW Diode Lasers", *IEEE Journal of Quantum Electronics*, **24** (11), (1988), pp 2191-2212,

Dapkus P.D., Manasevit H.M., Hess K.L., Low T.S. and Stillman G.E., "High Purity GaAs Prepared from Trimethylgallium and Arsine", *J. Crystal Growth*, **55**, (1981), pp 10-23.

Dingle R., Logan R.A. and Arthur Jr J.R., *Inst.Phys.Conf.Ser.*, **33a**, (1977), pp 210.

Duchemin J.P., Bonnet M., Koelsch F. and Huyghe D., "A New Method for the Growth of GaAs Epilayer at Low H_2 Pressure", *J. Crystal Growth*, **45**, (1978), pp 181-186.

Escobosa A., Krautle H. and Beneking H., "Rectifying GaAs-GaAlAs-GaAs structures by MOCVD compositional grading", *Electronic Letters*, **18** (20), (1982), pp 888-889.

Field R.J. and Ghandhi S.K., "Doping of Gallium Arsenide in a low pressure Organometallic CVD system. *J.Crystal Growth*, **74**, (1986), pp 543-550.

Fletcher J.C.Q. and Dickens P., "OMVPE Reactor : Modeling horizontal OMVPE reactor flow dynamics and thermal environment for improved wafer uniformity and abruptness", *SA Journal of Science*, Vol.87, (1991), pp 106-112.

Fletcher J.C.Q. and Dickens P., "OMVPE Reactor : Modeling flow dynamics, thermal environment and resulting wafer uniformity", *CSIR Internal Report IMICO 51*, No. 540/19617, (1990).

Givens M.E., Miller L.M. and Coleman J.J., "Effect of Design variations on the threshold current density of AlGaAs SCH-SQW lasers", *J.Appl.Phys.*, 71 (9), (1992), pp 4583-4588.

Hadley G.R., Hohomer J.P. and Owyoung A., "Comprehensive Modeling of Diode Arrays and Broad-Area Devices with Applications to Lateral Index Tailoring", *IEEE Journal of Quantum Electronics*, **24** (11), (1988), pp 2138-2152.

Heckingbottom R. and Prior K.A., "Kinetic and Thermodynamic Aspects of Metal Organic MBE", *3rd European Molecular Beam Epitaxy Workshop*, Aussois, France, (March 18-20, 1985).

Heinecke H., Weyers M., Putz N., Heyen M., Luth H. and Balk P., "Growth and P-Type Doping of GaAs in The Metalorganic MBE System", *3rd European Co Molecular Beam Epitaxy Worshop*, Aussois, France (March 18-20, 1985).

Hersee S.D., Baldy M., de Cremoux B. and Duchemin L.P., "Very Low Threshold GRIN-SCH GaAs/AlGaAs Laser Structures Grown by OMVPE", *Inst. Phys. Conf. Ser.*, No. 65, Chap. 4, (1982), pp 281.

Hersee S.D., Baldy M. and Assenat P., "The growth of quantum well GaAs/GaAlAs laser structures", *Journal de Physique*, Colloque C5, supplement au no 12, Tome 43, (1982), pp C5-193 to C5-199.

Hersee S.D., Baldy M. and Duchemin J.P., "The Variation of the P/N Junction Position in GaAs/AlGaAs Double Heterostructures Grown by Low Pressure MOVPE", *J.Electron.Mat.*, **12**, (1983), pp 345-357.

Hirayama H., Miyaki Y. and Asada M., "Analysis of Current Injection Efficiency of Separate-Confinement-Heterostructure Quantum-Film Lasers", *IEEE Journal of Quantum Electronics*, **28** (1), (1992), pp 68-74.

Holonyak N. Kolbas R.M., Dupuis R.D. and Dapkus P.D., "Quantum-Well Heterostructure Lasers", *IEEE Journal of Quantum Electronics*, **QE-16** (2), (1980), pp 170-186.

Honstra J. and Bartels W.J., *J. Crystal Growth*, 44, (1978), pp 521.

Johnson E.S. and Legg G.E., *J.Cryst.Growth*, **88**, (1988), pp 53-66.

Kaneko K., Ayabe M. and Watanabe N., *Inst. Phys.Conf.Ser.*, No.**33a**, Chap.4, (1977), pp 216-226.

Kasemset D., Hong C-S.,Patel N.B. and Dapkus P.D., "Graded barrier single quantum well lasers - Theory and experiment", *IEEE Journal of Quantum Electronics*, **QE-19**, (1983), pp 1025-1030.

Kuech T.F., Wolford D.J., Potemski R., Bradley J.A. and Kelleher K.H., "Dependance of the $Al_xGa_{1-x}As$ band edge on alloy composition based on the absolute measurement of x", *Appl.Phys.Lett.*, **51** (7), (1987), pp 505-507.

Kuech T.F., Wolford D.J., Veuhoff E., Deline V., Mooney R., Potemski R., Bradley J.A., "Properties of high-purity $Al_xGa_{1-x}As$ grown by the metal-organic-vapor-phase-epitaxy technique using methyl precursors", *J.Appl.Phys.*, **62** (2), (1987), pp 632-643.

Lang R.J., Larsson A.G. and Cody J.G., "Lateral Modes of Broad Area Semiconductor Lasers: Theory and Experiment", *IEEE Journal of Quantum Electronics*, **27** (3), (1991), pp 312-320.

Leys M.R and Veenvliet H., *J Crystal Growth*, 55, (1981), pp 145.

Liu Chee-Wee, Chen Sheng-Li, Lay Jyh-pyng, Lee Si-Chen and Lin Hao-Hsiung, "Characteristics of Si-doped GaAs epilayers grown by metalorganic chemical vapor deposition using a silane source", *Appl.Phys.Lett.*, **51** (20), (1987), pp 1634-1636.

Makarov Y.N. and Zhmakin A.I.,"Numerical Simulation MOVPE $Al_xGa_{1-x}As$: Control of Composition Variation", *Cryst.Res.Technol.*, **25** (1), (1990), pp 30-40

Makarov Y.N. and Zhmakin A.I.,"Control of Composition Variation in AlGaAs Growth", *J. of Crystal Growth*, 100, (1990), pp 646-650.

Manasevit H.M. , *Appl.Phys.Lett.*, **12**, (1968), pp 156.

Manasevit H.M., "Recollections and Reflections of MOCVD", *J.Crystal Growth*, 55, (1981), pp 1-9.

Manasevit H.M. and Simpsom W.I., "The use of Metal-Organics in the Preparation of Semiconductor Materials, I.Epitaxial Gallium-V Compounds", *J.Electrochem. Soc.: Solid State Science*, 116, (1969), pp 1725-1732.

Manasevit H.M., "The use of Metal-Organics in the Preparation of Semiconductor Materials, III. Studies of Epitaxial III-V Aluminum Compound Formation using Trimethylaluminum", *J. Electrochem. Soc.*, 118, (1971), PP 647-650.

Mashito M, "Mass Spectrometric Studies on Silicon Doping of OMVPE GaAs", *Jap.J.Appl.Phys.*, **28** (8), (1989), pp 1298-1306.

Masu K., Konagai M. and Takahashi K., "Acceptor Energy Level for Zn in AlGaAs", *J.Appl.Phys.*, 51, (1980), pp 1060-1064.

McIlroy P.W.A., Kurobe A. and Uematsu Y., "Analysis and Application of Theoretical Gain Curves to the Design of Multi-Quantum-Well Lasers", *IEEE Journal of Quantum Electronics*, **QE-21** (12), (1985), pp 1958-1963.

Menna R.J., Narayan S.Y., Smith R.T., Abrahams M.S. and Magee C.W., *RCA Review*, **47**, (1986), pp 578-617.

Monemar B., Shih K.K. and Pettit G.D., *J.appl.Phys.*, **47**, (1976), pp 371.

Nakanisi T., Udagawa T., Tanaka A. and Kamei K., "Growth of High-Purity GaAs Epilayers by MOCVD and Their Applications to Microwave MESFET's", *J. Crystal Growth*, **55**, (1981), pp 255-262.

Neylon S., Spooner H., Worley D., Couch N. and Ondria J., "High efficiency millimetre wave GaAs Gunn diodes using Graded Gap Hot Electron Injectors", *Mikrowellen und Optoelektronik MIOP '89*, Sindelfingen (Stuttgard), Federal Republic of Germany, Poster, February 1989, P-1.

Olsen G.H. and Ettenberg M., "Universal stain/etchant for interfaces in III-V compounds", *J.Applied Phys.*, **45** (11), (1974), pp 5112-5114.

Onton A., Lorenz M.R. and Woodall J.M., *Bull.Amer.Phys.Soc.*, **16**, (1971), pp 371.

Paolella A., Ross R.L. and Ondria J., "Advanced mm-Wave Sources by Automated MBE", *Microwave Journal*, USA, (1986), pp 148-160.

Pastrnak J., Oswald J., Laznicka M., Bosacchi A. and Salokatve A., "The Photoluminescence Spectra of Thin Si-Doped GaAs Layers Grown by MBE", *Phys.Stat.Sol.(a)*, **118**, (1990), pp 567-576.

Prakash H., *Prog.Crystal Growth and Charact.*, **12**, (1986), pp 243-256.

Rai-Choudhury P., "Epitaxial Gallium Arsenide from Trimethyl Gallium and Arsine", *J. Electrochem. Soc.*, **116**, (1969), pp 1745-1746.

Ruyven L.J. van, "Double Heterojunction Lasers and Quantum Well Lasers", *Journal of Luminescence*, **29**, North Holland, Amsterdam, (1984), pp 123-161.

Saxena R.R., Cooper III C.B., Ludowise M.J., Hikido S., Sardi V.M. and Borden P.G., "Studies of GaAs and AlGaAs Layers Grown by OM-VPE", *J. Crystal Growth*, **55**, (1981), pp 58-63.

Schaus C.F., Shealy J.R. and Eastman L.F., "Optimised growth of GRIN-SCH quantum well lasers by low pressure organometallic vapour phase epitaxy", *Journal of Crystal Growth*, 73, (1985), pp 37-42.

Schaus C.F., "Optoelectronic Devices and Materials Grown by Organometallic Vapor Phase Epitaxy", Ph.D. thesis, University of Cornell, 1986.

Seki Y., Tanno K., Iada K. and Ichiki E., *J. Electrochem. Soc.*, 122, (1975), pp 1108.

Shealy J.R., "Optimizing the performance of AlGaAs GRIN-QW lasers", *Appl.Phys.Lett.*, 50 (23), (1987), pp 1634-1636.

Shealy J.R., "The Growth and Characterization of GaAS, AlGaAs and Their Heterostructures by Organometallic Vapor Phase Epitaxy", Ph.D. Thesis, Cornell University (1983).

Shimazu M., Kamon K., Kimura K., Mashita M., Mihara M. and Ishii M., "Silicon Doping using Disilane in low-pressure OMVPE of GaAs", *J.Crystal Growth*, 83, (1987), pp 327-333.

Spooner H. and Couch N.R., "Advances in hot electron injector Gunn diodes", *GEC Journal of Research*, 7 (1), (1987), pp 34-45.

Stringfellow G.B., "Organometallic Vapour Phase Epitaxy. Theory and Practice", *Academic Press*, CA, USA, (1989), ISBN 0-12-673840-8.

Stringfellow G.B., "OMVPE Growth of $Al_xGa_{1-x}As$", *J. Crystal Growth*, 53, (1981), pp 42-52.

Stringfellow G.B. and Linnebach R., "Photoluminescence of shallow acceptors in epitaxial $Al_xGa_{1-x}As$", *J.Appl.Phys.*, 51 (4), (1980), pp 2212-2217.

Swart P.L., Lacquet B.M. and Thavar R., "Physical characterisation of OMVPE-grown $Al_xGa_{1-x}As$ multi-layer films by means of non-destructive optical reflectometry", *Appl. Surface Science*, 50, (1991), pp 330-336.

Sze S.M., "Physics of Semiconductor Devices", *Wiley*, New York, 1969.

Terao H. and Sunakawa H., "The Effects of Oxygen and Water Vapour Introduction during MOCVD Growth of AlGaAs", *J.Crystal Growth*, 68, (1984), pp 157-162.

Thavar R., Marais M.A., Mundell F.N. and Olivier L.T., "Development of a Millimeter Wave Gunn Diode: OMVPE Growth and Characterisation", Proceedings of Stedcon '92, *S.A. J. of Physics*, (to be published).

Thavar R., Callanan J. and Lombard O.J., "Effects of GaAs substrate preparation and damage on resulting morphology of epilayers grown by OMVPE", *S.A. J.of Science*, **84**, (1988), pp 694-695.

Tischler M.A., *IBM Journal of Res. Development*, **34**, (1990), pp 828.

Tsang W.T., "Extremely Low Threshold (AlGa)As Graded Index Waveguide Separate Confinement Heterostructure Lasers Grown by Molecular Beam Epitaxy", *Appl. Phys. Lett.*, **40**, (1982), pp 217-219.

Van der Pauw L.J., *Phillips Res.Rep.*, 13, (1958), pp 1.

Wang C.A., Choi H.K. and Connors M.K., "Highly Uniform GaAs/AlGaAs GRIN-SCH SQW Diode Lasers Grown by Organometallic Vapor Phase Epitaxy", *IEEE Photonics Technology Letters*, 1 (11), (1989), pp 351-353.

Watanabe M.O., Morizuka K., Mashita M., Ashizawa Y. and Zohta Y., "Donor Levels in Si-doped AlGaAs grown by MBE", *Jap.J.Appl.Phys.*, **23**, (1984), pp L103-L105.

Yang J.J., Simpson W.I. and Moudy L.A., "Electrical Properties of Se and Zn in MO-CVD AlGaAs", *Int.Symp.on GaAs and Related Compounds*, (1982), pp 107-112.

Zhu L.D., Zheng B.Z., Xu Z.Y., Xu J.Z. and Feak G.A.B., "Optical Gain in GaAs/AlGaAs Graded-Index Separate-Confinement Single-Quantum-Well Heterostructures", *IEEE Journal of Quantum Electronics*, **25** (6), (1989), pp 1171-1181.

Appendix I

Examples of Calculation Procedures to obtain Compositional Grading Equations

Example 1

The following is based on deriving a time-based grading equation for the compositional grading of $Al_xGa_{1-x}As$ from x = 0 to x = 0.5 over a thickness of 1000 nm. A fixed growth rate of 0.889 nm is assumed for all compositions and is based on the growth rate of the median composition at x = 0.25.

The function has the general form :

$$x = at + b \qquad \text{(I-1)}$$

where,

x : compostion of AlAs in AlGaAs

t : time in seconds

a,b : constants.

At $x_1 = 0$, $t_2 = 0$ and based on a growth rate of 0.889 nms^{-1} we can derive the total time of growth t_2 at $x_2 = 0.5$; $t_2 = 1125$ s.

Substituting these known conditions into the equation (I-1) and solving for the constants, the following equation is derived :

$$x = 0.00044t + 0 \qquad \text{(I-2)}$$

Example 2.

The following is based on deriving a time-based grading equation for the compositional grading of $Al_xGa_{1-x}As$ from x = 0 to x = 0.5 over a thickness of d = 1000 nm.
The desired shape of grading should be linear as follows :

$$d = ax + b \tag{I-3}$$

If d = 0 nm at x = 0 and d = 1000 nm at x = 0.5, equation (I-3) becomes

$$d = 2000x + 0 \tag{I-4}$$

Also, from the second calibration of AlGaAs (Section 3.1.2.1),

$$t_g = 0.8798 + 0.6880x \tag{I-5}$$

or,

$$x = 1.4535t_g - 1.2788 \tag{I-6}$$

Since,

$$t_g = \frac{\Delta d}{\Delta t}\Big|_x \tag{I-7}$$

equation (I-6) becomes

$$x = 1.4535\frac{\Delta d}{\Delta t}\Big|_x - 1.2788 \tag{I-8}$$

Assuming a fixed composition x in the solution for the equation, substitute equation (I-4) for d (always starts at d = 0 nm) in equation (8), the following solution is obtained :

$$x = \frac{1.2788t}{2906.0 - t} \tag{I-9}$$

This solution is not correct since a constantly changing x is incurred in the growth process. Example 3 shows the derivations using solutions for linear differential equations.

Example 3.

In the previous example, the substitution for d in equation (I-6) is not correct since x is constantly changing in the growth of a graded layer. The equation can then be solved using solutions for linear differential equations or Laplace transforms.

The following is based on deriving a time-based grading equation for the compositional grading of $Al_xGa_{1-x}As$ from x = 0 to x = 0.45 over a thickness of d = 1000 nm. Growth rate equations are used from the fourth calibration of AlGaAs (Section 3.1.2.1).

The growth rate equation from the fourth calibration of AlGaAs is :

$$t_g = 0.6204x + 0.7643 \tag{I-10}$$

The desired shape of the grade, using x = 0 at d = 0 and x = 0.45 at d = 1000 nm, should be linear as follows :

$$d = 2222.22x \tag{I-11}$$

Now,

$$t_g = \frac{dd}{dt} \tag{I-12}$$

Equation (I-10) and (I-11) in the general forms are :

$$t_g = ax + b \tag{I-13}$$

and,

$$d = cx \tag{I-14}$$

where,

a,b,c : constants.

Substituting (I-13) and (I-14) in (I-12), the following is obtained :

$$ax + b = c\frac{dx}{dt} \tag{I-15}$$

re-arranging (I-15),

$$\frac{dx}{dt} - \frac{a}{c}x = \frac{b}{c} \tag{I-16}$$

using D-operator notation,

$$x(D - \frac{a}{c}) = \frac{b}{c} \tag{I-17}$$

Where A,B are arbitrary constants,

$$C.F. : \quad L.H.S. = 0 ; \quad \therefore \quad x(t) = A\, e^{\frac{a}{c}t} \tag{I-18}$$

$$P.I. : \quad x(t) = B ; \quad \therefore \quad (D-\frac{a}{c})B = \frac{b}{c} \tag{I-19}$$

Therefore,

$$B = -\frac{b}{a} \tag{I-20}$$

and,

$$x(t) = \frac{b}{a}\, e^{\frac{a}{c}t} - \frac{b}{a} \tag{I-21}$$

using t = 0 at x = 0,

$$A = \frac{b}{a} \tag{I-22}$$

Finally, the general solution is as follows :

$$x(t) = \frac{b}{a} e^{\frac{a}{c}t} - \frac{b}{a} \tag{1-23}$$

By substituting actual figures for a = 0.6204, b = 0.7643 and c = 2222.2,

$$x(t) = 1.2319\ e^{0.000279t} - 1.2319 \tag{1-24}$$

Appendix II

X-ray Diffraction and Photoluminescence Curves

of Single AlGaAs Epilayers

(Note : Sample numbers are indicated on diffractograms and spectra)

OMA007 (% AlAs = 11.0)

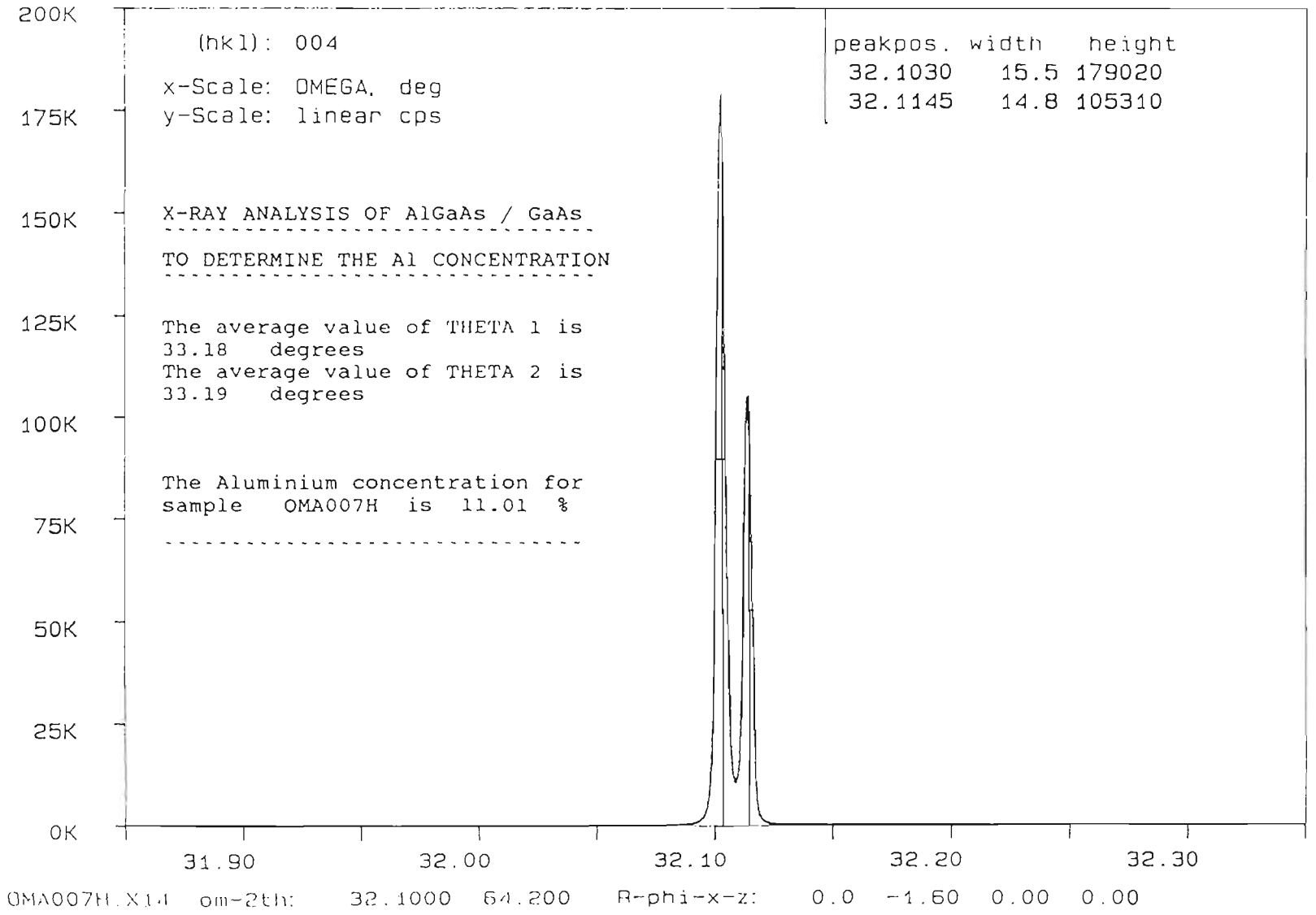

SPECTRUM 1

OMA007 (%AlAs = 11.0)

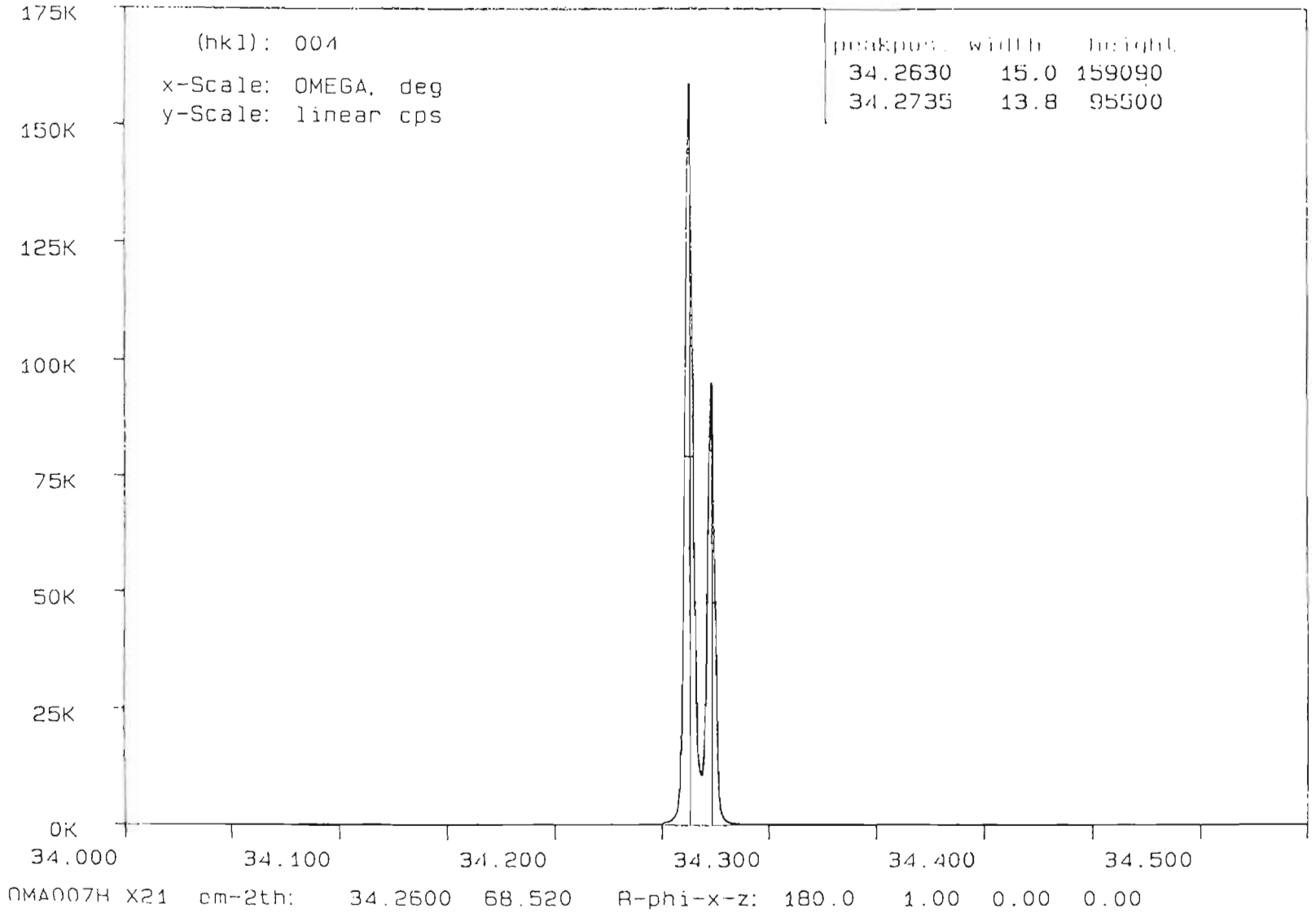

SPECTRUM 2

OMA011 (%AlAs = 6.5)

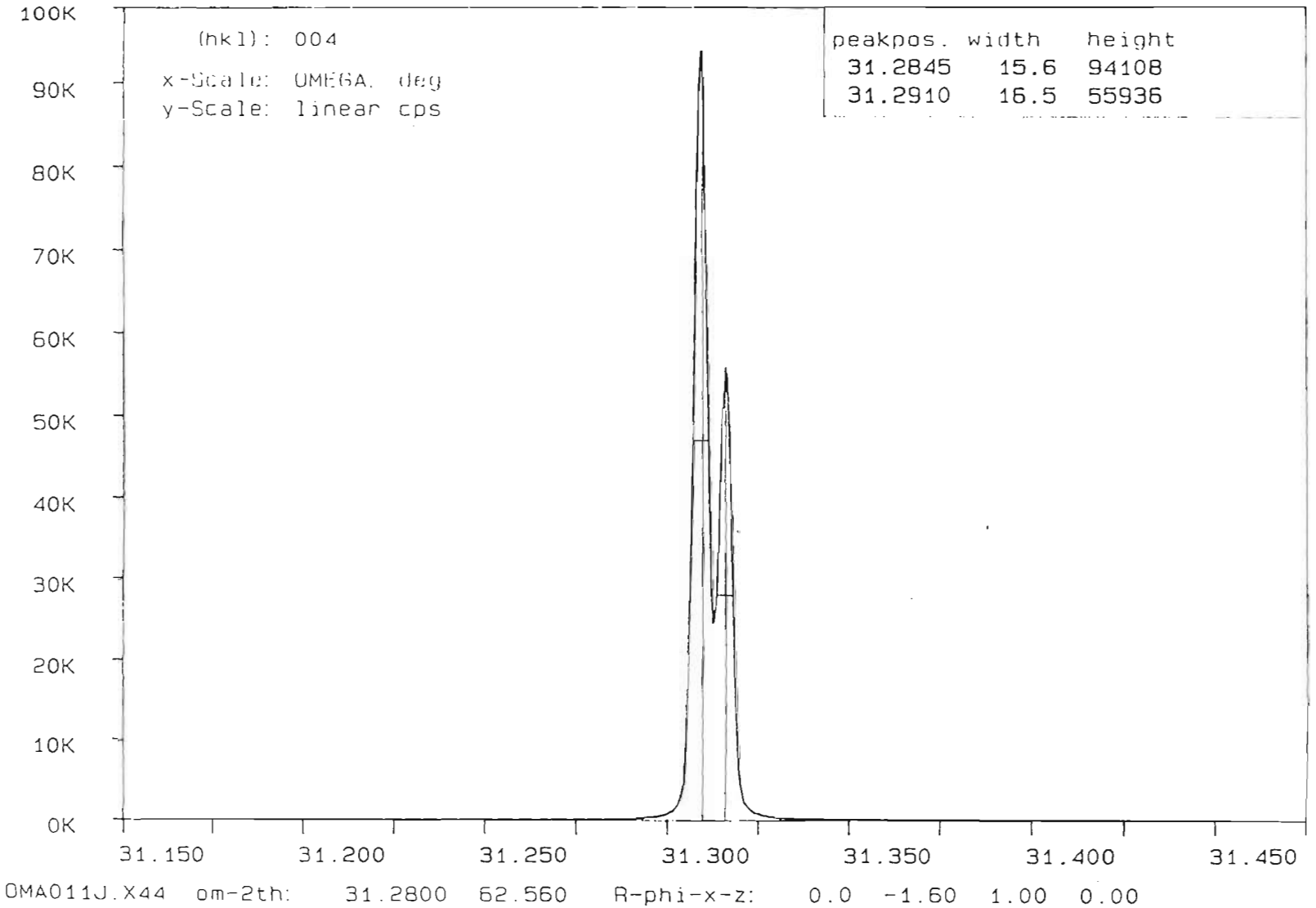

SPECTRUM 1

OMA011 (%AlAs = 6.5)

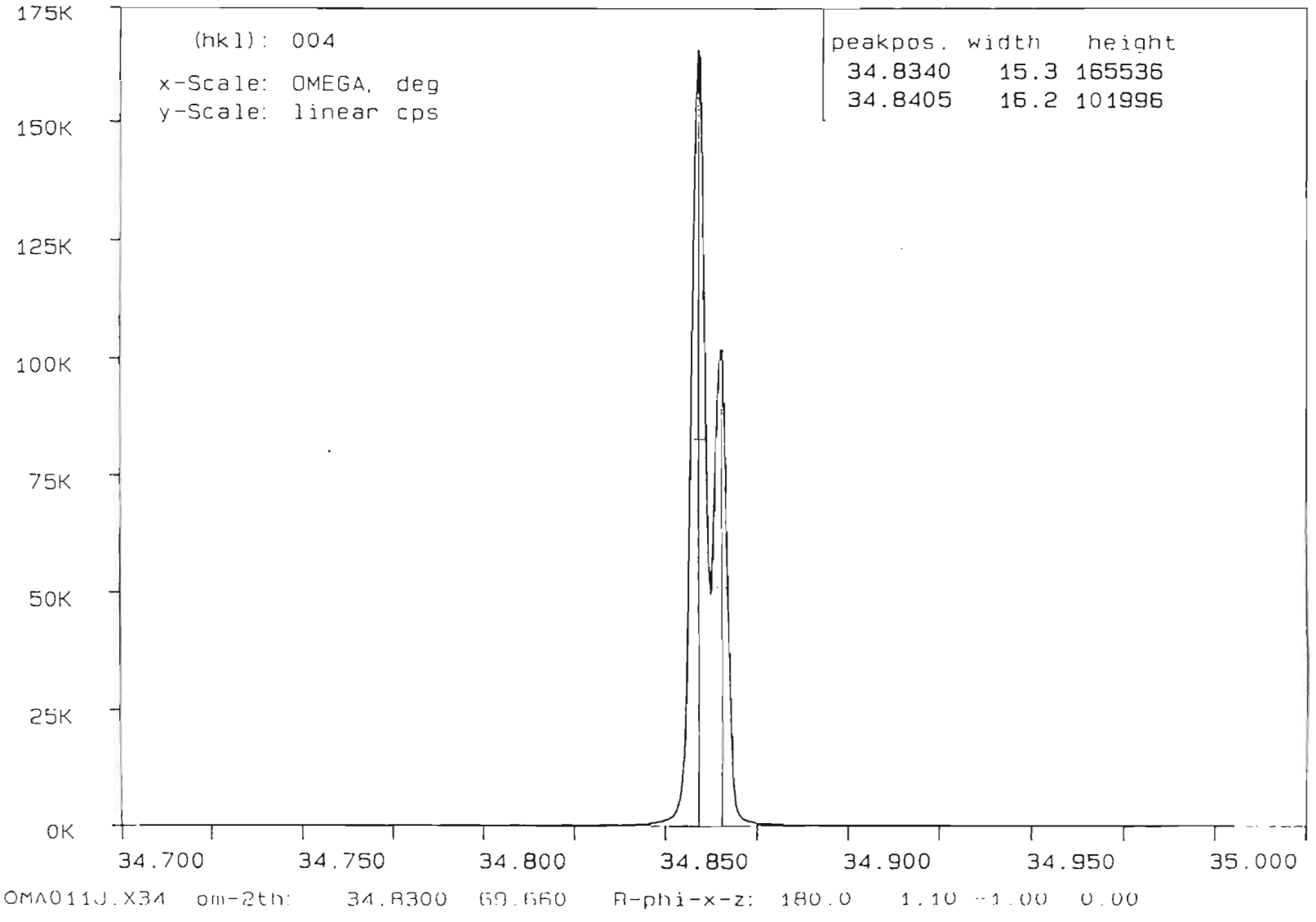

SPECTRUM 2

AGA47 (%AlAs = 20.8)

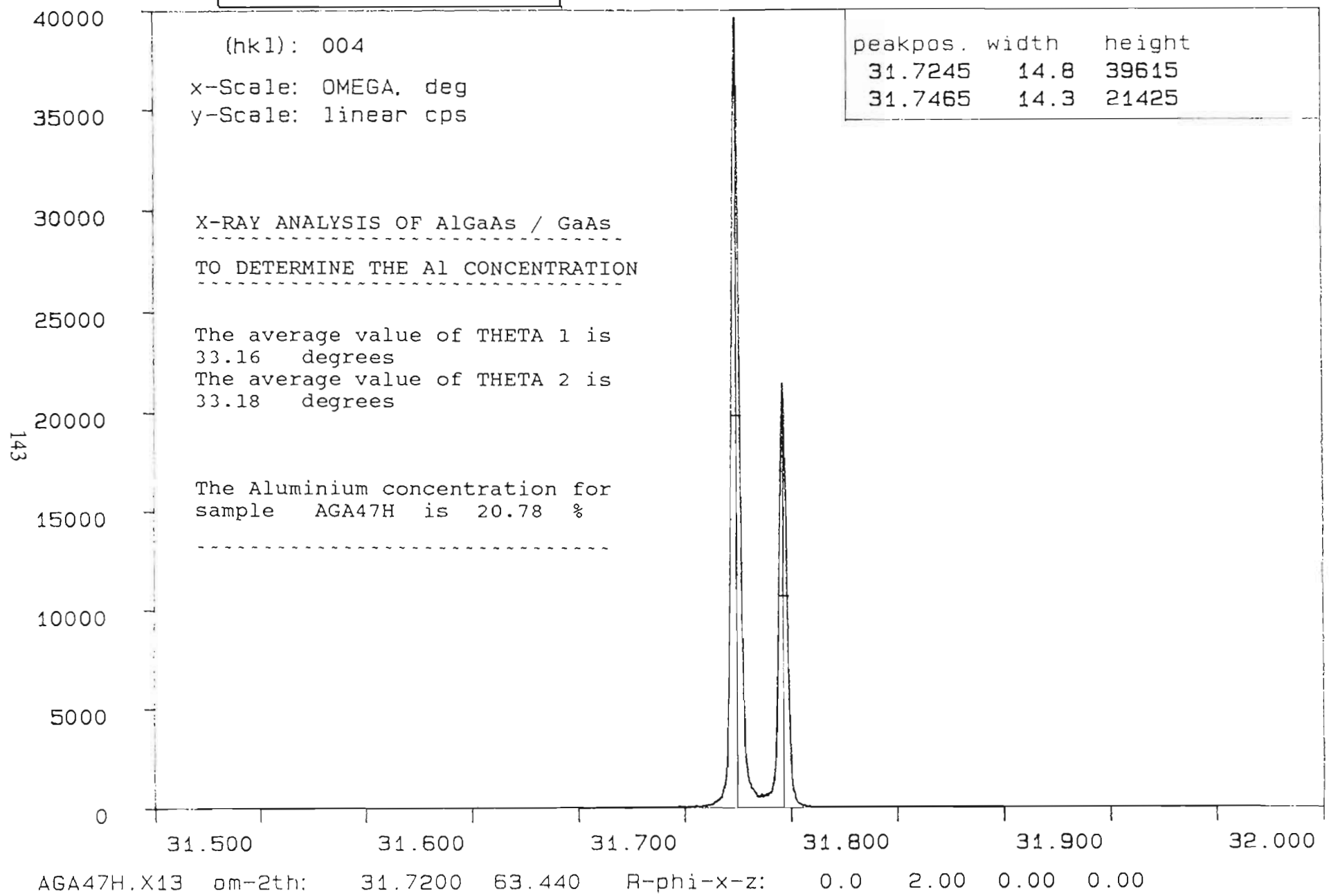

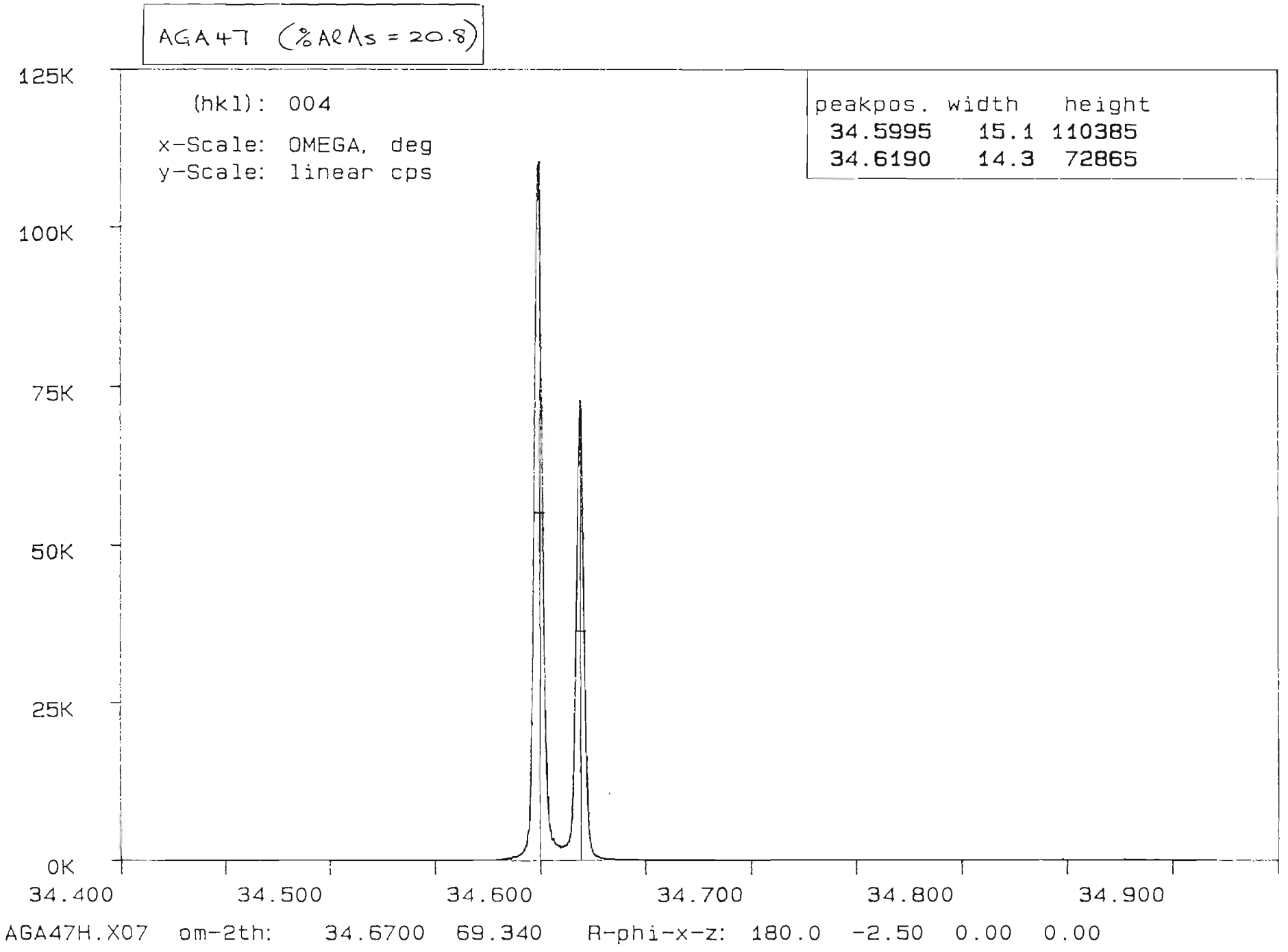
AGA47 (%AlAs = 20.8)
(hkl): 004
x-Scale: OMEGA, deg
y-Scale: linear cps
peakpos. width height
34.5995 15.1 110385
34.6190 14.3 72865
125K
100K
75K
50K
25K
0K
34.400
34.500
34.600
34.700
34.800
34.900
AGA47H.X07 om-2th: 34.6700 69.340 R-phi-x-z: 180.0 -2.50 0.00 0.00

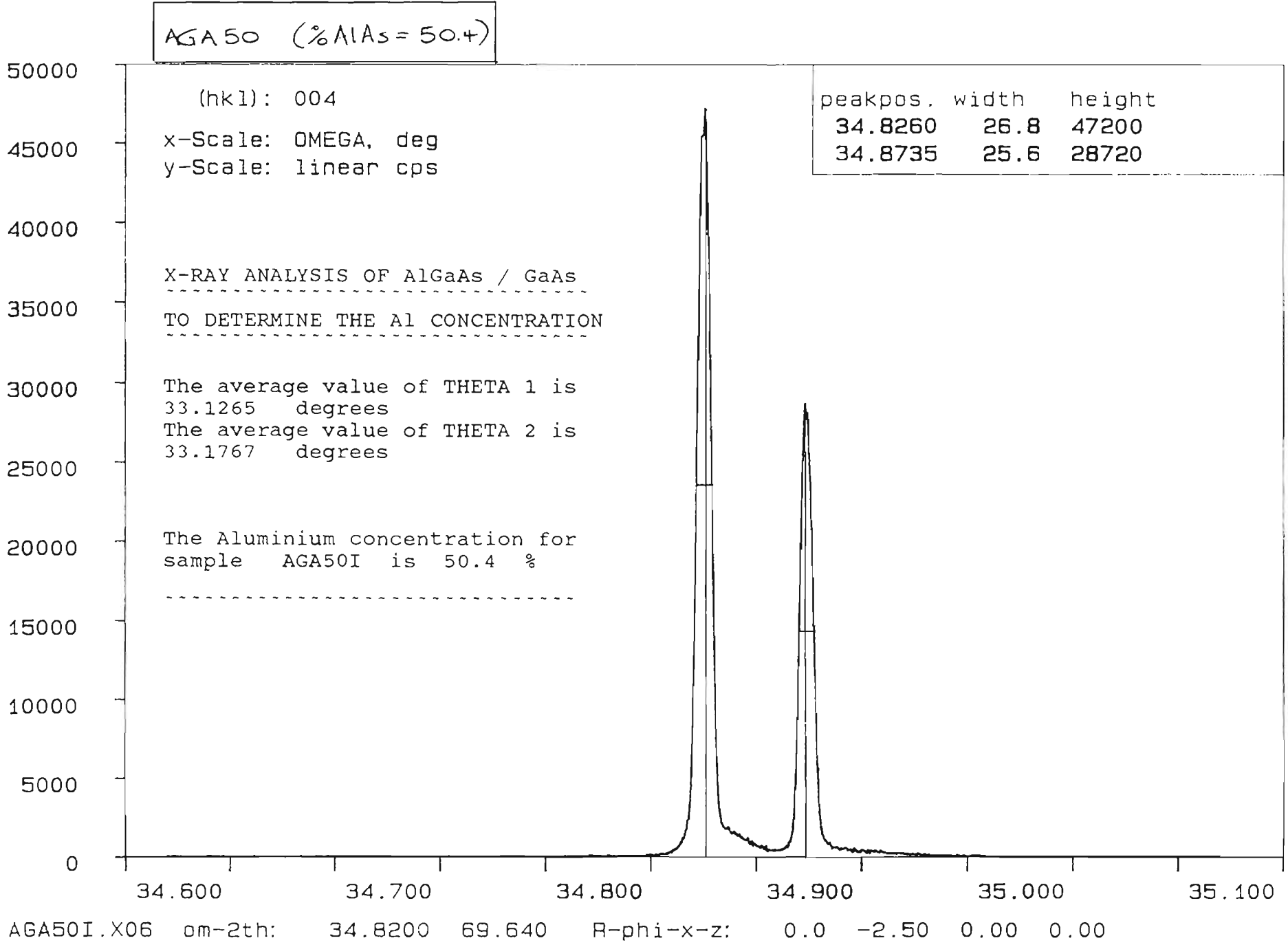
AGA50 (%AlAs = 50.4)
(hkl): 004
x-Scale: OMEGA, deg
y-Scale: linear cps
peakpos. width height
34.8260 26.8 47200
34.8735 25.6 28720
X-RAY ANALYSIS OF AlGaAs / GaAs
TO DETERMINE THE Al CONCENTRATION
The average value of THETA 1 is
33.1265 degrees
The average value of THETA 2 is
33.1767 degrees
The Aluminium concentration for
sample AGA50I is 50.4 %
50000
45000
40000
35000
30000
25000
20000
15000
10000
5000
0
34.600
34.700
34.800
34.900
35.000
35.100
AGA50I.X06 om-2th: 34.8200 69.640 R-phi-x-z: 0.0 -2.50 0.00 0.00

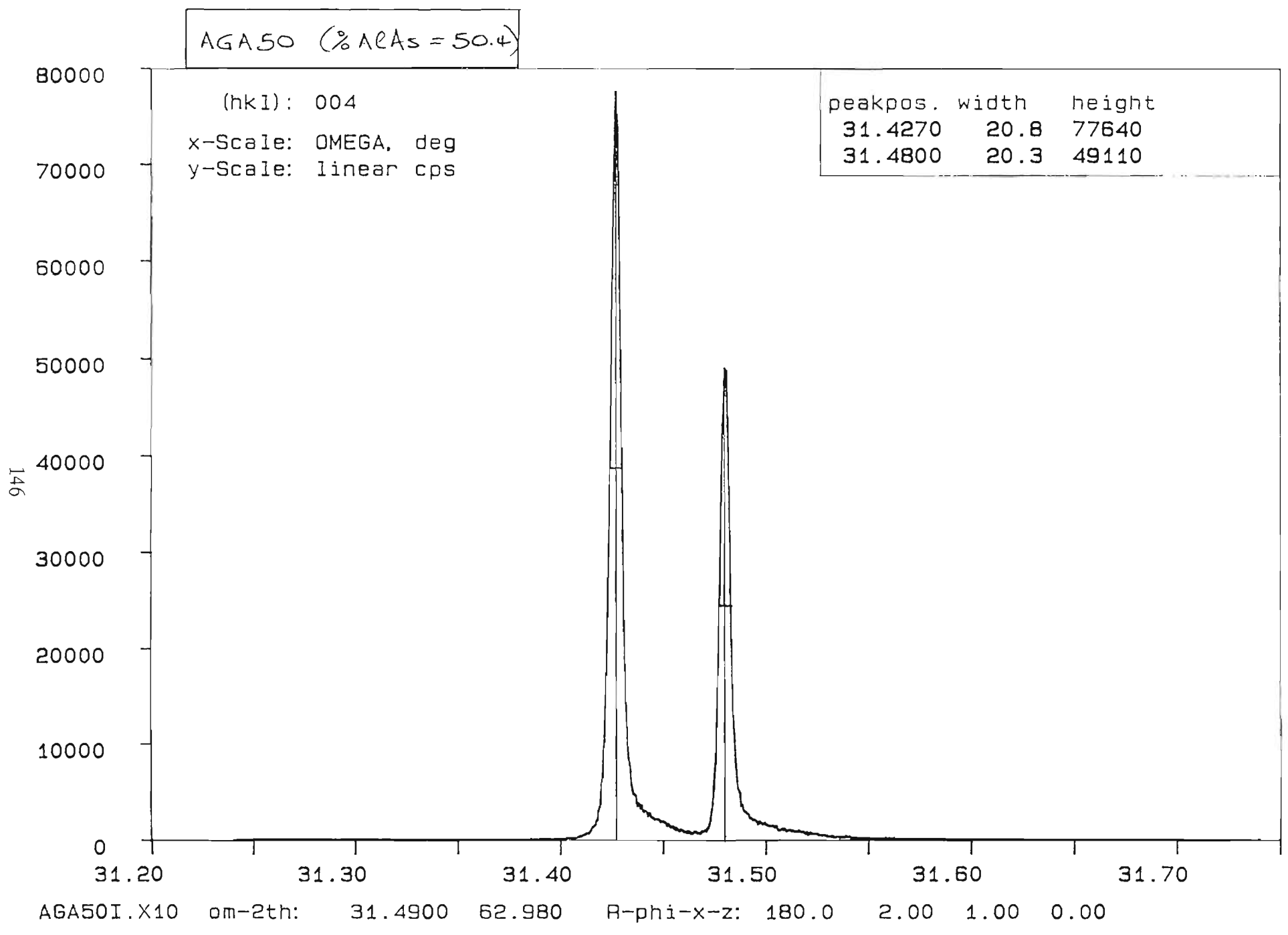
AGA50 (% AlAs = 50.4)
(hkl): 004
x-Scale: OMEGA, deg
y-Scale: linear cps
peakpos. width height
31.4270 20.8 77640
31.4800 20.3 49110
80000
70000
60000
50000
40000
30000
20000
10000
0
31.20
31.30
31.40
31.50
31.60
31.70
AGA50I.X10 om-2th: 31.4900 62.980 R-phi-x-z: 180.0 2.00 1.00 0.00

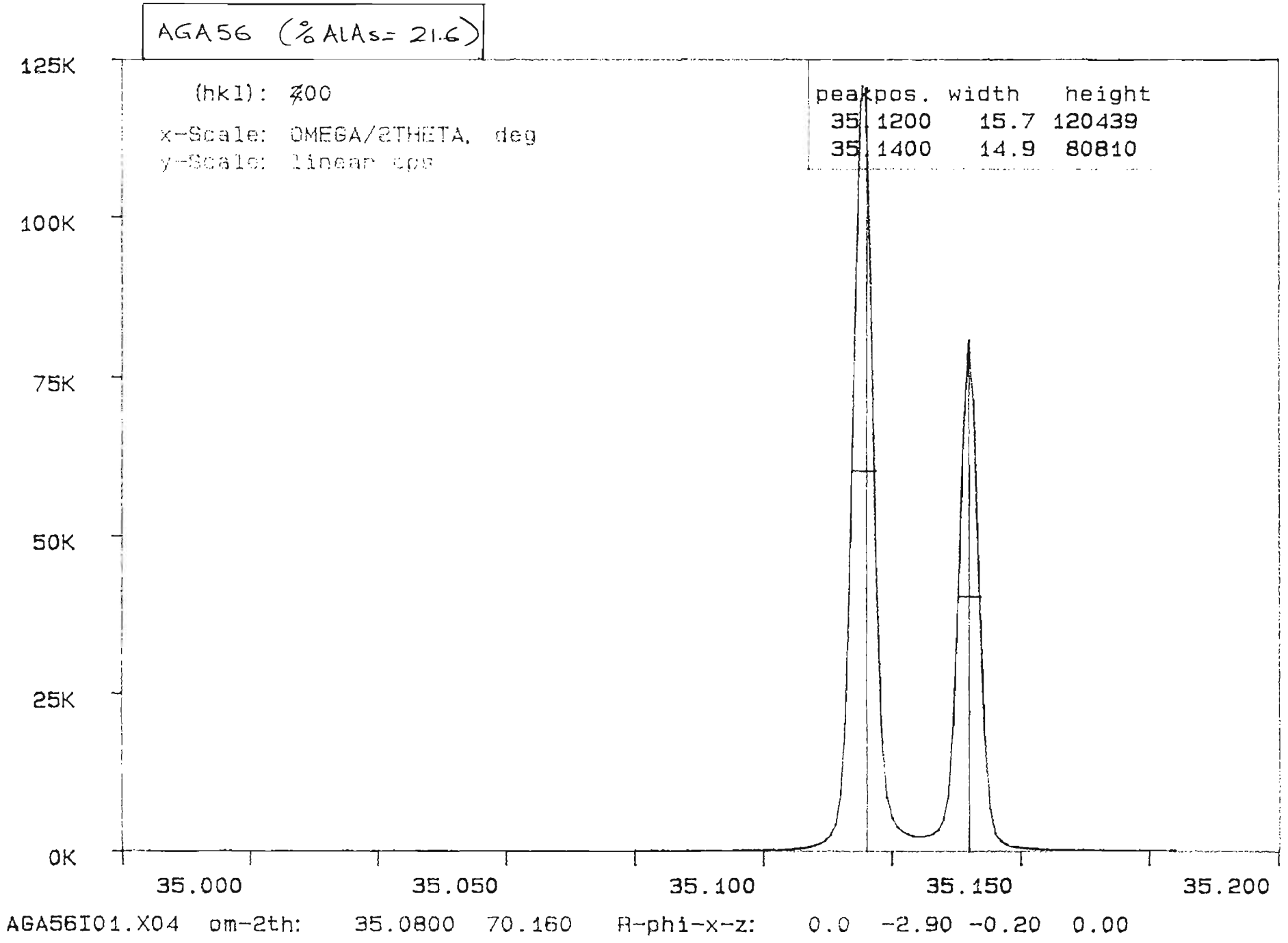
AGA56 (% AlAs= 21.6)
(hkl): ⁄00
x-Scale: OMEGA/2THETA, deg
y-Scale: linear cps
peak pos. width height
35.1200 15.7 120439
35.1400 14.9 80810
125K
100K
75K
50K
25K
0K
35.000
35.050
35.100
35.150
35.200
AGA56I01.X04 om-2th: 35.0800 70.160 R-phi-x-z: 0.0 -2.90 -0.20 0.00

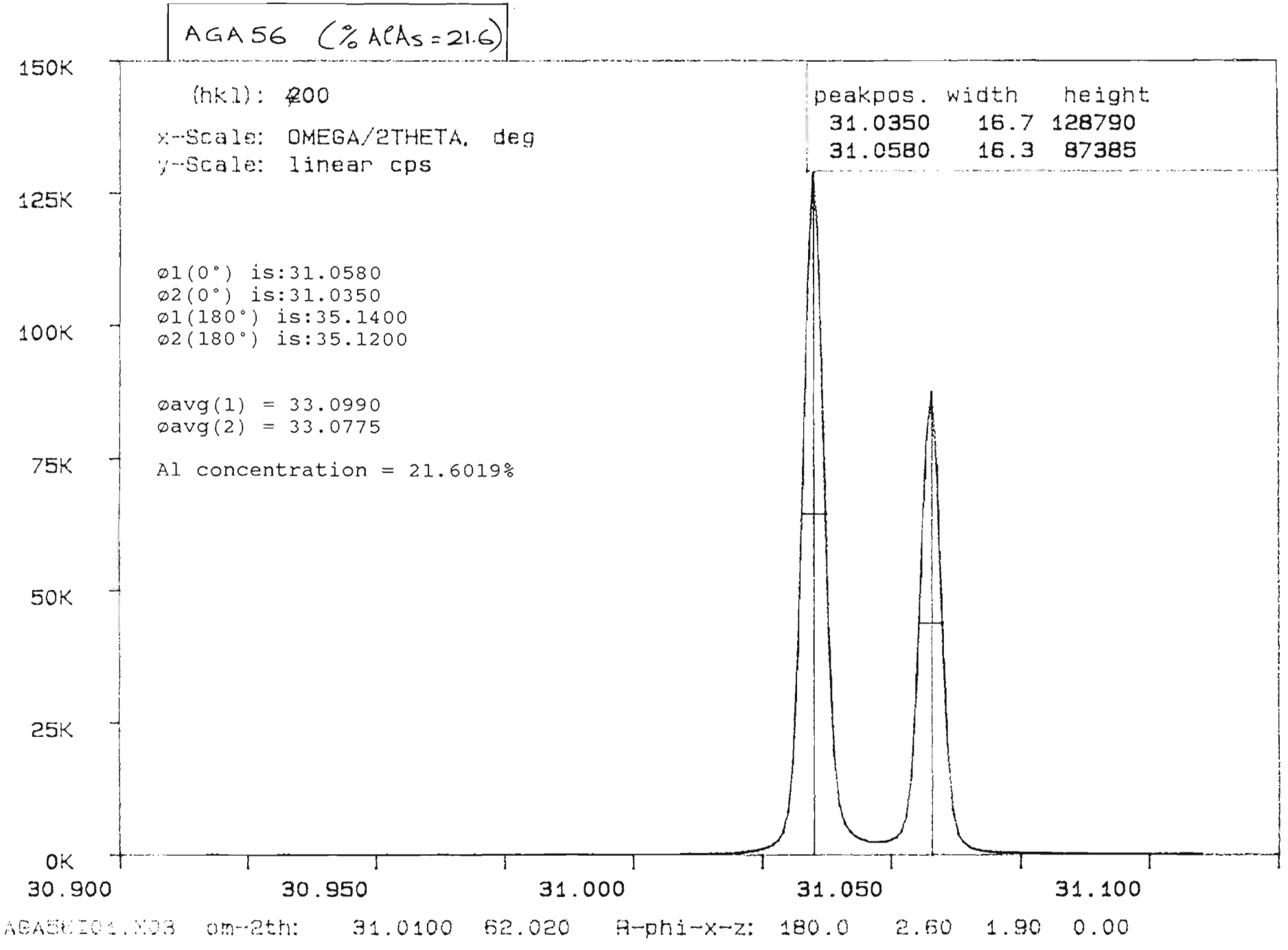
AGA56 (% AlAs = 21.6)
(hkl): 200
x-Scale: OMEGA/2THETA, deg
y-Scale: linear cps
peakpos. width height
31.0350 16.7 128790
31.0580 16.3 87385
ø1(0°) is:31.0580
ø2(0°) is:31.0350
ø1(180°) is:35.1400
ø2(180°) is:35.1200
øavg(1) = 33.0990
øavg(2) = 33.0775
Al concentration = 21.6019%
150K
125K
100K
75K
50K
25K
0K
30.900
30.950
31.000
31.050
31.100
om-2th: 31.0100 62.020 R-phi-x-z: 180.0 2.60 1.90 0.00

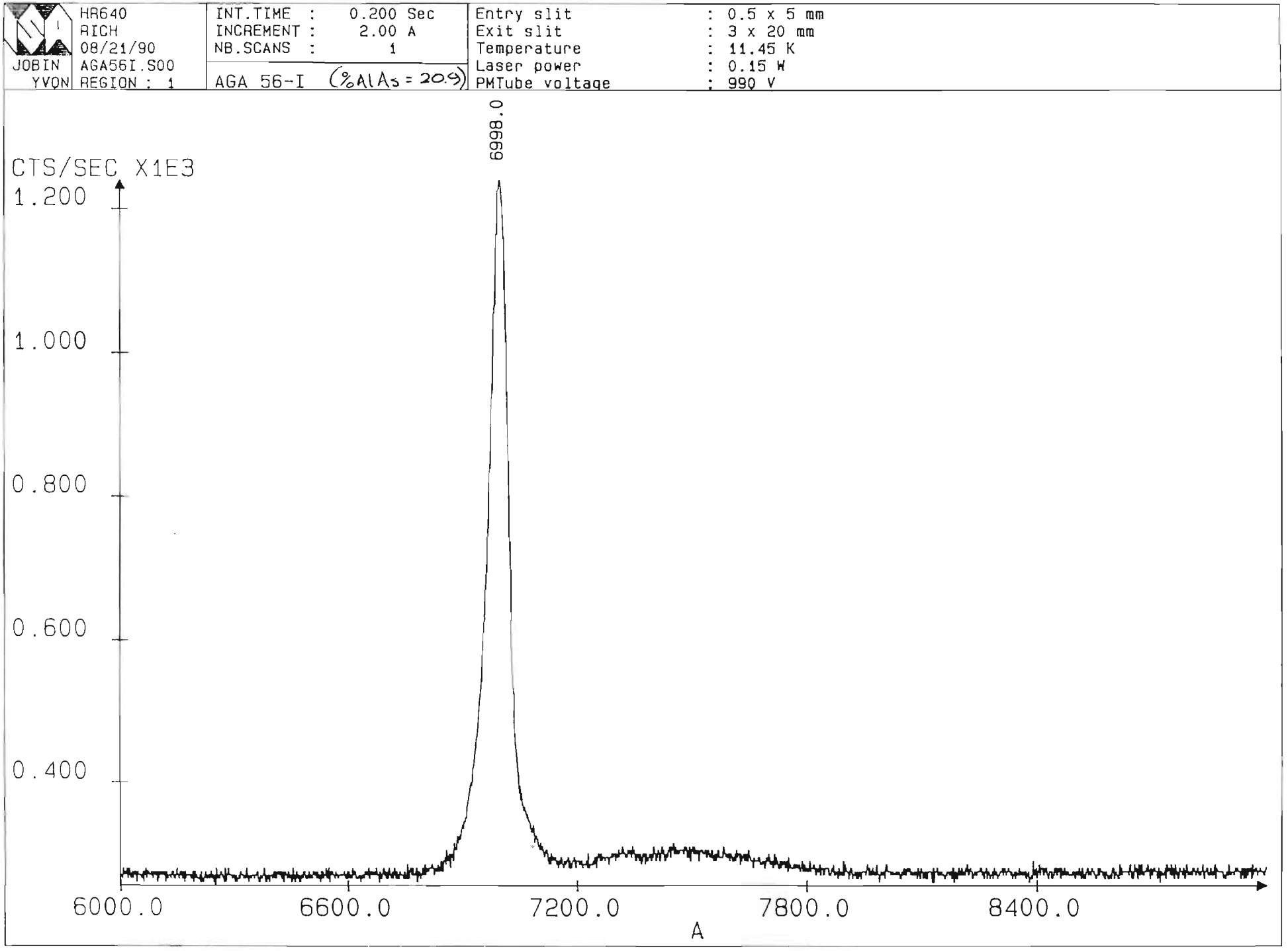
HR640
RICH
08/21/90
JOBIN AGA56I.S00
YVON REGION : 1
INT.TIME : 0.200 Sec
INCREMENT : 2.00 A
NB.SCANS : 1
AGA 56-I (%AlAs = 20.9)
Entry slit : 0.5 x 5 mm
Exit slit : 3 x 20 mm
Temperature : 11.45 K
Laser power : 0.15 W
PMTube voltage : 990 V
6998.0
CTS/SEC X1E3
1.200
1.000
0.800
0.600
0.400
6000.0
6600.0
7200.0
7800.0
8400.0
A

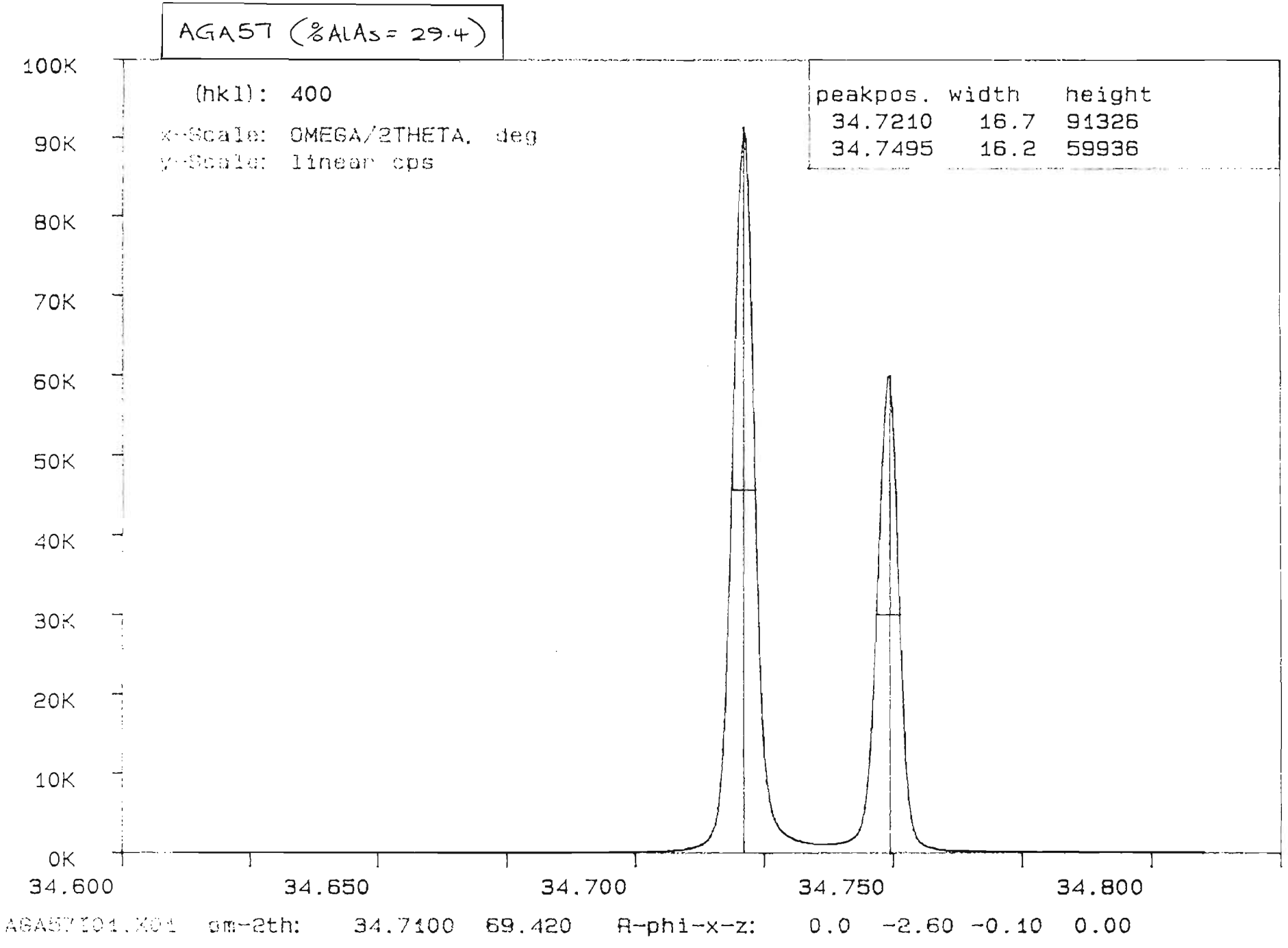
AGA57 (%AlAs = 29.4)
(hkl): 400
x-Scale: OMEGA/2THETA, deg
y-Scale: linear cps
peakpos. width height
34.7210 16.7 91326
34.7495 16.2 59936
100K
90K
80K
70K
60K
50K
40K
30K
20K
10K
0K
34.600
34.650
34.700
34.750
34.800
AGA57101.X01 gm-2th: 34.7100 69.420 R-phi-x-z: 0.0 -2.60 -0.10 0.00

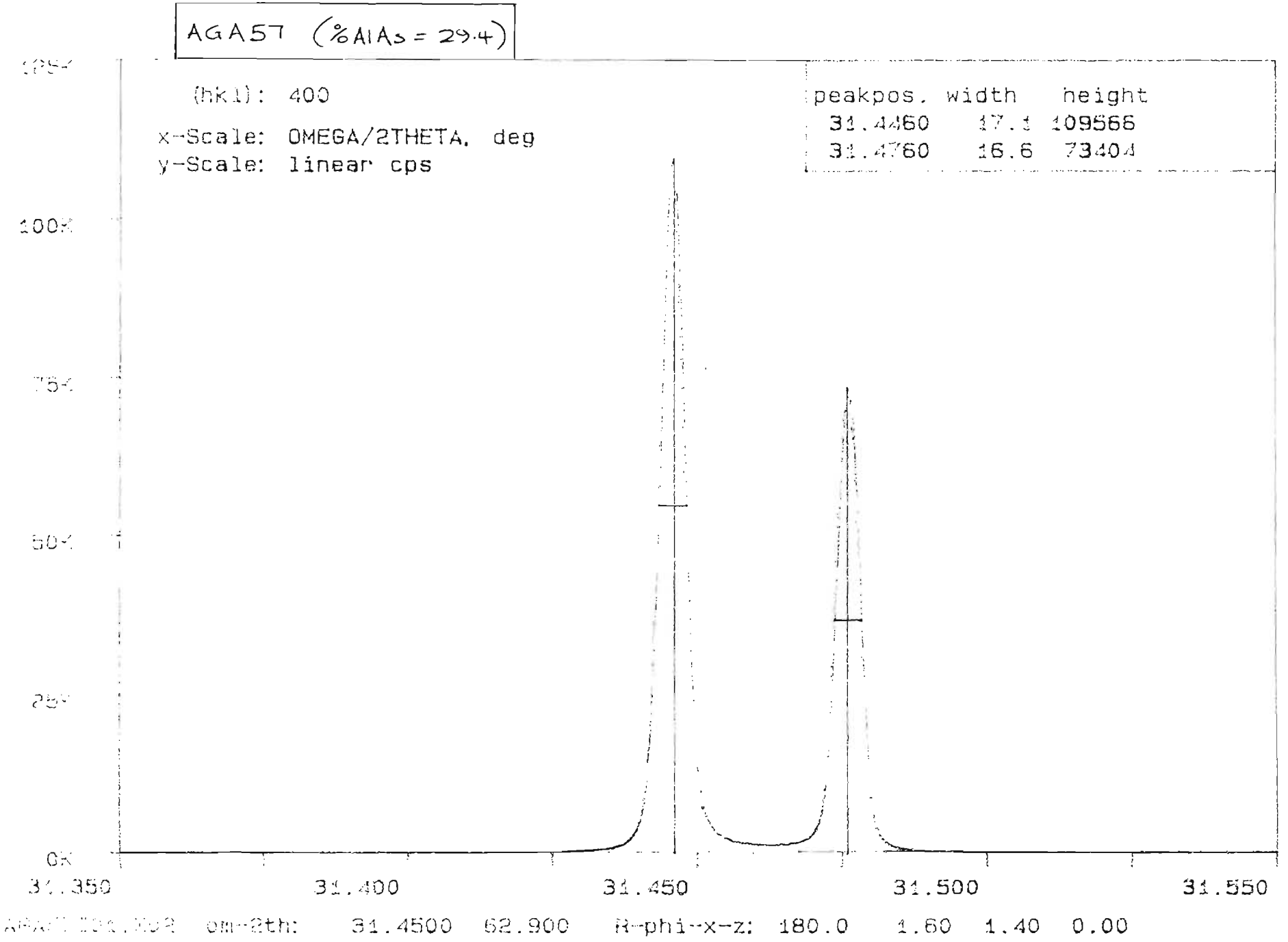
AGA57 (%AlAs = 29.4)
(hkl): 400
x-Scale: OMEGA/2THETA, deg
y-Scale: linear cps
peakpos. width height
31.4460 17.1 109566
31.4760 16.6 73404
100%
75%
50%
25%
0%
31.350
31.400
31.450
31.500
31.550
om-2th: 31.4500 62.900 R-phi-x-z: 180.0 1.60 1.40 0.00

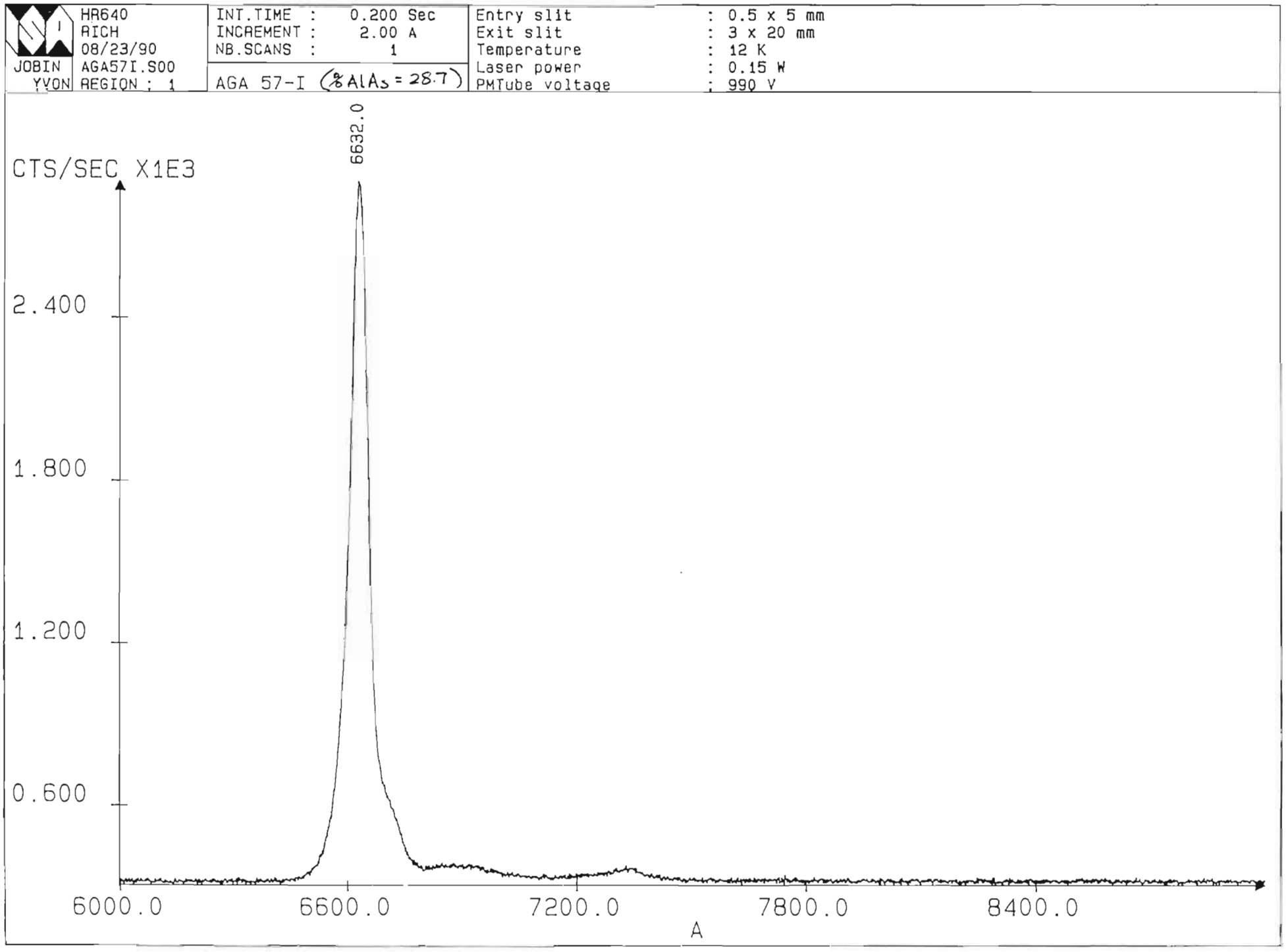
HR640
RICH
08/23/90
JOBIN YVON
AGA57I.S00
REGION : 1
INT.TIME : 0.200 Sec
INCREMENT : 2.00 A
NB.SCANS : 1
AGA 57-I (%AlAs = 28.7)
Entry slit : 0.5 x 5 mm
Exit slit : 3 x 20 mm
Temperature : 12 K
Laser power : 0.15 W
PMTube voltage : 990 V
6632.0
CTS/SEC X1E3
2.400
1.800
1.200
0.600
6000.0
6600.0
7200.0
7800.0
8400.0
A

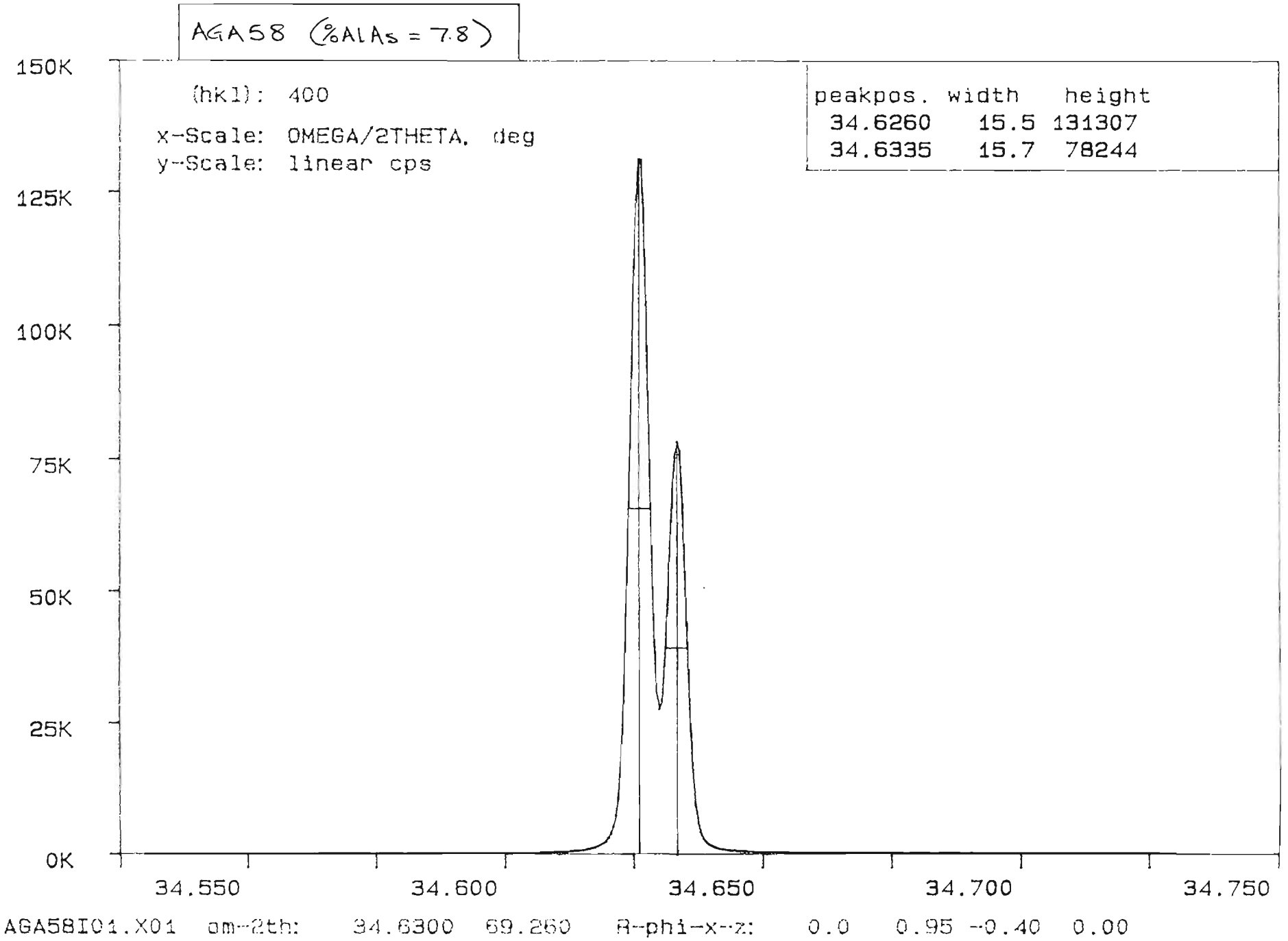
AGA58 (%AlAs = 7.8)
(hkl): 400
x-Scale: OMEGA/2THETA, deg
y-Scale: linear cps
peakpos. width height
34.6260 15.5 131307
34.6335 15.7 78244
150K
125K
100K
75K
50K
25K
0K
34.550
34.600
34.650
34.700
34.750
AGA58I01.X01 om-2th: 34.6300 69.260 R-phi-x-z: 0.0 0.95 -0.40 0.00

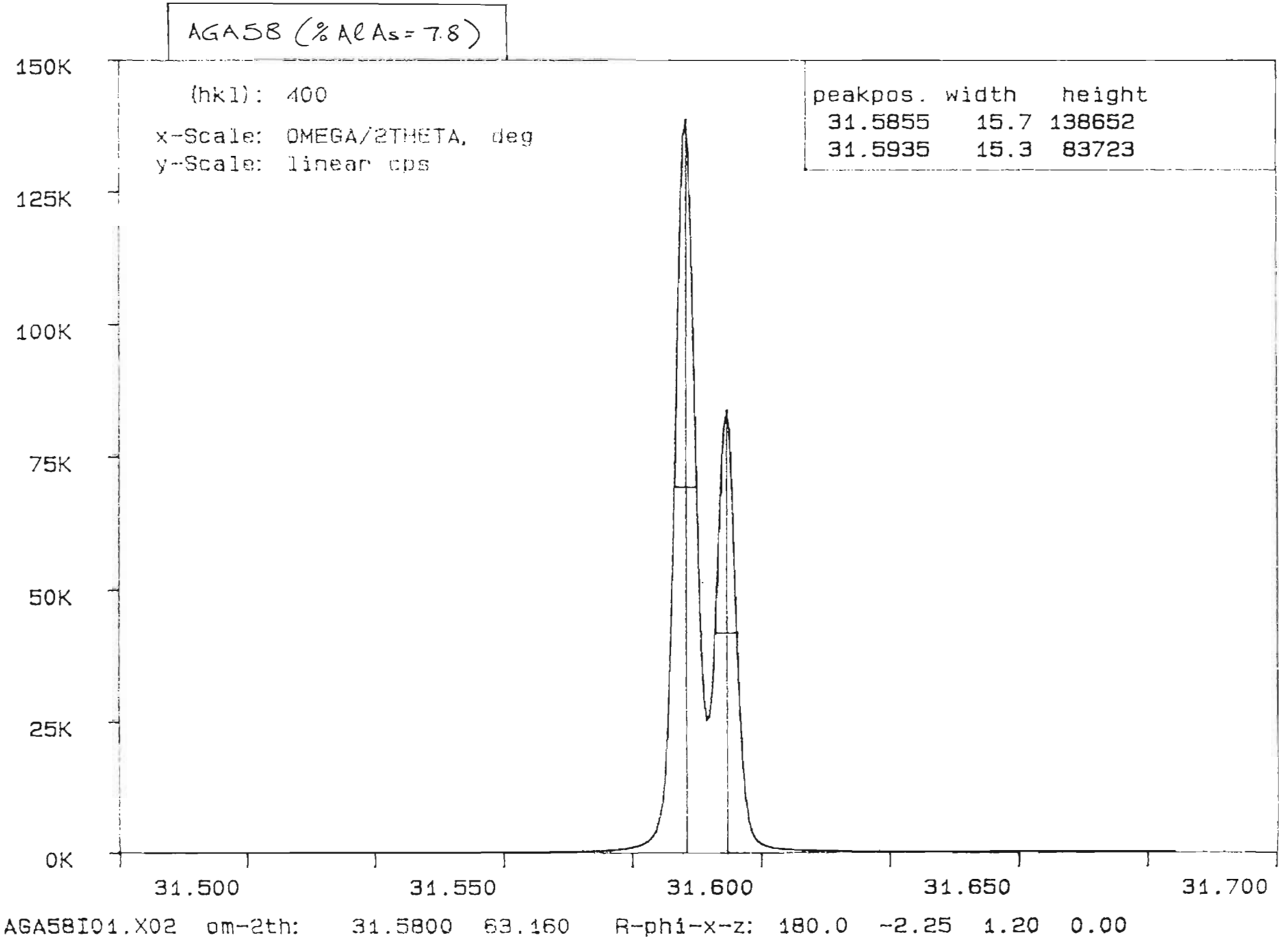
AGA58 (% AlAs = 7.8)
(hkl): 400
x-Scale: OMEGA/2THETA, deg
y-Scale: linear cps
peakpos. width height
31.5855 15.7 138652
31.5935 15.3 83723
150K
125K
100K
75K
50K
25K
0K
31.500
31.550
31.600
31.650
31.700
AGA58I01.X02 om-2th: 31.5800 63.160 R-phi-x-z: 180.0 -2.25 1.20 0.00

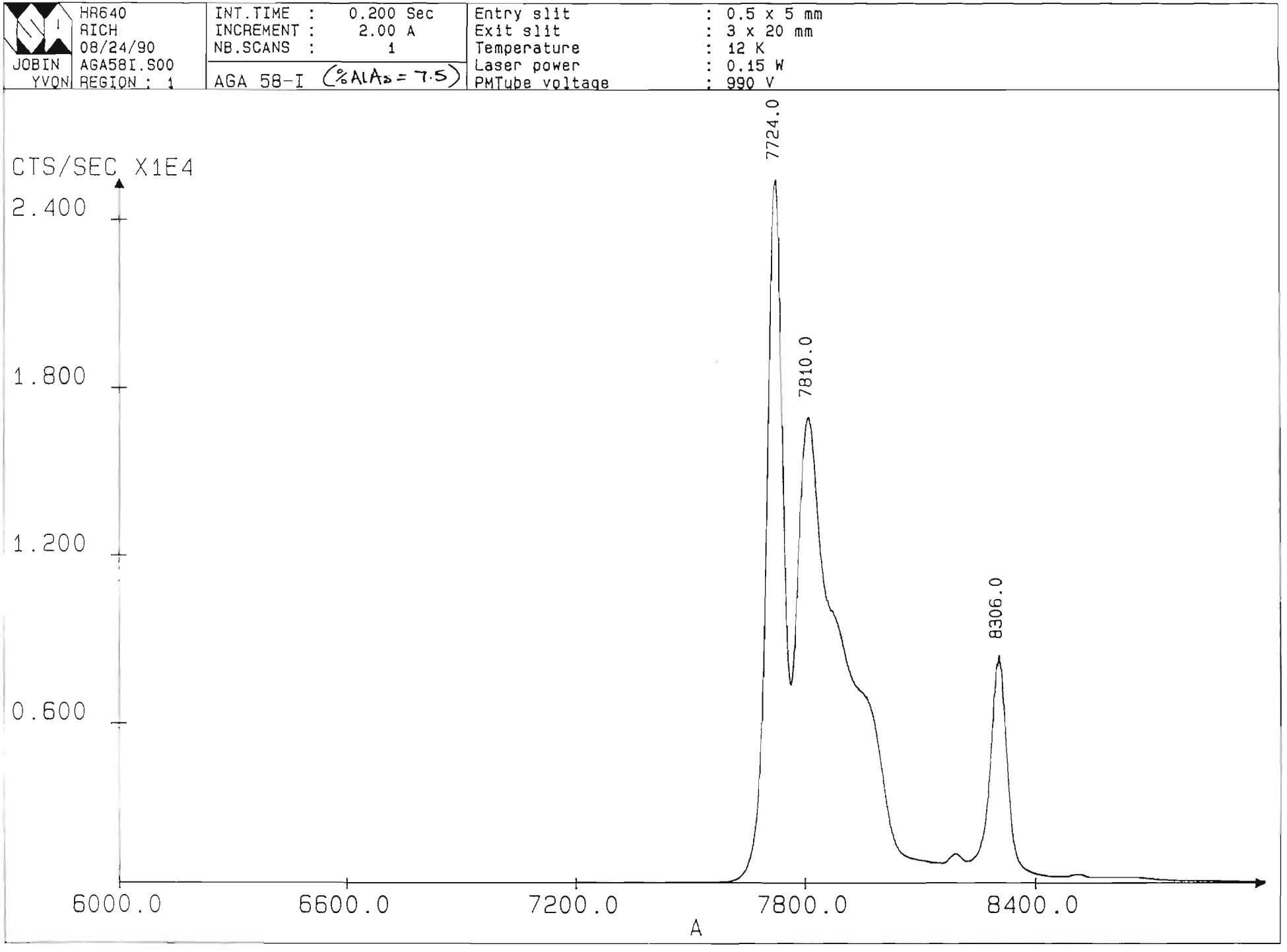
HR640
RICH
08/24/90
JOBIN YVON
AGA58I.S00
REGION : 1
INT.TIME : 0.200 Sec
INCREMENT : 2.00 A
NB.SCANS : 1
AGA 58-I (%AlAs = 7.5)
Entry slit : 0.5 x 5 mm
Exit slit : 3 x 20 mm
Temperature : 12 K
Laser power : 0.15 W
PMTube voltage : 990 V
CTS/SEC X1E4
2.400
1.800
1.200
0.600
7724.0
7810.0
8306.0
6000.0
6600.0
7200.0
7800.0
8400.0
A

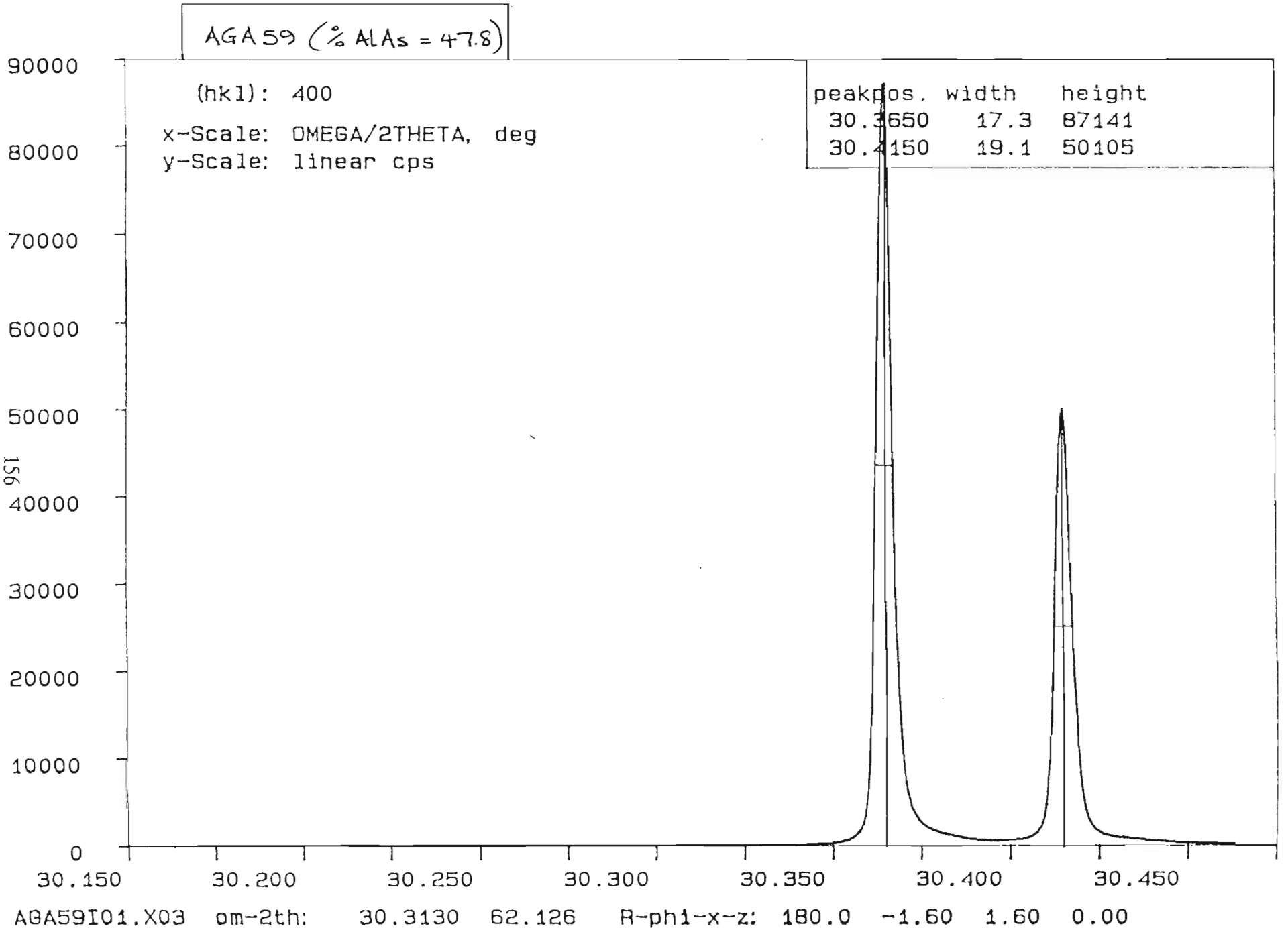
AGA59 (% AlAs = 47.8)
(hkl): 400
x-Scale: OMEGA/2THETA, deg
y-Scale: linear cps
peakpos. width height
30.3650 17.3 87141
30.4150 19.1 50105
90000
80000
70000
60000
50000
40000
30000
20000
10000
0
30.150
30.200
30.250
30.300
30.350
30.400
30.450
AGA59I01.X03 om-2th: 30.3130 62.126 R-phi-x-z: 180.0 -1.60 1.60 0.00

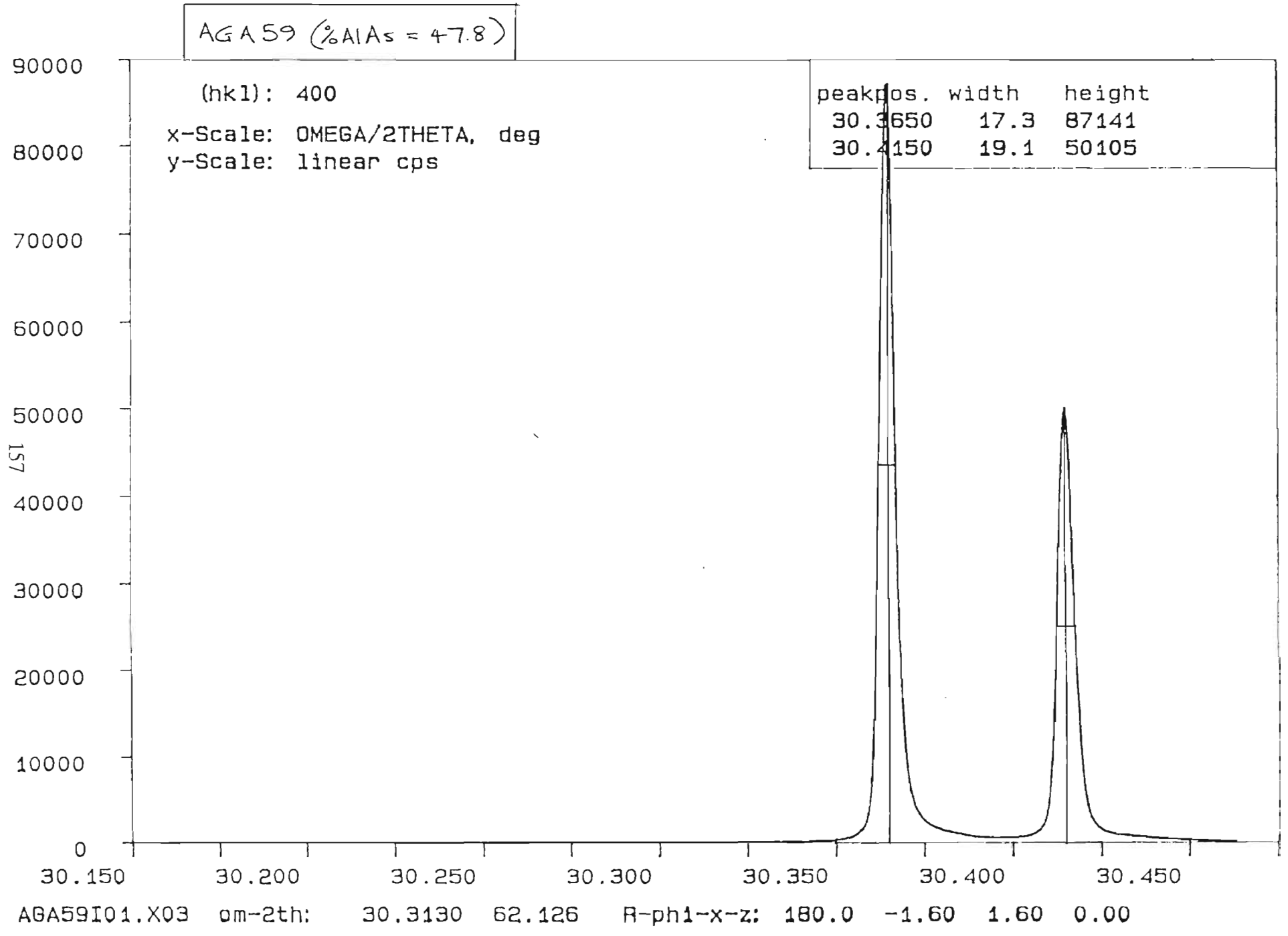
AGA59 (%AlAs = 47.8)
(hkl): 400
x-Scale: OMEGA/2THETA, deg
y-Scale: linear cps
peakpos. width height
30.3650 17.3 87141
30.4150 19.1 50105
90000
80000
70000
60000
50000
40000
30000
20000
10000
0
30.150
30.200
30.250
30.300
30.350
30.400
30.450
AGA59I01.X03 om-2th: 30.3130 62.126 R-ph1-x-z: 180.0 -1.60 1.60 0.00

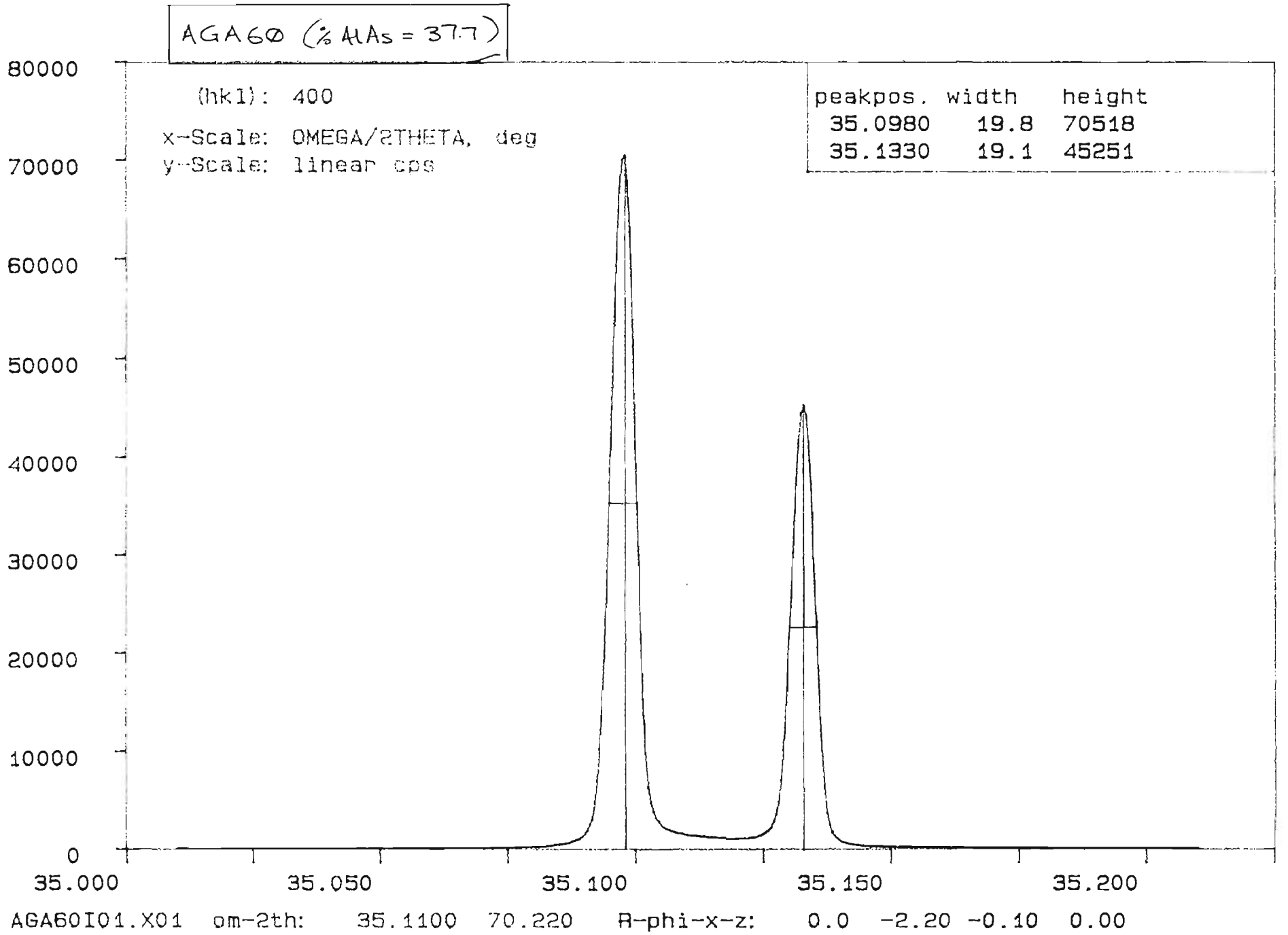
AGA60 (% AlAs = 37.7)
(hkl): 400
x-Scale: OMEGA/2THETA, deg
y-Scale: linear cps
peakpos. width height
35.0980 19.8 70518
35.1330 19.1 45251
80000
70000
60000
50000
40000
30000
20000
10000
0
35.000
35.050
35.100
35.150
35.200
AGA60I01.X01 om-2th: 35.1100 70.220 R-phi-x-z: 0.0 -2.20 -0.10 0.00

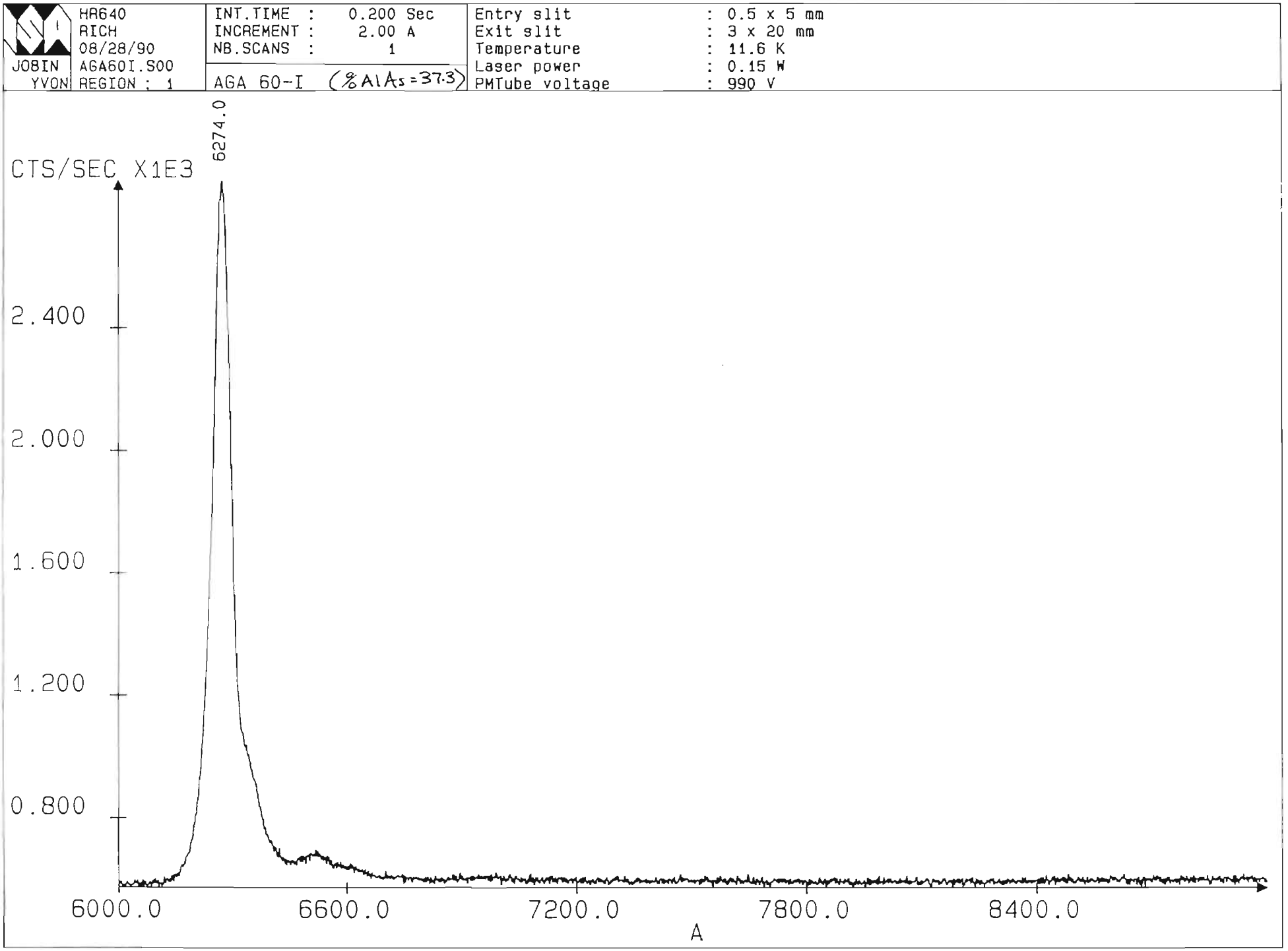
HR640
RICH
08/28/90
JOBIN YVON
AGA60I.S00
REGION : 1
INT.TIME : 0.200 Sec
INCREMENT : 2.00 A
NB.SCANS : 1
AGA 60-I (%AlAs=37.3)
Entry slit : 0.5 x 5 mm
Exit slit : 3 x 20 mm
Temperature : 11.6 K
Laser power : 0.15 W
PMTube voltage : 990 V
6274.0
CTS/SEC X1E3
2.400
2.000
1.600
1.200
0.800
6000.0
6600.0
7200.0
7800.0
8400.0
A

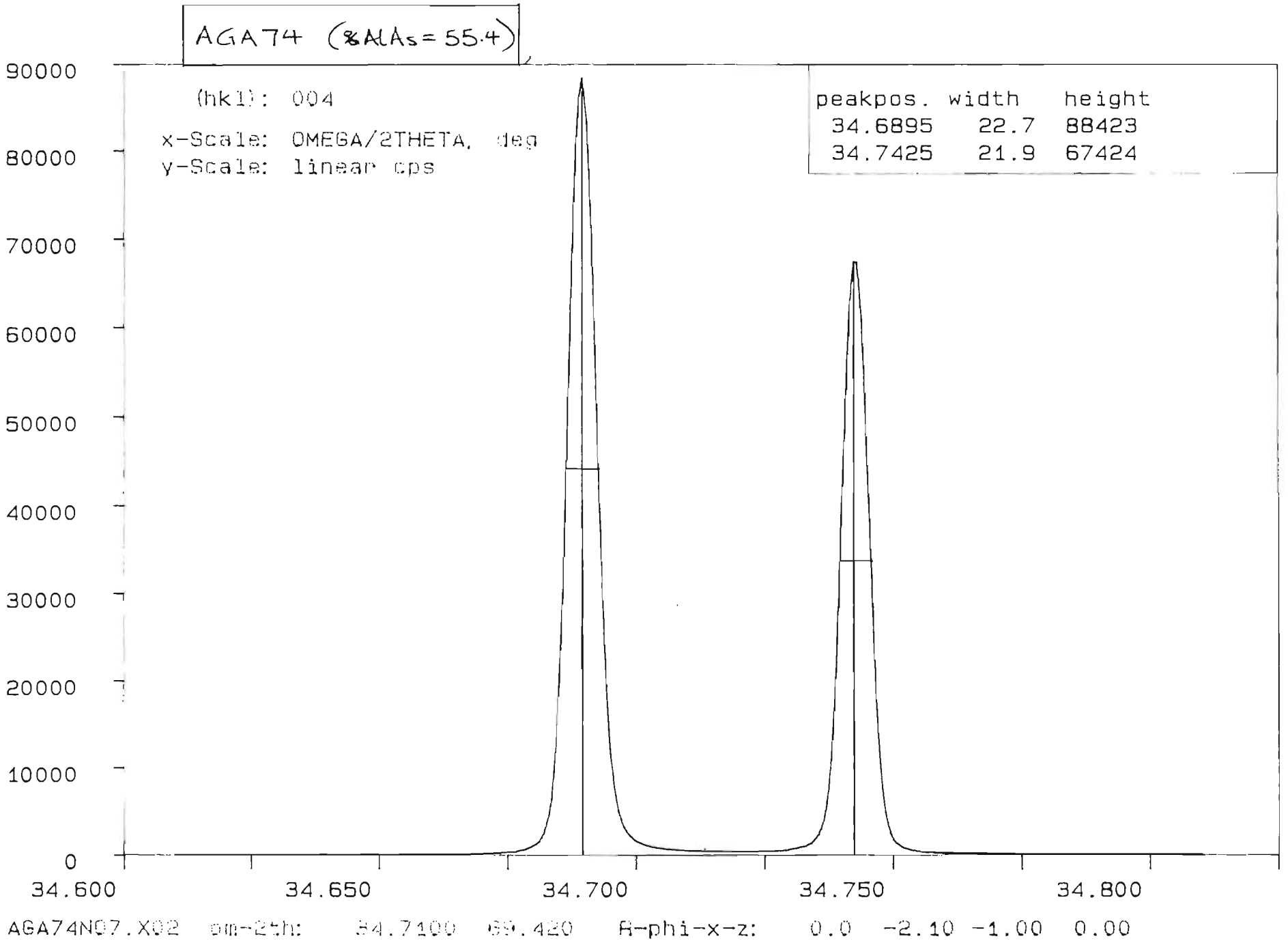
AGA74 (%AlAs=55.4)
(hkl): 004
x-Scale: OMEGA/2THETA, deg
y-Scale: linear cps
peakpos. width height
34.6895 22.7 88423
34.7425 21.9 67424
90000
80000
70000
60000
50000
40000
30000
20000
10000
0
34.600
34.650
34.700
34.750
34.800
AGA74N07.X02 om-2th: 34.7100 69.420 A-phi-x-z: 0.0 -2.10 -1.00 0.00

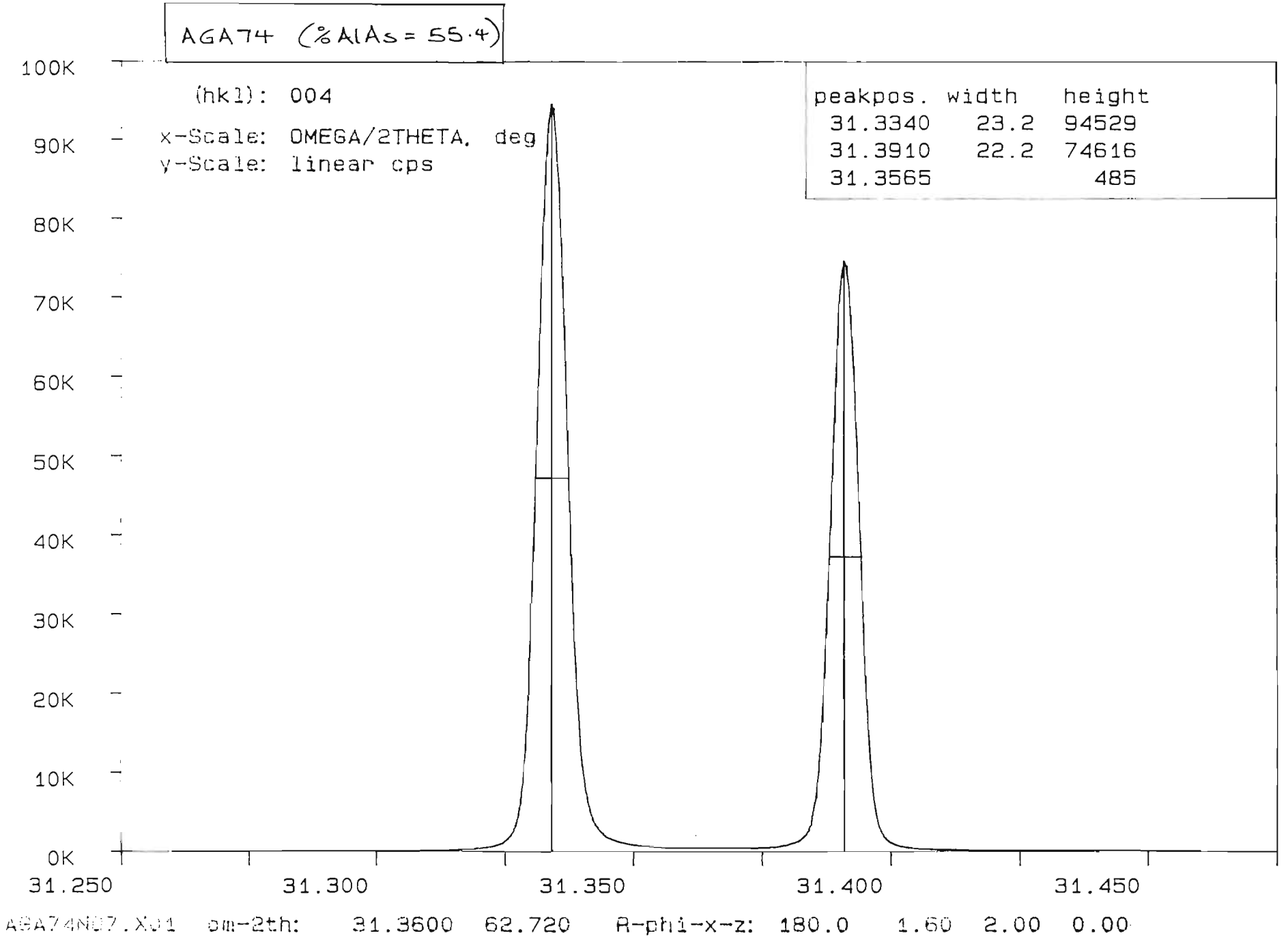
AGA74 (%AlAs = 55.4)
(hkl): 004
x-Scale: OMEGA/2THETA, deg
y-Scale: linear cps
peakpos. width height
31.3340 23.2 94529
31.3910 22.2 74616
31.3565 485
100K
90K
80K
70K
60K
50K
40K
30K
20K
10K
0K
31.250
31.300
31.350
31.400
31.450
AGA74N07.XU1 om-2th: 31.3600 62.720 R-phi-x-z: 180.0 1.60 2.00 0.00

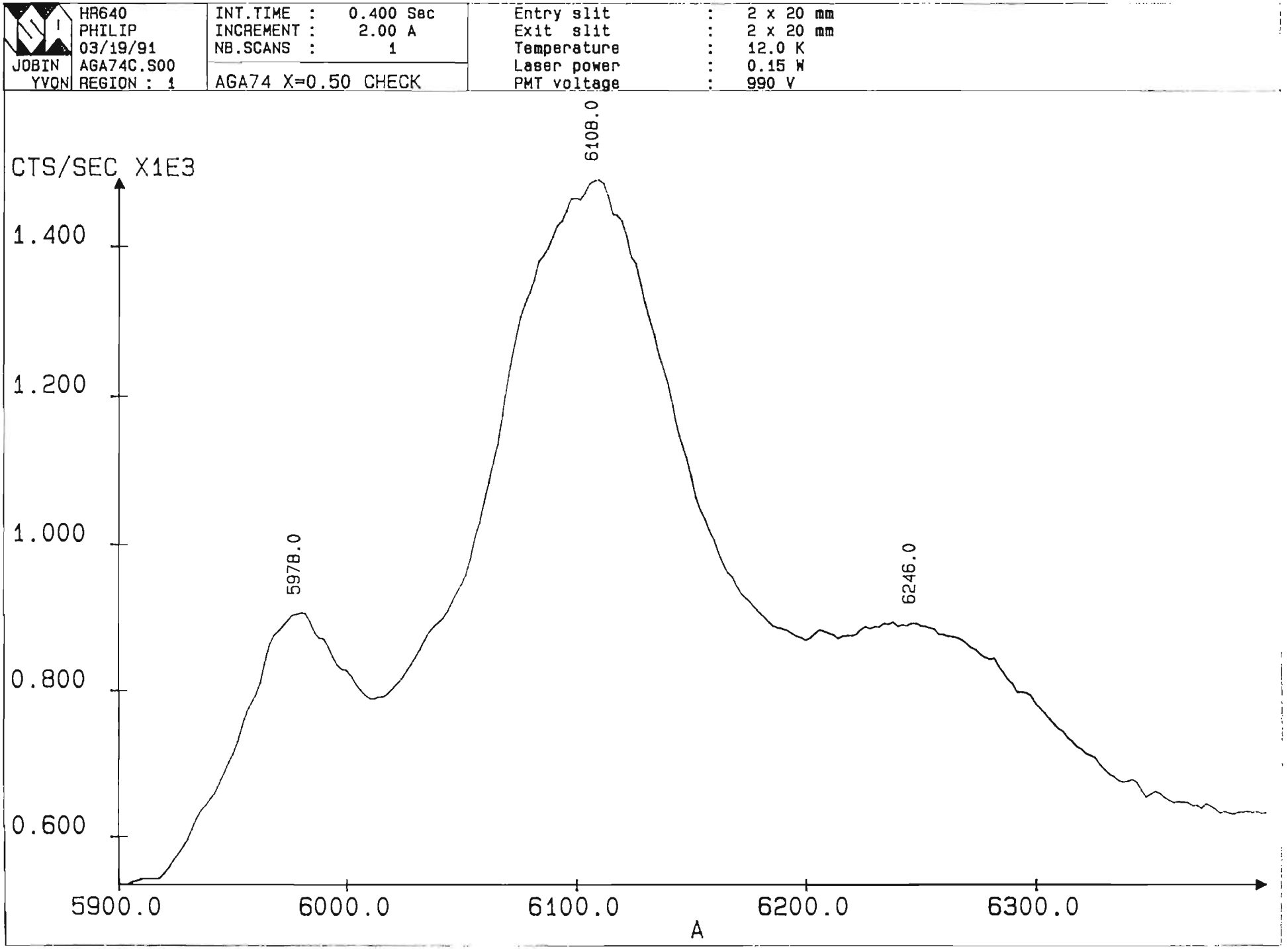
HR640
PHILIP
03/19/91
JOBIN
AGA74C.S00
YVON
REGION : 1
INT.TIME : 0.400 Sec
INCREMENT : 2.00 A
NB.SCANS : 1
AGA74 X=0.50 CHECK
Entry slit : 2 x 20 mm
Exit slit : 2 x 20 mm
Temperature : 12.0 K
Laser power : 0.15 W
PMT voltage : 990 V
CTS/SEC X1E3
1.400
1.200
1.000
0.800
0.600
6108.0
5978.0
6246.0
5900.0
6000.0
6100.0
6200.0
6300.0
A

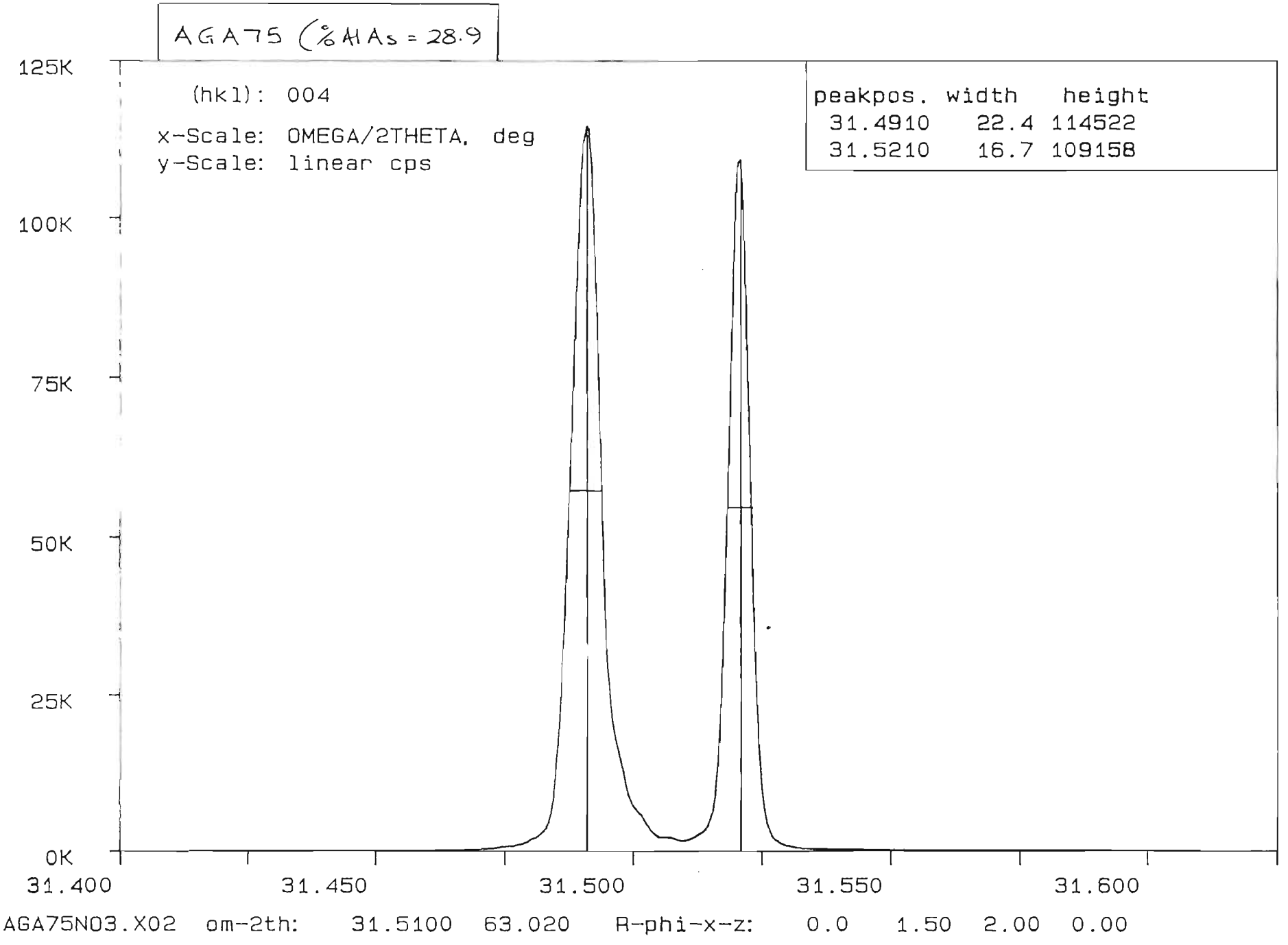
AGA75 (%MAs = 28.9
(hkl): 004
x-Scale: OMEGA/2THETA, deg
y-Scale: linear cps
peakpos. width height
31.4910 22.4 114522
31.5210 16.7 109158
125K
100K
75K
50K
25K
0K
31.400
31.450
31.500
31.550
31.600
AGA75N03.X02 om-2th: 31.5100 63.020 R-phi-x-z: 0.0 1.50 2.00 0.00

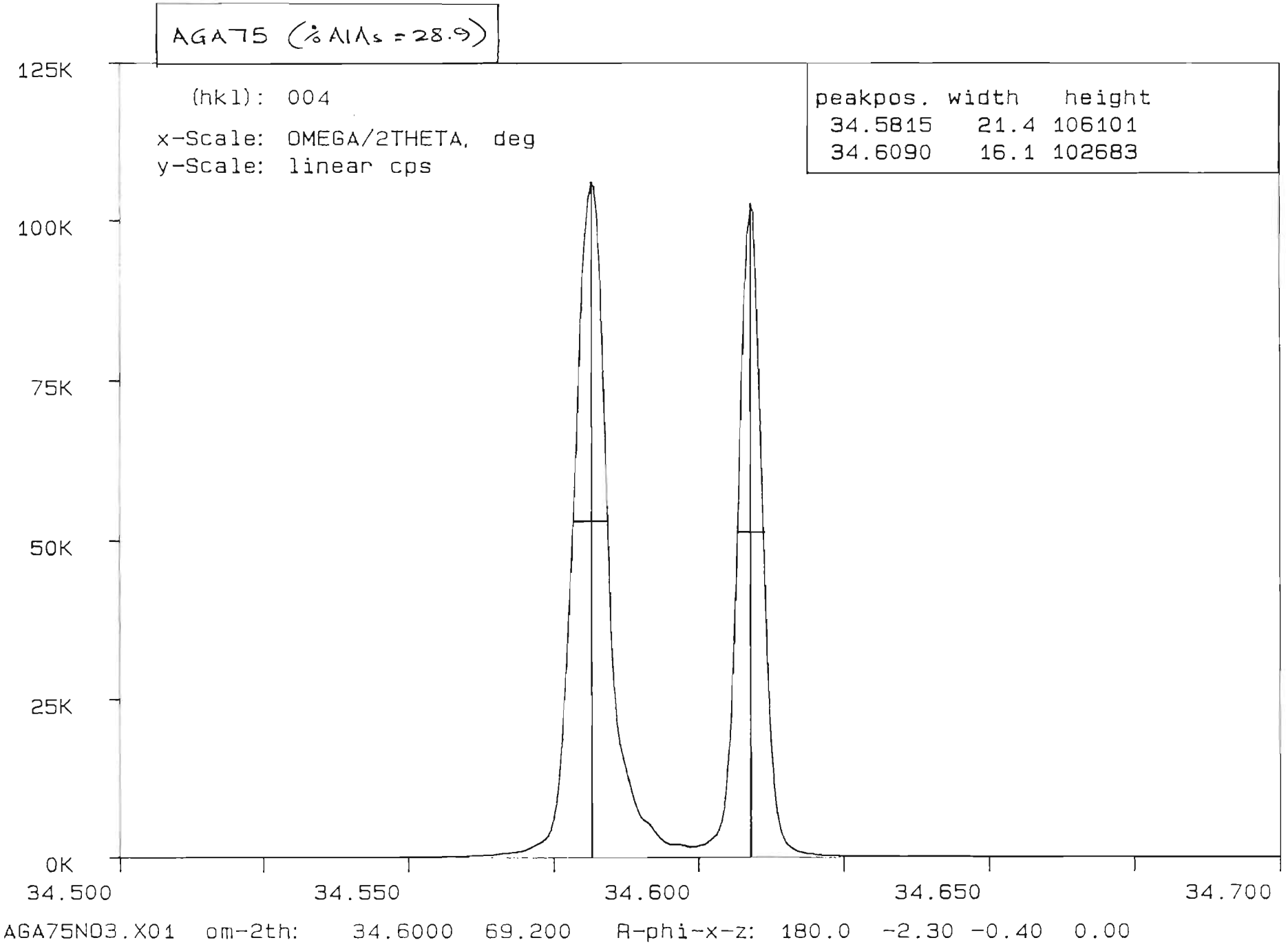
AGA75 (% AlAs = 28.9)
(hkl): 004
x-Scale: OMEGA/2THETA, deg
y-Scale: linear cps
peakpos. width height
34.5815 21.4 106101
34.6090 16.1 102683
125K
100K
75K
50K
25K
0K
34.500
34.550
34.600
34.650
34.700
AGA75N03.X01 om-2th: 34.6000 69.200 R-phi-x-z: 180.0 -2.30 -0.40 0.00

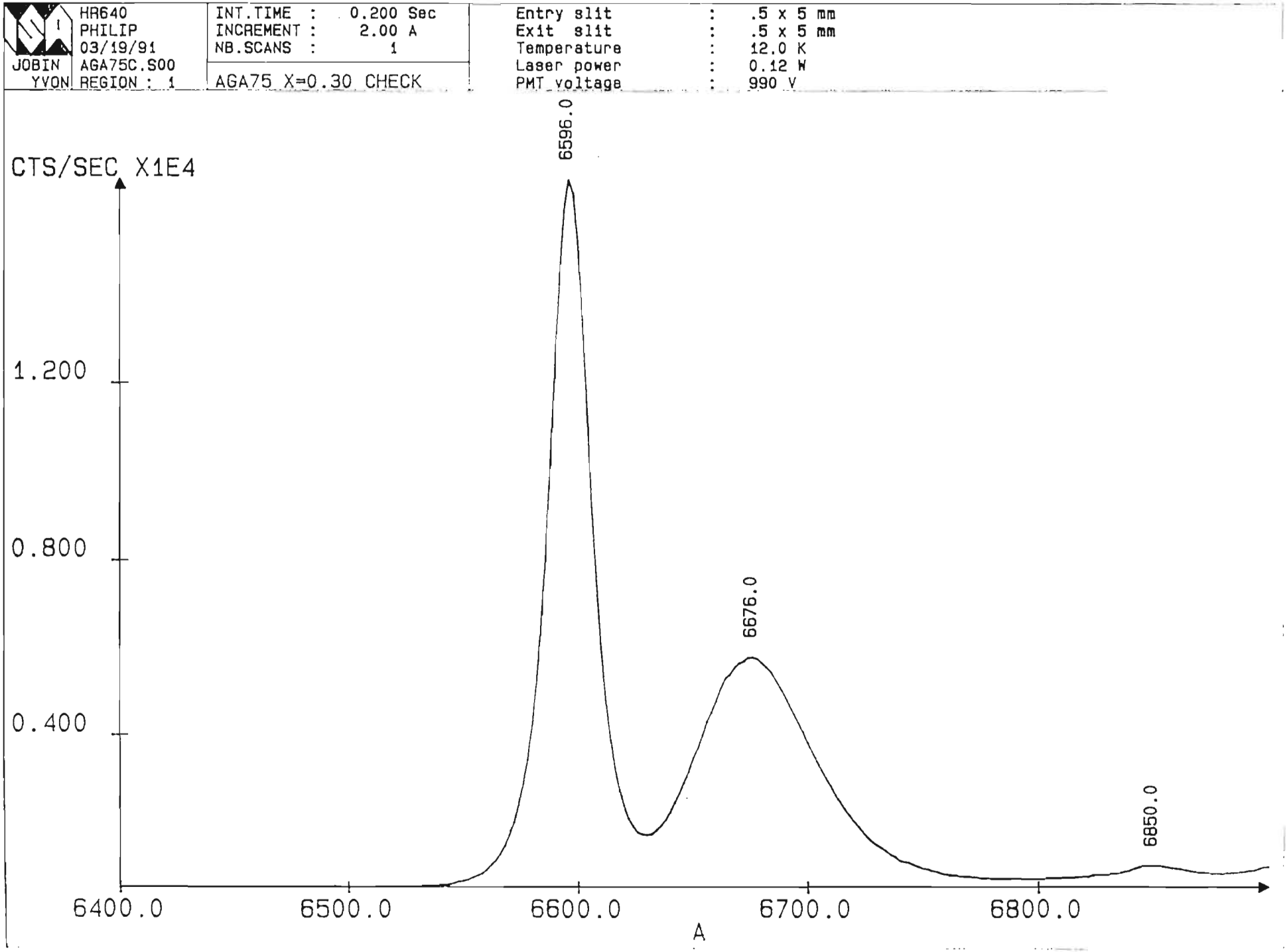
HR640
PHILIP
03/19/91
JOBIN
YVON
AGA75C.S00
REGION : 1
INT.TIME : 0.200 Sec
INCREMENT : 2.00 A
NB.SCANS : 1
AGA75 X=0.30 CHECK
Entry slit : .5 x 5 mm
Exit slit : .5 x 5 mm
Temperature : 12.0 K
Laser power : 0.12 W
PMT voltage : 990 V
CTS/SEC X1E4
1.200
0.800
0.400
6596.0
6676.0
6850.0
6400.0
6500.0
6600.0
6700.0
6800.0
A

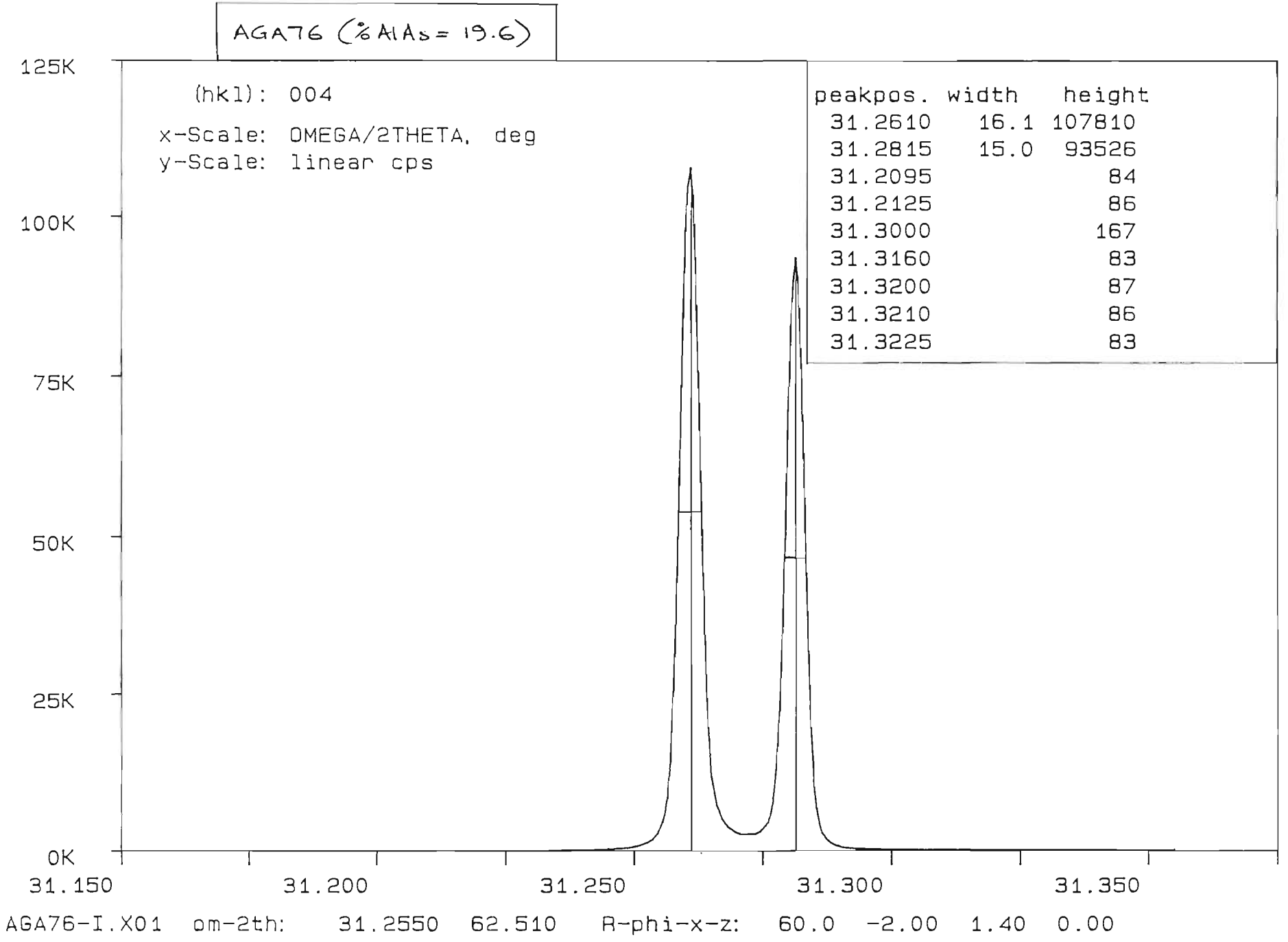
AGA76 (%AlAs = 19.6)
(hkl): 004
x-Scale: OMEGA/2THETA, deg
y-Scale: linear cps
peakpos. width height
31.2610 16.1 107810
31.2815 15.0 93526
31.2095 84
31.2125 86
31.3000 167
31.3160 83
31.3200 87
31.3210 86
31.3225 83
125K
100K
75K
50K
25K
0K
31.150
31.200
31.250
31.300
31.350
AGA76-I.X01 om-2th: 31.2550 62.510 R-phi-x-z: 60.0 -2.00 1.40 0.00

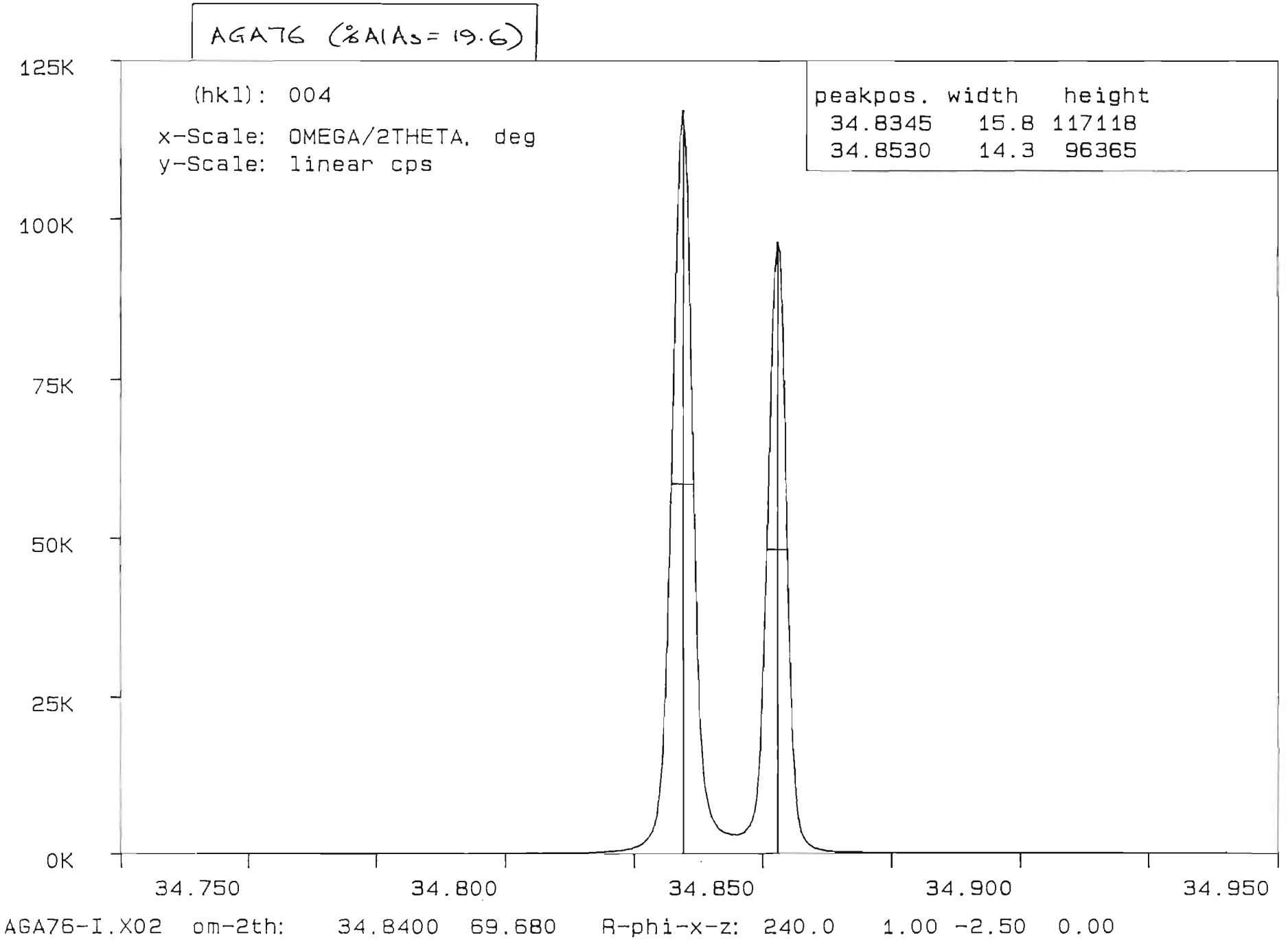
AGA76 (%AlAs = 19.6)
(hkl): 004
x-Scale: OMEGA/2THETA, deg
y-Scale: linear cps
peakpos. width height
34.8345 15.8 117118
34.8530 14.3 96365
125K
100K
75K
50K
25K
0K
34.750
34.800
34.850
34.900
34.950
AGA76-I.X02 om-2th: 34.8400 69.680 R-phi-x-z: 240.0 1.00 -2.50 0.00

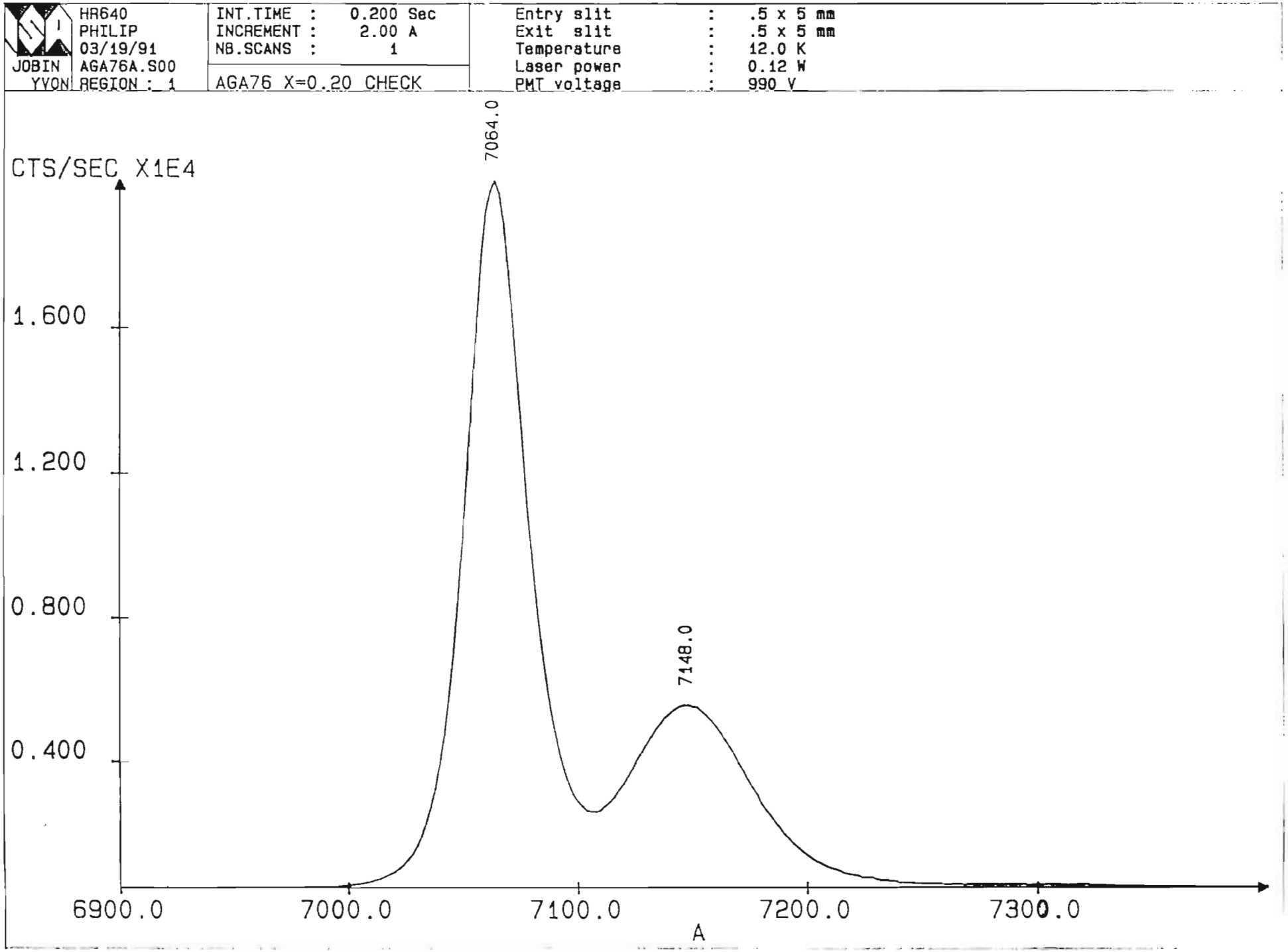
HR640
PHILIP
03/19/91
JOBIN
AGA76A.S00
YVON
REGION : 1
INT.TIME : 0.200 Sec
INCREMENT : 2.00 A
NB.SCANS : 1
AGA76 X=0.20 CHECK
Entry slit : .5 x 5 mm
Exit slit : .5 x 5 mm
Temperature : 12.0 K
Laser power : 0.12 W
PMT voltage : 990 V
CTS/SEC X1E4
1.600
1.200
0.800
0.400
7064.0
7148.0
6900.0
7000.0
7100.0
7200.0
7300.0
A

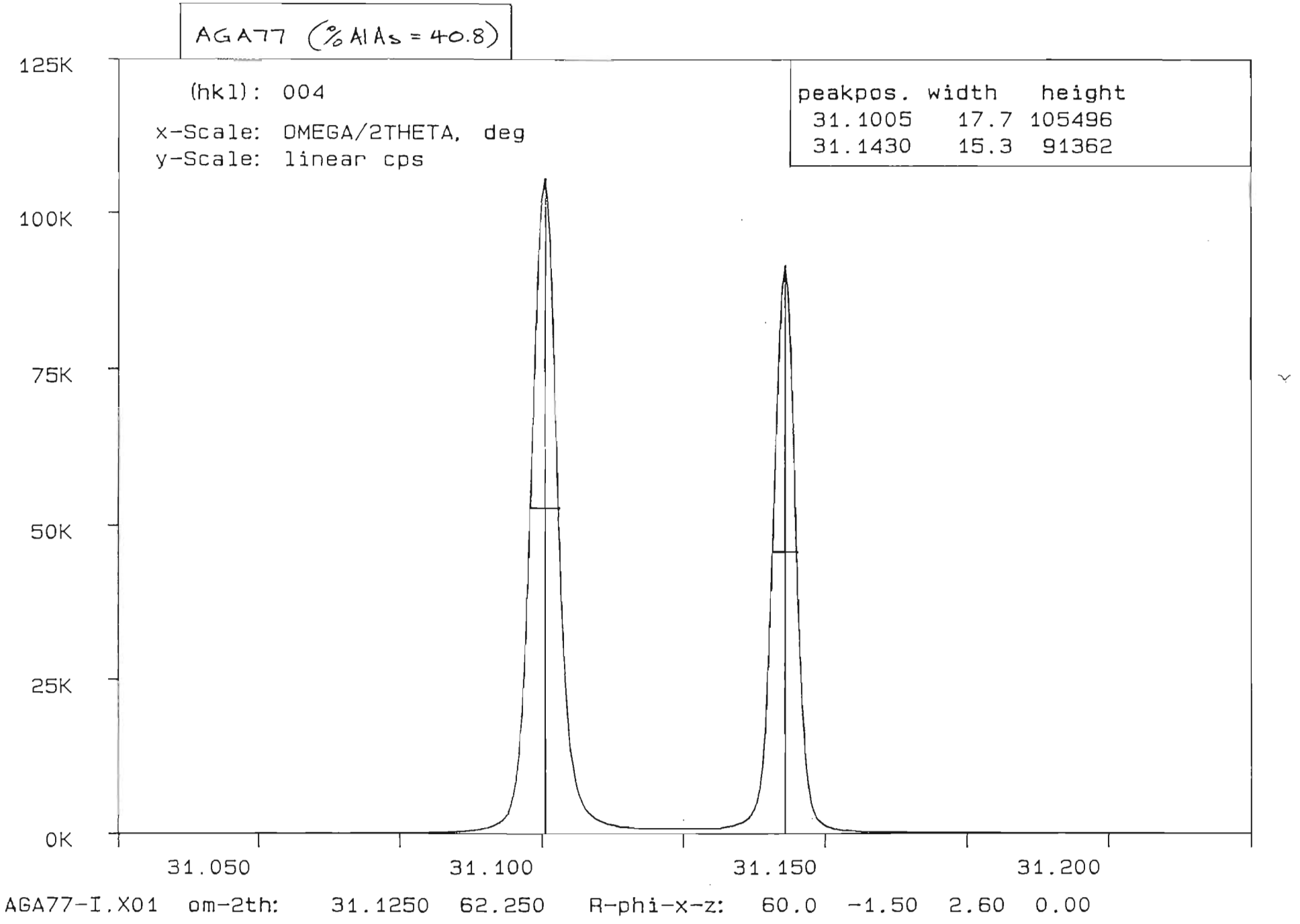
AGA77 (%AlAs = 40.8)
(hkl): 004
x-Scale: OMEGA/2THETA, deg
y-Scale: linear cps
peakpos. width height
31.1005 17.7 105496
31.1430 15.3 91362
125K
100K
75K
50K
25K
0K
31.050
31.100
31.150
31.200
AGA77-I.X01 om-2th: 31.1250 62.250 R-phi-x-z: 60.0 -1.50 2.60 0.00

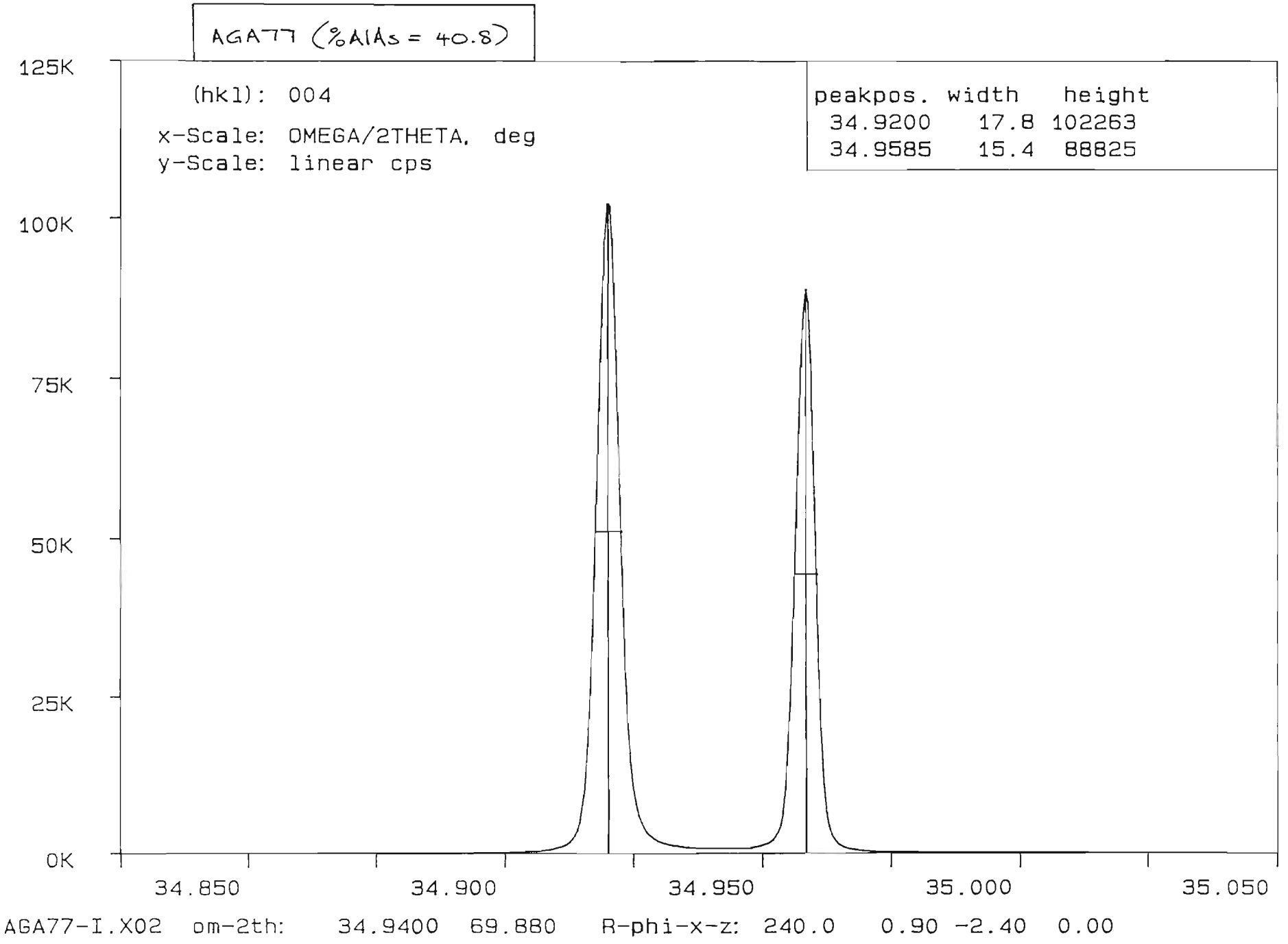
AGA77 (%AlAs = 40.8)
(hkl): 004
x-Scale: OMEGA/2THETA, deg
y-Scale: linear cps
peakpos. width height
34.9200 17.8 102263
34.9585 15.4 88825
125K
100K
75K
50K
25K
0K
34.850
34.900
34.950
35.000
35.050
AGA77-I.X02 om-2th: 34.9400 69.880 R-phi-x-z: 240.0 0.90 -2.40 0.00

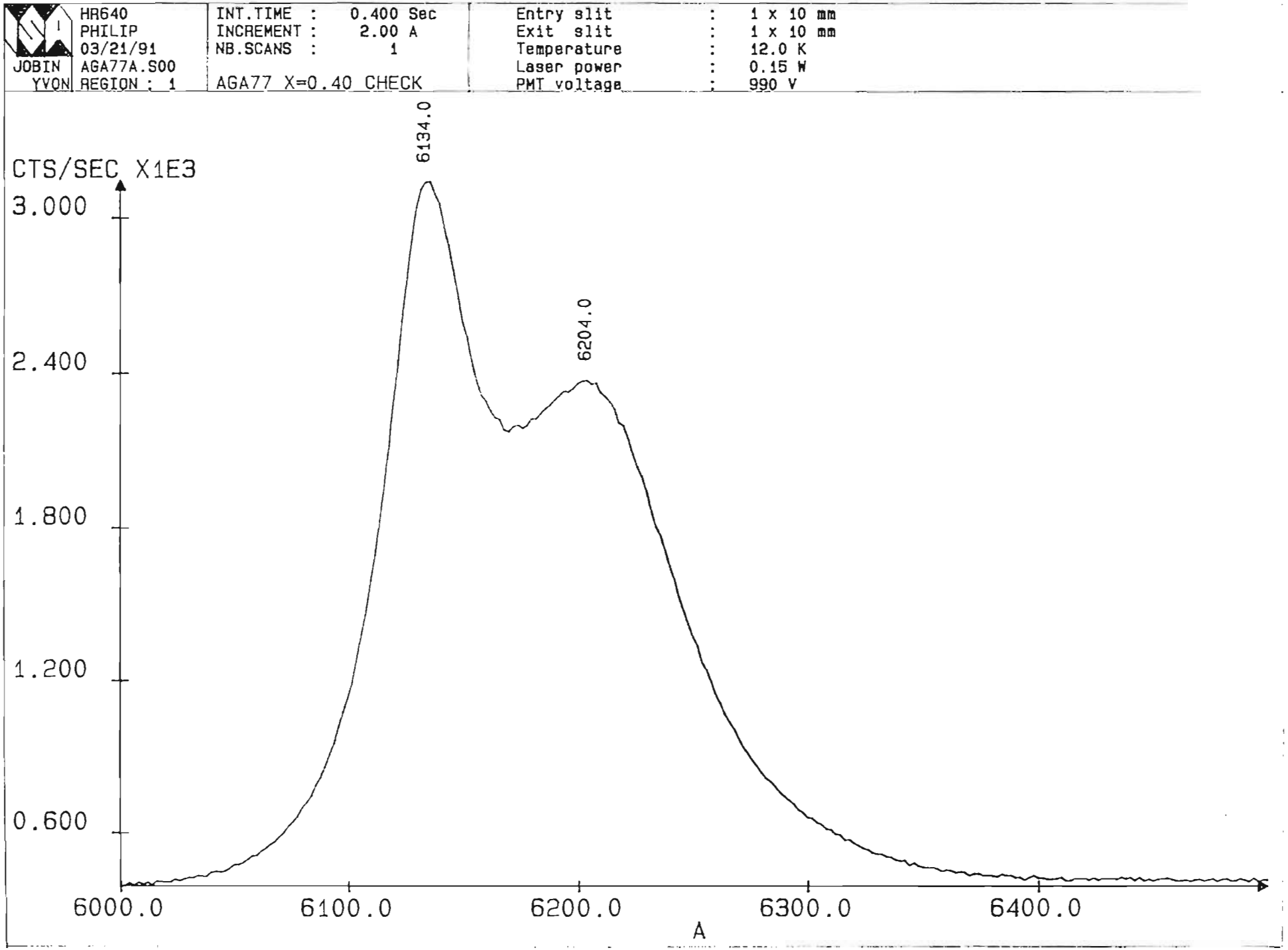
HR640
PHILIP
03/21/91
JOBIN
YVON
AGA77A.S00
REGION : 1
INT.TIME : 0.400 Sec
INCREMENT : 2.00 A
NB.SCANS : 1
AGA77 X=0.40 CHECK
Entry slit : 1 x 10 mm
Exit slit : 1 x 10 mm
Temperature : 12.0 K
Laser power : 0.15 W
PMT voltage : 990 V
6134.0
6204.0
CTS/SEC X1E3
3.000
2.400
1.800
1.200
0.600
6000.0
6100.0
6200.0
6300.0
6400.0
A

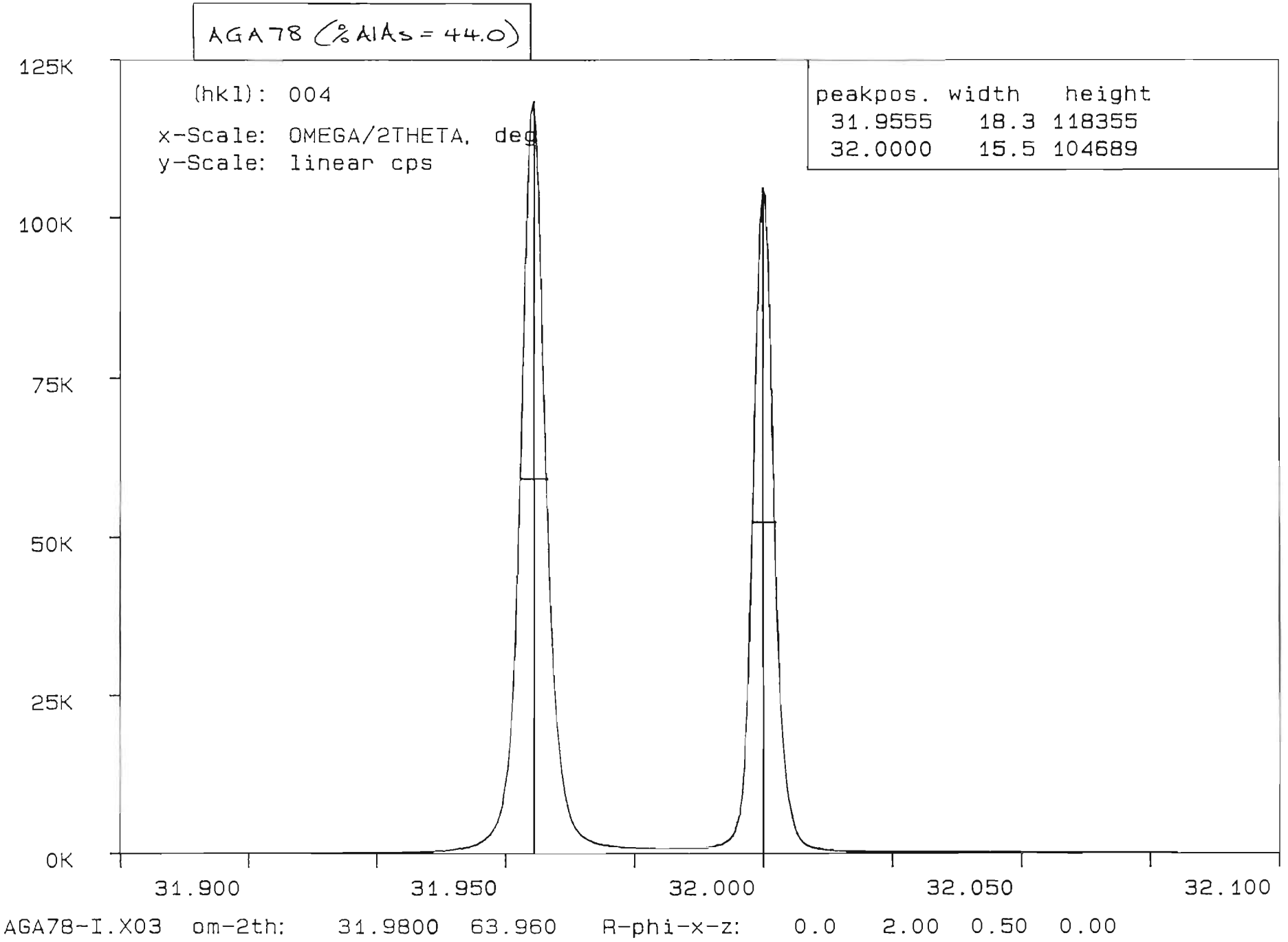
AGA78 (%AlAs = 44.0)
(hkl): 004
x-Scale: OMEGA/2THETA, deg
y-Scale: linear cps
peakpos. width height
31.9555 18.3 118355
32.0000 15.5 104689
125K
100K
75K
50K
25K
0K
31.900
31.950
32.000
32.050
32.100
AGA78-I.X03 om-2th: 31.9800 63.960 R-phi-x-z: 0.0 2.00 0.50 0.00

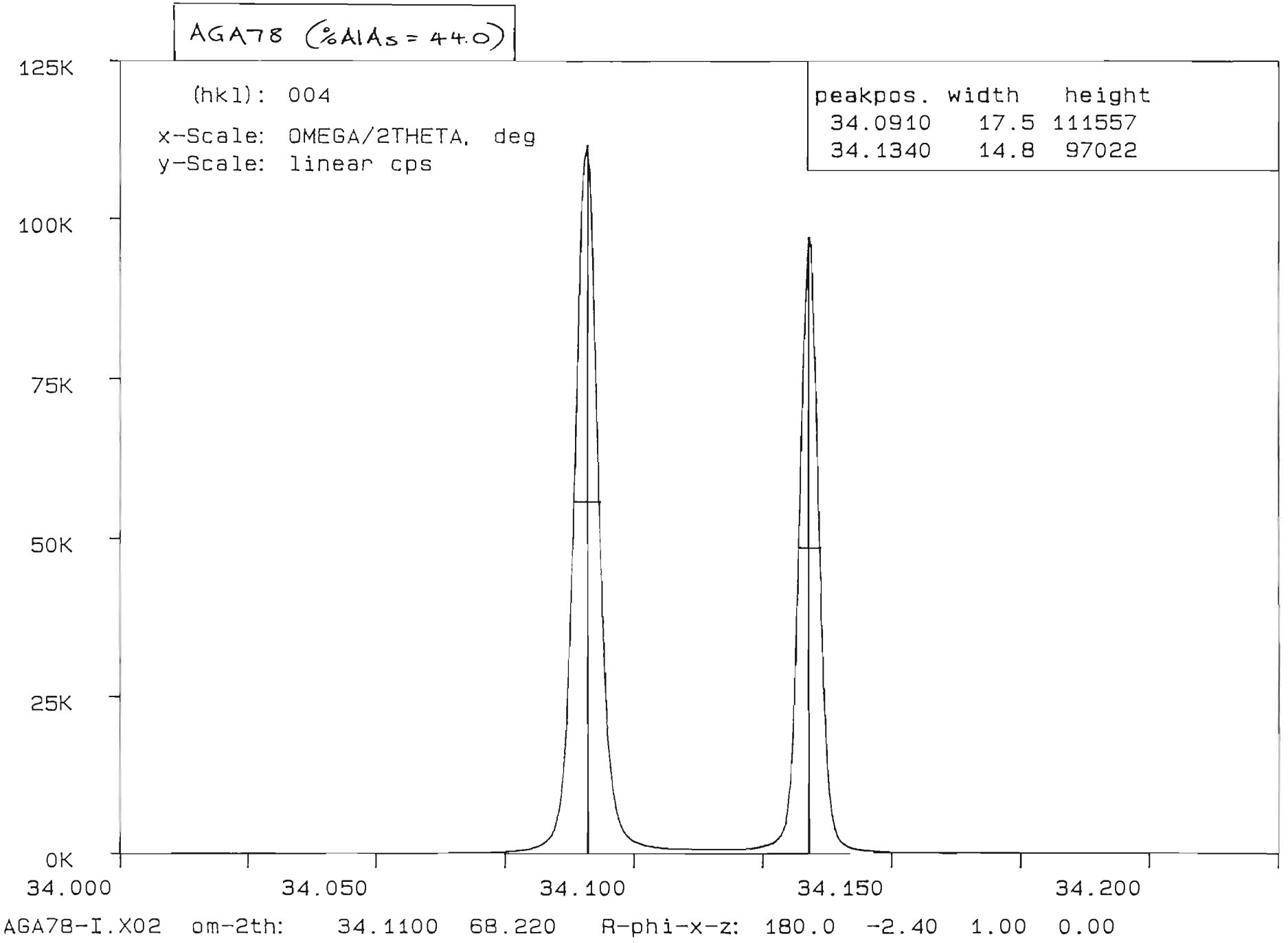
AGA78 (%AlAs = 44.0)
(hkl): 004
x-Scale: OMEGA/2THETA, deg
y-Scale: linear cps
peakpos. width height
34.0910 17.5 111557
34.1340 14.8 97022
125K
100K
75K
50K
25K
0K
34.000
34.050
34.100
34.150
34.200
AGA78-I.X02 om-2th: 34.1100 68.220 R-phi-x-z: 180.0 -2.40 1.00 0.00

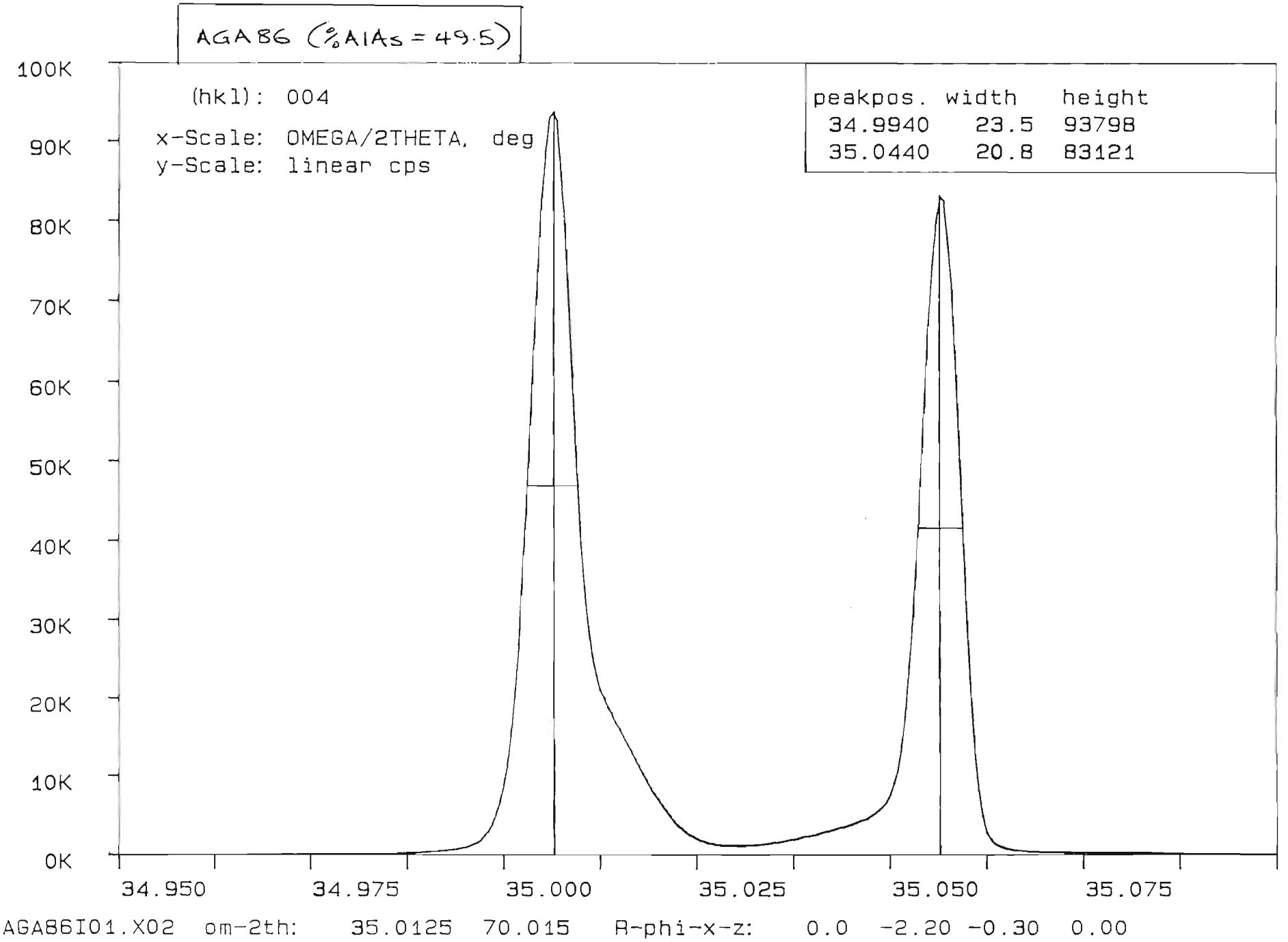
AGA86 (%AlAs = 49.5)
(hkl): 004
x-Scale: OMEGA/2THETA, deg
y-Scale: linear cps
peakpos. width height
34.9940 23.5 93798
35.0440 20.8 83121
100K
90K
80K
70K
60K
50K
40K
30K
20K
10K
0K
34.950
34.975
35.000
35.025
35.050
35.075
AGA86I01.X02 om-2th: 35.0125 70.015 R-phi-x-z: 0.0 -2.20 -0.30 0.00

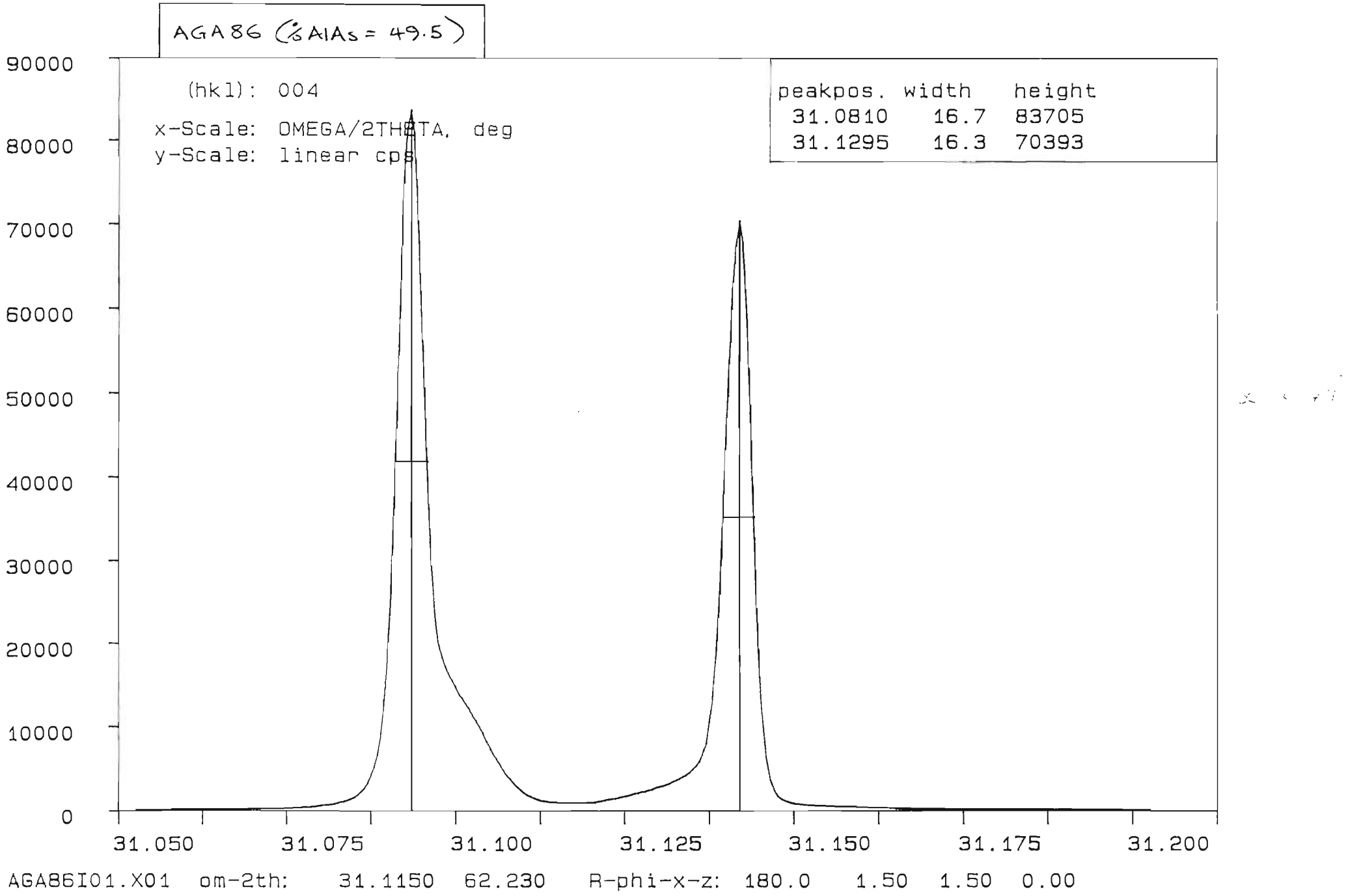
AGA86 (%AlAs = 49.5)
(hkl): 004
x-Scale: OMEGA/2THETA, deg
y-Scale: linear cps
peakpos. width height
31.0810 16.7 83705
31.1295 16.3 70393
90000
80000
70000
60000
50000
40000
30000
20000
10000
0
31.050
31.075
31.100
31.125
31.150
31.175
31.200
AGA86I01.X01 om-2th: 31.1150 62.230 R-phi-x-z: 180.0 1.50 1.50 0.00

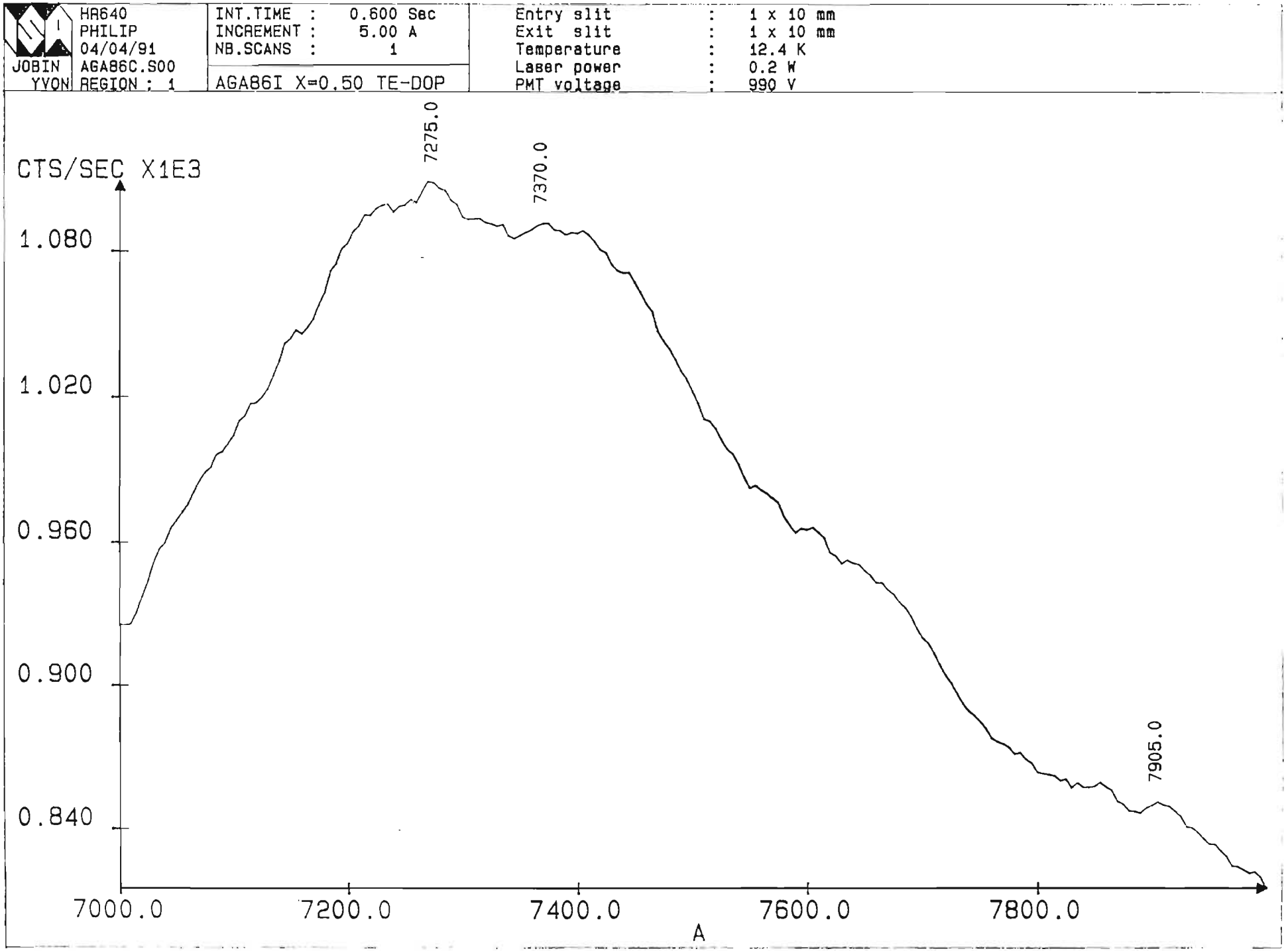
HR640
PHILIP
04/04/91
JOBIN
YVON
AGA86C.S00
REGION : 1
INT.TIME : 0.600 Sec
INCREMENT : 5.00 A
NB.SCANS : 1
AGA86I X=0.50 TE-DOP
Entry slit : 1 x 10 mm
Exit slit : 1 x 10 mm
Temperature : 12.4 K
Laser power : 0.2 W
PMT voltage : 990 V
CTS/SEC X1E3
1.080
1.020
0.960
0.900
0.840
7275.0
7370.0
7905.0
7000.0
7200.0
7400.0
7600.0
7800.0
A

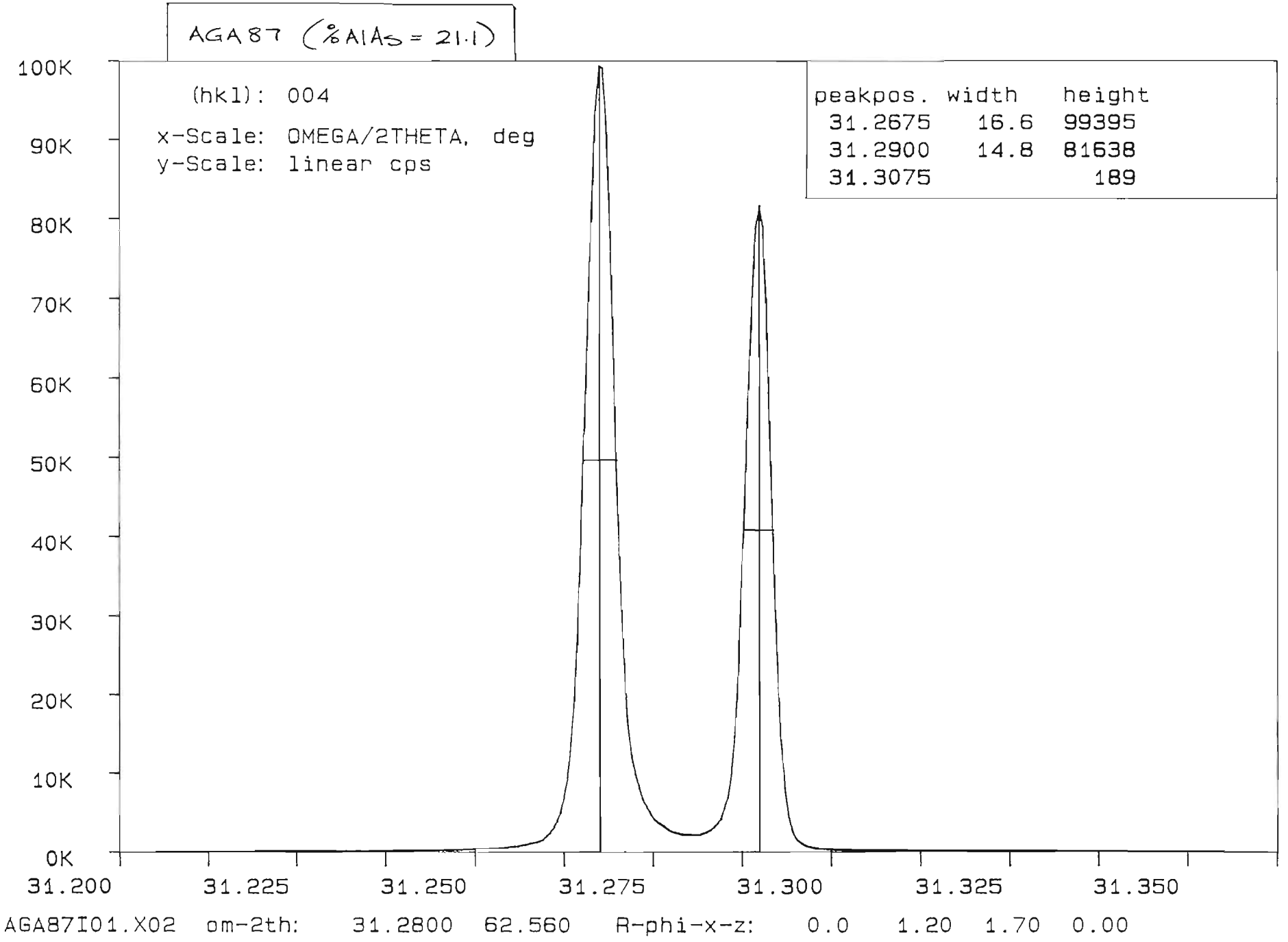
AGA87 (%AlAs = 21.1)
(hkl): 004
x-Scale: OMEGA/2THETA, deg
y-Scale: linear cps
peakpos. width height
31.2675 16.6 99395
31.2900 14.8 81638
31.3075 189
100K
90K
80K
70K
60K
50K
40K
30K
20K
10K
0K
31.200
31.225
31.250
31.275
31.300
31.325
31.350
AGA87I01.X02 om-2th: 31.2800 62.560 R-phi-x-z: 0.0 1.20 1.70 0.00

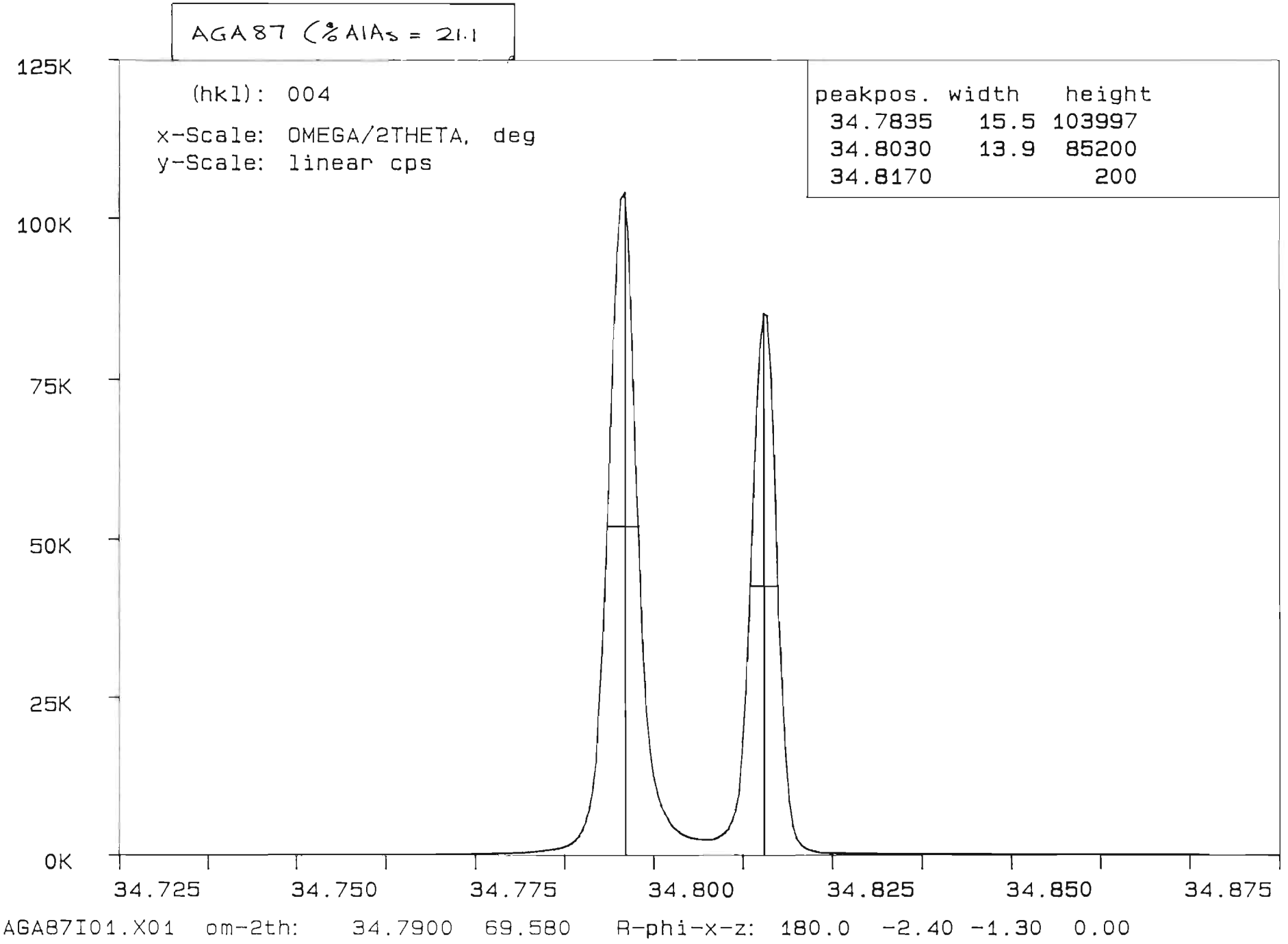
AGA87 (%AlAs = 21.1
(hkl): 004
x-Scale: OMEGA/2THETA, deg
y-Scale: linear cps
peakpos. width height
34.7835 15.5 103997
34.8030 13.9 85200
34.8170 200
125K
100K
75K
50K
25K
0K
34.725
34.750
34.775
34.800
34.825
34.850
34.875
AGA87I01.X01 om-2th: 34.7900 69.580 R-phi-x-z: 180.0 -2.40 -1.30 0.00

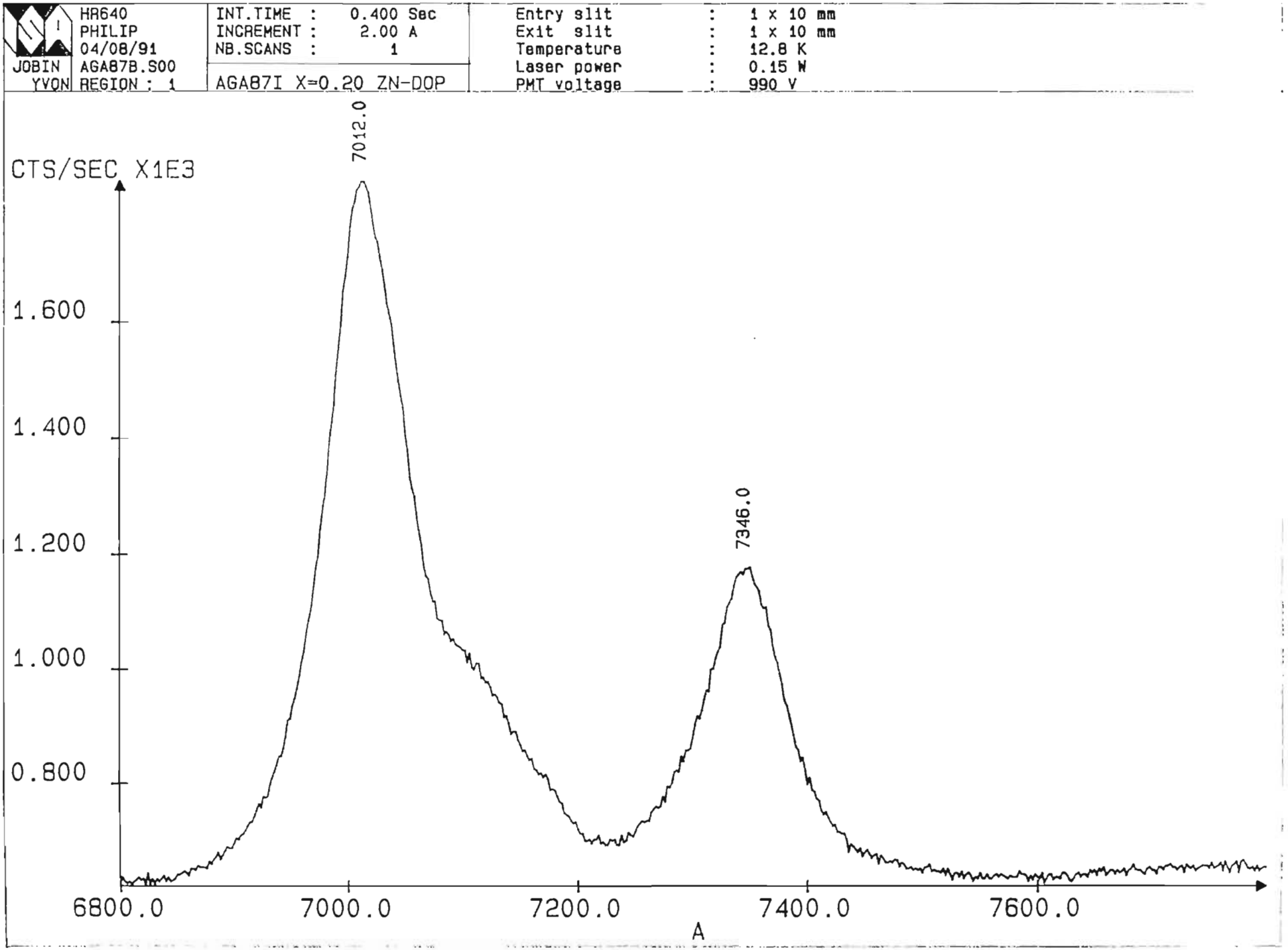
HR640
PHILIP
04/08/91
JOBIN YVON
AGA87B.S00
REGION : 1
INT.TIME : 0.400 Sec
INCREMENT : 2.00 A
NB.SCANS : 1
AGA87I X=0.20 ZN-DOP
Entry slit : 1 x 10 mm
Exit slit : 1 x 10 mm
Temperature : 12.8 K
Laser power : 0.15 W
PMT voltage : 990 V
7012.0
7346.0
CTS/SEC X1E3
1.600
1.400
1.200
1.000
0.800
6800.0
7000.0
7200.0
7400.0
7600.0
A

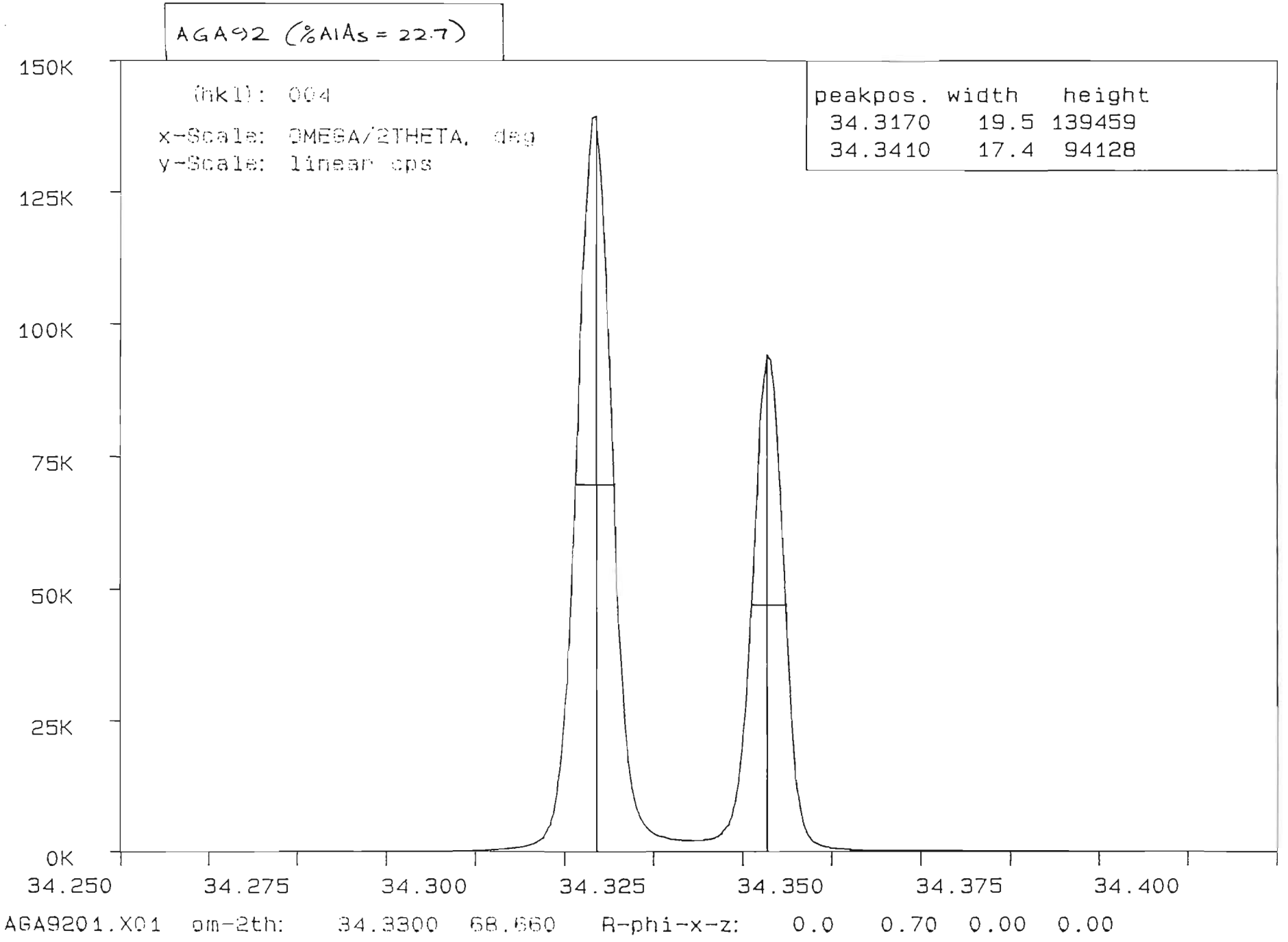
AGA92 (%AlAs = 22.7)
(hkl): 004
x-Scale: OMEGA/2THETA, deg
y-Scale: linear cps
peakpos. width height
34.3170 19.5 139459
34.3410 17.4 94128
150K
125K
100K
75K
50K
25K
0K
34.250
34.275
34.300
34.325
34.350
34.375
34.400
AGA9201.X01 om-2th: 34.3300 68.660 R-phi-x-z: 0.0 0.70 0.00 0.00

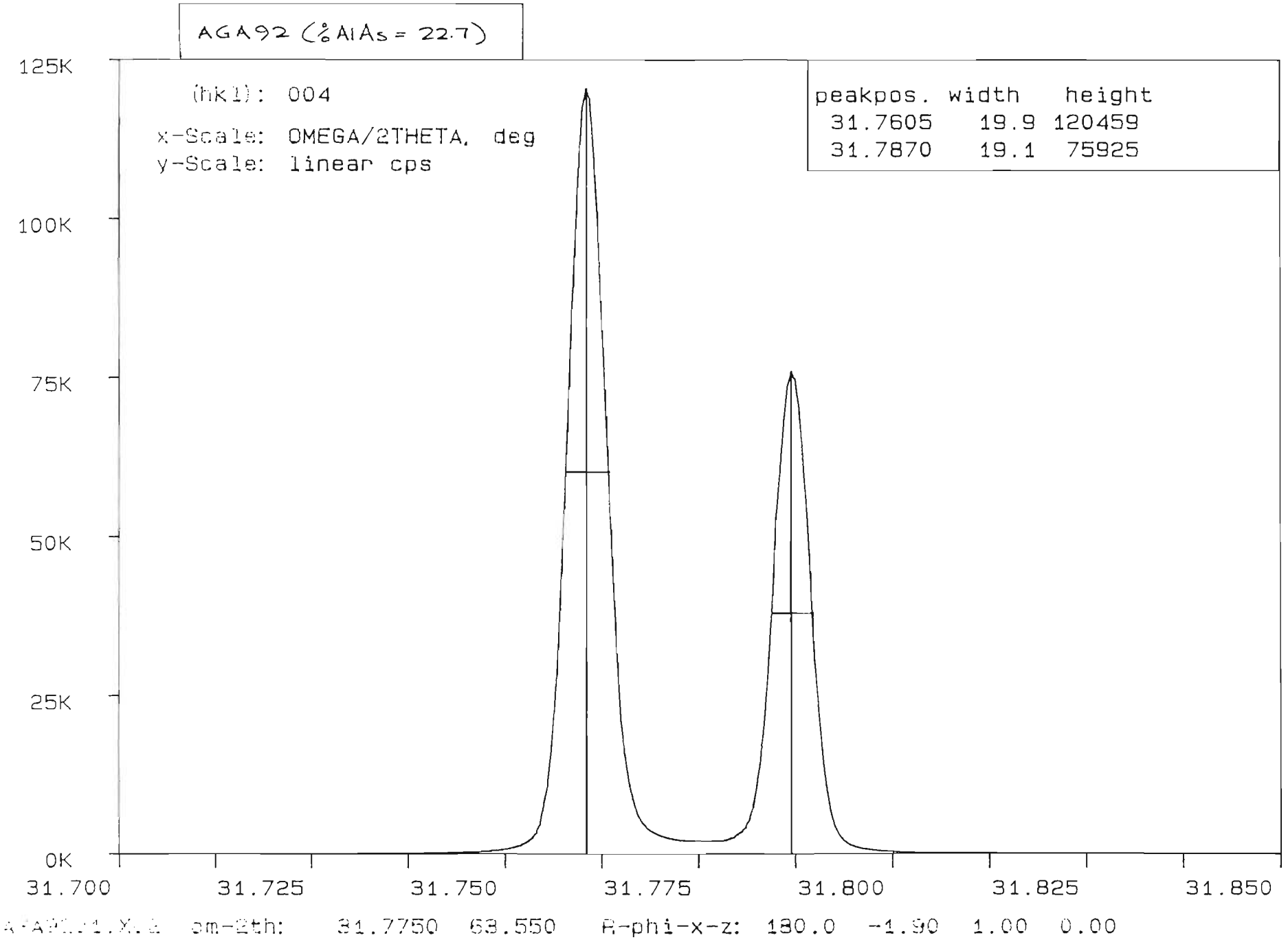
AGA92 (% AlAs = 22.7)
(hkl): 004
x-Scale: OMEGA/2THETA, deg
y-Scale: linear cps
peakpos. width height
31.7605 19.9 120459
31.7870 19.1 75925
125K
100K
75K
50K
25K
0K
31.700
31.725
31.750
31.775
31.800
31.825
31.850
A-API.11.X.2 om-2th: 31.7750 63.550 R-phi-x-z: 180.0 -1.90 1.00 0.00

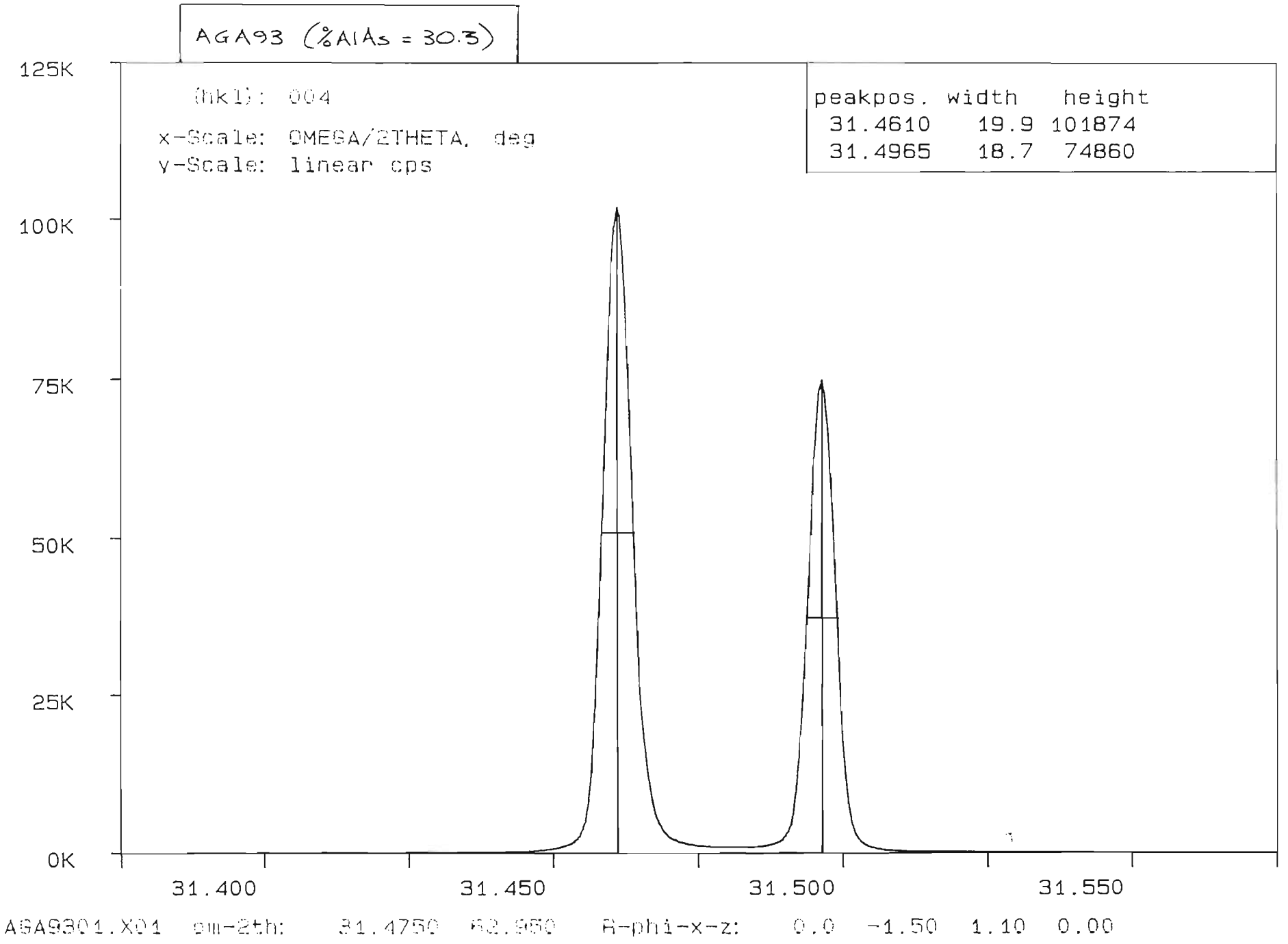
AGA93 (%AlAs = 30.3)
(hkl): 004
x-Scale: OMEGA/2THETA, deg
y-Scale: linear cps
peakpos. width height
31.4610 19.9 101874
31.4965 18.7 74860
125K
100K
75K
50K
25K
0K
31.400
31.450
31.500
31.550
AGA9301.X01 om-2th: 31.4750 62.950 R-phi-x-z: 0.0 -1.50 1.10 0.00

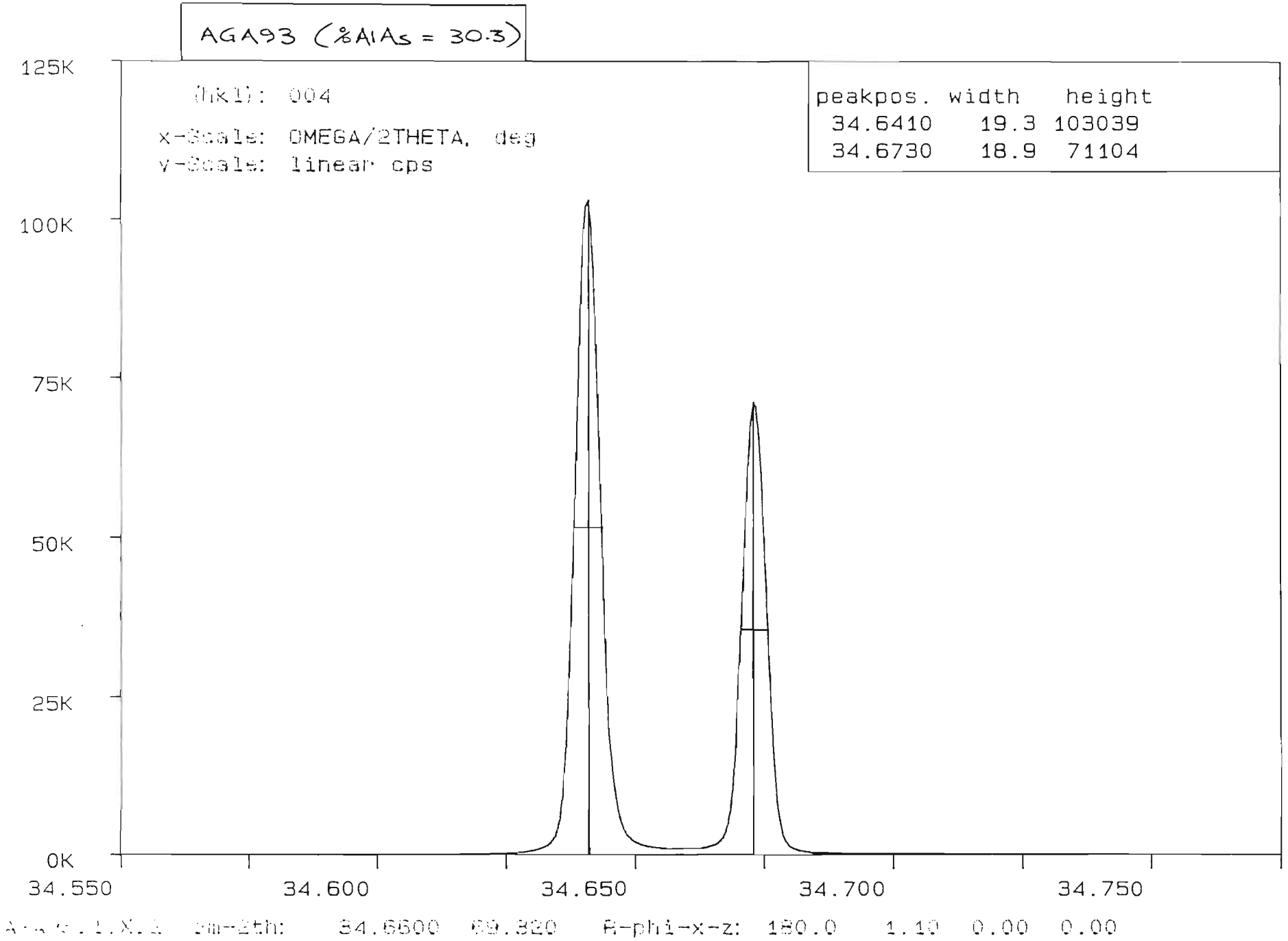
AGA93 (%AlAs = 30.3)
(hkl): 004
x-Scale: OMEGA/2THETA, deg
y-Scale: linear cps
peakpos. width height
34.6410 19.3 103039
34.6730 18.9 71104
125K
100K
75K
50K
25K
0K
34.550
34.600
34.650
34.700
34.750
Omega-2th: 34.6600 69.320 A-phi-x-z: 180.0 1.10 0.00 0.00

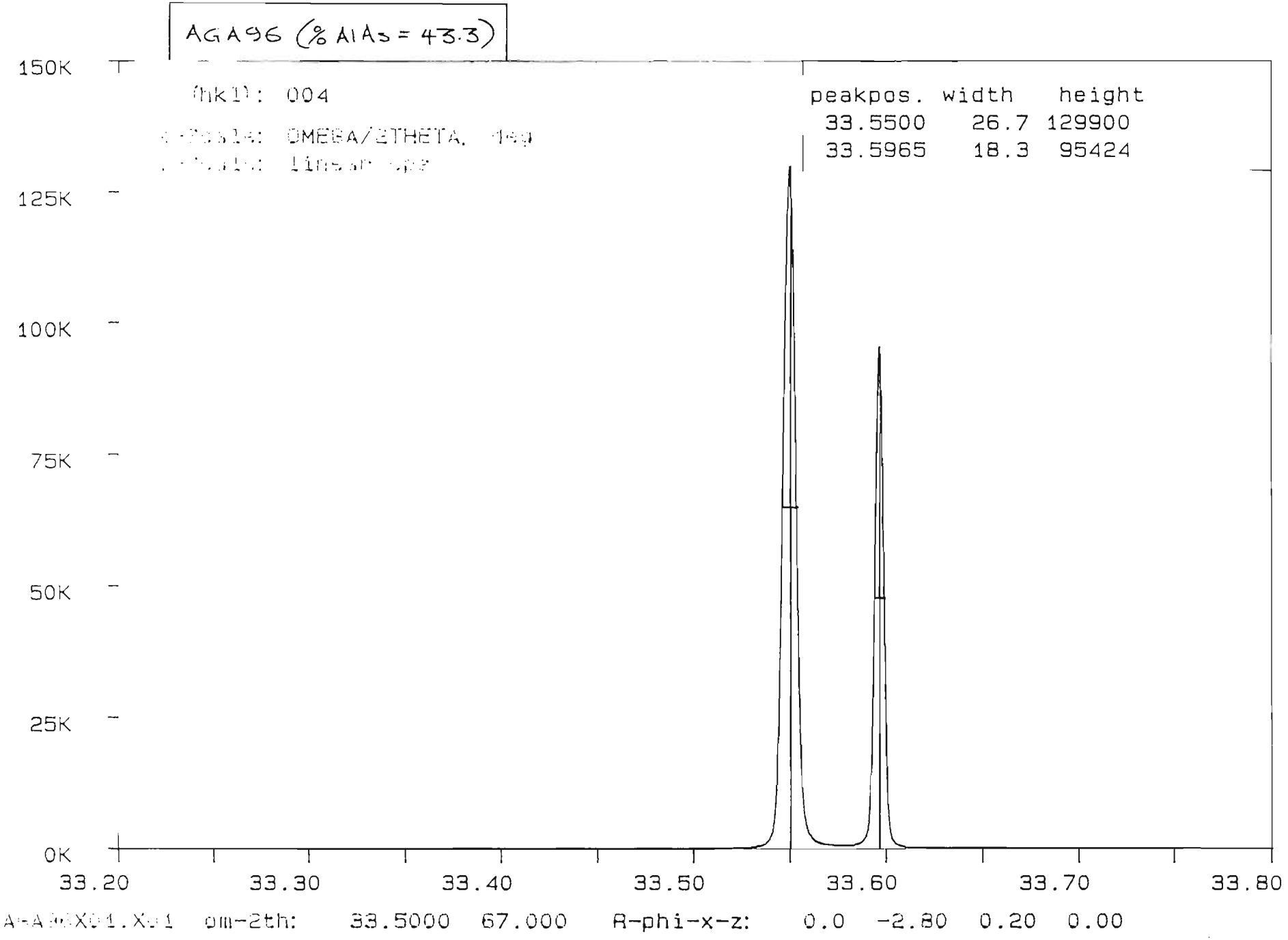
AGA96 (% AlAs = 43.3)
hkl: 004
peakpos. width height
33.5500 26.7 129900
33.5965 18.3 95424
150K
125K
100K
75K
50K
25K
0K
33.20
33.30
33.40
33.50
33.60
33.70
33.80
om-2th: 33.5000 67.000
R-phi-x-z: 0.0 -2.80 0.20 0.00

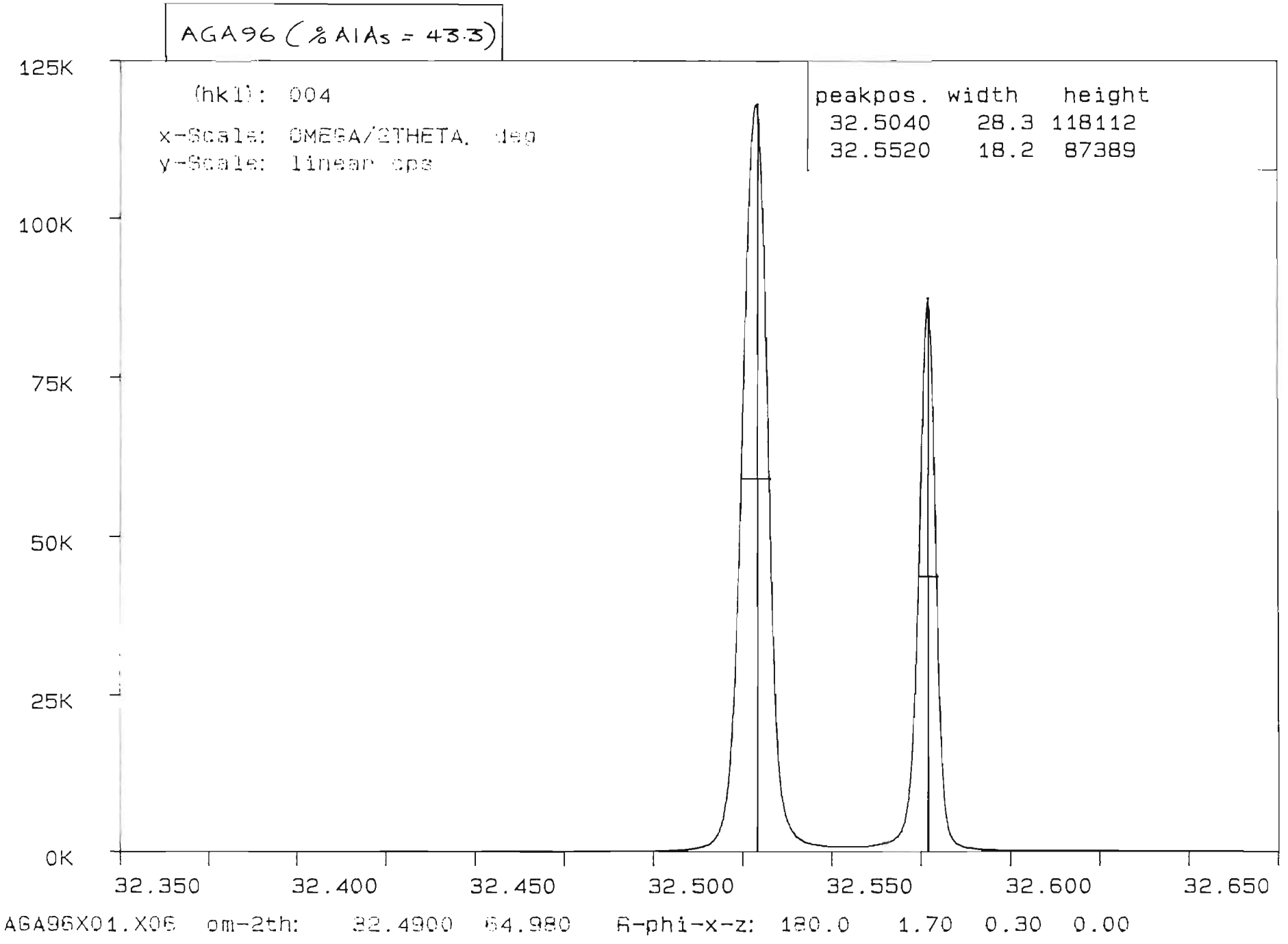
AGA96 (% AlAs = 43.3)
(hkl): 004
x-Scale: OMEGA/2THETA, deg
y-Scale: linear cps
peakpos. width height
32.5040 28.3 118112
32.5520 18.2 87389
125K
100K
75K
50K
25K
0K
32.350
32.400
32.450
32.500
32.550
32.600
32.650
AGA96X01.X06 om-2th: 32.4900 64.980 R-phi-x-z: 180.0 1.70 0.30 0.00

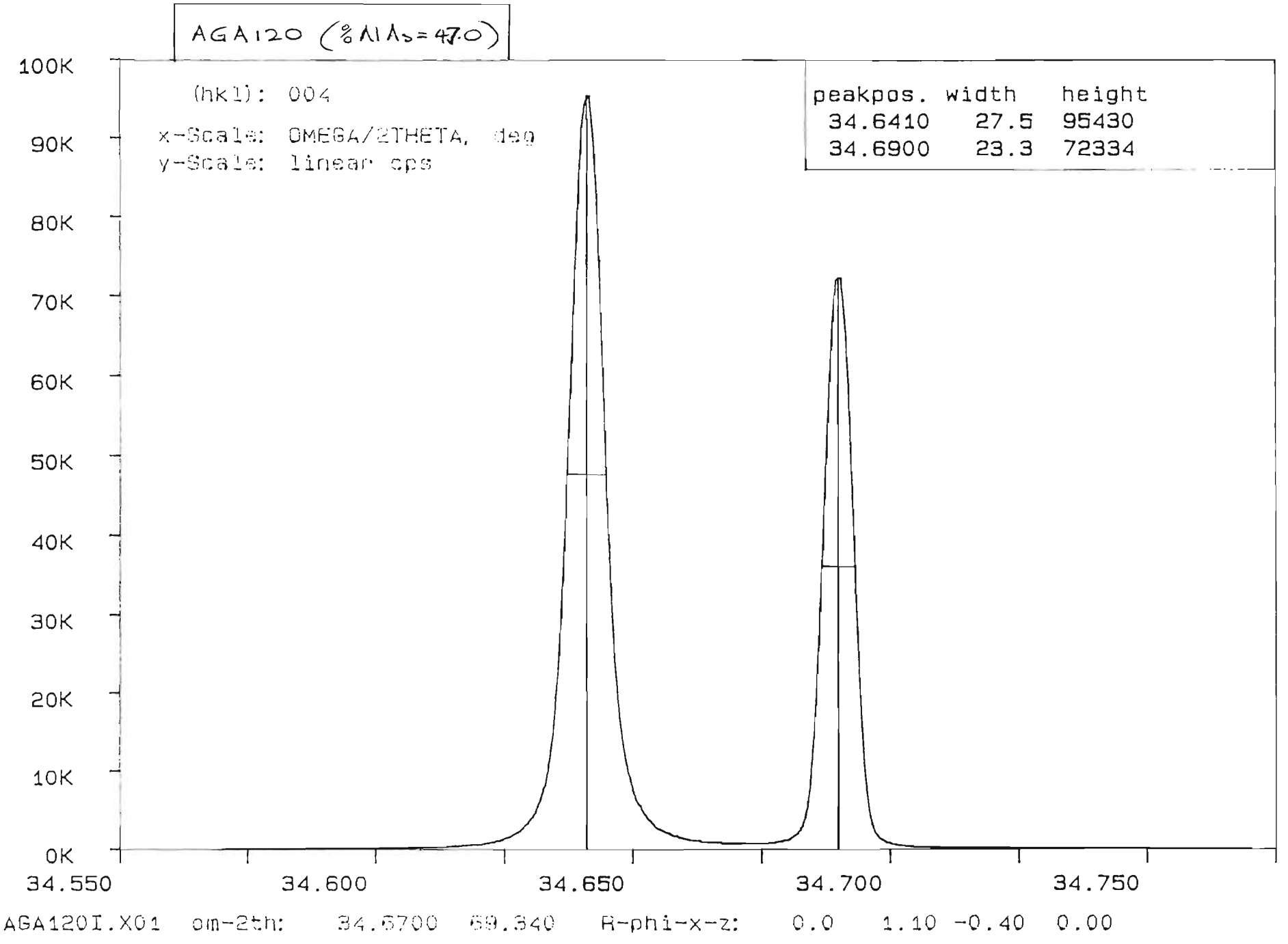
AGA120 (%MIAs=47.0)
(hkl): 004
x-Scale: OMEGA/2THETA, deg
y-Scale: linear cps
peakpos. width height
34.6410 27.5 95430
34.6900 23.3 72334
100K
90K
80K
70K
60K
50K
40K
30K
20K
10K
0K
34.550
34.600
34.650
34.700
34.750
AGA120I.X01 om-2th: 34.6700 69.340 R-phi-x-z: 0.0 1.10 -0.40 0.00

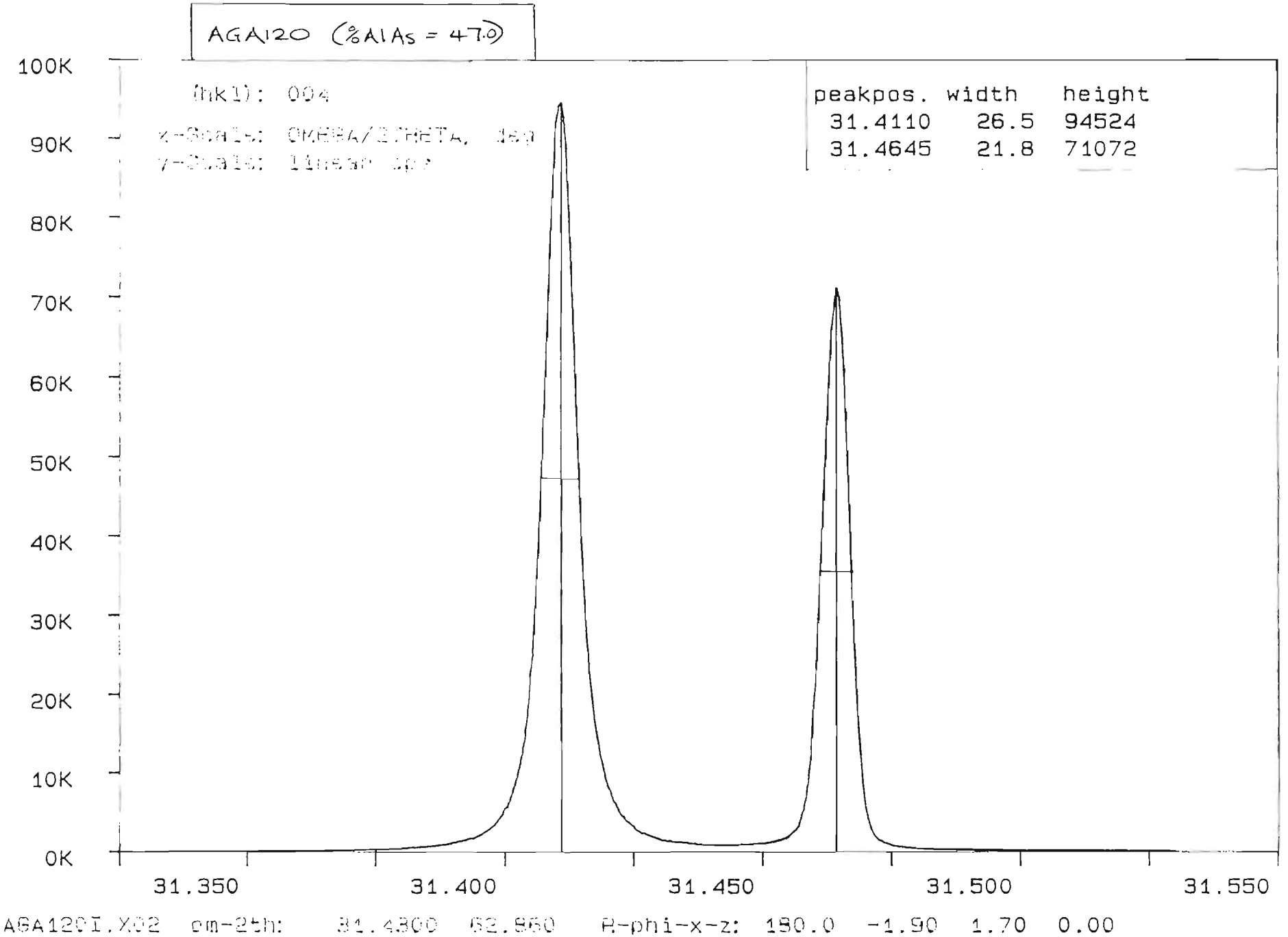
AGA120 (%AlAs = 47.0)
(hkl): 004
peakpos. width height
31.4110 26.5 94524
31.4645 21.8 71072
100K
90K
80K
70K
60K
50K
40K
30K
20K
10K
0K
31.350
31.400
31.450
31.500
31.550
AGA120I.X02 om-2th: 31.4800 62.860 R-phi-x-z: 180.0 -1.90 1.70 0.00

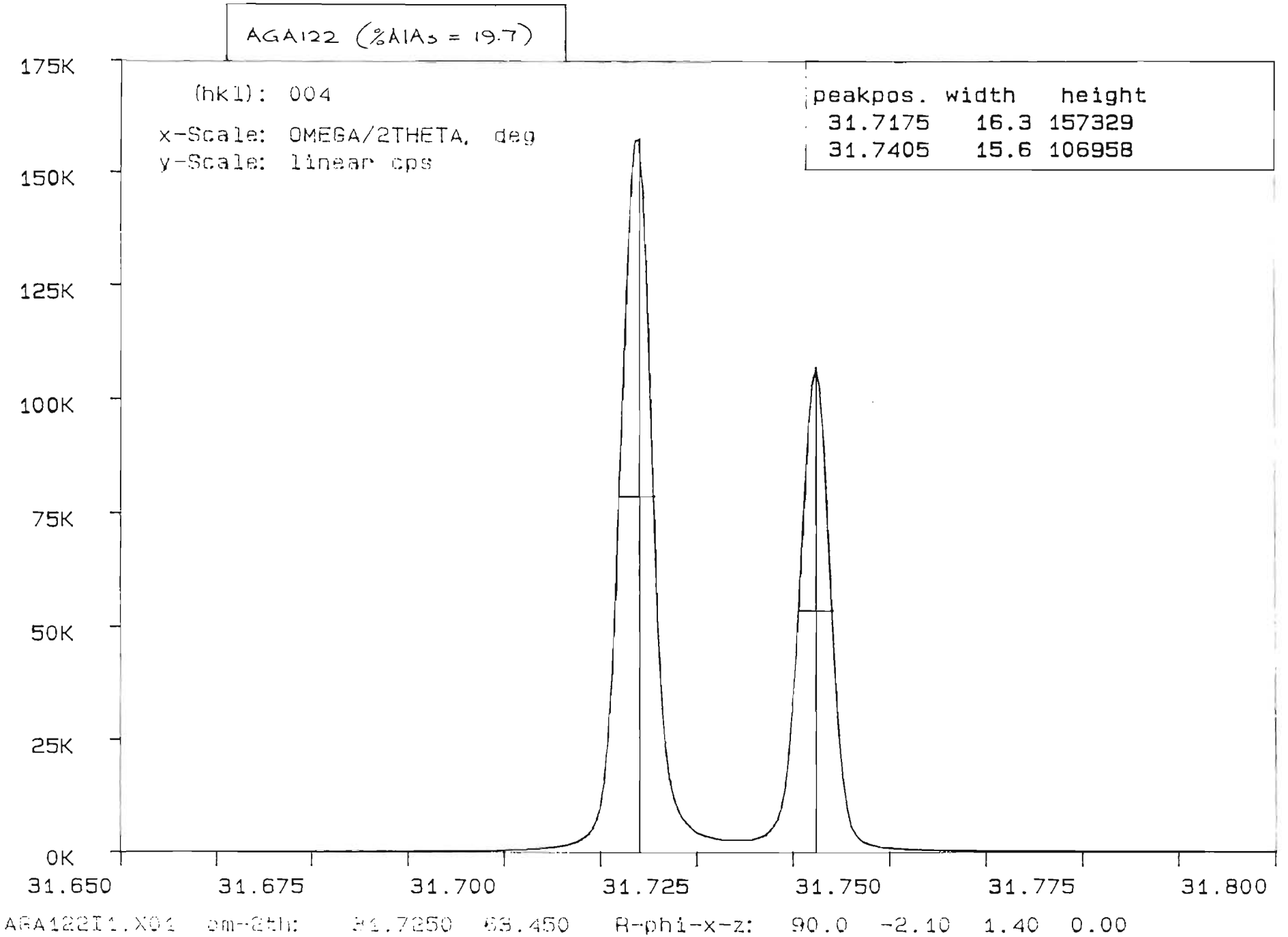
AGA122 (%AlAs = 19.7)
(hkl): 004
x-Scale: OMEGA/2THETA, deg
y-Scale: linear cps
peakpos. width height
31.7175 16.3 157329
31.7405 15.6 106958
175K
150K
125K
100K
75K
50K
25K
0K
31.650
31.675
31.700
31.725
31.750
31.775
31.800
AGA122I1.X01 em-eth: 31.7250 68.450 R-phi-x-z: 90.0 -2.10 1.40 0.00

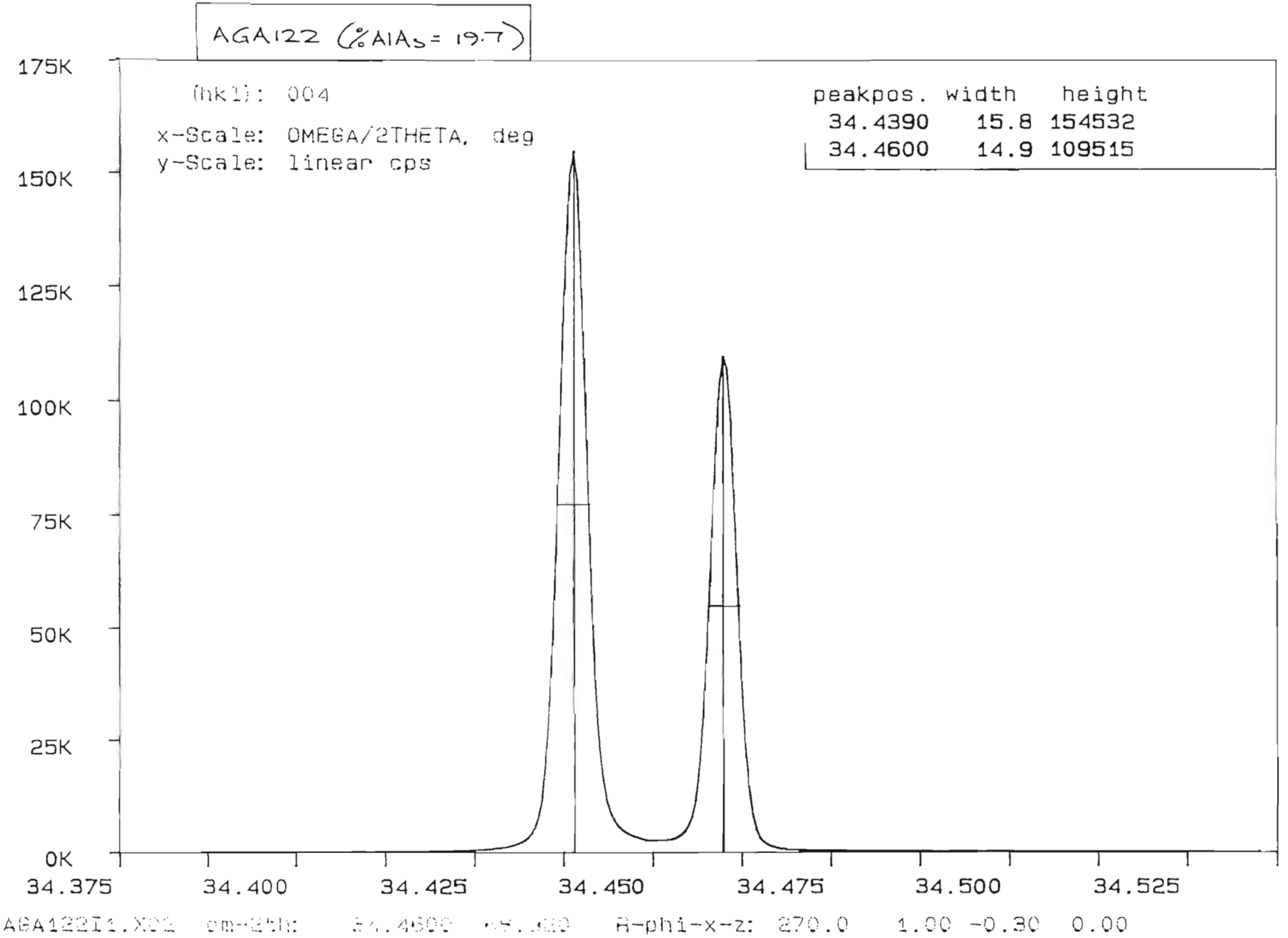
AGA122 (%AlAs = 19.7)
(hkl): 004
x-Scale: OMEGA/2THETA, deg
y-Scale: linear cps
peakpos. width height
34.4390 15.8 154532
34.4600 14.9 109515
175K
150K
125K
100K
75K
50K
25K
0K
34.375
34.400
34.425
34.450
34.475
34.500
34.525
AGA122I1.XRD om-2th: 34.4300 45.000 A-phi-x-z: 270.0 1.00 -0.30 0.00

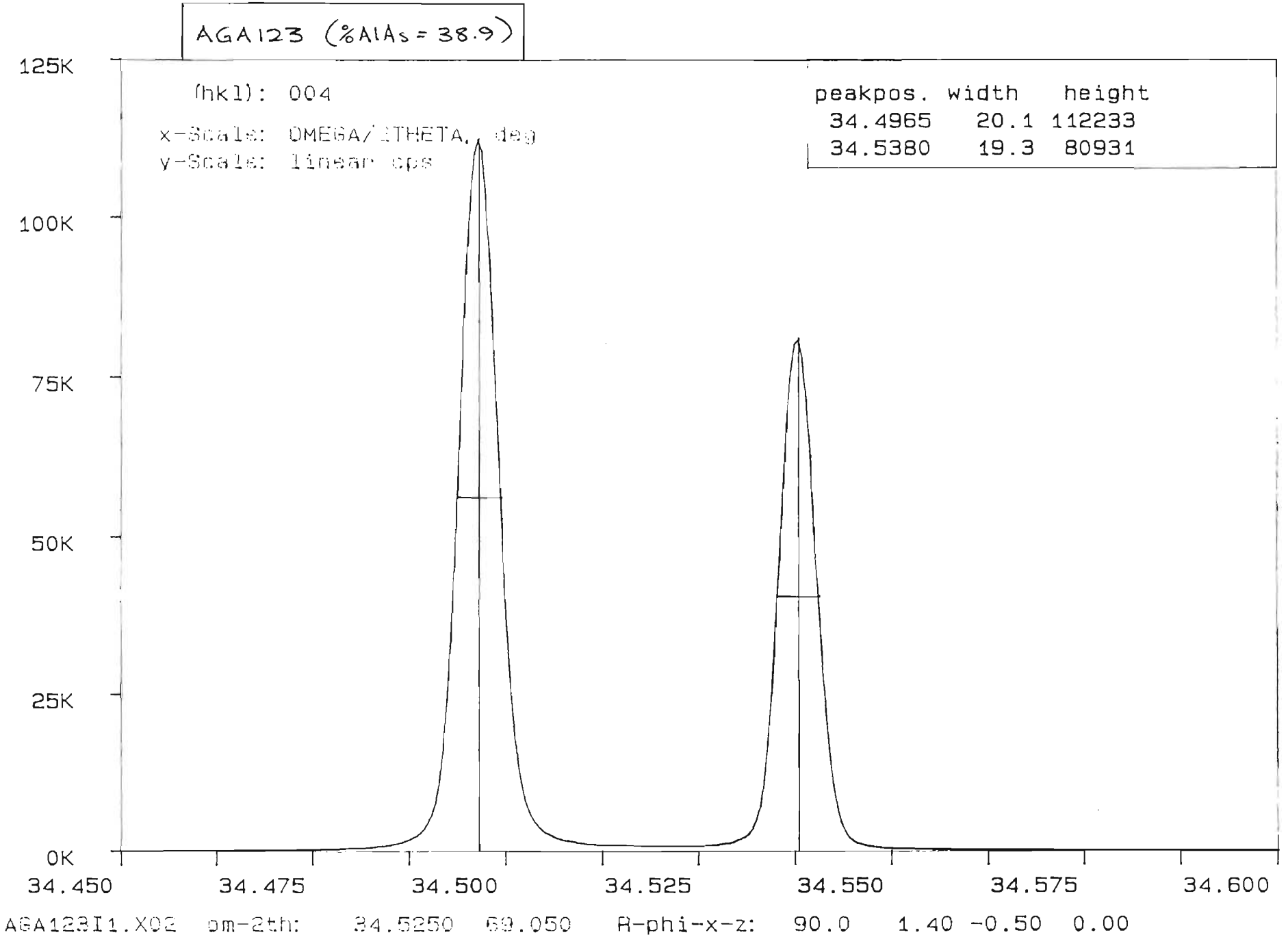
AGA123 (%AlAs = 38.9)
(hkl): 004
x-Scale: OMEGA/2THETA, deg
y-Scale: linear cps
peakpos. width height
34.4965 20.1 112233
34.5380 19.3 80931
125K
100K
75K
50K
25K
0K
34.450
34.475
34.500
34.525
34.550
34.575
34.600
AGA123I1.X02 bm-2th: 34.5250 69.050 R-phi-x-z: 90.0 1.40 -0.50 0.00

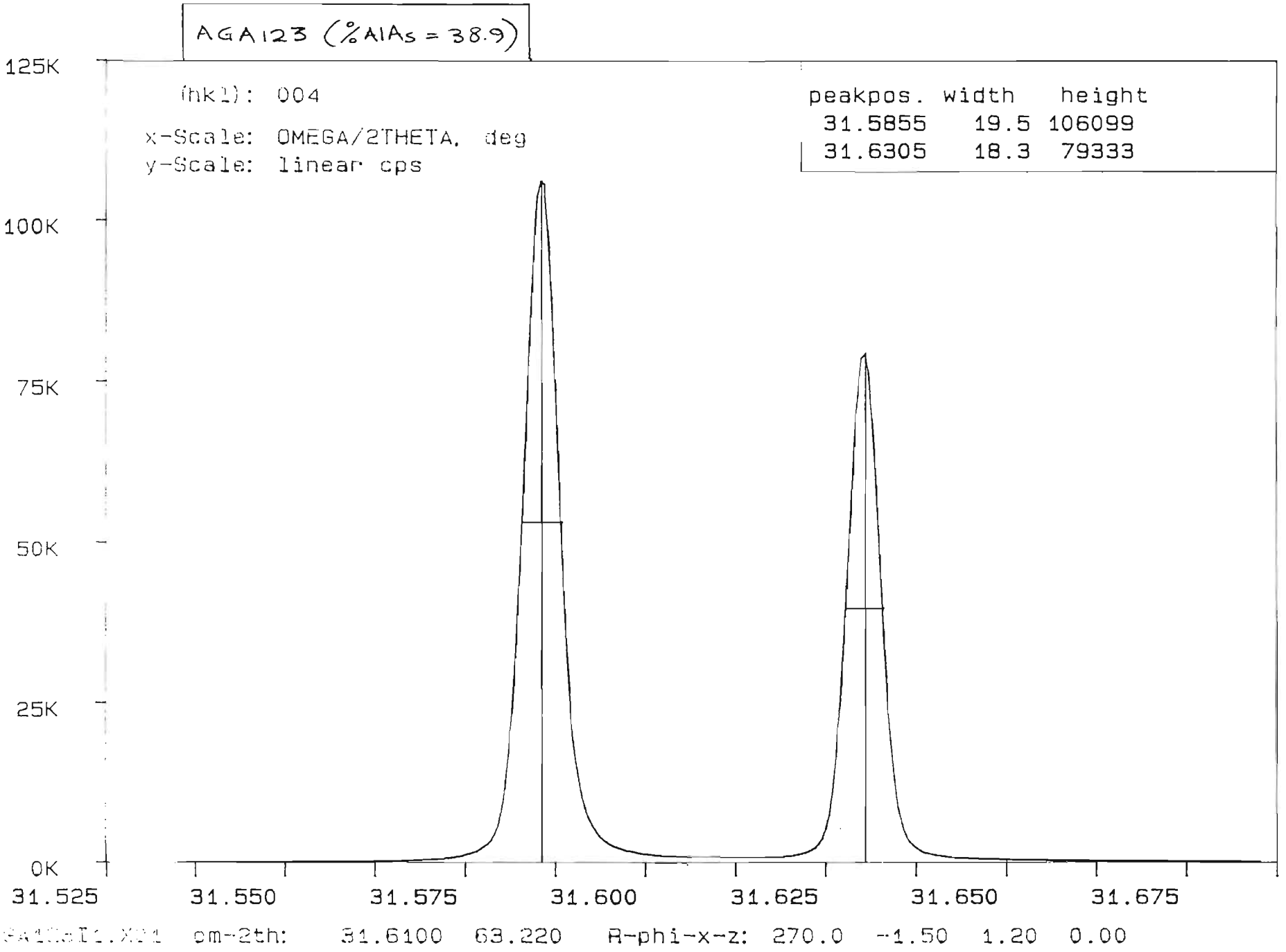
AGA123 (%AlAs = 38.9)
(hkl): 004
x-Scale: OMEGA/2THETA, deg
y-Scale: linear cps
peakpos. width height
31.5855 19.5 106099
31.6305 18.3 79333
125K
100K
75K
50K
25K
0K
31.525
31.550
31.575
31.600
31.625
31.650
31.675
om-2th: 31.6100 63.220 R-phi-x-z: 270.0 -1.50 1.20 0.00

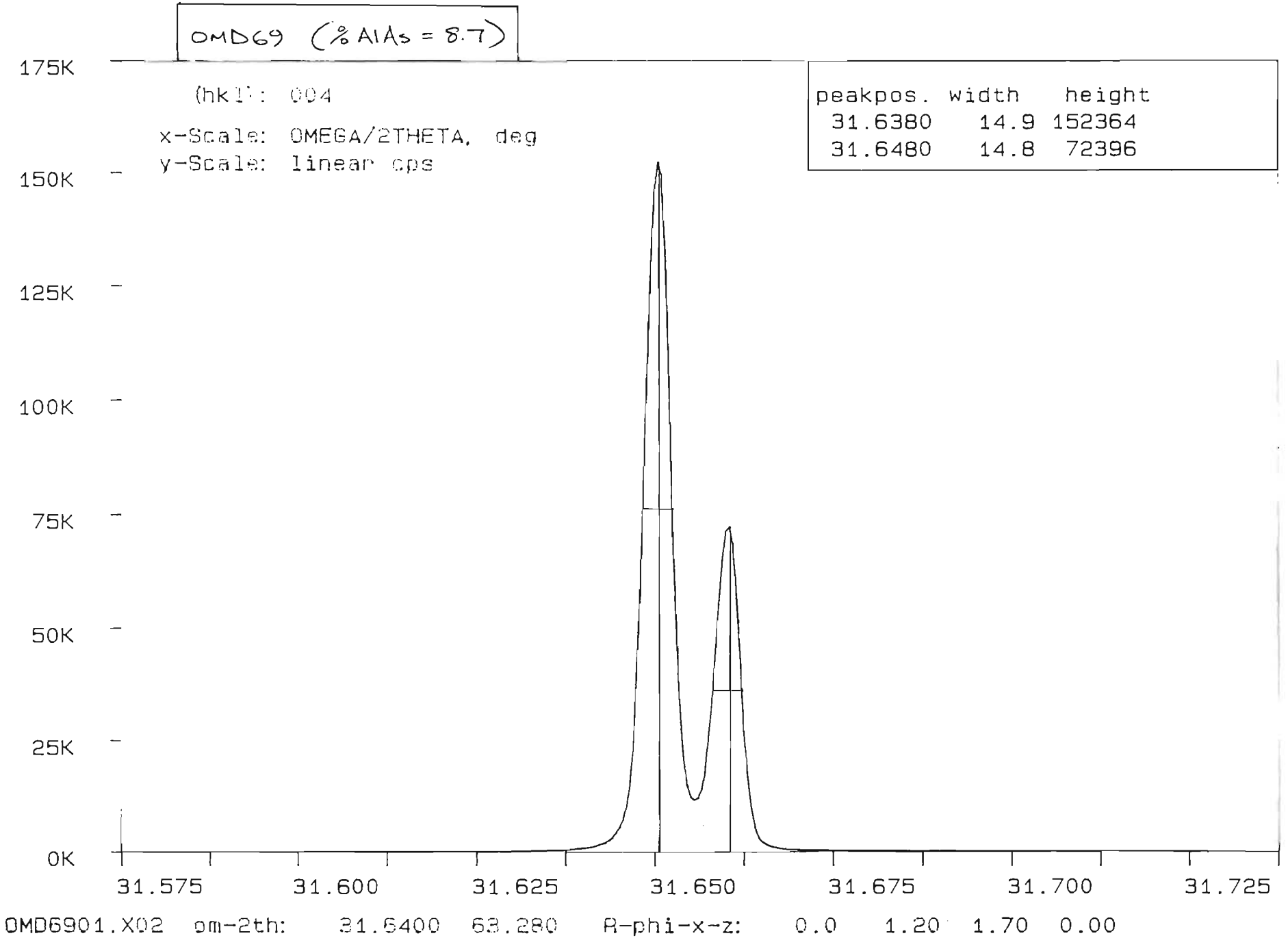
OMD69 (% AlAs = 8.7)
(hkl): 004
x-Scale: OMEGA/2THETA, deg
y-Scale: linear cps
peakpos. width height
31.6380 14.9 152364
31.6480 14.8 72396
175K
150K
125K
100K
75K
50K
25K
0K
31.575
31.600
31.625
31.650
31.675
31.700
31.725
OMD6901.X02 om-2th: 31.6400 63.280 R-phi-x-z: 0.0 1.20 1.70 0.00

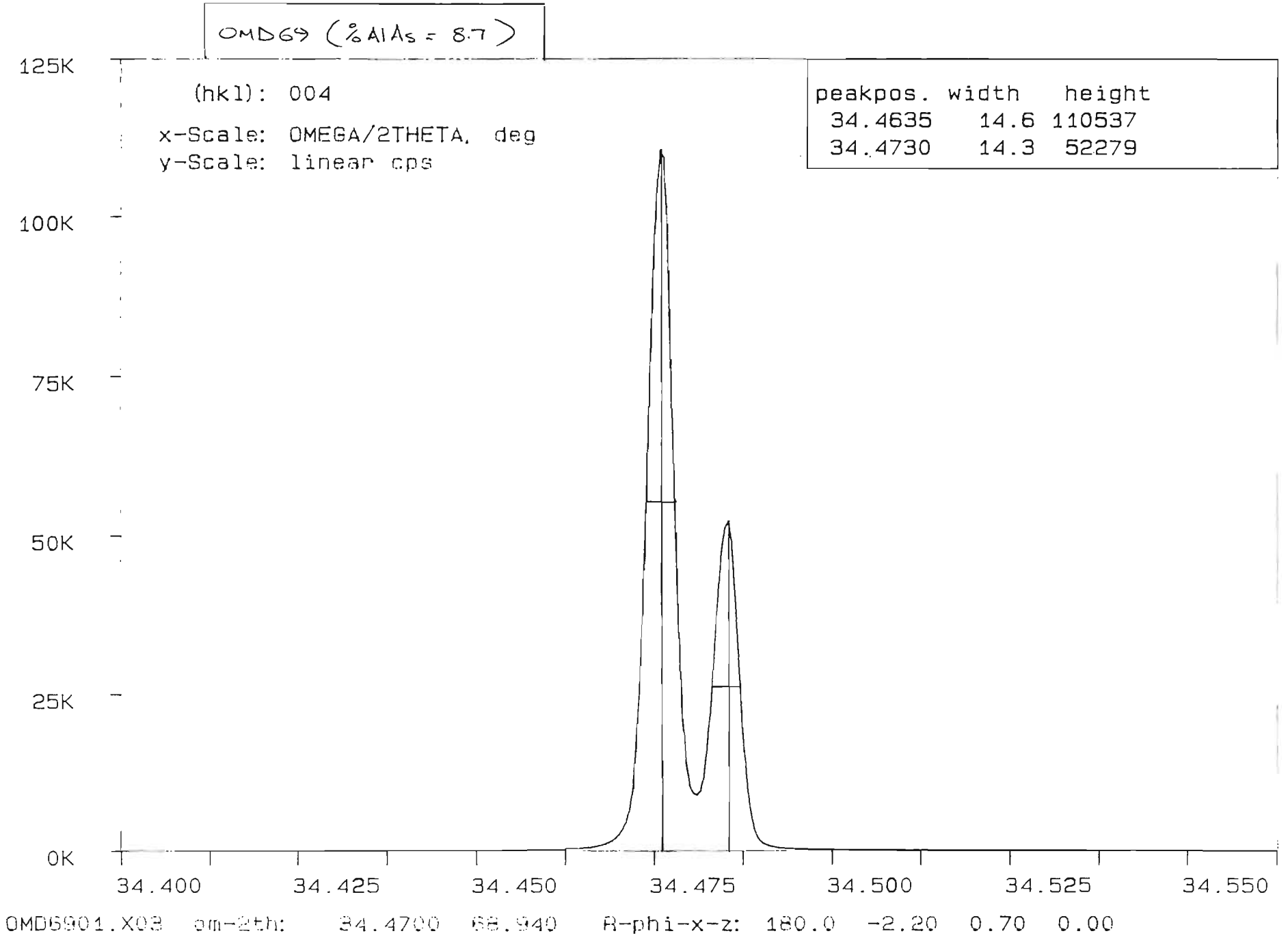
OMD69 (%AlAs = 8.7)
(hkl): 004
x-Scale: OMEGA/2THETA, deg
y-Scale: linear cps
peakpos. width height
34.4635 14.6 110537
34.4730 14.3 52279
125K
100K
75K
50K
25K
0K
34.400
34.425
34.450
34.475
34.500
34.525
34.550
OMD6901.X08 om-2th: 34.4700 68.940 R-phi-x-z: 180.0 -2.20 0.70 0.00

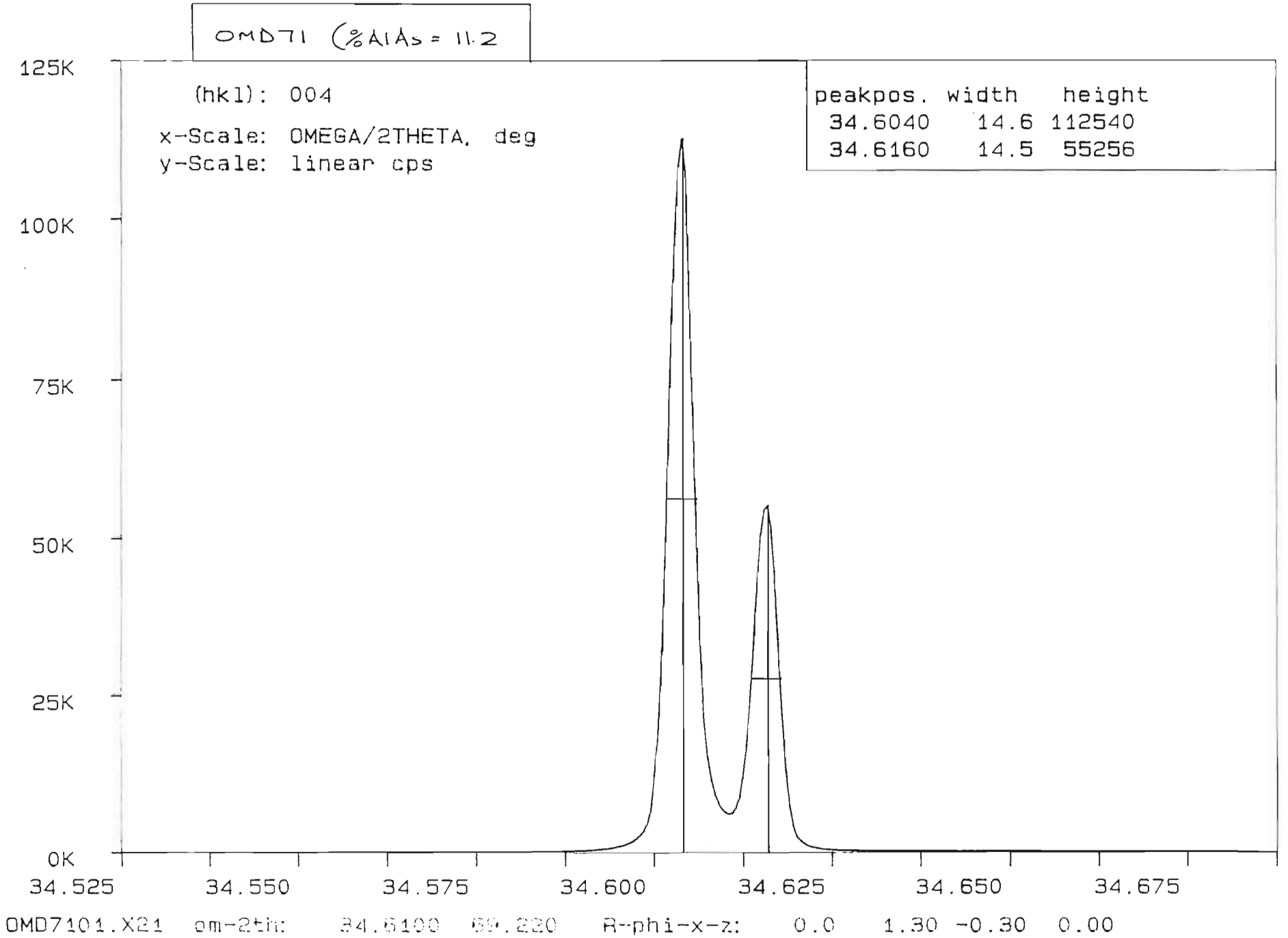
OMD71 (%AlAs = 11.2
(hkl): 004
x-Scale: OMEGA/2THETA, deg
y-Scale: linear cps
peakpos. width height
34.6040 14.6 112540
34.6160 14.5 55256
125K
100K
75K
50K
25K
0K
34.525
34.550
34.575
34.600
34.625
34.650
34.675
OMD7101.X21 om-2th: 34.6100 69.220 R-phi-x-z: 0.0 1.30 -0.30 0.00

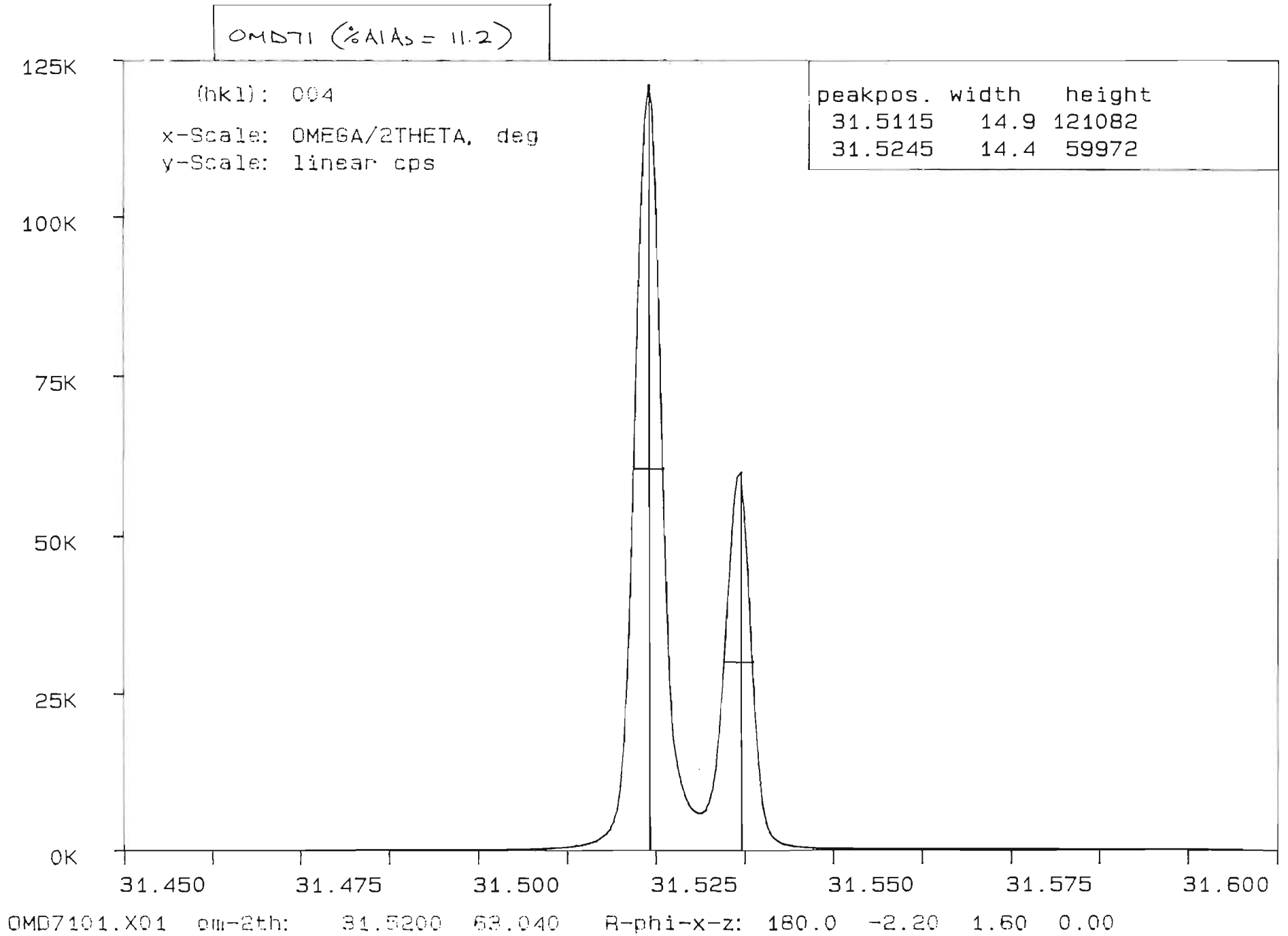
OMD71 (%AlAs = 11.2)
(hkl): 004
x-Scale: OMEGA/2THETA, deg
y-Scale: linear cps
peakpos. width height
31.5115 14.9 121082
31.5245 14.4 59972
125K
100K
75K
50K
25K
0K
31.450
31.475
31.500
31.525
31.550
31.575
31.600
OMD7101.X01 om-2th: 31.5200 63.040 R-phi-x-z: 180.0 -2.20 1.60 0.00